NAGOYA UNIVERSITY

DOCTORAL THESIS

Influence of Primordial Non-Gaussianities on statistical properties of galaxy shapes

---

Author:
Kazuhiro KOGAI

Supervisor:
Dr. Kiyotomo ICHIKI

February 14, 2022

Abstract

According to the current prevailing cosmological scenario, the very early Universe experienced an inflation period, which was highlighted by rapid accelerated expansion. In this scenario, the inflation was caused by a scalar field, called inflaton. The quantum fluctuations of the inflaton became seeds of the fluctuations in the current structure formation.

To determine the features of the fluctuations, a statistical treatment needs to be adopted since the theory cannot uniquely predict the amplitude of the fluctuations at each point. However, it can predict the expectation value of the correlations between the fluctuations. The initial fluctuations closely obey the Gaussian. However, the non-Gaussianity, which is a slight deviation from the Gaussian, reflects the nature of physics in the early Universe.

The physics beyond the Standard Model, such as string theory, predicts new particles at ultra-high energy, which are not yet discovered. If new particles interact with the inflaton, their existences can be tested by investigating the nature of the initial fluctuations. String theory predicts the particles with a higher spin as new ones. If higher spin particles interact with the inflaton, they leave imprints characterized by the non-Gaussianity of the primordial fluctuations.

This thesis discusses the relationship between galaxy shape correlations and primordial fluctuations. The shape of elliptical galaxies, whose formation started early and long ago, correlates with the tidal field of the surrounding dark matter halos. Since the primordial fluctuations generate the tidal field, the correlations of galaxy shapes could give us access to the nature of the primordial fluctuations. We investigate the effect of the primordial non-Gaussianity induced by the spin particles on the galaxy shape correlations. We find that the contribution of the angular-dependent primordial non-Gaussianity induced by the spin-2 particle in the correlations of the galaxy shapes appears on different scales, which depends on the mass of the particle. Moreover, we propose a method to investigate the imprint of higher-spin particles using galaxy shape correlations. We find that the imprint of the primordial non-Gaussianity generated by spin-n particle could be detectable through the decomposition of the galaxy shapes into n-th moment.

Acknowledgements

I would like to thank those who have allowed me to be involved in research related to cosmology. To begin with, I thank Professor Naoshi Sugiyama, who is the PI of C-lab and the Vice President Director at Nagoya University. He supported me for six years after I was assigned to the Cosmology group and taught me the basics of cosmology. I would like to thank my supervisor Kiyotomo Ichiki who always gave me practical advice on my research. I cannot thank Yuko Urakawa enough, who mainly supervised me. She was kind enough to teach me about the research project and about basic things I did not understand and gave me many opportunities to interact with other people.

I am grateful for my other collaborators. Fabian Schmidt gave me the idea for the basis of my research. Takahiko Matsubara and Atsushi J. Nishizawa are professionals in the theory and data analysis in large-scale structures, and they have given me a significant step forward in my research. Kazuyuki Akitsu was always ready to help me if I had any problems with my research. If even one of them had been missing, this research would not have been possible. In another research project from this thesis, Yuichiro Tada gave me a detailed and concise interpretation of the models of the early Universe, and we were able to complete that project.

I would also like to thank the other current and former C-lab faculty members. Especially, Shuichiro Yokoyama, Hiroyuki Tashiro, and Takeshi Kobayashi made many comments on my research and made my research life more enjoyable.

I financially was supported as the Research Fellowship for Young Scientists of JSPS KAKENHI Grant No. JP19J22018. This grant supports enabled me to discuss my research with people from all over the world.

Lastly, I would like to thank my family for supporting my research life.

Contents

Chapter 1

Introduction

Modern cosmology can mostly explain the picture of the Universe with high precision observational data, assuming simple models. However, some problems remain unsolved. There is still much left to interpret all the cosmological scenarios in physical terms. For example, there is the origin of primordial fluctuations, which lead to the initial seeds of various structures of the Universe. Currently, reliable tracers on cosmological scales are mainly the cosmic microwave background (CMB) which is the photon coming towards us from the last scattering surface, and the large-scale structure (LSS) which comprises the distributions of galaxies, clusters of galaxy and so on. If the Universe were completely isotropy and homogeneity in the early epoch, it would not be able to produce the temperature fluctuations measured by the CMB and the density fluctuations on the LSS. As a theoretical approach, it was proposed that the Universe went through rapid accelerated expansion before the hot big bang, namely *inflation* [1, 2]. This is a powerful paradigm to describe physics in the early Universe and provides a mechanism for generating primordial fluctuations.

So far, many theoretical models have been proposed, which are compatible with observations. However, the detailed mechanism is yet to be determined. The upper constraint on the energy scale during inflation is estimated to be $H_{\rm inf} \lesssim 10^{13}$[GeV], where $H_{\rm inf}$ is the Hubble scale at the inflation epoch, from the CMB observation under the assumption of the simple inflation model [3]. From a different point of view, this implies that the analysis for the physics during inflation leads to testing the ultra-high-energy physics beyond the reach of any accelerator on the ground.

The Planck satellite, which is the telescope for the CMB in space, measures the temperature fluctuations up to $\mathcal{O}(10^{-4})$ around the uniform temperature $T \sim 2.7$K on the sky. The CMB observations suggest that tiny primordial fluctuations were adiabatic, a nearly scale-invariant, and an almost Gaussian distribution. One of the simplest models that broadly predict the measured properties is the single-field inflation model, in which the background dynamics during inflation is governed by a scalar field called *inflaton*, and the observed fluctuations are generated by stretching the inflaton's quantum fluctuations. Nevertheless, the origin of the inflaton has not been completely identified. The primordial gravitational waves generated during inflation also play an important role in making a piece of evidence for inflation. The primordial gravitational waves left the imprint as the CMB B-mode on large scales, which is the rotation part of the polarization of the CMB photons. For the detection, the forthcoming surveys such as *LiteBIRD* [4] are remarkable and have the potential to constrain the inflation energy scale tightly.

While the CMB observations provide rich information about the early Universe, the LSS reflects the current state of the Universe. Comparing the results of both observations is essential as it will reveal the time evolution of the Universe and is complementary to understanding the origin of the primordial fluctuations. Since astronomical objects such as galaxies are formed by the gravitational instability, their origin must be the primordial perturbations. This means that the LSS has the imprint of the primordial perturbations and can provide the information of physics in the early Universe. In addition, galaxy surveys to investigate the LSS have advantages compared to the CMB measurements since they can give the three-dimensional distribution of galaxies with redshift. In contrast, the CMB provides information only on the two-dimensional surface. The forthcoming galaxy surveys that target huge volumes, such as *the Nancy Grace Roman Space Telescope* [5], *Euclid* [6], and *Spectro-Photometer for the History of the Universe, Epoch of Reionization, and Ices Explorer*(SPHEREx) [7], *the Rubin Observatory Legacy Survey of Space and Time* (LSST) [8], have the potential to give tighter constraints on parameters compared to the CMB observations. In addition, galaxy surveys allow us to explore the structure of the Universe on broader scales, which is not possible by the CMB observations.

Moreover, galaxy imaging surveys provide not only the distribution but also the shape of the galaxy, similar to the polarization of CMB. The cosmic shear, which is the distortion of the galaxy by the weak lensing effect, is the powerful tracer of dark matter distribution since the weak lensing effect deforms the background intrinsic galaxy shape by foreground gravitational potentials (almost equivalent to the dark matter.) Recent notable results by the Dark Energy Survey [9], the Kilo-Degree Survey [10], and Subaru HSC observation [11] have reported the analysis of weak lensing with cosmic shear, which will provide material for a deeper understanding of the nature of dark energy and dark matter. For the weak lensing analysis, we must consider the nature of the intrinsic galaxy shapes generated by the large-scale tidal fields around the individual galaxy, which are known as Intrinsic Alignments [12, 13, 14, 15]. The intrinsic alignments reflect abundant information on the natures of the Universe.

We introduce some more about the primordial non-Gaussianities and intrinsic alignments, which are the main topics of this thesis.

Primordial non-Gaussianities

At present, the measured primordial perturbations nearly obey the Gaussian. However, it is still allowed that the distribution slightly deviates from the Gaussian, which is characterized by primordial non-Gaussianities (PNGs). The existence of the PNGs is not so unnatural from a theoretical viewpoint.

For example, the PNGs are related to the interactions of fields during inflation. The search of the PNGs provides an insight into the dynamics during inflation and the fundamental physics at the inflation energy scale. The lowest order of the PNGs is the bispectrum which is the three-point correlation function in the Fourier space. Under the assumptions of homogeneity and isotropy, the bispectrum is given by the function of the norm of the three momenta and is characterized by triangle forms, which correspond to the momentum conservation. The shapes and the associated amplitudes of primordial bispectra allow us to classify the physics of inflation. The simplest type of non-Gaussianities is the local (squeezed) type, which is constructed by two short-wavelength modes and a long-wavelength mode. This type is known to be an indicator to distinguish between single-field inflation and multi-field inflation. For the simple single-field case, the amplitude of the squeezed bispectrum $f_{\rm NL}^{\rm loc}$ is expected to be very close to zero [16, 17], while some multi-field models can generate the large $f_{\rm NL}^{\rm loc}$, for example, Refs. [18, 19, 20]. Moreover, if massive higher spin particles, which are motivated by the beyond standard model such as string theory, exist at the inflation energy scale, they can produce nontrivial correlations and leave unique signatures in the squeezed bispectrum with an oscillation feature and angular dependence corresponding to the spin of particles [21]. The search for these PNGs may lead to observational evidence for the existence of the higher-spin particles.

The current tight constraint is $f_{\rm NL}^{\rm loc} = -0.9 \pm 5.1$ at 68 percent confidence level from the CMB measurement by Planck satellite [3]. However, due to the cosmic variance, a further improvement on the constraint is no longer expected by the CMB observations. In order to distinguish inflationary models, it is necessary to introduce other approaches. As a possibility, the scale-dependent bias can be used to give the constraint on $f_{\rm NL}^{\rm loc}$. The tracers of density fluctuations such as galaxy at low redshift are biased by the local density fields. Since the local-type primordial non-Gaussianities modulate the amplitude of the short-wavelength modes, the biased tracers have the position dependence via the long-wavelength mode. This causes the scaling k^{-2} on the large scales. By using this scale-dependent bias [22, 23, 24, 25, 26, 27], the tightest constraint from the low redshift large-scale structure is $f_{\rm NL}^{\rm loc} = -12 \pm 21$ at 68 percent confidence level [28] and the forthcoming galaxy survey, SPHEREx, will reach to $|\Delta f_{\rm NL}^{\rm loc}| = \mathcal{O}(1)$ by increasing the survey areas and depth. In deeper galaxy surveys, the cosmic variance can be reduced to investigate long-wavelength modes than the CMB. This could provide the PNGs with tighter constraints complementary to the CMB.

Galaxy shape as Intrinsic Alignments

The galaxy imaging surveys supply not only the distribution of galaxies but also the individual galaxy shapes. Recently, much attention has been paid to the intrinsic alignments, which originate in the distortion of the intrinsic galaxy. Given that the Universe follows homogeneity and isotropy on large scales, it can be assumed that the orientations of galaxies are distributed randomly when we obtain a sufficient number of samples. Thus, the intrinsic alignments may be handled as systematic errors for the weak lensing analysis. However, in practice, galaxies evolve following local physical processes and their anisotropy is induced by the environments around galaxies at each time. The local physical processes depend on many elements, for instance, whether the galaxy is an elliptical or a spiral disk, red (ellipticals dominant with old stellar population) or blue (spiral disks dominant with active star formation). These elements may have an impact on how the galaxy is aligned, depending on the surrounding structures.

In particular, the intrinsic alignment for elliptical galaxies that is supported by observational data [29, 30, 31, 32, 33] and N-body simulations [34, 35, 36, 37, 38, 39] is a tracer of the surrounding tidal fields. This is understood by the stretching in the direction of higher density regions around a halo or galaxy on the large scales, which is known as the linear alignment model [40]. As in the case of the galaxy number density, this reflects cosmological information and is a promising tracer for precise observations of galaxy shapes. Focusing on the PNGs, the galaxy shape as intrinsic alignments would be a unique tracer for the angular-dependent PNGs. As mentioned above, the galaxy number density is influenced by the contribution of the isotropic squeezed bispectrum via scale-dependent bias. Similarly, the angular-dependent PNGs, which can be generated by a spin-2 particle, induce a scale-dependent bias for the intrinsic alignment correlations of the 2nd shape moment [41], which is the usual cosmic shear. This effect was confirmed by N-body simulations [42] where, interestingly, the contribution induced by the spin-2 in the bispectrum does not affect the number density but changes only the second shape moment on the large scales. Therefore, an ideal galaxy imaging survey that can separately observe the different shape moments of galaxies may allow us to separately measure the PNGs produced by massive particles with different spins.

This thesis provides prospects of the constraints on the angular-dependent PNGs for the forthcoming galaxy imaging surveys via the moment decomposition of the galaxy shape. The outline of this thesis is as follows. In chapter. 2, we brief the fundamental cosmology and the primordial non-Gaussianity. We summarize the structure formation based on the perturbation theory in chapter. 3, the galaxy bias and the scale-dependent bias from the viewpoint of the effective field theory of LSS in chapter. 4. This helps interpret the bias of the shape. Following Refs. [43, 44], chapter. 5 is the main part of this thesis and is a summary of the relationship between galaxy shape and angular-dependent PNGs, especially the global isotropic case. In appendix. B, we discuss various imprints of a violation of the global rotation symmetry in the primordial bispectrum. This allows us to understand whether the signal of the PNGs induced by spin particles is unique or not by examining the differences from the case with the global symmetry. We use the unit as $c = \hbar = 1$ and the reduced Planck mass as $M_{\rm pl} = (8\pi G)^{-1/2} = 2.4 \times 10^{18}$ GeV.

Chapter 2

Fundamental Cosmology

2.1 Standard Cosmology

The Universe that we view on a large enough scale features homogenous and isotropy, which is known as the cosmological principle. From this point of view, the general metric satisfying these features, which called the Friedmann-Lemaître-Robertson-Walker (FLRW) metric, is introduced as

$$ds^2 = -dt^2 + a^2(t)\left[\frac{dr^2}{1-kr^2} + r^2 d\Omega\right], \tag{2.1}$$

where $a(t)$ is the scale factor, which is normalized as $a(t_0) = 1$ at present time t_0, and k decides the spatial form of the metric. Specifically, $k = 0, -1$ and 1 mean a flat, a sphere, and a hyperbolic space, respectively [1].

Since the radius direction in Eq. (2.1) has the spatial curvature, this expression is complicated to handle distances. However, the following variable transformation make it easier to understand,

$$d\chi = \frac{dr}{\sqrt{1-kr^2}}, \tag{2.2}$$

where χ is called the comoving distance and corresponds to the distance from the origin of the coordinate. Then, we find that Eq. (2.1) is transformed as

$$ds^2 = -dt^2 + a^2(t)[d\chi^2 + S_k(\chi)d\Omega], \tag{2.3}$$

where

$$S_k(\chi) = \begin{cases} \sinh^2\chi & (k=-1) \\ \chi^2 & (k=0) \\ \sin^2\chi & (k=1) \end{cases}. \tag{2.4}$$

---

[1] We can, in principle, choose arbitrary k by using the 3-dimensional Ricci scalar.

Since the photon passes through the null geodesic ($ds = 0$) on the spatially isotropy condition, the comoving distance can be related as

$$\chi \equiv \int_0^{\chi} \frac{dr}{\sqrt{1-kr^2}} = \int_t^{t_0} \frac{dt}{a(t)} = \int_a^1 \frac{da}{a\dot{a}}\,, \tag{2.5}$$

where t_0 denotes the observer time and the $a = 1$ means the scale factor at present.

Besides, we introduce the conformal time as

$$\tau \equiv \int_0^t \frac{dt'}{a(t')}\,, \tag{2.6}$$

where we set $t = 0$ as the initial time. In this case, the line element Eq. (2.1) can also be written as

$$ds^2 = a^2(\tau)[-d\tau^2 + d\chi^2 + S_k(\chi)d\Omega]\,. \tag{2.7}$$

Next, we investigate the dynamics of the metric, following the Einstein equation given by

$$G_{\mu\nu} + \Lambda g_{\mu\nu} = \frac{1}{M_{\rm Pl}^2} T_{\mu\nu}\,, \tag{2.8}$$

where $g_{\mu\nu}$ denotes the 4-dimensional metric which is derived from the line element, $G_{\mu\nu}$ is the Einstein tensor, Λ is the cosmological constant and $T_{\mu\nu}$ is the energy-momentum tensor.

Assuming the homogenous and isotropy, the energy-momentum tensor is given by

$$T^{\mu}_{\nu} = \mathrm{diag}(-\rho, p, p, p) \tag{2.9}$$

with the energy density ρ and the pressure p.

Solving the Einstein equation, Eq. (2.8), the independent equations about the evolutions of the scale factor are given by

$$H^2 \equiv \left(\frac{\dot{a}}{a}\right)^2 = \frac{1}{3M_{\rm Pl}^2}\rho - \frac{k}{a^2} + \frac{\Lambda}{3}\,, \tag{2.10}$$

$$\frac{\ddot{a}}{a} = H^2 + \dot{H} = -\frac{1}{6M_{\rm Pl}^2}(\rho + 3p)\,, \tag{2.11}$$

which are known as the Friedmann equations. Convining these equations, we also obtain the energy conservation as

$$\dot{\rho} + 3H(\rho + p) = 0\,. \tag{2.12}$$

While there are three variables with time-dependent parameters as a, ρ, p, there are only two independent equations. Therefore, it is necessary to add the equation of state that describes the properties of matters. The matter components can be divided into relativistic and non-relativistic parts. Here, relativistic matters, called the radiation components, refer to matters in which the kinetic energy is not negligible compared to the rest of energy. In contrast, non-relativistic matter, called the matter components, represents the case in which the kinetic energy is negligible. Futhermore, Eq. (2.12) can rewritten as

$$\frac{d(\rho a^3)}{dt} = -p\frac{da^3}{dt}\,, \tag{2.13}$$

which can be read as adiabatic in the Universe compared to $dU = -pdV + TdS$ of the first law of thermodynamics. We can use the relation between the energy density and the pressure as $\rho \propto p$.

For the radiation components, since the radiation pressure is given by $p_\mathrm{r} = \rho_\mathrm{r}/3$, we find that the dependency on the scale factor is given by $\rho_\mathrm{r} \propto a^{-4}$ from Eq. (2.12). The pressure of the matter components is negligible, $p = 0$. For example, on the situation of an ideal gas, this can be understood as follows. When n particles in a unit volume are in thermal equilibrium at temperature T, the equation of state is given by $p = nk_\mathrm{B}T$ with the Boltzmann factor k_B. Furthermore, assuming the average mass of the particles μ, the energy density becomes $\rho = n\mu$. Consequently, the relation between pressure and energy density is expressed as

$$p = \frac{k_\mathrm{B}T}{\mu}\rho\,. \tag{2.14}$$

However, for the matter component, since the kinetic energy is negligible compared to the rest of the energy ($k_\mathrm{B}T \ll \mu$), the pressure becomes negligible compared to the energy density ($p \ll \rho$). Thus, the matter components depend on $\rho_\mathrm{m} \propto a^{-3}$ from Eq. (2.12). Combined with Eq. (2.12), the time dependency of the scale factor are given by $a \propto t^{2/3}$ in the matter dominant Universe and $a \propto t^{1/2}$. In general, using the equation of state parameter $w = p/\rho$ under the adiabatic condition, we find the solution as $a \propto t^{\frac{2}{3(1+w)}}$.

The proportions of each component are needed to describe the structure evolution of the Universe, and these characteristic values determined by observation are called cosmological parameters, which are determined as

$$\Omega_\mathrm{X0} \equiv \frac{\rho_\mathrm{X0}}{3M_\mathrm{Pl}^2 H_0^2}\,, \quad \Omega_\mathrm{K0} \equiv -\frac{k}{H_0^2}\,, \quad \Omega_{\Lambda 0} \equiv \frac{\Lambda}{3H_0^2}\,, \tag{2.15}$$

where are known as the density parameter, the curvature parameter, and the cosmological constant parameter at present, respectively. Here we denote the Hubble constant at present as H_0. The Frieedmann equation Eq. (2.10) becomes

$$\begin{aligned} H^2 &= H_0^2\left[\frac{\Omega_\mathrm{r0}}{a^4} + \frac{\Omega_\mathrm{m0}}{a^3} + \frac{\Omega_\mathrm{K0}}{a^2} + \Omega_\Lambda\right] && (2.16)\\ &= H_0^2\left[\Omega_\mathrm{r0}(1+z)^4 + \Omega_\mathrm{m0}(1+z)^3 + \Omega_\mathrm{K0}(1+z)^2 + \Omega_{\Lambda 0}\right]\,, && (2.17)\end{aligned}$$

where we used $a = 1/(1+z)$ with the redshift z. This expression indicates that multiple components with different time dependencies form cosmic expansion. If the Universe goes back in time, the dominant component at the epoch appears according to the scale factor of each element. Since, in the early epoch, the radiation component is dominant, and gradually the matter component becomes dominant, the instant of matter-radiation equality epoch divides the two main periods of the Universe evolution, radiation domination and matter domination.

From the Planck observation with the Cosmic Microwave Background (CMB) radiation, these parameters are measured as

$$h = \frac{H_0}{100} = 0.67\,, \quad \Omega_{\mathrm{m}0} = 0.31\,, \quad \Omega_{\Lambda 0} = 0.69\,, \quad \Omega_{\mathrm{K}0} = 0.0007\,, \tag{2.18}$$

and since the scale of matter-radiation equallity is given by $a_{\mathrm{eq}} = (1+z_{\mathrm{eq}})^{-1} = \rho_{\mathrm{r}0}/\rho_{\mathrm{m}0}$, the Planck observation esimates the matter-radiation epoch as $z_{\mathrm{eq}} \sim 3400$ [45].

2.2 Inflation

While the standard hot big bang cosmology can explain a lot of phenomenology in our Universe, this theory has the following representative problems at the early epoch.

Flatness problem As seen in the previous section, the curvature parameter at present is estimated as $\mathcal{O}(10^{-3})$, which is close to zero. Now let us see the time evolution of the curvature in the early Universe. For simplicity, assuming that the cosmic expansion is dominated by some form of matter with the equation of state equal to w. The curvature parameter in time is given by

$$\Omega_{\mathrm{K}} = -\frac{k}{a^2 H^2} = \Omega_{\mathrm{K}0}\, a^{(1+3w)}\,. \tag{2.19}$$

This means that if $w > -1/3$, Ω_{K} keeps growing (if $\Omega_{\mathrm{K}0}$ is the positive value) or decreasing (if $\Omega_{\mathrm{K}0}$ is the negative value). Considered the current cosmological history, for example, the curvature parameter at the Planck scale is required as $|\Omega_{\mathrm{K}}| \lesssim \mathcal{O}(10^{-63})$. Since the scale factor dependency of the curvature parameter is proportional to a^{-2}, it becomes dominant after the matter-dominated epoch. As you can see from Eq. (2.18), the curvature already is not dominant at present, and the value of Ω_{K} at the early epoch should be a remarkable small value. The easiest way to solve this problem is to assume that the initial curvature is zero ($k = 0$), which is one answer. Another solution is the presence of the matter with $w < -1/3$ in the Universe for some period. In this case, if the initial curvature parameter is significant, the scale factor dilutes it.

Horizon problem The fluctuation of the CMB temperature is observed as $\mathcal{O}(10^{-5})$ and distributed by isotropic and homogeneous. This distribution indicates that the Universe at recombination epoch ($z \sim 1100$) is already isotropic and homogeneous. However, since the signals with causality can only propagate at the speed of light at best, they have a limited spatial region to keep causality.

Let us consider the particle horizon χ_{p}, where causality is kept at a given time. In the matter-dominated Universe with the equation of state w, the particle horizon is roughly given by

$$\chi_{\mathrm{p}} \equiv \tau - \tau_{\mathrm{ini}} = \int_{a_{\mathrm{ini}}}^{a} \frac{da}{a^2 H} \sim a^{(1+3w)/2} - a_{\mathrm{ini}}^{(1+3w)/2} \,, \tag{2.20}$$

where a_{ini} means the initial time, which corresponds to the singularity point in the hot big bang cosmology. If $w > -1/3$, the particle horizon grows in time. This means that the farthest distance with causality grows in time and the new region at a certain time never interacts with another region until that time. This contradicts the CMB observation. Only the horizon patch at the recombination epoch can be causal, while the CMB temperature fluctuation is homogenous and isotropic at the current horizon size.

The solution to these above problems is the period when some matter with $w < -1/3$ dominates before the hot big bang history. This condition implies that the Universe undergoes the accelerated expansion from Eq. (2.11)[2], namely,

$$w < -\frac{1}{3} \Longrightarrow \ddot{a} > 0 \,. \tag{2.21}$$

Inflation is a period of accelerated expansion before the standard hot big bang. In the standard cosmology, which is composed of well-known matters, the Universe always undergoes a decelerating expansion. In this case, since the scale factor obeys $a \propto \tau^{2/(1+3w)}$ in terms of the conformal time, there exists the singularity $a \to 0$ as $\tau \to 0$. This implies the particle horizon is determined at a late time since this size is the order of τ. However, if there exists a phase with $w < -1/3$, the scale factor is proportional to the negative power of the conformal time. This implies that the conformal time can be extended to negative times. For example, for $w = -1$, since the Hubble parameter H is constant, the scale factor becomes $a(\tau) = -1/(H\tau)$, which means $a \to 0$ as $\tau \to -\infty$. This allows us to confront the horizon problem.

2.2.1 Slow-roll inflation with single scalar field

We summarize the typical inflation mechanism. The simplest example of an inflationary system is the origin of a scalar field on an almost flat potential (Fig. 2.1). These kinds of models are known as slow-roll inflation.

The action for gravity and a scalar field $\varphi(t, \boldsymbol{x})$ which drives to expand the Universe, which is called inflaton, is

$$\mathcal{S} = \int d^4x \sqrt{-g} \left[\frac{M_{\mathrm{pl}}^2}{2} R + \mathcal{L} \right] \,, \tag{2.22}$$

$$\mathcal{L} = -\frac{1}{2} g^{\mu\nu} (\partial_\mu \varphi)(\partial_\nu \varphi) - V(\varphi) \,, \tag{2.23}$$

---

[2] We assumed that the energy density is positive.

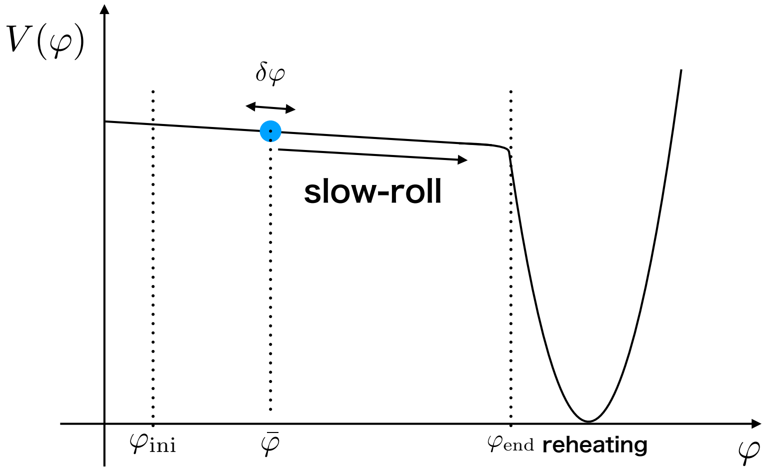

FIGURE 2.1: The schematic picture of the slow-roll inflation. One of the examples of inflation scenarios is a picture of a potential that was a vacuum state around the origin at the pre-inflation energy scale, but which undergoes a phase transition to a slow-roll potential during inflation as the energy scale decreases. In this case, the inflaton was originally around the origin, but it moves to the true vacuum due to the phase transition. The false vacuum energy causes inflation while the inflaton rolls towards the true vacuum. When the true vacuum is reached, the false vacuum energy is used for reheating, raising the temperature of the Universe.

where R is the Ricci scalar and $V(\varphi)$ is the potential for the scalar field. The first term of the first line corresponds to the Einstein Hilbert term. The rest terms correspond to the Lagrangian density of the inflaton. For minimal setups, assuming that gravity only plays a role in the cosmic expansion, we can ignore the Einstein Hilbert term for inflaton dynamics.

Let us focus on the dynamics of the inflaton. The energy-momentum tensor of the scalar field is given by

$$T^{\mu}_{\nu} = (\partial^{\mu}\varphi)(\partial_{\nu}\varphi) - \delta^{\mu}_{\nu}\left[\frac{1}{2}(\partial_{\lambda}\varphi)(\partial^{\lambda}\varphi) + V(\varphi)\right] , \tag{2.24}$$

and we obtain the energy density and pressure of the homogeneous part from Eq. (2.9) by

$$\rho_{\varphi} = \frac{1}{2}\dot{\varphi}^2 + V(\varphi) , \qquad p_{\varphi} = \frac{1}{2}\dot{\varphi}^2 - V(\varphi) . \tag{2.25}$$

Inserting the energy density into the Friedmann equation, we get

$$H^2 = \frac{1}{3M_{\text{pl}}^2}\left[\frac{1}{2}\dot{\varphi}^2 + V(\varphi)\right] , \tag{2.26}$$

where we ignore the cosmological constant and set the flat space. If the kinetic energy is negligible compared to the potential energy, $\dot{\varphi} \ll V(\varphi)$, we find that the equation of state becomes $w \simeq -1$ because of $\rho_{\varphi} \simeq -p_{\varphi}$. Moreover, the equation of motion is derived from Euler-Lagrange equation[3], and we obtain

$$\ddot{\varphi} + 3H\dot{\varphi} + V_\varphi(\varphi) = 0\,, \tag{2.27}$$

where V_φ means $\partial_\varphi V(\varphi)$. This expression is similar to the damped oscillation. The second term is a friction term due to cosmic expansion. Although the solution to the equation of motion for a scalar field requires a specific potential, the condition that the potential is flat enough allows us to discuss general solutions. This condition requires that the Hubble friction balances the external force. Consequently, the slow-roll inflation requires

$$\dot{\varphi}^2 \ll 2V(\varphi)\,, \qquad |\ddot{\varphi}| \ll 3H|\dot{\varphi}|\,, \tag{2.28}$$

which are known as the slow-roll condition. Let us consider the relation between the slow-roll condition and the potential. Under the slow-roll condition, since the Friedmann equation Eq. (2.26) and the equation of motion Eq. (2.27) can be approximated by $H^2 \simeq V/(3M_{\rm pl}^2)$ and $3H\dot{\varphi} \simeq -V_\varphi(\varphi)$, respectively. Then, the slow-roll condition reads with respect to the potential,

$$\epsilon_V \equiv \frac{M_{\rm Pl}^2}{2}\left(\frac{V_\varphi}{V}\right)^2\,, \quad \eta_V \equiv M_{\rm Pl}^2\frac{V_{\varphi\varphi}}{V}\,, \tag{2.29}$$

which are known as the slow-roll parameters and should satisfy $\epsilon_V \ll 1, |\eta_V| \ll 1$. By using the dynamics of the scale factor, another definition of the slow-roll parameters are given by

$$\epsilon_H \equiv -\frac{\dot{H}}{H^2}\,, \quad \eta_H \equiv \frac{\dot{\epsilon_H}}{H\epsilon_H}\,. \tag{2.30}$$

Satisfying the slow-roll condition, these parameters are related by

$$\epsilon_H = \epsilon_V + \mathcal{O}(\epsilon_V^2, \eta_V^2)\,, \quad \eta_H = 4\epsilon_V - 2\eta_V + \mathcal{O}(\epsilon_V^2, \eta_V^2)\,. \tag{2.31}$$

The end of inflation is defined by $\epsilon_H \sim 1$. This corresponds to a steepening of the potential slope so that the kinetic energy is no longer negligible.

2.2.2 Primordial perturbation

The inflationary cosmology was introduced in order to confront the shortcoming of the standard cosmology. Of course, this is an important point. However, more importantly, the inflationary cosmology can supply the origin of the cosmological perturbation after inflation, which leads to the initial fluctuation to form the cosmic structure.

---

[3] The Euler-Lagrange equation for the Lagrangian density is given by $\partial_\varphi(\sqrt{-g}\mathcal{L}) = \partial_\mu[\partial_{\partial_\mu\varphi}(\sqrt{-g}\mathcal{L})]$

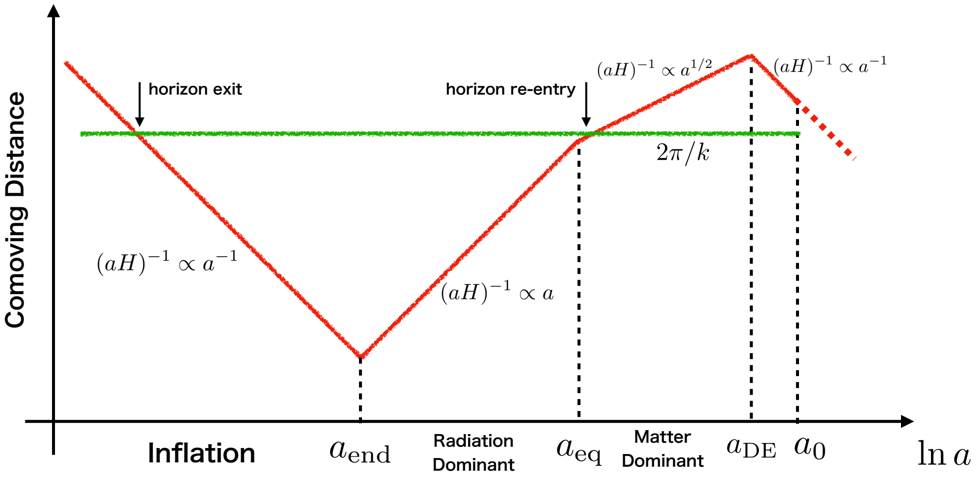

FIGURE 2.2: The time evolution of the comoving Hubble radius and the constant comoving scale. Since the fluctuations do not grow outside the horizon, the fluctuations of the Hubble horizon scale during inflation correspond to the fluctuations coming into the horizon again. This is the primordial fluctuation, which is the seed for structure formation.

Even if the fluctuations within the Hubble patch before inflation are homogeneous and isotropy, the inflaton field has quantum fluctuation. In a particle-like picture, this means that the particles are being created and annihilated repeatedly. On the other hand, the inflationary expansion stretches its quantum fluctuations so that quantum correlations do not occur and the produced particles remain outside the Hubble scale. After the inflation ends, these fluctuations come back into the Hubble horizon and become the seeds of structure formation (Fig. 2.2).

If there exists the fluctuation of the inflaton, the time at which the inflation ends varies by location. Let us consider the deviation from the background field value $\delta\varphi$. In this case, the time evolution of perturbation is shifted by $\delta t = \delta\varphi/\dot{\varphi}$ compared to the time evolution of background. This means that the field value at time $\bar{t} + \delta t$ evolve in time ahead of the background $\bar{t}$.

Following Ref. [46, 47, 48], we set the spatially-flat gauge. Since the action of the first order perturbation vanishes because of the background equations of motion, the action of the second order perturbation is given by

$$\mathcal{S}^{(2)} = \frac{1}{2}\int d^3x dt\, a^3 \left[\delta\dot{\varphi}^2 - \frac{1}{a^2}(\partial_i \delta\varphi)^2\right] , \tag{2.32}$$

where we neglected the inflaton mass due to slow-roll inflation and the equation of motion in $\delta\varphi$ is in Fourier space,

$$\delta\ddot{\varphi}_{\boldsymbol{k}} + 3H\delta\dot{\varphi}_{\boldsymbol{k}} + \frac{k^2}{a^2}\delta\varphi_{\boldsymbol{k}} = 0\,. \tag{2.33}$$

Since the quantity of the gauge invariant is $u = a\delta\varphi$ in the spatially-flat gauge, this equation of motion can be rewritten with the conformal time,

$$u''_{\boldsymbol{k}} + \left(k^2 - \frac{a''}{a}\right) u_{\boldsymbol{k}} = 0\,, \tag{2.34}$$

where the prime means the conformal time derivative ∂_τ. Moreover, the conjugated momentum for u field is given by $\pi \equiv \partial\mathcal{L}/\partial u' = u'$[4].

Let us consider quantizing the classical fields u and π to the operators $\hat{u}$ and $\hat{\pi}$ by the equal time commutation relations, which are given by

$$[\hat{u}(\boldsymbol{x},\tau), \hat{\pi}(\boldsymbol{y},\tau)] = i\delta_{\rm D}(\boldsymbol{x}-\boldsymbol{y})\,, \quad [\hat{u}(\boldsymbol{x},\tau), \hat{u}(\boldsymbol{y},\tau)] = [\hat{\pi}(\boldsymbol{x},\tau), \hat{\pi}(\boldsymbol{y},\tau)] = 0\,. \tag{2.35}$$

Following the Heizenberg picture, we can expand the operator $\hat{u}$ as

$$\hat{u}(\boldsymbol{x},\tau) = \int \frac{d^3k}{(2\pi)^3} [u_k(\tau)\hat{a}_{\boldsymbol{k}} + u_k^*(\tau)\hat{a}^\dagger_{-\boldsymbol{k}}] e^{i\boldsymbol{k}\cdot\boldsymbol{x}}\,, \tag{2.36}$$

where u_k is the mode function which follows the solution of Eq. (2.34), and $\hat{a}_{\boldsymbol{k}}, \hat{a}^\dagger_{\boldsymbol{k}}$ are anihilation and creation operators, which satisfy [5]

$$[\hat{a}_{\boldsymbol{k}}, \hat{a}^\dagger_{\boldsymbol{k}'}] = (2\pi)^3\delta_{\rm D}(\boldsymbol{k}-\boldsymbol{k}')\,, \quad [\hat{a}_{\boldsymbol{k}}, \hat{a}_{\boldsymbol{k}'}] = [\hat{a}^\dagger_{\boldsymbol{k}}, \hat{a}^\dagger_{\boldsymbol{k}'}] = 0\,, \tag{2.37}$$

and the vacuum state $|0\rangle$ is defined as $\hat{a}_{\boldsymbol{k}}|0\rangle = 0$.

Let us consider to find the solution of the mode function. Since the scale factor for de-Sitter Universe is $a = -1/(H\tau)$, $a''/a = 2/\tau^2$. Then, we find that the equation of motion has the following solution,

$$u_k(\tau) = C_1 e^{ik\tau}\left(1 + \frac{i}{k\tau}\right) + C_2 e^{-ik\tau}\left(1 - \frac{i}{k\tau}\right)\,, \tag{2.38}$$

where C_1, C_2 are the integration constants. In the limit to the subhorizon scale ($|k\tau| \gg 1$), since this solution is expected to approach asymptotically to the solution in flat space, the solutions of the coefficients are given by[6]

$$C_1 = 0\,, \quad C_2 = \frac{1}{\sqrt{2k}}\,. \tag{2.39}$$

---

[4] The action Eq. (2.32) can be rewritten with the conformal time and the Mukhanov-Sasaki variable as

$$\mathcal{S}^{(2)} = \int d\tau d^3x \mathcal{L} = \frac{1}{2}\int d\tau d^3x \left[u'^2 + \frac{a''}{a}u^2 - (\partial_i u)^2\right]\,.$$

[5] We normalized the time-independent Wronskian as $u_k u_k^{*'} - u'_k u_k^* = i$ because there is not the first time derivative in the mode function.

[6] In the subhorizon limit, the mode function has both the solustions as the $u_k(\tau) \propto e^{\pm ik\tau}$. However, when the wave function in non-relativistic limit follows $i\partial_t\phi(\boldsymbol{x},t) = E\phi(\boldsymbol{x},t)\,(E > 0)$, the wave function is given by $\phi \propto e^{-iEt}$. Then, we find that the mode function has $u \propto e^{-ik\tau}$ when the energy is positive.

Before the horizon exit $|k\tau| \gg 1$, since the mode function is proportional to $e^{-ik\tau}$ and the eigenstates change in time, the sub-horizon fluctuations have quantum behavior. On the other hand, after the horizon exit $|k\tau| \ll 1$, since we can approximate the mode function as $u_k(\tau) \sim -iC_2/(k\tau)$, the field operator $\hat{u}$ becomes

$$\hat{u}(\boldsymbol{k}, \tau) = -\frac{i}{\sqrt{2k}(k\tau)}(\hat{a}_{\boldsymbol{k}} - \hat{a}^{\dagger}_{-\boldsymbol{k}}) \,. \tag{2.40}$$

On the super-horizon scale, the operator $\hat{u}$ only changes the amplitude and does not change the coefficients of the commutation operators. This implies that $\hat{u}$ has time-invariant eigenstates on super-horizon and thus behaves as the classical fluctuations.

Let us compute the curvature power spectrum after horizon exit. The fluctuations on sub-horizon during inflation are equalized by the rapid accelerated expansion so that after the horizon exit, the fluctuation of the vacuum energy only dominates. We define the power spectrum of the fluctuaion of infaltion as

$$\langle \delta\varphi^*(\boldsymbol{k}, \tau)\delta\varphi(\boldsymbol{k}', \tau)\rangle \equiv (2\pi)^3 P_{\delta\varphi}(k, \tau)\delta_{\rm D}(\boldsymbol{k} - \boldsymbol{k}') \tag{2.41}$$

$$\equiv \frac{1}{a^2}\langle 0|\hat{u}^{\dagger}(\boldsymbol{k}, \tau)\hat{u}(\boldsymbol{k}', \tau)|0\rangle \,, \tag{2.42}$$

where we used the condition of the spatial- and rotation-symmetry in the first line. Using the solution of mode function on the super-horizon Eq. (2.40), we obtain the power spectrum as

$$P_{\delta\varphi}(k, \tau) = \frac{1}{2k^3 a^2 \tau^2} = \frac{H^2}{2k^3} \,, \tag{2.43}$$

where we used $a(\tau) = -1/(H\tau)$. Moreover, we find that the dimensionless power spectrum is given by

$$\mathcal{P}_{\delta\varphi}(k, \tau) \equiv \frac{k^3}{2\pi^2} P_{\delta\varphi}(k, \tau) = \left(\frac{H}{2\pi}\right)^2 \,. \tag{2.44}$$

Since the Hubble parameter during inflation is almost constant, the dimensionless power spectrum becomes scale-invariant regardless of scale k. In the spatially-flat gauge, the curvature perturbation, which is conserved in time on the super-horizon, is given by

$$\zeta = -H\delta t = -H\frac{\delta\varphi}{\dot{\bar{\varphi}}} \,. \tag{2.45}$$

Then, we obtain the curvature power spectrum at horizon exit as

$$\mathcal{P}_{\zeta}(k) = \left(\frac{H^2}{2\pi\dot{\bar{\varphi}}}\right)^2 = \frac{H^2}{8\pi^2 M_{\rm pl}^2 \epsilon_H} \,, \tag{2.46}$$

where we used $\dot{\varphi}^2 = 2M_{\rm pl}^2 H^2 \epsilon_H$[7]. Though we considered the lowest order of perturbation, a slight scale-dependence appears when treated up to first-order approximation. The scale-dependency of the power spectrum can be expressed by the spectral index n_s, which is defined as

$$n_s - 1 = \frac{d\ln \mathcal{P}_\zeta}{d\ln k}\,, \tag{2.47}$$

and under the slow-roll approximation up to first order $n_s - 1 = 2\eta_V - 6\epsilon_V$. Since the Planck result of the CMB observation measured $n_s = 0.9659$ [45] and the amplitude $\mathcal{A}_{\rm s} \equiv \mathcal{P}_\zeta(k_*) = 2.1 \times 10^{-9}$ at the pivot scale $k_* = 0.05\,{\rm Mpc}^{-1}$, unless otherwise noted, we use the curvature power spectrum as scale-invariant. We can estimate the inflation energy scale on the single slow-roll inflation (e.g., Ref. [47]) by using the tensor-to-scalar ratio r, which is the ratio of the primordial curvature power spectrum to the primordial tensor one and given by $r = 16\epsilon_H$. Since the CMB B-mode measurement provides $r < 0.056$ at the pivot scale $k_* = 0.002\,{\rm Mpc}^{-1}$ [45], the uppder bound to the inflation energy scale can be estimated by $(H_{\rm inf}/M_{\rm pl}) < 1.2 \times 10^{-5}$, which is $V^{1/4} < 10^{16}$GeV.

In order to focus on the structure formation in this thesis, we describe the relation between the gravitational potential and the curvature perturbation. The Bardeen potential on super-horizon, which corresponds to the gravitational potential in conformal Newtonian gauge, is related to the curvature perturbation by

$$\Psi = \frac{3(1+w)}{5+3w}\zeta = \begin{cases} (2/3)\zeta & ({\rm radiation\,dominant}: w = 1/3) \\ (3/5)\zeta & ({\rm matter\,dominant}: w = 0) \end{cases}\,, \tag{2.48}$$

which we ignored the anisotropic stress. Note that when the fluctuations which exit the horizon during inflation come back into the horizon after inflation, the coefficients are different in the relation between the curvature perturbation and the primordial potential, depending on the horizon reentry epoch.

2.2.3 Primordial non-Gaussianity

In this section, we consider the statistical properties of fluctuations. Suppose the fluctuation obeys the Gaussian distribution, which is determined by the two variables of the average and variance. In that case, the higher-order correlators of the fluctuation are characterized by only the two-point correlator. The primordial perturbation following the action Eq. (2.32) can be approximated as Gaussian, which is similar to the quantum harmonic oscillation, and this means that the curvature power spectrum contains all the information during inflation.

However, if a higher-order correlation exists beyond the two-point correlation, the fluctuation obeys the non-Gaussian distribution and supplies additional information about inflation. In order to study such non-Gaussian effects, we expand the action

---

[7] This is exact relation. We can derive this relation by using the time derivative for the Hubble paramter is $6M_{\rm pl}^2 H\dot{H} = \dot{\varphi}(\ddot{\varphi} + V_\varphi)$ and the equation of motion Eq. (2.27)

to the third order, and we need to compute the time evolution of vacuum based on the interaction picture such as the in-in formalism, which requires complicated calculations. Here, we do not derive the higher-order correlators but only give a rough outline and introduce the templates of the primordial bispectra used for observations, which we use to examine the effect on the galaxy. You can know the details and derivations of the primordial non-Gaussianity, e.g., Refs. [49, 46, 50].

We define the three point correlation of the curvature perturbation in Fourier space by using the primoridal bispectrum B_ζ as

$$\langle\zeta(\boldsymbol{k}_1)\zeta(\boldsymbol{k}_2)\zeta(\boldsymbol{k}_3)\rangle = (2\pi)^3\delta_{\rm D}(\boldsymbol{k}_1+\boldsymbol{k}_2+\boldsymbol{k}_3)B_\zeta(\boldsymbol{k}_1,\boldsymbol{k}_2,\boldsymbol{k}_3)\,, \tag{2.49}$$

which is the lowest order quantity that characterizes the non-Gaussianity effect. We consider the degrees of freedom in the bispectrum. The delta function due to the background homogeneity allows us to reduce the three degrees. In addition, since the background rotational symmetry is due to isotropy, which means that the wavevector depends only on the length, the independent degrees of freedom become two. Therefore, the bispectrum is determined by the two ratios, e.g., k_3/k_1 and k_2/k_1.

We summarize the representative shapes of bispectrum, which are used as the templates of bispectra for the observation. Since the curvature perturbation is linearly related to the Newtonian potential as Eq. (2.48), we use Ψ instead of ζ and denote the Gaussian field as ϕ.

As the most simple case, we consider the non-Gaussian correction in real space as follows,

$$\Psi(\boldsymbol{x}) = \phi(\boldsymbol{x}) + f_{\rm NL}^{\rm loc}\left[\phi^2(\boldsymbol{x}) - \langle\phi^2\rangle\right]\,, \tag{2.50}$$

where $f_{\rm NL}^{\rm loc}$ is the non-Gaussianity parameter, $\langle\cdot\rangle$ denotes the ensemble average and $\langle\Psi\rangle$ ensures zero[8]. This is called the local-type non-Gaussianity because this is defined as the local function. Let us consider the relation between the local-type non-Gaussianity and the bispectrum. In Fourier space, we can express

$$\Psi(\boldsymbol{k}) = \phi(\boldsymbol{k}) + f_{\rm NL}^{\rm loc}\int\frac{d^3\boldsymbol{p}}{(2\pi)^3}\phi(\boldsymbol{p})\phi(\boldsymbol{k}-\boldsymbol{p})\,. \tag{2.51}$$

Using the Wick theorem and the power spectrum P_ϕ, the bispectrum of the local type takes

$$B_\Psi(\boldsymbol{k}_1,\boldsymbol{k}_2,\boldsymbol{k}_3) = 2f_{\rm NL}^{\rm loc}\left[P_\phi(k_1)P_\phi(k_2) + P_\phi(k_2)P_\phi(k_3) + P_\phi(k_3)P_\phi(k_1)\right]\,. \tag{2.52}$$

In order to examine the shape features of the bispectrum, we may assume without loss of generality that $k_3 \leq k_2 \leq k_1$ and the triangle inequality requires $k_1 < k_2 + k_3$. This type has the peak in the squeezed limit such as $k_3 \ll k_2 \simeq k_1$ (see the left

---

[8] Using the curvature perturbation, we can write $\zeta(\boldsymbol{x}) = \zeta_{\rm G}(\boldsymbol{x}) + \frac{3}{5}f_{\rm NL}^{\rm loc}[\zeta_{\rm G}^2(\boldsymbol{x}) - \langle\zeta_{\rm G}^2\rangle]$ with the Gaussian perturbation $\zeta_{\rm G}$ and in matter dominant.

panel of Fig. 2.3). Theoretical inflation models that have a large amplitude in the squeezed-limit are the curvaton senario[9] [20], the model with the multiple light scalar fields [53, 19, 54], and so on. Meanwhile, for the single field slow-roll inflation, the bispectrum in the squeezed limit ($k_3 \ll k_2 \simeq k_1$) becomes [16, 55]

$$B_\Psi(\boldsymbol{k}_1, \boldsymbol{k}_2, \boldsymbol{k}_3) \simeq (1 - n_\mathrm{s}) P_\phi(k_1) P_\phi(k_3) \,. \tag{2.53}$$

This result is independent of the potential shape and is called the consistency relation. This means the $f_\mathrm{NL}^\mathrm{loc}$ becomes the order of the slow-roll parameters, and if the observation suggests that the $f_\mathrm{NL}^\mathrm{loc}$ is not zero, the single field slow-roll inflation model will be ruled out.

As other shapes, the bispectra of the equilateral is given by

$$\begin{aligned} B_\Psi(\boldsymbol{k}_1, \boldsymbol{k}_2, \boldsymbol{k}_3) = 6 f_\mathrm{NL}^\mathrm{eq} \Big[&-(P_\phi(k_1) P_\phi(k_2) + \text{perms.}) - 2(P_\phi(k_1) P_\phi(k_2) P_\phi(k_3))^{2/3} \\ &+ (P_\phi^{1/3}(k_1) P_\phi^{2/3}(k_2) P_\phi(k_3) + \text{perms.}) \Big] \,, \end{aligned} \tag{2.54}$$

which has the peak at $k_1 \sim k_2 \sim k_3$ (see the right panel of Fig. 2.3). For example, this type is motivated by models with the non-trivial sounds of speed and higher-derivative interactions [56]. A non-Bunch-Davies vacuum as the initial state of inflation leads to the peak of the bispectrum for the flatten triangle configuration such as $k_1 = 2k_2 = 2k_3$ [57, 49], of which the shape anzats is given by

$$\begin{aligned} B_\Psi(\boldsymbol{k}_1, \boldsymbol{k}_2, \boldsymbol{k}_3) = 6 f_\mathrm{NL}^\mathrm{folded} \Big[&(P_\phi(k_1) P_\phi(k_2) + \text{perms.}) + 3(P_\phi(k_1) P_\phi(k_2) P_\phi(k_3))^{2/3} \\ &- (P_\phi^{1/3}(k_1) P_\phi^{2/3}(k_2) P_\phi(k_3) + \text{perms.}) \Big] \,. \end{aligned} \tag{2.55}$$

In this thesis, since we focus on the scale-dependent bias of galaxy power spectrum, which will describe in Chapter. 4, the bispectrum in the squeezed limit becomes the key to examining the galaxy statistics because the short-mode wavelength power spectrum could modulate the two-point galaxy correlation at the position of the long-wavelength mode. The bispectra in the squeezed limit for local, equilateral, and folded are given by

$$B_\Psi(\boldsymbol{k}_1, \boldsymbol{k}_2, \boldsymbol{k}_3) \simeq P_\phi(k_\mathrm{S}) P_\phi(k_\mathrm{L}) \times \begin{cases} 4 f_\mathrm{NL}^\mathrm{loc} & \text{Local} \\ 12 f_\mathrm{NL}^\mathrm{eq} \left(\dfrac{k_\mathrm{L}}{k_\mathrm{S}} \right)^2 & \text{Equilateral} \\ 6 f_\mathrm{NL}^\mathrm{folded} \left(\dfrac{k_\mathrm{L}}{k_\mathrm{S}} \right) & \text{Folded} \end{cases} \,, \tag{2.56}$$

denoting $k_\mathrm{L} \equiv k_3 \ll k_1 \simeq k_2$ and $|\boldsymbol{k}_\mathrm{S}| = |\boldsymbol{k}_1 - \boldsymbol{k}_\mathrm{L}/2| \simeq |\boldsymbol{k}_2 + \boldsymbol{k}_\mathrm{L}/2|$. We droped the higher order terms of $k_\mathrm{L}/k_\mathrm{S}$. The Planck result with the bispectrum analysis of the CMB observation supplies the constraints of $f_\mathrm{NL}^\mathrm{loc} = -0.9 \pm 5.1$ and $f_\mathrm{NL}^\mathrm{eq} = -26 \pm 47$

---

[9] The curvaton is a hypothetical scalar particle different from the inflaton [51, 52]. The curvaton itself does not drive the inflation and generates the curvature perturbation. After inflation, the curvaton oscillates while the inflaton decays into the radiation. When the energy density of the curvation becomes non-negligible, this leads to generating the adiabatic curvature perturbation.

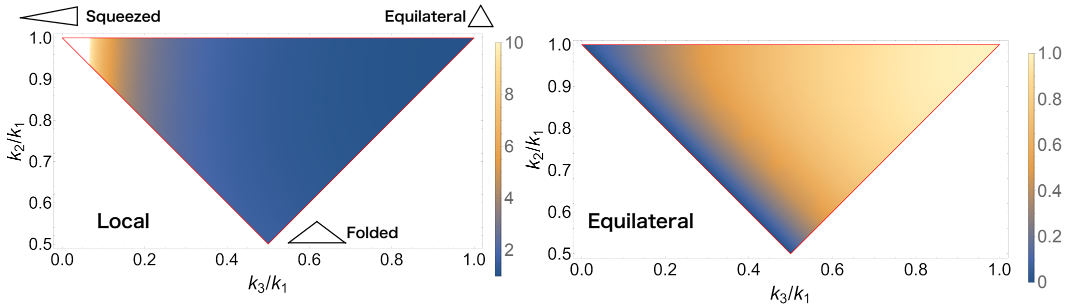

FIGURE 2.3: The shape of bispectra. The left panel is the local bispectrum Eq. (2.52). The right panel is the equilateral bispectrum Eq. (2.55). Each bispectrum was normalized by $B_\Psi(1,1,1)/(k_1k_2k_3)^2$. The squeezed limit is $k_3 \ll k_2 \sim k_1$, the equilateral shape is $k_1 = k_2 = k_3$ and the folded shape is $k_1 = 2k_2 = 2k_3$.

at 68 percent confidence level [58] and the anaysis of the galaxy clustering with spectroscopic survey suggests $f_{\rm NL}^{\rm loc} = -12 \pm 21$ at 68 percent confidence level [59].

From now, we will comment on the primordial non-Gaussianity (PNG) induced by the higher-spin particles during inflation and introduce the general bispectrum template in the squeezed limit.

Ref. [60] showed the quasi-single inflation, which is the model that there is an additional scalar particle with the mass $m \sim H$ apart from the inflaton, left the imprints with the oscillating contribution in the squeezed bispectrum. This was extended to a general even spin particle in Ref. [21] and to a general integer spin particle, including odd spin particles in Ref. [61] (see also Refs. [62, 63]). These higher spin particles are predicted as parts of the infinite tower of the higher spin states in theory describing the high energy physics beyond standard model such as string theory [64] (see also Ref. [65]). The oscillatory feature in the bispectrum depends on the spin s and mass M_s of the particle with the non-local scaling. A precise measurement of such bispectrum may prove these particles around the inflation energy scale. This program was dubbed the cosmological collider [21].

When the mass of the exchanged particle among the inflatons[10], M_s, is much heavier than the Hubble scale $H \ll M_s$, this massive particle contributes to the Lagrangian of the inflaton locally[11]. On the other hand, when the exchange mass M_s is the order of the inflation Hubble scale $H_{\rm inf}$, the non-local contribution appears.

---

[10] In the context of the effective field theory of inflation, the scalar cosmological perturbations can be understood as a Goldstone boson because of the time symmetry breaking, which is developed in Ref. [66].

[11] Let us assume the interaction Lagrangian given by $\mathcal{L}_{\rm int} = \lambda\pi\sigma$, where λ is the coupling constant, σ is the additional scalar field with mass M and π is a Goldstone boson. For example, when the mass of the additional scalar field σ is heavier than the Hubble scale, the equation of motion suppose $\sigma \propto (\lambda/M)\pi$. This allows us to write the Lagrangian by using only π.

The squeezed bispectrum with the soft exchange of the even spin particles in the slow-roll limit is given by [21]

$$B_\Psi(\boldsymbol{k}_1, \boldsymbol{k}_2, \boldsymbol{k}_3) = \sum_{s=0,2,4,\cdots} A_s \mathcal{P}_s(\hat{\boldsymbol{k}}_\mathrm{L} \cdot \hat{\boldsymbol{k}}_\mathrm{S}) f_s\left(\frac{k_\mathrm{L}}{k_\mathrm{S}}\right) P_\Psi(k_\mathrm{L}) P_\Psi(k_\mathrm{S}) \left[1 + \mathcal{O}\left(\frac{k_\mathrm{L}^2}{k_\mathrm{S}^2}\right)\right], \tag{2.57}$$

with $k_\mathrm{L}/k_\mathrm{S} \ll 1$, $\hat{\boldsymbol{k}}_\alpha \equiv \boldsymbol{k}_\alpha / k_\alpha$ $(\alpha = \mathrm{L}, \mathrm{S})$ and $\mathcal{P}_s$ denotes the Legendre polynomials. We used the configuration in Eq. (2.56). As an example, the function f_s for a particle in the principal mass series is given by

$$f_s\left(\frac{k_\mathrm{L}}{k_\mathrm{S}}\right) = \left(\frac{k_\mathrm{L}}{k_\mathrm{S}}\right)^{\frac{3}{2}} \cos\left[\nu_s \ln\left(\frac{k_\mathrm{L}}{k_\mathrm{S}}\right) + \psi_s\right], \tag{2.58}$$

with

$$\nu_s = \begin{cases} \sqrt{\left(\dfrac{M_0}{H}\right)^2 - \dfrac{9}{4}} & (s = 0) \\ \sqrt{\left(\dfrac{M_s}{H}\right)^2 - \left(s - \dfrac{1}{2}\right)^2} & (s = 2, 4, \cdots) \end{cases}. \tag{2.59}$$

Let us examine how to modulate the local power spectrum. When the function f_s can be rewritten into the separable form as

$$f_s\left(\frac{k_\mathrm{L}}{k_\mathrm{S}}\right) = g_s\left(\frac{k_\mathrm{L}}{k_\mathrm{p}}\right) h_s\left(\frac{k_\mathrm{p}}{k_\mathrm{S}}\right), \tag{2.60}$$

with a pivot scale k_p, the squeezed bispectrum (2.57) modifies the local power spectrum at $\boldsymbol{x}$ as [67, 68]

$$P_\Psi(\boldsymbol{k}_\mathrm{S}; \boldsymbol{x} | \Psi_\mathrm{L}) = \left[1 + \sum_{s=0,1,2,3,\cdots} h_s\left(\frac{k_\mathrm{p}}{k_\mathrm{S}}\right) [\hat{k}_\mathrm{S}^{i_1} \cdots \hat{k}_\mathrm{S}^{i_s}]^{\mathrm{TL}_3} \alpha_{\mathrm{L}\, i_1 \cdots i_s}(\boldsymbol{x})\right] P_\Psi(k_\mathrm{S}), \tag{2.61}$$

where $\alpha_{\mathrm{L}\, i_1 \cdots i_s}$ is given by

$$\alpha_{\mathrm{L}\, i_1 \cdots i_s}(\boldsymbol{x}) \equiv \frac{(2s-1)!!}{s!} \int \frac{d^3 \boldsymbol{k}_\mathrm{L}}{(2\pi)^3} A_s g_s\left(\frac{k_\mathrm{L}}{k_\mathrm{p}}\right) [\hat{k}_{\mathrm{L}, i_1} \cdots \hat{k}_{\mathrm{L}, i_s}]^{\mathrm{TL}_3} \Psi(\boldsymbol{k}_\mathrm{L}) e^{i \boldsymbol{k}_\mathrm{L} \cdot \boldsymbol{x}}. \tag{2.62}$$

Here, we used Eq. (D.31) in App. D.4.1. These results are straightforwardly generalized to the case where the squeezed bispectrum is given by a sum of separable contributions. When f_s is given by a linear combination of a power of $k_\mathrm{L}/k_\mathrm{S}$, e.g., Eq. (2.58), which is given by

$$f_s\left(\frac{k_\mathrm{L}}{k_\mathrm{S}}\right) = \frac{1}{2}\left[\left(\frac{k_\mathrm{L}}{k_\mathrm{S}}\right)^{\Delta_s} e^{i\psi_s} + \mathrm{c.c.}\right], \tag{2.63}$$

with $\Delta_s = 3/2 + i\nu_s$, each term can be rewritten as in Eq. (2.60). Reflecting the fact that the contribution of the massive particle is non-local, the bispectrum acquires the oscillatory contribution as a consequence of the non-analytic scaling. The contribution from the odd spin particles is cancelled in the leading order of $k_{\rm L}/k_{\rm S}$ [21], but appears in the sub-leading order with $(k_{\rm L}/k_{\rm S})^{5/2}$ [61] (see also Ref. [69]).

In a simple setup, the squeezed PNG from massive particles is suppressed by the smallness of the coupling, the Boltzmann factor, $e^{-M_s/T_{\rm H}}$ with $T_{\rm H}$ being the Hawking temperature $T_{\rm H} = H_{\rm inf}/(2\pi)$, and the dilution factor $(k_{\rm L}/k_{\rm S})^{3/2}$ (see Eq. (2.58))[12]. A larger coupling between the inflaton and the massive particles enhances the radiative corrections, leading to the breakdown of the EFT description. In Ref. [71], Kumar and Sundrum showed that the PNG mediated by heavy particles in several scenarios is too small to be detected when we require the validity of the EFT description. They also showed that this difficulty could be circumvented in a curvaton scenario, where two different cutoff scales can be introduced. The Boltzmann suppression is not significant for a model where M_s is around $H_{\rm inf}$ as discussed in Refs. [69, 72] by considering explicit models. In Ref. [73], Wang and Xianyu pointed out that a coupling between the inflaton and the massive sector is strictly restricted to evade the Boltzmann suppression without fine-tuning since a large coupling leads to a large radiative correction to M_s. This restriction has guided their attention to parity odd dimension five operators, which can relax the Boltzmann suppression [73, 74] (see also Refs. [75, 76]). Finally, the suppression by the dilution factor $(k_{\rm L}/k_{\rm S})^{3/2}$ for $M_s \geq \mathcal{O}(H_{\rm inf})$ can be evaded by lowering M_s, while the straightforward attempt conflicts with the Higuchi bound for $s \geq 2$ [77]. In Refs. [78, 79], it was argued that the Higuchi bound and subsequently the suppression by the dilution can be avoided when the de Sitter symmetry is explicitly broken, which allows the existence of an additional light spin particle. The model proposed by Kehagias and Riotto in Ref. [78] violates the global rotation symmetry.

Based on the above discussion, we prepare the generalized bispectrum template in the squeezed-limit as follows:

$$B_\Psi(\boldsymbol{k}_1, \boldsymbol{k}_2, \boldsymbol{k}_3) = \sum_\ell A_\ell \,{\rm Re}\left[\left(\frac{k_{\rm L}}{k_{\rm S}}\right)^{\Delta_\ell}\right] \mathcal{P}_\ell(\hat{\boldsymbol{k}}_{\rm S}\cdot\hat{\boldsymbol{k}}_{\rm L}) P_\Psi(k_{\rm L}) P_\Psi(k_{\rm S})\,. \tag{2.64}$$

We can see that $\Delta_0 = 0, 1, 2$ are reproduced as the local, folded and equilateral type bispectrum in Eq. (2.56). In addition, $\Delta_\ell = 3/2 + i\nu_\ell$ are reproduced as the bispectrum induced by the massive even spin-l particles.

For our forecast, we consider both cases with and without the dilution, i.e. ${\rm Re}[\Delta_s] = 3/2$ and $\Delta_s = 0$, respectively. The tightest constraint on the angular-dependent PNG parameters has been obtained from the CMB observation by Planck satellite. The Planck result put the limit on A_2 for $\Delta_2 = 0$ as $\sigma(A_2) \sim 77$ [58]. In Ref. [80], this analysis was extended to a more general angular dependence with

---

[12] The mode function of the scalar massive particles is given by adding the mass term to Eq. (2.33), and the solution becomes $\delta\sigma \propto e^{\pi\nu_0}(-\tau)^{3/2}$ well after horizon exit [46, 47]. When the short-wavelength mode crosses the horizon, the long-wavelength mode shifts the background. This leads to dilution factor $(k_{\rm L}/k_{\rm S})^{3/2}$ [70].

even numbers of s, including the PNG generated by higher spin particles. However, the CMB constraint almost reaches the cosmic variance limit [81]. In Ref. [82], it was argued that from the bispectrum of the galaxy number density, A_s can be constrained as $\sigma(A_2) \sim 15$ for $\Delta_2 = 0$ and $\sigma(A_4) \sim 21$ for $\Delta_4 = 0$. Ref. [83] discussed the constraint on A_s for $\mathrm{Re}[\Delta_s] = 3/2$ by combining the galaxy power spectrum and bispectrum. These analyses require the bispectrum information, which is more complex than the power spectrum analysis, especially in galaxy surveys (e.g., the decomposition of anisotropic signals in the galaxy bispectrum [68, 84, 85]), and the angular dependent PNG signals are mixed up in the bispectrum. Here, one can find an advantage to use galaxy shape [41, 43, 42], whose observation enables us to pick up the imprints of particles with different spins separately.

Chapter 3

Large scale structure formation

The current large-scale structure of the Universe is known from observations to have a huge bubble structure formed by the distribution of galaxies. Such structures do not be formed in a homogeneous universe. This implies that the seeds of the fluctuation are needed in the early Universe, which is often explained by the inflation theory we described in Sec. 2.2. The presence of such initial fluctuations causes the inhomogeneous due to the gravitational evolution, as matter collects where the density is slightly higher.

In this chapter, we summarize the evolution of density fluctuations in order to understand the formation of such a structure. The initial density fluctuations are expected to be sufficiently small in the early Universe, and the CMB observation also shows the amplitude of the primordial curvature perturbation $\mathcal{O}(10^{-4})$. Then, we can understand the evolution of the density fluctuation via the linearized Einstein equation at the early Universe (Sec. 3.1). As the density fluctuation grows, the contribution of non-linear effects appears, and this contribution cannot be expressed in the linear theory. Here, we introduce the methods for describing nonlinear effects based on perturbation theory, which is known as the standard perturbation theory (Sec. 3.3) [86, 87], and based on the self-similar solution (Sec. 3.4) [88].

Furthermore, to compare the theory with the observational data, we need to focus on the statistics of density fluctuations. Since the initial fluctuations are the origin of quantum fluctuations in inflation theory, which is understood as stochastic, the theory cannot uniquely predict the amplitude of the fluctuations at every position and can only predict the expectation of the amplitudes of the fluctuations. Therefore, we introduce the power spectrum as a correlation function in Fourier space (Sec. 3.2). We also refered to Refs. [89, 90, 91].

3.1 Linear perturbation

First of all, let us start with the amount of perturbations added to the metric as

$$ds^2 = a^2(\tau)\left[-(1+2\Psi)d\tau^2 + (1+2\Phi)\delta_{ij}dx^i dx^j\right] , \tag{3.1}$$

where Φ is the curvature perturbation, and Ψ leads to the gravitational potential, which is known as the conformal Newtonian gauge.

We introduce the conformal Friedmann equations, defined as

$$\mathcal{H}^2 = \frac{1}{3M_{\rm Pl}^2}a^2\rho - k + \frac{\Lambda a^2}{3}\,, \quad \mathcal{H}' = -\frac{1}{6M_{\rm Pl}^2}a^2(\rho+3p) + \frac{\Lambda a^2}{3}\,, \tag{3.2}$$

where we denote the prime ($'$) as the derivative with respect to the conformal time τ. From the discussion in Sec. 2.1, the scale factor in the matter dominant epoch depends on $a \propto \tau$ and the one in the radiation dominant epoch depends on $a \propto \tau^2$.

From Eq. (2.8) in absence of the consmological constant Λ, the linearlized Einstein equation is given by

$$a^2G^0_0 = -\left[3\mathcal{H}^2\left(1-2\Psi\right) + 6\mathcal{H}\Phi' - 2\nabla^2\Phi\right]\,, \tag{3.3}$$

$$a^2G^0_i = -2\left(\mathcal{H}\Psi - \Phi'\right)_{,i}\,, \tag{3.4}$$

$$a^2G^i_0 = 2\left(\mathcal{H}\Psi - \Phi'\right)^{,i}\,, \tag{3.5}$$

$$\begin{aligned} a^2G^i_j = &-\left[(2\mathcal{H}'+\mathcal{H}^2)(1-2\Psi) + 2(\Phi''+2\mathcal{H}\Phi'-\mathcal{H}\Psi') - \nabla^2(\Phi+\Psi)\right]\delta^i_j \\ &-(\Psi+\Phi)^{,i}_{,j}\,, \end{aligned} \tag{3.6}$$

with $\nabla^2 \equiv \partial_i\partial^i$ and $X_{,i} \equiv \partial_i X$.

For a simple case, the energy-momentum tensor considers the case of a perfect fluid, where the anisotropic pressure is neglected. In this case, using the 4-momentum u_μ, the energy-momentum tensor becomes

$$T^\mu_\nu = (\rho+p)u^\mu u_\nu + p\delta^\mu_\nu\,. \tag{3.7}$$

With the normalization condition $g_{\mu\nu}u^\mu u^\nu = -1$, the 4-momentum in the perturbed metric is given by

$$u^\mu = \frac{1}{a}(1-\Psi, v^i)\,, \quad u_\mu = a(1+\Psi, v_i),\,, \tag{3.8}$$

with the velocity perturbation $v^i \equiv au^i$. Furthermore, we also divide the energy density and the pressure into background and other quantities as follows:

$$\rho(\boldsymbol{x},\tau) = \bar\rho(\tau) + \delta\rho(\boldsymbol{x},\tau)\,, \quad p(\boldsymbol{x},\tau) = \bar p(\tau) + \delta p(\boldsymbol{x},\tau)\,, \tag{3.9}$$

where $\bar X$ denotes background values with respect to X. Then, the perturbed energy momentum tensor becomes

$$T^0_0 = -\bar\rho(1+\delta)\,, \tag{3.10}$$

$$T^0_i = (\bar\rho+\bar p)v_i\,, \tag{3.11}$$

$$T^i_0 = -(\bar\rho+\bar p)v_i\,, \tag{3.12}$$

$$T^i_j = (\bar p+\delta p)\delta^i_j\,. \tag{3.13}$$

Here we defined the relative energy density perturbation δ as $\delta\rho/\bar\rho$.

Finally, extracting only the perturbations from the Einstein equations with Eq. (3.2), we get

$$3\mathcal{H}(-\Phi' + \mathcal{H}\Psi) + \nabla^2\Phi = -\frac{1}{2M_{\text{Pl}}^2}a^2\delta\rho\,, \tag{3.14}$$

$$(-\Phi' + \mathcal{H}\Psi)_{,i} = \frac{1}{2M_{\text{Pl}}^2}a^2(\bar{\rho}+\bar{p})v_i\,, \tag{3.15}$$

$$(2\mathcal{H}' + \mathcal{H}^2)\Psi - \Phi'' + \mathcal{H}(\Psi' - 2\Phi') + \frac{1}{3}\nabla^2(\Psi + \Phi) = \frac{1}{2M_{\text{Pl}}^2}a^2\delta p\,, \tag{3.16}$$

$$\Phi + \Psi = 0\,. \tag{3.17}$$

The last equation derived from the non-diagonal component and means that there exists no the non-anisotropic tensor. Using the Helmholtz theorem, the velocity vector is decomposed into the divergence and rotation components as

$$v_i = \partial_i v + \epsilon_{ijk}\partial_j V_k\,, \tag{3.18}$$

where v is the scalor field and V_i is the veclor field. From Eqs. (3.14) and (3.15), we find

$$\nabla^2\Psi = \frac{1}{2M_{\text{Pl}}^2}a^2\bar{\rho}\mathit{\Delta} = \frac{3}{2}\mathcal{H}^2\mathit{\Delta}\,, \tag{3.19}$$

where $\mathit{\Delta} \equiv \delta + 3\mathcal{H}(1+w)v$. This leads to the relativistic Poisson equation. The scalar velocity perturbation depends on $v \propto (\mathcal{H}/k)^2$ in Fourier space. Then, when the length of the wavelength is smaller than the Hubble radius ($k \gg \mathcal{H}$), the scalar velocity perturbation becomes negligible and Eq. (3.19) recovers the (classical) Poisson equation.

Due to thermodynamics, with the entropy S, since the pressure perturbation is given by

$$\delta p = \left(\frac{\partial p}{\partial \rho}\right)_S \delta\rho + \left(\frac{\partial p}{\partial S}\right)_\rho \delta S = c_s^2\delta\rho + T\delta S\,, \tag{3.20}$$

the adiabatic condition leads to $\delta p = c_s^2\delta\rho$. Under the adiabatic condition, the evolution of the gravitational potential, conbining Eqs. (3.14)-(3.17), is given by

$$\Psi'' + 3(1+c_s^2)\mathcal{H}\Psi' + 3(c_s^2 - w)\Psi - c_s^2\nabla^2\Psi = 0\,, \tag{3.21}$$

where $w \equiv \bar{p}/\bar{\rho}$. For the radiation dominant epoch, imposing $w = c_s^2 = 1/3$ and $\mathcal{H} = 1/\tau$, we find the solution as

$$\Psi(\boldsymbol{k}, \tau) = C_1\frac{1}{x}n_1(x) + C_2\frac{1}{x}j_1(x)\,, \tag{3.22}$$

where $x \equiv k\tau/\sqrt{3}$, and n_1, j_1 are the first mode of the spherical Neumann function and the spherical Bessel function, respectively. To avoid divergence on the superhorizon scale ($x \ll 1$), which leads to the non-physical effect, it is necessary that $C_1 = 0$. Consequencely, denoting the initial potential as Ψ_r, the behavior of the potential is given by

$$\Psi \propto \begin{cases} \Psi_\mathrm{r} & (k\tau \sim k/\mathcal{H} \ll 1) \\ -\dfrac{\Psi_\mathrm{r}}{(k\tau)^2} \cos\left(\dfrac{k\tau}{\sqrt{3}}\right) & (k\tau \sim k/\mathcal{H} \gg 1) \end{cases} . \tag{3.23}$$

This indicates that the gravitational potential of the wavelength of fluctuations larger than the Hubble horizon is time-invariant, while once the potential enters the Hubble horizon, it oscillates and decays at a^{-2}. On the other hand, from Eq. (3.19), since the density perturbation behaves $\mathit{\Delta} \propto (k/\mathcal{H})^2\Psi$, the density perturbation of the wavelength of fluctuations larger than the Hubble radius grows with a^2 while the one smaller than the Hubble size has only oscillation.

In the matter dominant case ($w = c_s^2 = 0$), since Ψ is independent of the wavelength k, we find that Ψ becomes constant for the growing mode. Then, regardless of the size of the fluctuation, the density fluctuation grows with a.

The linear theory provides the evolution of the fluctuations as the differential of each independent mode k. Then, the fluctuations at the target mode become proportional to the initial fluctuations. As discussed above, the short mode can be interpreted as entering the Hubble horizon earlier. Therefore, the amplitude of the fluctuations depends on when the mode entered the Hubble horizon. Then, it is convenient to describe the behavior of fluctuations with respect to the matter-dominant epoch in which we live. Then, we introduce the transfer function as

$$T(k,\tau) = \frac{D(\tau_\mathrm{in})}{D(\tau)} \frac{\mathit{\Delta}(\boldsymbol{k},\tau)}{\mathit{\Delta}_\mathrm{in}(\boldsymbol{k})} , \tag{3.24}$$

where $D(\tau)$ is the linear growth factor as $D \propto a^2$ for the radiation dominant epoch and $D \propto a$ for the matter dominant epoch (see also Sec. 3.3.) Here we denoted the density fluctuation at the initial time τ_in as $\mathit{\Delta}_\mathrm{in}$. For modes larger than Hubble size ($k < \mathcal{H}$), it is simply because the density fluctuation grows with the growth factors $\mathit{\Delta}(\boldsymbol{k},\tau) \propto D(\tau)$, and this leads to $T(k,\tau) = 1$.

In the radiation dominant epoch, since the density fluctuation does not grow in the Hubble horizon, when the short-wavelength mode enters the horizon before the long-wavelength mode, the amplitude at the short-wavelength mode becomes suppressed. On the other hand, we found that the density fluctuation could grow regardless of the wavelength in the matter dominant epoch. Thus, we find that the transfer function is different before and after the matter-radiation equality epoch. This can be roughly estimated as follows.

Since the wavenumber corresponding to the Hubble radius in the radiation dominant epoch depends on $k = \mathcal{H} \propto a^{-1}$, the scale factor at a given wavenumber can be estimated as $a_\mathrm{H}(k) \propto k^{-1}$. At the matter-radiation epoch, the modes that have already entered the Hubble horizon grow with a^2 during the horizon out while stop growing when enter the horizon, namely

$$\mathit{\Delta}(\boldsymbol{k}, \tau_{\rm eq}) \propto (a_{\rm H})^2 \mathit{\Delta}_{\rm in}(\boldsymbol{k}) \propto k^{-2} \mathit{\Delta}_{\rm in}(\boldsymbol{k})\,. \tag{3.25}$$

Since the fluctuations that enter after the matter-radiation equality epoch can grow, there is no change in the transfer function. To summarize, the transfer function can be expressed as

$$T(k) \propto \left\{ \begin{array}{ll} 1 & (k \ll k_{\rm eq}) \\ k^{-2} & (k \gg k_{\rm eq}) \end{array} \right. , \tag{3.26}$$

where $k_{\rm eq} \equiv \mathcal{H}_{\rm eq} \sim 1.6 \times 10^{-2}[\mathrm{h/Mpc}]\,.$ Since we found that the scalar velocity perturbation on the subhorizon was negligble and $\mathit{\Delta} = \delta$, the relation between the density fluctuation and the initial gravitatinal potential in Fourier space is given by

$$\delta(\boldsymbol{k}, \tau) = \mathcal{M}(k, \tau) \Psi_{\rm i}(\boldsymbol{k}),, \tag{3.27}$$

with $\mathcal{M}$, defined as

$$\mathcal{M}(k, \tau) = \frac{2}{3} \frac{k^2 T(k) D(\tau)}{H_0^2 \Omega_{\rm m0}}\,. \tag{3.28}$$

Hereafter, we may replace τ with z.

3.2 Power spectrum

We brief the statistical treatment for the observation. Though the density fluctuation is an observable quantity, we cannot directly determine the value of the fluctuations at each point. However, we can predict the statistical property of the fluctuations. Since the spatial average of the density fluctuation becomes zero by definition, the fundamental statistical role is played by the *Power spectrum*, which corresponds to the 2-point correlation on Fourier space.

The correlation of the density fluctuations on the Fourier space is given by

$$\langle \delta(\boldsymbol{k}) \delta(\boldsymbol{k}') \rangle = \int d^3x d^3x' e^{-i\boldsymbol{k}\cdot\boldsymbol{x}} e^{-i\boldsymbol{k}'\cdot\boldsymbol{x}'} \langle \delta(\boldsymbol{x}) \delta(\boldsymbol{x}') \rangle\,. \tag{3.29}$$

Here we drop the time-dependent since the density fluctuations are evaluated at the same time. Based on the assumption that the Universe has the global isotropic and homogeneous, there is no particular place or direction in space, which only depends on the relative length. Thus, we introduce the correlation function as

$$\xi(|\boldsymbol{r}|) \equiv \langle \delta(\boldsymbol{x}) \delta(\boldsymbol{x} + \boldsymbol{r}) \rangle\,. \tag{3.30}$$

This function depends on the only distance in real space and how well the density fluctuations are correlated at a distance r.

Inserting Eq. (3.30) into Eq. (3.29), we obtain the matter power spectum, defined as

$$\begin{aligned}\langle\delta(\boldsymbol{k})\delta(\boldsymbol{k}')\rangle &= \int d^3x e^{-i(\boldsymbol{k}+\boldsymbol{k}')\cdot\boldsymbol{x}}\int d^3r e^{-i\boldsymbol{k}'\cdot\boldsymbol{r}}\xi(|\boldsymbol{r}|)\\ &= (2\pi)^3\delta_{\rm D}(\boldsymbol{k}+\boldsymbol{k}')(4\pi)\int r^2 dr j_0(kr)\xi(r)\\ &\equiv (2\pi)^3\delta_{\rm D}(\boldsymbol{k}+\boldsymbol{k}')P_{\rm m}(k)\,,\end{aligned} \tag{3.31}$$

where $j_0(kr)$ is the 0th spherical Bessel function. In the second line, we used the partial wave expansion for $e^{i\boldsymbol{k}\cdot\boldsymbol{r}}$. The delta function implies the homogeneous, and the non-directional vector means the isotropy in the (statistical) Universe. Note that the power spectrum by the definition has the dimension of cubic of the length and the dimensionless power spectrum can be defined as

$$\Delta^2(k,\tau)\equiv\frac{k^3}{2\pi^2}P_{\rm m}(k,\tau)\,. \tag{3.32}$$

Similarly, we can also define the spectra for the higher points correlation. The 3-point function is defined as

$$\langle\delta(\boldsymbol{k}_1)\delta(\boldsymbol{k}_2)\delta(\boldsymbol{k}_3)\rangle\equiv(2\pi)^3\delta_{\rm D}(\boldsymbol{k}_1+\boldsymbol{k}_2+\boldsymbol{k}_3)B_{\rm m}(\boldsymbol{k}_1,\boldsymbol{k}_2,\boldsymbol{k}_3)\,, \tag{3.33}$$

where we introduced the bispectrum $B_{\rm m}$. The bispectrum vanishes if δ is Gaussian, which implies that the bispectrum becomes the lowest order correlator in order to distinguish the non-Gaussian from the Gaussian perturbations. Imposing the homogeneous and isotropy, the bispectrum should be the global rotation invariant. Thus, the bispectrum only depends on the length of wavevectors and is formed as the triangle due to the momentum conservation from the delta function.

We can also define the 4-point function as

$$\langle\delta(\boldsymbol{k}_1)\delta(\boldsymbol{k}_2)\delta(\boldsymbol{k}_3)\delta(\boldsymbol{k}_4)\rangle_{\rm c}\equiv(2\pi)^3\delta_{\rm D}(\boldsymbol{k}_1+\boldsymbol{k}_2+\boldsymbol{k}_3+\boldsymbol{k}_4)T_{\rm m}(\boldsymbol{k}_1,\boldsymbol{k}_2,\boldsymbol{k}_3,\boldsymbol{k}_4)\,, \tag{3.34}$$

where we introduced the trispectrum $T_{\rm m}$. Here we denote the subscript $\langle\cdots\rangle_{\rm c}$ as the connected part. The connected part is given by

$$\begin{aligned}\langle\delta(\boldsymbol{k}_1)\delta(\boldsymbol{k}_2)\delta(\boldsymbol{k}_3)\delta(\boldsymbol{k}_4)\rangle_{\rm c} &= \langle\delta(\boldsymbol{k}_1)\delta(\boldsymbol{k}_2)\delta(\boldsymbol{k}_3)\delta(\boldsymbol{k}_4)\rangle\\ &\quad -\left(\langle\delta(\boldsymbol{k}_1)\delta(\boldsymbol{k}_2)\rangle\langle\delta(\boldsymbol{k}_3)\delta(\boldsymbol{k}_4)\rangle+\text{perms.}\right).\end{aligned} \tag{3.35}$$

The trispectrum also vanishes if δ is Gaussian and the 4-point correlation becomes the order of the square of the matter power spectrum.

As discussed in Sec. 2.2.3, when there exist the primordial non-Gaussianities, using the Poisson equation in the linear theory Eq. (3.27), the bispectrum and trispectrum can be related to the primordial spectra as

$$B_{\rm m}(\boldsymbol{k}_1,\boldsymbol{k}_2,\boldsymbol{k}_3) = \mathcal{M}(k_1)\mathcal{M}(k_2)\mathcal{M}(k_3)B_\Psi(\boldsymbol{k}_1,\boldsymbol{k}_2,\boldsymbol{k}_3)\,, \tag{3.36}$$

$$T_{\rm m}(\boldsymbol{k}_1,\boldsymbol{k}_2,\boldsymbol{k}_3,\boldsymbol{k}_4) = \mathcal{M}(k_1)\mathcal{M}(k_2)\mathcal{M}(k_3)\mathcal{M}(k_4)T_\Psi(\boldsymbol{k}_1,\boldsymbol{k}_2,\boldsymbol{k}_3,\boldsymbol{k}_4)\,. \tag{3.37}$$

3.3 Non-linear Perturbation

When the amplitudes of fluctuations are small enough ($\delta \ll 1$), thier evolution can be described by linear theory. As the fluctuations become growth, the non-linear effects can no longer be ignored. However, from the perspective of perturbation theory, we can investigate the quasi-nonlinear region analytically. Such analysis may be necessary for the late Universe when structure formation is evolved due to the gravitational evolution. Here, since we are interested in the structure in the subhorizon, we summarize the non-linear treatment to use the Newtonian approximation.

In the rest freme, by using the density $\rho(\boldsymbol{r},t)$, velocity $\boldsymbol{u}(\boldsymbol{r},t)$, pressure $p(\boldsymbol{r},t)$ fields and the gravitational potential $\Psi_{\rm res}(\boldsymbol{r},t)$, the continuity, Eular and Poisson equation in the rest frame are given by

$$\partial_t\rho + \nabla_{\boldsymbol{r}}\cdot(\rho\boldsymbol{u}) = 0\,, \tag{3.38}$$

$$\frac{d}{dt}\boldsymbol{u} = \partial_t\boldsymbol{u} + (\boldsymbol{u}\cdot\nabla_{\boldsymbol{r}})\,\boldsymbol{u} = -\frac{1}{\rho}\nabla_{\boldsymbol{r}}p - \nabla_{\boldsymbol{r}}\Psi_{\rm res}\,, \tag{3.39}$$

$$\nabla^2_{\boldsymbol{r}}\Psi_{\rm res} = 4\pi G\rho - \Lambda\,, \tag{3.40}$$

where $\nabla_{\boldsymbol{r}}$ denotes the spatial derivative with respect to the coordinate in the rest frame. For ΛCDM, the Poisson equation is added the cosmological constant. The first equation corresponds to the energy conservation and the second equation corresponds to the equation of motion for fluid systems.

Considering the influence of cosmic expansion, we change the coordinates system from the rest frame to the comoving frame. The relation between the comoving coordiante $\boldsymbol{x}$ and the physical coordiate $\boldsymbol{r}$ is given by

$$\boldsymbol{r} = a(t)\boldsymbol{x}\,, \tag{3.41}$$

and the velocity in comoving frame is defined as

$$\boldsymbol{v} \equiv a\partial_t\boldsymbol{x}\,. \tag{3.42}$$

From Eqs. (3.41) and (3.42), the continutity and Eular equations in the comoving system are converted as

$$\rho' + 3\mathcal{H}\rho + \nabla\cdot(\rho\boldsymbol{v}) = 0\,, \tag{3.43}$$

$$\boldsymbol{v}' + \mathcal{H}\boldsymbol{v} + (\boldsymbol{v}\cdot\nabla)\,\boldsymbol{v} = -\frac{1}{\rho}\nabla p - \nabla\Psi\,, \tag{3.44}$$

where the gravitatinal potential in the comoving system Ψ is defined as $\Psi \equiv \Psi_{\rm res} + \frac{1}{2}\mathcal{H}'x^2$. Redefined in this way, the Poisson equation in comoving system becomes

$$\nabla^2\Psi = \frac{3}{2}\mathcal{H}^2\Omega_{\rm m}(\tau)\delta(\boldsymbol{x},\tau)\,, \tag{3.45}$$

with the density fluctuation $\delta(\boldsymbol{x},\tau)$. This means that the homogeneous density does not influence the gravitational potential of the comoving system. In other words, the gravitational potential is given by the density contrast.

Averaging spatially over Eq. (3.43), we obtain

$$\frac{d}{d\tau}(a^3\rho) = 0\,. \tag{3.46}$$

The density decays as a^{-3}, and this is the same result as the energy conservation on the Einstein de-Sitter (EdS) cosmology. The equations for the perturbed part in the EdS cosmology, with the background component removed, are given by

$$\delta'(\boldsymbol{x},\tau) + \nabla\cdot[(1+\delta(\boldsymbol{x},\tau))\boldsymbol{v}(\boldsymbol{x},\tau)] = 0\,, \tag{3.47}$$

$$\boldsymbol{v}'(\boldsymbol{x},\tau) + [\boldsymbol{v}(\boldsymbol{x},\tau)\cdot\nabla]\,\boldsymbol{v}(\boldsymbol{x},\tau) + \mathcal{H}\boldsymbol{v}(\boldsymbol{x},\tau) = -\nabla\Psi(\boldsymbol{x},\tau)\,, \tag{3.48}$$

where we used to ignore the pressure in the EdS cosmology. In general, vector fields can be decomposed into rotation-free and divergence-free components by using Helmholtz's theorem. We consider the divergence-free component of the velocity, corresponding to the vorticity. Applying the curl operator to Eq. (3.48), the vorticity $\nabla\times\boldsymbol{v}$ in the linear order becomes

$$\frac{d}{d\tau}(a\nabla\times\boldsymbol{v}) = 0\,. \tag{3.49}$$

Since the evolution of the vorticity field decays as a^{-1}, so after enough time, this becomes negligible due to cosmic expansion.

Focusing on the principle part of the velocity, we introduce the longitudinal velocity field as $\theta \equiv \nabla\cdot\boldsymbol{v}(\boldsymbol{x},\tau)$. Eq. (3.48) to which applied the divergence operator can be combined with the Poisson equation. In Fourier space, we can obtain

$$\delta'(\boldsymbol{k}) + \theta(\boldsymbol{k}) = -\int_{\boldsymbol{k}_1}\int_{\boldsymbol{k}_2}\bar{\delta}_{\rm D}(\boldsymbol{k}-\boldsymbol{k}_{12})\alpha(\boldsymbol{k}_1,\boldsymbol{k}_2)\theta(\boldsymbol{k}_1)\delta(\boldsymbol{k}_2)\,, \tag{3.50}$$

$$\theta'(\boldsymbol{k}) + \mathcal{H}\theta(\boldsymbol{k}) + \frac{3}{2}\mathcal{H}^2\Omega_{\rm m}\delta(\boldsymbol{k}) = -\int_{\boldsymbol{k}_1}\int_{\boldsymbol{k}_2}\bar{\delta}_{\rm D}(\boldsymbol{k}-\boldsymbol{k}_{12})\beta(\boldsymbol{k}_1,\boldsymbol{k}_2)\theta(\boldsymbol{k}_1)\theta(\boldsymbol{k}_2)\,, \tag{3.51}$$

with

$$\alpha(\boldsymbol{k}_1,\boldsymbol{k}_2) = 1 + \frac{\boldsymbol{k}_1\cdot\boldsymbol{k}_2}{k_1^2}\,,\quad \beta(\boldsymbol{k}_1,\boldsymbol{k}_2) = \frac{k_{12}^2(\boldsymbol{k}_1\cdot\boldsymbol{k}_2)}{2k_1^2k_2^2}\,. \tag{3.52}$$

Here we used $\boldsymbol{k}_{12\cdots n} = \boldsymbol{k}_1 + \boldsymbol{k}_2 + \cdots \boldsymbol{k}_n$, $\int_{\boldsymbol{k}_i} = \int \frac{d^3\boldsymbol{k}_i}{(2\pi)^3}$ and $\bar{\delta}_{\rm D}(\boldsymbol{k}) = (2\pi)^3\delta_{\rm D}(\boldsymbol{k})$. We use these notations from now on. Since the terms in the right-hand sides of

Eqs. (3.50) and (3.51) have the couplings between the different modes, it is difficult to lead the analytical solutions for $\delta\,,\theta$. However, in the context of perturbation theory, the goal is to find an analytic solution by assuming that the linear component is a sufficiently small quantity and expecting that it can be expanded by the power of the linear component. Thus, the density fluctuation and the velocity divergence are pertutbatively given by

$$\delta(\boldsymbol{k}) = \sum_{n=1}^{\infty} \delta^{(n)}(\boldsymbol{k})\,, \quad \theta(\boldsymbol{k}) = \sum_{n=1}^{\infty} \theta^{(n)}(\boldsymbol{k})\,, \tag{3.53}$$

where the superscript (n) means a term involving n powers of the linear component.

In the limit of long-wavelength ($k \to 0$), the time evolution of the fields can be applied to the linear theory. Thus, the quadratic terms in Eqs. (3.50) and (3.51) can be neglected. The time evolution of the linear density contrast is given by

$$\delta^{(1)''}(\boldsymbol{k}) + \mathcal{H}\delta^{(1)'}(\boldsymbol{k}) - \frac{3}{2}\mathcal{H}^2\Omega_{\rm m}\delta^{(1)}(\boldsymbol{k}) = 0\,. \tag{3.54}$$

Since the terms corresponding to spatial derivatives disappear, the time evolution of $\delta^{(1)}$ is the same regardless of modes. This implies $\delta^{(1)}$ can be separatable into time and modes components as $\delta^{(1)}(\boldsymbol{k},\tau) = [D(\tau)/D(\tilde{\tau})]\delta^{(1)}(\boldsymbol{k},\tilde{\tau})$, where $\tilde{\tau}$ is a reference time. Then, the time evolution can be expressed by

$$D(\tau)'' + \mathcal{H}D(\tau)' - \frac{3}{2}\mathcal{H}^2\Omega_{\rm m}D(\tau) = 0\,. \tag{3.55}$$

The solutions are the growing mode $D_+ \propto a$ and the decaying mode $D_- \propto a^{-3/2}$ during matter domination. In general, the time evolution solutions of the density contrast always have both the growing and decaying modes. However, since we are interested in the growth of the structure, we only have to consider the growing mode. From now on, we refer to the growing mode as $D(\tau)$, which is called the *(linear) growth factor*. Moreover, since we set the time evolution of the density fluctuation as how the density fluctuation changes with respect to the reference time, we need not decide the normalized factor, and the linear growth factor D during matter domination can be set as $D(\tau) = a(\tau)$. Since the epoch around today ($a \sim 1$) has a dark energy contribution, the growth factor slightly deviates from the EdS cosmology, and the exact growth factor is given by

$$D(\tau) \propto \frac{\mathcal{H}}{a}\int_0^a \frac{da}{\mathcal{H}^3}\,. \tag{3.56}$$

From Eq. (3.50), the soution of the linear velocity divergence field $\theta^{(1)}$ can be given by

$$\theta^{(1)}(\boldsymbol{k}) = -\delta^{(1)'}(\boldsymbol{k}) = -f\mathcal{H}\delta^{(1)}(\boldsymbol{k})\,, \tag{3.57}$$

where f is defined as the logarithmic growth rate $f \equiv d\ln D/d\ln a$. This implies the divergence velocity is proportional to the density field. Straightforwardly, we can get the time evolution of the logarithmic growth rate as

$$(\mathcal{H}f)' = \mathcal{H}^2\left(\frac{3}{2}\Omega_{\rm m} - f + f^2\right) . \tag{3.58}$$

From the consequence of Eqs. (3.53) and (3.57), we assume an ansatz of the n-th order solutions to Eq. (3.53) as

$$\delta^{(n)}(\boldsymbol{k},\tau) = \int_{\boldsymbol{k}_1}\cdots\int_{\boldsymbol{k}_n}\bar{\delta}_{\rm D}(\boldsymbol{k}-\boldsymbol{k}_{1\cdots n})F_n(\boldsymbol{k}_1,\cdots,\boldsymbol{k}_n,\tau)\delta^{(1)}(\boldsymbol{k}_1,\tau)\cdots\delta^{(1)}(\boldsymbol{k}_n,\tau) , \tag{3.59}$$

$$\frac{\theta^{(n)}(\boldsymbol{k},\tau)}{\mathcal{H}f} = -\int_{\boldsymbol{k}_1}\cdots\int_{\boldsymbol{k}_n}\bar{\delta}_{\rm D}(\boldsymbol{k}-\boldsymbol{k}_{1\cdots n})G_n(\boldsymbol{k}_1,\cdots,\boldsymbol{k}_n,\tau)\delta^{(1)}(\boldsymbol{k}_1,\tau)\cdots\delta^{(1)}(\boldsymbol{k}_n,\tau) , \tag{3.60}$$

where F_n and G_n are the symmetrized ($\boldsymbol{k}_i \leftrightarrow \boldsymbol{k}_j$) density and velocity divergence kernels. Inserting these expressions into Eqs. (3.50) and (3.51), these kernels can be computed recursively while evaluating the order of the perturbations. (The recursion relations can be found, for example, Refs. [92, 87].) From the momentum conservation, the kernel F_n becomes proportional to k^2 as $\boldsymbol{k} = \boldsymbol{k}_{12\cdots n}$ goes to zero but each mode $\boldsymbol{k}_i$ is non-zero [91].

The kernels for $n = 1$ correspond to the linear components, $F_1 = G_1 = 1$, obviously. The kernels for $n = 2, 3$ are explicitly expressed by

$$F_2(\boldsymbol{k}_1,\boldsymbol{k}_2) = \frac{5}{7} + \frac{2}{7}\frac{(\boldsymbol{k}_1\cdot\boldsymbol{k}_2)^2}{k_1^2k_2^2} + \frac{\boldsymbol{k}_1\cdot\boldsymbol{k}_2}{2k_1k_2}\left(\frac{k_1}{k_2}+\frac{k_2}{k_1}\right) , \tag{3.61}$$

$$G_2(\boldsymbol{k}_1,\boldsymbol{k}_2) = \frac{3}{7} + \frac{4}{7}\frac{(\boldsymbol{k}_1\cdot\boldsymbol{k}_2)^2}{k_1^2k_2^2} + \frac{\boldsymbol{k}_1\cdot\boldsymbol{k}_2}{2k_1k_2}\left(\frac{k_1}{k_2}+\frac{k_2}{k_1}\right) , \tag{3.62}$$

$$\begin{aligned} F_3(\boldsymbol{k}_1,\boldsymbol{k}_2,\boldsymbol{k}_3) = \frac{1}{6}\Bigg\{ & \frac{7}{9}\frac{\boldsymbol{k}_{123}\cdot\boldsymbol{k}_3}{k_3^2}F_2(\boldsymbol{k}_1,\boldsymbol{k}_2) \\ & + \left[\frac{7}{9}\frac{\boldsymbol{k}_{123}\cdot\boldsymbol{k}_{12}}{k_{12}^2} + \frac{2}{9}\frac{k_{123}^2(\boldsymbol{k}_{12}\cdot\boldsymbol{k}_3)}{k_3^2k_{12}^2}\right]G_2(\boldsymbol{k}_1,\boldsymbol{k}_2) + (\text{perms.})\Bigg\} , \end{aligned} \tag{3.63}$$

$$\begin{aligned} G_3(\boldsymbol{k}_1,\boldsymbol{k}_2,\boldsymbol{k}_3) = \frac{1}{6}\Bigg\{ & \frac{1}{3}\frac{\boldsymbol{k}_{123}\cdot\boldsymbol{k}_3}{k_3^2}F_2(\boldsymbol{k}_1,\boldsymbol{k}_2) \\ & + \left[\frac{1}{3}\frac{\boldsymbol{k}_{123}\cdot\boldsymbol{k}_{12}}{k_{12}^2} + \frac{2}{3}\frac{k_{123}^2(\boldsymbol{k}_{12}\cdot\boldsymbol{k}_3)}{k_3^2k_{12}^2}\right]G_2(\boldsymbol{k}_1,\boldsymbol{k}_2) + (\text{perms.})\Bigg\} . \end{aligned} \tag{3.64}$$

Strictly speaking, such an exact solution can be given only for EdS cosmology, but it is known to be approximately valid for ΛCDM cosmology as well. (see for more accurate calculation for ΛCDM cosmology, e.g., Ref. [93].)

Based on the results so far, we discuss the density power spectrum. The density power spectra corresponding to the orders n, n' are defined as

$$\langle \delta^{(1)}(\boldsymbol{k})\delta^{(1)}(\boldsymbol{k}')\rangle \equiv \bar{\delta}_{\rm D}(\boldsymbol{k}+\boldsymbol{k}')P_{\rm L}(k)\,, \tag{3.65}$$

$$\langle \delta^{(n)}(\boldsymbol{k})\delta^{(n')}(\boldsymbol{k}')\rangle \equiv \bar{\delta}_{\rm D}(\boldsymbol{k}+\boldsymbol{k}')P_{\rm m}^{(nn')}(k) \qquad \text{for } n = n' \neq 1\,. \tag{3.66}$$

Let us derive the next-to-leading order (NLO) contribution (1-loop) to the matter power spectrum. The auto-correlation of matter density with Eq. (3.53) is given by

$$\begin{aligned}\langle \delta(\boldsymbol{k})\delta(\boldsymbol{k}')\rangle &= \langle \delta^{(1)}(\boldsymbol{k})\delta^{(1)}(\boldsymbol{k}')\rangle + 2\langle \delta^{(1)}(\boldsymbol{k})\delta^{(2)}(\boldsymbol{k}')\rangle \\ &\quad + 2\langle \delta^{(1)}(\boldsymbol{k})\delta^{(3)}(\boldsymbol{k}')\rangle + \langle \delta^{(2)}(\boldsymbol{k})\delta^{(2)}(\boldsymbol{k}')\rangle + \mathcal{O}(\delta^5)\,.\end{aligned} \tag{3.67}$$

We can calculate each of the correlations straightforwardly by using the Wick theorem. The NLO power spectrum is given by

$$P_{\rm m}^{\rm NLO}(k) = 2P^{(12)}(k) + P_{\rm m}^{(22)}(k) + 2P_{\rm m}^{(13)}(k)\,, \tag{3.68}$$

$$P_{\rm m}^{(12)}(k) = \int_{\boldsymbol{p}} F_2(\boldsymbol{p},\boldsymbol{k}-\boldsymbol{p})B_{\rm L}(-\boldsymbol{k},\boldsymbol{p},\boldsymbol{k}-\boldsymbol{p})\,, \tag{3.69}$$

$$\begin{aligned}P_{\rm m}^{(22)}(k) &= 2\int_{\boldsymbol{p}} [F_2(\boldsymbol{p},\boldsymbol{k}-\boldsymbol{p})]^2 P_{\rm L}(p)P_{\rm L}(|\boldsymbol{k}-\boldsymbol{p}|) \\ &\quad + \int_{\boldsymbol{p}}\int_{\boldsymbol{p}'} F_2(\boldsymbol{p},\boldsymbol{k}-\boldsymbol{p})F_2(\boldsymbol{p}',\boldsymbol{k}-\boldsymbol{p}')T_{\rm L}(\boldsymbol{p},\boldsymbol{k}-\boldsymbol{p},-\boldsymbol{p}',\boldsymbol{p}'-\boldsymbol{k})\,,\end{aligned} \tag{3.70}$$

$$\begin{aligned}P_{\rm m}^{(13)}(k) &= 3P_{\rm L}(k)\int_{\rm p} F_3(\boldsymbol{p},-\boldsymbol{p},\boldsymbol{k})P_{\rm L}(p) \\ &\quad + \int_{\boldsymbol{p}}\int_{\boldsymbol{p}'} F_3(\boldsymbol{p},\boldsymbol{p}',\boldsymbol{k}-\boldsymbol{p}-\boldsymbol{p}')T_{\rm L}(-\boldsymbol{k},\boldsymbol{p},\boldsymbol{p}',\boldsymbol{k}-\boldsymbol{p}-\boldsymbol{p}')\,,\end{aligned} \tag{3.71}$$

where $B_{\rm L}$ and $T_{\rm L}$ are the bispectrum and the trispectrum from the 3-point / 4-point functions among the linear density contrast, respectively. When the initial density condition follows the Gaussian distribution, $P_{\rm m}^{(12)}$ and the terms involving the trispectrum $T_{\rm L}$ vanish.

One can think of incorporating the contributions of higher-order loops to handle non-linearity effects in principle accurately. This has been investigated using N-body simulations, and according to [94], they showed that the non-linear matter power spectrum with the contributions up to three loops predicted worse than when one of the contributions up to two loops at low redshifts if even low-k (Fig. 3.1). The loop contributions perturbatively incorporate the contribution of the small scale fluctuations (at high-k), which in turn affects the large scale (at low-k). Since the gravitational evolution increases the small-scale fluctuations as the redshift gets smaller, this effect becomes more apparent at low redshifts. Consequently, this implies that adding loop contributions improves the agreement only up to a certain order for any redshift.

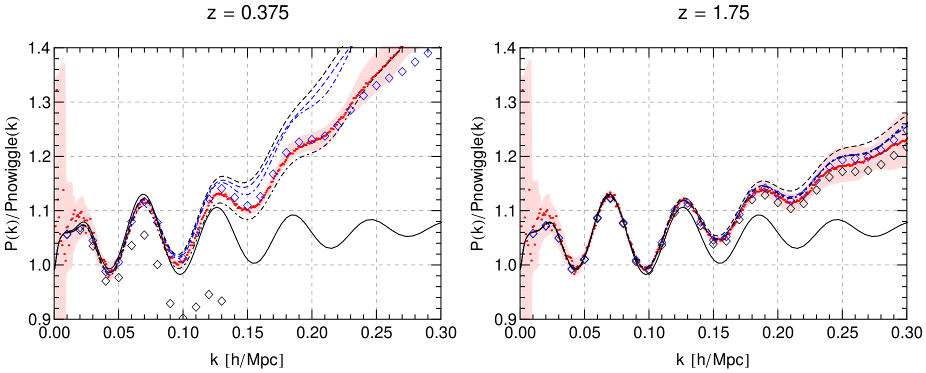

FIGURE 3.1: This shows that the comparison at some redshifts $z = 0.375, 1.75$ of SPT up to one loop (black dashed lines), two loops (black dot-dashed) and three loops (black diamonds) with N-body results ((red dots). The black line corresponds to the linear result. (adapted from [94])

3.4 Loop contributions by self-similar solution

We summarize the qualitative discussion of the loop contributions by using self-similar solution. In the EdS cosmology, the equation of motion has a scalling symmetry as follows,

$$\tilde{\delta}(\boldsymbol{x},\tau) = \delta(\lambda_x\boldsymbol{x},\lambda_\tau\tau)\,, \tag{3.72}$$

$$\tilde{v}^i(\boldsymbol{x},\tau) = \frac{\lambda_\tau}{\lambda_x}v^i(\lambda_x\boldsymbol{x},\lambda_\tau\tau)\,, \tag{3.73}$$

$$\tilde{\Psi}(\boldsymbol{x},\tau) = \left(\frac{\lambda_\tau}{\lambda_x}\right)^2\Psi(\lambda_x\boldsymbol{x},\lambda_\tau\tau)\,, \tag{3.74}$$

where λ_x, λ_τ are arbitrary scalling factors. Inserting Eq. (3.74) into Eqs. (3.47), (3.48) and (3.45), we can check the scaling solution follows the same equations of motion. Though new solutions can be obtained by arbitrarily choosing scaling factors λ_x, λ_τ, not all solutions correspond to a realization of the same cosmology, and by choosing the appropriate one, similar solutions can be obtained from the different realizations with the same initial conditions.

Under the above scaling, the dimensionless matter power spectrum Eq. (3.32) becomes

$$\bar{\Delta}^2(k,\tau) = \Delta^2\left(\frac{k}{\lambda_x},\lambda_\tau\tau\right)\,. \tag{3.75}$$

Assuming that all perturbations are Gaussian since the perturbation at each mode grows independently, the time dependency of the scaled solutions is the same as that of the solutions before scaling. After all, we only have to examine if the scaled solutions follow the same power spectrum at initial time. If the initial dimensionless matter power spectrum is written by $\Delta^2_{\rm in} \propto \tau^4 k^{n+3}$, which the growth factor in EdS cosmology is $D(\tau) \propto \tau^2$, we find the scaled initial dimentionalless matter power spectrum is given by

$$\bar{\Delta}_{\rm in}(k,\tau) \propto \frac{\lambda_\tau^4}{\lambda_x^{n+3}} \Delta_{\rm in}^2(k,\tau)\,. \tag{3.76}$$

If we choise $\lambda_\tau^4 = \lambda_x^{n+3}$, the rescaled solutions correspond to different realizations of the same initial power spectrum and the power spectra of the rescaled solutions at any time should be the one of the same as the unsclaed solution. Then we find that the relation between the scaled power spectrum and the unscaled one becomes

$$\Delta^2(k,\tau) = \bar{\Delta}^2(k,\tau) = \Delta^2\left(\frac{k}{\lambda^{4/(n+3)}}, \lambda\tau\right)\,. \tag{3.77}$$

To be more practical, we introduce the non-linear scale $k_{\rm NL}$ such as $\Delta_{\rm L}(k_{\rm NL}) = 1$, of which the time denpence is $k_{\rm NL}^{3+n} \propto \tau^{-4}$. Then using the arbitrary function of the self-similarity combination $k/k_{\rm NL}$, Eq. (3.77) can be rewritten as

$$\Delta^2(k,\tau) = \Delta^2(k/k_{\rm NL})\,. \tag{3.78}$$

This means that the power spectrum at the non-linear scale should be evaluated at the only corresponding scale. Consequently, in the quasi-nonlinear region, by using the contributions of the loop appears roughly as the loop times the linear power spectrum, the dimensionless power spectrum can be evaluated as

$$\Delta^2 = \Delta_{\rm L}^2 + \sum_l \Delta_{l-{\rm loop}}^2\,, \tag{3.79}$$

with

$$\Delta_{\rm L}^2 = \left(\frac{k}{k_{\rm NL}}\right)^{n_{\rm L}+3}\,, \quad \Delta_{l-{\rm loop}}^2 \propto \left(\frac{k}{k_{\rm NL}}\right)^{(l+1)(n_{\rm L}+3)}\,, \tag{3.80}$$

where $n_{\rm L}$ is defined as

$$n_{\rm L} \equiv d\ln P_{\rm L}(k)/d\ln k|_{k=k_{\rm NL}}\,. \tag{3.81}$$

Though we have discussed the case of the EdS cosmology and the simple power law matter power spectrum, it is known that this result can be well approximated with the present ΛCDM cosmology where the power of scale is explicitly given by $n_{\rm L} = -1.7$ at $k_{\rm NL} = 0.25\,h{\rm Mpc}^{-1}$ (Fig. 3.2).

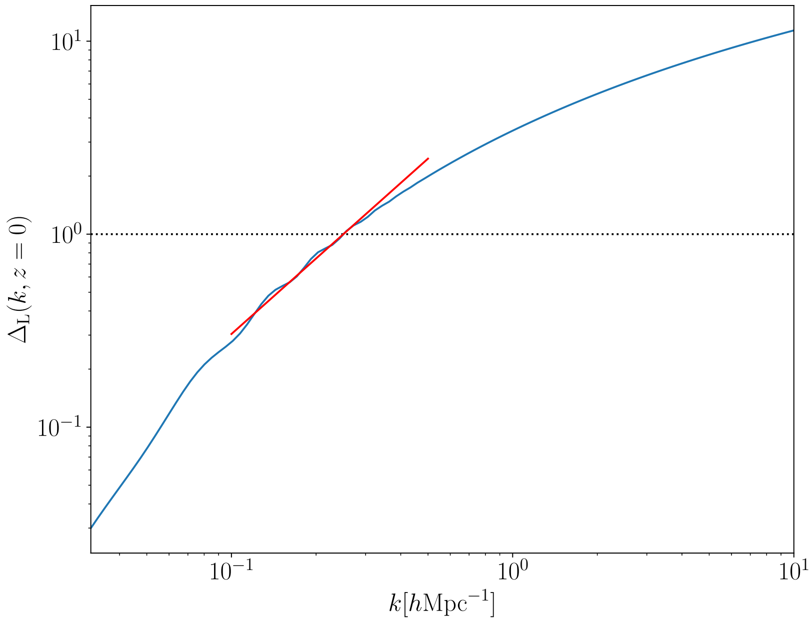

FIGURE 3.2: This shows the dimensionless linear matter spectrum at $z = 0$. The black dot line indicates that the amplitude of the spectrum is unity. The red solid line is the line of fitting around which the amplitude of the spectrum is unity, corresponding to $k_{\mathrm{NL}} = 0.25\,h\mathrm{Mpc}^{-1}$ and $n_{\mathrm{L}} = -1.7$. We set the Planck fiducial result Eq. (2.18) as the cosmological parameters.

Chapter 4

Galaxy Bias and scale dependent bias

The distribution of galaxies and galaxy clusters, which is known as the *Large Scale Structure (LSS)*, provides the cosmological history because the observation of tracers at cosmological distances leads to the search for deviations from homogeneous Universe. Such the structure can be expected to be formed by tracing the fluctuation of the matter component of the Universe. However, we can only observe sources emitting enough light to be observable, and we cannot directly observe anything else (including dark matters). Therefore, we investigate the relationship between the luminous tracer and matter, which is known as *bias*, to understand the observed picture of the LSS and thus the evolution of the cosmological components.

As a simple case, for example, in a region where a sufficiently linear approximation holds, we expect that the fluctuation of the number of the objects such as galaxies or halos is given by

$$\delta_{\rm n}(\boldsymbol{x},\tau) \equiv \frac{n(\boldsymbol{x},\tau)-\bar{n}(\tau)}{\bar{n}(\tau)} = b(\tau)\delta(\boldsymbol{x},\tau)\,, \tag{4.1}$$

where n denotes the comoving number of objects per volume, $\bar{n}$ means the comoving spatial average of n and b is the bias parameter, which depends on the time and the small scale physics. Though the spatial average of the 1-point functions is zero by definition, the 2-point correlation provides the function with the square of the bias parameter b^2. Considering specific bias mechanisms such as peak bias or halo bias, we can capture a physical picture of the bias mechanism. The peak bias is a simple picture that the collapse objects are formed at the peak of linear density fluctuations above threshold in spherically symmetric density fluctuations (see Fig. 4.1). In contrast, halo bias is a mechanism based on the distribution of mass components at the initial time based on Lagrangian pictures, not limited to spherical symmetry [95]. On the other hand, the bias parameter can also be treated as a just coefficient without specifying a unique bias mechanism in the analysis by expanding the perturbations.

In this chapter, according to Refs. [67, 68, 41, 96], we review the galaxy bias, which is based on the galaxy shapes statistics without a specific bias mechanism. Note that although we assume *galaxy* bias, this discussion is used in general tracers,

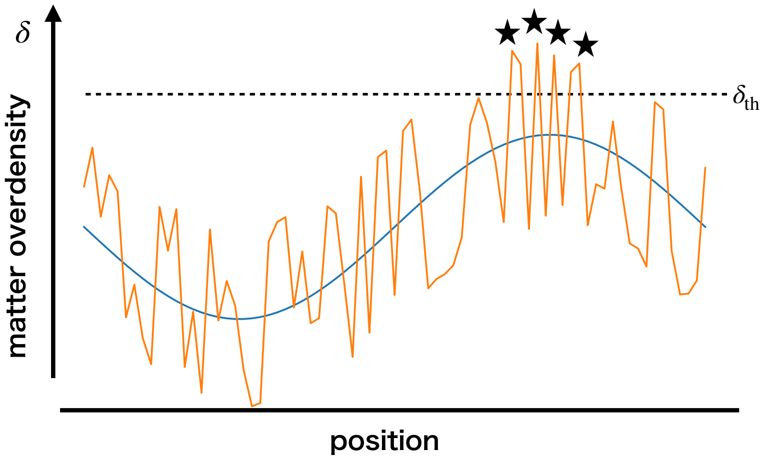

FIGURE 4.1: We show the schematic picture of the peak bias. The blue line shows the course-grained matter density field, and the orange line indicates a matter density field. In the context of the peak bias, the halos are formed at the peak above the threshold $\delta_{\rm th}$, which is the critical density $\delta_{\rm c} \simeq 1.69$ for the spherical collapse. We can interpret that the halos tend to be formed where the amplitude of the long-wavelength mode is larger and the halo (or galaxy) is biased by the long-wavelength perturbation.

including dark matter halos.

4.1 Bias expansion with primordial non-Gaussianity

Here we discuss the bias in accordance with the main interpretation of the *effective field theory* (EFT), which is known as EFTofLSS. The EFTofLSS is one of the analytical frameworks to understand the LSS through the perturbative expansion of the fluctuation and parameterizes by integrating out the contribution of short distance non-linear physics at the long distances, such as the sound of speeds and viscosity and so on. The details for these parameters require understanding all small-scale physics. Therefore, the parameters themselves are determined from numerical simulations or observations.

Let us consider the bias of the galaxy number density fluctuation. Using the non-local functional $\mathcal{N}$, the number density of the object at Eulerian position $\boldsymbol{x}$ and time τ is given by

$$n(\boldsymbol{x},\tau) = \mathcal{N}[\Psi_{\rm i}(\boldsymbol{y})](\boldsymbol{x},\tau)\,, \tag{4.2}$$

where $\Psi_{\rm i}$ denotes the primordial gravitational potential. This is the general relational equation and includes all non-linear regions. However, the base function in the functional can be simplified by using the equivalent principle, which states that only the second derivatives of the metric become the local gravitational observable.From the view of the equivalent principle, we can always transform to the free-falling frame along the fluid of the object. That is why we can remove any uniform and pure-gradient potential perturbations.

Thus, the bias should be expanded with the tidal tensor Π_{ij}, defined as

$$\Pi_{ij}(\boldsymbol{x},\tau) \equiv \frac{2}{3\mathcal{H}^2\Omega_{\rm m}}\partial_i\partial_j\Psi(\boldsymbol{x},\tau) = K_{ij}(\boldsymbol{x},\tau) + \frac{1}{3}\delta_{ij}\delta(\boldsymbol{x},\tau)\,, \tag{4.3}$$

with the tidal field K_{ij}, defined as

$$K_{ij}(\boldsymbol{x},\tau) \equiv \left[\frac{\partial_i\partial_j}{\nabla^2} - \frac{1}{3}\delta_{ij}\right]\delta(\boldsymbol{x},\tau) = \mathcal{D}_{ij}\delta(\boldsymbol{x},\tau)\,, \tag{4.4}$$

which is a symmetric and traceless tensor. Consequencely, Eq. (4.2) becomes

$$n(\boldsymbol{x},\tau) = \mathcal{N}[\Pi_{ij}(\boldsymbol{x}'_{\rm fl}(\tau'))](\boldsymbol{x},\tau)\,, \tag{4.5}$$

where $\boldsymbol{x}'_{\rm fl}(\tau')$ is the position of the the fluid element at the time $\tau > \tau'$ and at the position $\boldsymbol{x}'$ in the Eulerian coordinate. This still does not describe the fluid in local gravitational terms and includes the non-local scale, which indicates that the position argument in the functional $\mathcal{N}$ is not $\boldsymbol{x}$ but $\boldsymbol{x}'$. The non-local scale is expected to be about the object's size, R_*. In the case of the dark matter halo, the scale of spatial nonlocality corresponds to the Lagrangian radius, which defined as

$$R_*(M) \equiv \left(\frac{3M}{4\pi\bar{\rho}_{\rm m0}}\right)^{1/3} = 1.4h^{-1}[\mathrm{Mpc}]\left(\frac{M}{10^{12}h^{-1}M_\odot}\right)^{1/3}\left(\frac{\Omega_{\rm m0}}{0.31}\right)^{-1/3}\,. \tag{4.6}$$

In fact, when we consider the number deinsity correlation, we use a scale larger than the nonlocal scale. Therefore, spliting the perturbations into long- and short-wavelengths relative to a smoothing scale $\Lambda^{-1} > R_*$, the long-wavelength in the functional $\mathcal{N}$ becomes local in space and we obtain the cource-grained number denity contrast as

$$n_{\rm L}(\boldsymbol{x},\tau) = \mathcal{N}_{\rm L}[\Pi_{{\rm L}\,ij}(\boldsymbol{x}_{\rm fl}(\tau')); P_{\rm m}(\boldsymbol{k}_{\rm S}|\boldsymbol{x}_{\rm fl}(\tau')),\cdots](\boldsymbol{x},\tau)\,, \tag{4.7}$$

where $P_{\rm m}(\boldsymbol{k}_{\rm s}|\boldsymbol{x}_{\rm fl}(\tau'))$ is the local matter power spectrum of the small scale measured at a given point along the fluid trajectory. And we defined the long-mode fluctuation of a certain field X as

$$X_{\rm L}(\boldsymbol{x},\tau) = \int d\boldsymbol{y}\; W_{\rm L}(|\boldsymbol{x}-\boldsymbol{y}|)X(\boldsymbol{y},\tau)\,, \tag{4.8}$$

where $W_{\rm L}(x)$ is the window function which vanishes for $x > \Lambda^{-1}$ and the short-mode fluctuation is given by $X_{\rm S} = X - X_{\rm L}$. Furthermore, from the convolution theorem, the long-mode fluctuation in Fourier space becomes $X_{\rm L}(\boldsymbol{k},\tau) = W_{\rm L}(k)X(\boldsymbol{k},\tau)$.

We have split the perturbations so that the overdensity contrast $n_{\rm L}$ depends on the short-mode perturbation through only on the local statistics since there is no overlap between the long- and short-modes in Fourier space.

For simplicity, let us first consider the case where the initial fluctuations follow the Gaussian distribution. The initial Gaussian fluctuation leads to the long- and short-modes of the gravitational fluctuations do not interact with each other at the initial time and the local statistics of the short-mode depend on long-mode only through the mode-coupling in the gravitational evolution later. Here we consider large scales that the mode coupling due to gravitational evolution does not contribute significantly. In this case, we can expect to expand the functional in Eq. (4.7) with the powers of the long-mode fields and their derivatives, and the bias expansion up to the second order fluctuation can be expressed by

$$\delta_{\mathrm{n,L}}(\boldsymbol{x},\tau) = f_0 + f_{\Pi}^{ij}\Pi_{\mathrm{L}\,ij}(\boldsymbol{x},\tau) + f_{\Pi^2}^{ijkl}\Pi_{\mathrm{L}\,ij}(\boldsymbol{x},\tau)\Pi_{\mathrm{L}\,kl}(\boldsymbol{x},\tau) + \cdots\,, \tag{4.9}$$

where the coefficients f_O depend on the short-mode statistics such as $P_{\mathrm{m}}(\boldsymbol{k}_{\mathrm{S}}|\boldsymbol{x}_{\mathrm{fl}}(\tau'))$. However, as mentioned above, under the assumption that the mode couplings due to gravitational evolution are negligible and the initial fluctuation follows the Gaussian distribution, we stress that there is no position dependence of the local short-mode statistics in the fluid flow and the short-mode statistics do not contribute to the long-mode. Thus, for the Gaussian initial condition, the coefficients f_O are uncorrelated with the long-mode fields and depend on only the cutoff-dependent parameters. By imposing the homogenieity and isotropy, the coefficients f_O can be written as

$$f_0 = c_0 \tag{4.10}$$

$$f_{\Pi}^{ij} = c_\delta \delta^{ij} \tag{4.11}$$

$$f_{\Pi^2}^{ijkl} = c_{\delta^2}\delta^{ij}\delta^{kl} + \frac{1}{2}c_{\Pi^2}(\delta^{ik}\delta^{jl} + \delta^{il}\delta^{jk})\,, \tag{4.12}$$

where the coefficents c_O are the bare bias parameters. As a result, Eq. (4.9) can be rewritten as

$$\delta_{\mathrm{n,L}}(\boldsymbol{x},\tau) = c_0 + c_\delta\delta_{\mathrm{L}}(\boldsymbol{x},\tau) + c_{\delta^2}\delta_{\mathrm{L}}^2(\boldsymbol{x},\tau) + c_{K^2}(K_{\mathrm{L}\,ij}(\boldsymbol{x},\tau))^2 + \cdots\,. \tag{4.13}$$

We transformed several bare bias parameters as $c_{\delta^2} \to c_{\delta^2} + \frac{1}{3}c_{\Pi^2}$ and $c_{K^2} = c_{\Pi^2}$. While the spatial average of the left-hand side of Eq. (4.22) becomes zero by definition, the spatial average of the right-hand side does not. Since the bare bias parameters depend only on the cutoff scale, we regard them as constant. Then, while the coefficient c_0 and the term including the spatial average of the density field become zero, the products of fields evaluated at the same points such as δ_{L}^2 and K_{L}^2 are non-zero and, in particular, their terms diverge when considering the galaxy correlation. This divergence is a non-physical effect and therefore needs to be renormalized (see Sec. 4.2).

Next, we consider the initial non-Gaussian condition case, from Eq. (2.64) in the absence of the anisotropic stress, the short mode initial potential power spectrum at a given position of the long-mode fluctuation is modulated as

$$P_\Psi(\boldsymbol{k}_\mathrm{S}|\boldsymbol{q}) = \left[1 + \int_{\boldsymbol{k}_\mathrm{L}} \sum_{\ell=\mathrm{even}} A_\ell \left(\frac{k_\mathrm{L}}{k_\mathrm{S}}\right)^\Delta \mathcal{P}_\ell(\hat{\boldsymbol{k}}_\mathrm{S} \cdot \hat{\boldsymbol{k}}_\mathrm{L}) \phi(\boldsymbol{k}_\mathrm{L}) e^{i\boldsymbol{k}_\mathrm{L}\cdot\boldsymbol{q}}\right] P_\phi(k_\mathrm{S}) \,, \tag{4.14}$$

where $\boldsymbol{q} \equiv \boldsymbol{x}_\mathrm{fl}(\tau = 0)$. This modulation can be understood as follows. Following Eq. (4.14), we split the initial gravitational potential as

$$\Psi_\mathrm{i}(\boldsymbol{k}) = \Psi_\mathrm{i,L}(\boldsymbol{k}) + \Psi_\mathrm{i,S}(\boldsymbol{k}) \,. \tag{4.15}$$

For the initial non-Gaussian condition, using the separated Gaussian fields $\phi_\mathrm{L/S}$, we can written as

$$\begin{aligned}\Psi_\mathrm{i}(\boldsymbol{k}) \simeq{}& \phi_\mathrm{L}(\boldsymbol{k}) + \int_{\boldsymbol{p}} K_\mathrm{NL}(\boldsymbol{k}-\boldsymbol{p}, \boldsymbol{p}) \phi_\mathrm{S}(\boldsymbol{p}) \phi_\mathrm{S}(\boldsymbol{k}-\boldsymbol{p}) \\ &+ \phi_\mathrm{S}(\boldsymbol{k}) + 2\int_{\boldsymbol{p}} K_\mathrm{NL}(\boldsymbol{k}-\boldsymbol{p}, \boldsymbol{p}) \phi_\mathrm{L}(\boldsymbol{p}) \phi_\mathrm{S}(\boldsymbol{k}-\boldsymbol{p}) \,, \end{aligned} \tag{4.16}$$

where the kernel K_NL is given by the squeezed primordial bispectrum such as Eq. (2.64). We abbreviated the square of the long-mode Gaussian fields since the second-order becomes small enough to consider the perturbation in terms of the long-mode fields. The first line corresponds to the long-mode statistics and the second line corresponds to the short-mode statistics. While the term of ϕ_S^2 becomes the noise terms independent of the long-mode, the term of $\phi_\mathrm{S}\phi_\mathrm{L}$ encodes the dependence of the short-modes on the long-mode fluctuation at intial time. As a result, we find that the short-mode fluctuaion on the real space becomes

$$\Psi_\mathrm{i,S}(\boldsymbol{q}) \simeq \phi_\mathrm{S}(\boldsymbol{q}) + 2\int_{\boldsymbol{k}_\mathrm{L}} \int_{\boldsymbol{k}_\mathrm{S}} K_\mathrm{NL}(\boldsymbol{k}_\mathrm{L}, \boldsymbol{k}_\mathrm{S}) \phi_\mathrm{L}(\boldsymbol{k}_\mathrm{L}) \phi_\mathrm{S}(\boldsymbol{k}_\mathrm{S}) e^{i(\boldsymbol{k}_\mathrm{S}+\boldsymbol{k}_\mathrm{L})\cdot\boldsymbol{q}} \,, \tag{4.17}$$

and the modulated local short-mode power spectrum leads to Eq. (4.14).

For $\ell = 0$ in Eq. (4.14), this leads to the isotropic non-Gaussianity to the squeezed limit and Eq. (4.14) becomes

$$P_\Psi(\boldsymbol{k}_\mathrm{S}|\boldsymbol{q}) = \left[1 + A_0 \left(\frac{k_*}{k_\mathrm{S}}\right)^\Delta \varphi(\boldsymbol{q})\right] P_\phi(k_\mathrm{S}) \,, \tag{4.18}$$

where we defined the additional field as

$$\varphi(\boldsymbol{k}) = \left(\frac{k}{k_*}\right)^\Delta \phi_\mathrm{L}(\boldsymbol{k}) \,. \tag{4.19}$$

The scale k_* is an arbitrary reference scale. This field φ parametrizes the dependence of the initial short-scale statistics on the long-mode field. This means the coefficents in Eq. (4.9) depends on the field φ, and specifically,

$$f_0 = c_0 + c_\varphi \varphi(\boldsymbol{q}) \tag{4.20}$$

$$f_\mathrm{II}^{ij} = [c_\delta + c_{\varphi\delta}\varphi(\boldsymbol{q})]\delta^{ij} \,. \tag{4.21}$$

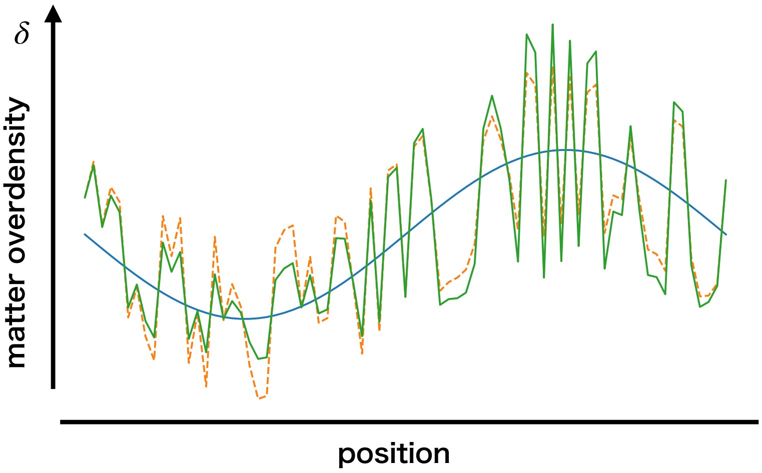

FIGURE 4.2: The schematic picture of the fluctuation with non-gaussianity. Since in the Gaussian initial condition, the fluctuations between the short-mode wavelength and the long-mode wavelength are independent, no difference in amplitude by position occurs (orange dashed-line). Since in the non-Gaussian initial condition, the fluctuation of the short-mode wavelength is modulated due to the mode-coupling, the fluctuation depends on the amplitude of the fluctuation of the long-wavelength mode (green solid-line).

We note that the field φ is evaluated in Lagrangian space. Definiting $\tilde{\varphi}(\boldsymbol{x},\tau) \equiv \varphi(\boldsymbol{q}(\boldsymbol{x},\tau))$ on the Eulerian space, the bias expansion with the isotropic non-gaussianity becomes

$$\delta_{\mathrm{n,L}}(\boldsymbol{x}) = c_0 + c_\varphi \tilde{\varphi}(\boldsymbol{x}) + c_\delta \delta_{\mathrm{L}}(\boldsymbol{x}) + c_{\varphi\delta}\tilde{\varphi}(\boldsymbol{x})\delta_{\mathrm{L}}(\boldsymbol{x}) + c_{\delta^2}\delta_{\mathrm{L}}^2(\boldsymbol{x}) + c_{K^2}(K_{\mathrm{L}\,ij}(\boldsymbol{x}))^2 + \cdots . \tag{4.22}$$

We dropped the time-dependent, but this is evaluated at the same time τ.

Using the Zel'dovich approximation, which provides $\boldsymbol{x}(\boldsymbol{q},\tau) = \boldsymbol{q} - \nabla_{\boldsymbol{q}}\Psi(\boldsymbol{q},\tau)$, the initial non-Gaussian field $\tilde{\varphi}$ can be expanded as

$$\tilde{\varphi}(\boldsymbol{x},\tau) = \varphi(\boldsymbol{x}) + \nabla\varphi(\boldsymbol{x}) \cdot \nabla\Psi(\boldsymbol{x},\tau) + \cdots . \tag{4.23}$$

The second terms in the right hand contains the single derivative of the gravitational potential, which disappear by the equivalent principle. Then, the leading order becomes $\tilde{\varphi}(\boldsymbol{x},\tau) = \varphi(\boldsymbol{x})$.

For $\ell = 2$, we can consider the contribution of the anisotropic non-Gaussianity to the squeezed limit with the same strategy of $\ell = 0$ case. Eq. (4.14) becomes

$$P_\Psi(\boldsymbol{k}_{\mathrm{S}}|\boldsymbol{q}) = \left[1 + A_2\left(\frac{k_*}{k_{\mathrm{S}}}\right)^{\Delta}[\hat{k}_{\mathrm{S},i}\hat{k}_{\mathrm{S},j} - \frac{1}{3}\delta_{ij}]\varphi^{ij}(\boldsymbol{q})\right] P_\phi(k_{\mathrm{S}}) , \tag{4.24}$$

where we defined the additional tensor field as

$$\varphi^{ij}(\boldsymbol{k}) = \frac{3}{2}[\hat{k}^i\hat{k}^j - \frac{1}{3}\delta^{ij}]\left(\frac{k}{k_*}\right)^{\Delta}\phi_{\mathrm{L}}(\boldsymbol{k}) , \tag{4.25}$$

with the relation between the Legendre polynomial and the traceless tensor given by Eq. (D.31). We denoted the unit vector of $\boldsymbol{k}$ as $\hat{\boldsymbol{k}}$.

Since this tensor field does not contribute to the scalar part, the contribution to the bias expansion appears as

$$\delta_{\mathrm{n,L}}(\boldsymbol{x},\tau) \ni \tilde{\varphi}^{ij}(\boldsymbol{x},\tau) K_{\mathrm{L}\,ij}(\boldsymbol{x},\tau)\,, \tag{4.26}$$

where $\tilde{\varphi}^{ij}(\boldsymbol{x},\tau) \equiv \varphi(\boldsymbol{q}(\boldsymbol{x},\tau))$. Since this leads to the effective second order statistics, the contribution to the 2-point statistics on galaxy bias is negligble on the large scale and this contributes significantly to the galaxy bispectrum [68].

In the same way, for $\ell > 2$, the additional tensor field corresponds to ℓ appears. However, since this contribution to the galaxy bias always appears the coupling to the (higher-)derivative terms, the galaxy bias is not significantly affected.

4.2 Renomarization

By definition, the number density contrast is supposed to be zero in the spatial average, and the bias expansion is expected to be zero as well. On the other hand, at a non-linear scale, the bias expansion involves composite operators such as products of fields evaluated at the same point. Since these operators generate a non-physical divergence, it is natural to renormalize the basis for the expansion.

In the simplest case, the expectation value at same point $\langle\delta^2\rangle$ logarithmicly divergences around large-k, since the matter power spectrum is proportional to k^{-3} on the $k > k_{\mathrm{eq}}$. On the other hand, since we separate the fields by cutoff scale, the expectation value of δ^2 becomes σ_Λ^2 with dependent on the cutoff scale Λ. The cutoff scale is determined by hand in the calculation process. On the other hand, since the actual analysis does not depend on such a cutoff scale, it should be expanded on a basis that does not depend on the cutoff. Then, we introduce the bias expansion in terms of the new basis of the renormalized operators.

The expectation value of δ^2 is given by the cutoff scale dependent variance $\langle\delta^2\rangle = \sigma_\Lambda^2$, where is defined

$$\sigma_\Lambda^2 = \int_0^\Lambda \frac{dp}{2\pi^2} p^2 P_{\mathrm{L}}(p)\,. \tag{4.27}$$

Then, we find that the renormalized basis is given by removing this dependence

$$[\delta^2] \equiv \delta^2 - \sigma_\Lambda^2\,, \tag{4.28}$$

where $[\cdots]$ means the renormalized operator. This is the lowest order result. Note that the renormalized operator needs to be considered up to the contributions of the loops when one expands the bias to the higher order. Significantly, the one-loop contribution is sufficient for the galaxy bispectrum. We find that the expectation value of K^2 is straightforwardly given by $2\sigma_\Lambda^2/3$.

Let us consider what happens to the bias parameters. For the simple discussion, we consider the follwoing bias expansion as

$$\delta_{\rm n}(\boldsymbol{k}) = c_\delta \delta(\boldsymbol{k}) + \frac{1}{2}c_{\delta^2}\delta^2(\boldsymbol{k}) + \frac{1}{6}c_{\delta^3}\delta^3(\boldsymbol{k}) + \epsilon(\boldsymbol{k}) + \mathcal{O}(\delta^4)\,, \tag{4.29}$$

where $\epsilon(\boldsymbol{k})$ is the stochastic noise, which does not correlate the density fluctuation, and we ignore the contribution from the tidal fields for simplicity. Moreover, we use the matter density fluctuation up to the 3rd order, following Eq. (3.59). Then, we obtain the galaxy auto-correlation as

$$\langle \delta_{\rm n}(\boldsymbol{k})\delta_{\rm n}(\boldsymbol{k}')\rangle (2\pi)^3\delta_{\rm D}(\boldsymbol{k}+\boldsymbol{k}')P_{\rm g}(k)\,, \tag{4.30}$$

with the galaxy power spectrum $P_{\rm g}(k)$, which is [1]

$$\begin{aligned} P_{\rm g}(k) = N_0 &+ [c_\delta^2 + c_\delta c_{\delta^3}\sigma_\Lambda^2 + \frac{68}{21}c_\delta c_{\delta^2}\sigma_\Lambda^2]P_{\rm L}(k) \\ &+ 2c_\delta c_{\delta^2}\int_{\boldsymbol{p}} F_2(\boldsymbol{p},\boldsymbol{k}-\boldsymbol{p})P_{\rm L}(p)P_{\rm L}(|\boldsymbol{k}-\boldsymbol{p}|) + \frac{1}{2}c_{\delta^2}\int_{\boldsymbol{p}} P_{\rm L}(p)P_{\rm L}(|\boldsymbol{k}-\boldsymbol{p}|)\,, \end{aligned} \tag{4.31}$$

where N_0 is the noise term derived from the auto-correlation of the stochastic term. This expression has the variance depending on the cutoff scale. However, on the large scale, we expect that the linear bias parameter becomes a constant value regardless of the cutoff scale. When we introduce the renormalize operators such as

$$c_\delta\delta \to b_\delta[\delta] \equiv b_\delta\delta\,, \tag{4.32}$$

$$c_{\delta^2}\delta^2 \to b_{\delta^2}[\delta^2] = b_{\delta^2}\left\{\delta^2 - \sigma_\Lambda^2\left(1+\frac{68}{21}\right)\right\}\,, \tag{4.33}$$

$$c_{\delta^3}\delta^3 \to b_{\delta^3}[\delta^3] = b_{\delta^3}(\delta^3 - 3\sigma_\Lambda^2\delta)\,, \tag{4.34}$$

the bias expansion with the renormalized operators does not depend on the arbitrary cutoff scale. Note that the last term in Eq. (4.31) is non-zero at $k \to 0$ and is k-independent on the large scale [97]. This term looks like the shot-noise term.

In the presence of PNGs, we should consider the contribution from $\tilde{\varphi}$. By using Eq. (2.64), this contribution appears through the linear matter bispectrum as

$$\langle [\delta^2](\boldsymbol{k})\delta(\boldsymbol{k}')\rangle = (2\pi)^3\delta_{\rm D}(\boldsymbol{k}+\boldsymbol{k}')\int_{\boldsymbol{p}} B(\boldsymbol{p},\boldsymbol{k}-\boldsymbol{p},\boldsymbol{k}') \tag{4.35}$$

$$\to (2\pi)^3\delta_{\rm D}(\boldsymbol{k}+\boldsymbol{k}')A_0\tilde{\sigma}_\Lambda^2 P_{{\rm m}\tilde{\varphi}}(k)\,, \tag{4.36}$$

where we used $k \ll p$ due to the squeezed bispectrum. Here we defined

$$P_{{\rm m}\tilde{\varphi}}(k) \equiv \left(\frac{k}{k_*}\right)^\Delta \mathcal{M}^{-1}(k)P_{\rm L}(k)\,, \quad \tilde{\sigma}_\Lambda^2 \equiv \int_0^\Lambda \frac{dp}{2\pi^2}p^2\left(\frac{k_*}{p}\right)P_{\rm L}(p)\,. \tag{4.37}$$

---

[1] We use $\langle \delta^2(\boldsymbol{k})\delta(\boldsymbol{k})\rangle = 2\langle(\delta^{(1)}\delta^{(2)})(\boldsymbol{k})\delta^{(1)}(\boldsymbol{k}')\rangle$

Since the renormalized operators $[\delta^2], [K_{ij}^2]$ are modulated by the non-Gaussian contribution up to the leading order,

$$[\delta^2] = \delta^2 - \sigma_\Lambda^2 - A_0 \tilde{\sigma}_\Lambda^2 \tilde{\varphi} \,, \tag{4.38}$$

$$[K_{ij}^2] = K_{ij}^2 - \frac{2}{3}\sigma_\Lambda^2 - \frac{2}{3} A_0 \tilde{\sigma}_\Lambda^2 \tilde{\varphi} \,, \tag{4.39}$$

the bias expansion in terms of the renormalized operators is given by

$$\delta_{\rm n} = b_\delta \delta + b_{\tilde{\varphi}} A_0 \tilde{\varphi} + b_{\delta^2}[\delta^2] + b_{K^2}[K_{ij}^2] + \cdots \,, \tag{4.40}$$

where b_X means the renormalized bias parameter with respect to X. While the bare bias parameters depend on the arbitrary cutoff scale, the renormalized bias parameters have the physical meanings such as $b_\delta = \partial \ln n / \partial \ln \rho$, which means the response of the galaxy density to a change in the matter density, $b_{\tilde{\varphi}} = \partial \ln n / \partial A_0$, which means the response of the galaxy density to a change in the amplitude of the primordial power spectrum [98, 23].

4.3 Galaxy statistics with primordial non-Gaussianity

We examine the galaxy statistics by using the power spectrum, especially focusing on the non-Gaussian contribution. As you can see from the bias expansion, since the one-point correlation, which is the spatial average of the galaxy density, is expected to be zero in leading order, the two-point correlation is the lowest order on the galaxy statistics.

We consider the cross-correlation at the same time between the galaxy density and the matter, which can reveal the bias parameters if we know the matter density fluctuation completely, such as N-body simulation. From Eq. (4.40), we get

$$\begin{aligned} \langle \delta(\boldsymbol{k}) \delta_{\rm n}(\boldsymbol{k}') \rangle &\equiv (2\pi)^3 \delta_{\rm D}(\boldsymbol{k}+\boldsymbol{k}') P_{\rm gm}(k) \\ &= b_\delta \langle \delta(\boldsymbol{k}) \delta(\boldsymbol{k}') \rangle + b_{\tilde{\varphi}} \langle \delta(\boldsymbol{k}) \tilde{\varphi}(\boldsymbol{k}') \rangle \\ &= (2\pi)^3 \delta_{\rm D}(\boldsymbol{k}+\boldsymbol{k}') \left[b_\delta + b_{\tilde{\varphi}} A_0 \left(\frac{k}{k_*} \right)^\Delta \mathcal{M}^{-1}(k) \right] P_{\rm m}(k) \,, \end{aligned} \tag{4.41}$$

where we used the Possion equation $\delta(k,\tau) = \mathcal{M}(k,\tau)\tilde{\varphi}(k)$ of Eq. (3.28). On the large scale limit, while the cross-correlation $P_{\rm gm}$ for the Gaussian initial condition has only the constant bias b_δ, the one for the non-Gaussian initial condition has the scale-dependent contribution, derived from $\mathcal{M}^{-1} \propto k^{-2}$. When $\Delta < 2$[2], this scale-dependency is important for the search of the primordial non-Gaussianities. For

---

[2] When $\Delta = 2$ (e.g., equilateral non-Gaussianity Eq. (2.56)), on the large scale, the bias from the non-Gaussian contribution behaves the same as the linear bias. One might think that the non-Gaussian contribution can be distinguished in principle, since the transfer function changes on smaller scales $k > k_{\rm eq}$, which leads us to $\mathcal{M} \propto$ const. However, on small scales, the linear analysis is not valid, and we should care of the degeneracy of the contribution of higher derivative terms such as $\nabla^2\delta$.

example, for local type non-Gaussianity, which corresponds to $\Delta = 0$, we can prove the behavior of the primordial non-Gaussianity on the large scale where is valid for the linear analysis. This is called the scale-dependent bias and confirmed by using N-body simulation firstly [22]. For actual observation, though the galaxy auto-correlation might be helpful, we must not forget that there is a shot-noise contribution.

Chapter 5

Galaxy Shapes as Cosmological Tracers

As mentioned in Chapter. 4, the distribution of galaxy and galaxy clusters obeys a biased tracer of the matter density distribution. Similar to this, the shape of the virialized galaxy or halo might become a biased tracer of the surrounding tidal fields, and these shapes correlate with the tidal fields, which is known as the intrinsic alignment (see Sec. 5.2 in more detail). All the contributions to the galaxy shapes $\tilde{I}_{i_1\cdots i_n}$ with moment decomposition, which we will describe in next section, can be constructed as

$$\text{Shape observable } \tilde{I}_{i_1\cdots i_n} \begin{cases} \text{(I) Intrinsic shape } \tilde{I}^{\rm int}_{i_1\cdots i_n} \begin{cases} \text{(A) Linear alignment} \\ \text{(B) Non-linear alignment} \\ \text{(C) Noise} \end{cases} \\ \text{(II) Weak lensing shear } \tilde{I}^{\rm WL}_{i_1\cdots i_n} \end{cases} .$$

While the intrinsic shape (I) can be directly measured when the observer is close to the galaxy, the weak lensing distortion (II) contributes the measurement of the distant galaxy as the projection effect since the path of the photon emitted by the galaxy is curved through the foreground inhomogeneous matter distribution. Furthermore, the intrinsic shape is divided into the linear alignment (A), which behaves as a biased tracer of the external tidal field at an individual galaxy, and the non-linear alignment (B), which becomes the higher-order correction to the linear alignment. Since galaxy shapes are non-spherical, even if we do not consider the environmental effects such as the intrinsic alignments, the statistical shape of the galaxy has the noise contribution.

First, we define the shape of the galaxy and observables. Next, we discuss these contributions, which appear regardless of the primordial non-Gaussianities. Finally, we estimate the contribution of the primordial non-Gaussianities, including the forecast for the future imaging survey. In this chapter, we mainly discuss the response of galaxy to the angular-dependent primordial non-Gaussianities with global isotropy given by Eq. (2.64) [41, 43, 44]. In other cases where angular-dependent primordial non-Gaussianity appears, if the vector field sources the primordial curvature perturbation, the primordial bispectrum depends on the direction of the vector field, which breaks the global isotropy (e.g., Ref. [99].) In this case, we investigated how the difference between the global symmetry case and the global symmetry case affects the galaxy shape [43]. This is summarized in App. B.

Unless otherwise noted, we use the FLRW metric and choose the conformal Newtonian Gauge to the perturbed FLRW metric, which is expressed as

$$ds^2 = a^2(\tau)\left[-(1+2\Psi)d\tau^2 + (1+2\Phi)\delta_{ij}dx^i dx^j\right] , \tag{5.1}$$

where Φ, Ψ correspond to the curvature perturbation and the gravitational potential, respectively. In addition, we assume the absence of the anisotropic stress tensor, which leads to $\Psi = -\Phi$. Since we set the background spatial curvature to flat, the raising and lowering of the indices are performed with a Kronecker delta.

5.1 Definition of galaxy shapes

In order to discuss the relation between the shape observables and the theoritical physics later, first, we define the 3D shape function for a galaxy which is located at $(\tau, \boldsymbol{x})$ and has the size of the radius R_* as

$$g_{i_1 i_2 \cdots i_n}(\boldsymbol{x}, \tau) \equiv \frac{1}{\bar{B}(\boldsymbol{x}, \tau) R_*^n} \int_{y \le R_*} d^3\boldsymbol{y}\, y_{i_1} y_{i_2} \cdots y_{i_n} B(\boldsymbol{x} + \boldsymbol{y}, \tau) , \tag{5.2}$$

where $\boldsymbol{x}$ and $\boldsymbol{y}$ denote the 3D spatial coordinates for the centroid of the galaxy and those measured from the 3D centroid of light emission from the galaxy, respectively. The indices i_n run from 1 to 3. We have introduced the weight by using the brightness of the emission, $B(\boldsymbol{x}, \tau)$. As is clear from the definition, $g_{i_1 i_2 \cdots i_n}$ is the rank-n symmetric tensor in 3D. $\bar{B}(\boldsymbol{x}, \tau)$ is the total brightness of the galaxy, defined as $\bar{B}(\boldsymbol{x}, \tau) = \int d^3\boldsymbol{y} B(\boldsymbol{x} + \boldsymbol{y}, \tau)$. The centroid is defined so that $g_i(\boldsymbol{x}, \tau)$ vanishes. As is obvious from Eq. (5.2), when one sets no indices, i.e., $n = 0$, it means the number count of galaxy, i.e., one object. Therefore, we turn out that this definition is generalized.

As mentioned above, the deformation of galaxy shape is construced by the two different origins such as

$$g_{i_1 i_2 \cdots i_n}(\boldsymbol{x}, \tau) = g^{\rm int}_{i_1 i_2 \cdots i_n}(\boldsymbol{x}, \tau) + g^{\rm WL}_{i_1 i_2 \cdots i_n}(\boldsymbol{x}, \tau) . \tag{5.3}$$

The first term is the intrinsic galaxy shape deformation (I) and the second term is the deformation due to the weak lensing (II).[1] On the large scale, the intrinsic shape deformation may respond to the large-scale tidal field.

In galaxy imaging surveys, we can only observe the galaxy shapes projected onto the 2D sky which is orthogonal to the line of sight $\hat{\boldsymbol{n}}$. This is why we need to convert the 3D shape observable to the 2D one on the sky. Operating with the projection

---

[1] Since the latter is the effect on appearance due to the gravitational field between galaxies and us, there are always only the components orthogonal to the line of sight.

tensor, defined as

$$\mathcal{P}_{ij} \equiv \delta_{ij} - \hat{n}_i \hat{n}_j \,, \tag{5.4}$$

with $\hat{n}_i$ being the unit vector along the line of sight, we obtain the galaxy shape on the projected plane as

$$I_{i_1 i_2 \cdots i_n}(\boldsymbol{x}, \tau) = \mathcal{P}_{i_1}{}^{j_1} \mathcal{P}_{i_2}{}^{j_2} \cdots \mathcal{P}_{i_n}{}^{j_n} g_{j_1 j_2 \cdots j_n}(\boldsymbol{x}, \tau) \,. \tag{5.5}$$

Over the area of an individual galaxy, which subtends a very small angle on the sky, we can approximate the line of sight $\hat{\boldsymbol{n}}$ as constant so that the sky can be approximated as a 2D plane with coordinates $\boldsymbol{\theta}$, where we choose the origin to correspond to the centroid of the galaxy image.

The surface brightness can be obtained by integrating the emission along the line of sight,

$$I(\bar{\boldsymbol{\theta}} + \boldsymbol{\theta}, \tau) = \int dy_{\parallel} B(\boldsymbol{x} + \boldsymbol{y}, \tau) \,, \tag{5.6}$$

with $y_{\parallel} \equiv \boldsymbol{y} \cdot \hat{\boldsymbol{n}}$ and $\bar{\theta}_i, \theta_i$ are defined as

$$\bar{\theta}_i \equiv \frac{1}{\chi} \mathcal{P}_i{}^j x_j \qquad \theta_i \equiv \frac{1}{\chi} \mathcal{P}_i{}^j y_j \,, \tag{5.7}$$

which we used the comoving distance to the source χ. We ignore any absorption or other radiative transfer effects. However, our results below are based solely on symmetry considerations, so they continue to hold even in the presence of a more complicated local mapping from emissivity to surface brightness. Here, the dependence on $\boldsymbol{x} \cdot \hat{\boldsymbol{n}}$ was identified with τ dependence. We then obtain the projected galaxy moment as

$$I_{i_1 i_2 \cdots i_n}(\bar{\boldsymbol{\theta}}, \tau) = \frac{1}{\bar{I}(\bar{\boldsymbol{\theta}}, \tau)} \left(\frac{\chi}{R_*} \right)^n \int d^2\boldsymbol{\theta}\, \theta_{i_1} \cdots \theta_{i_n} I(\bar{\boldsymbol{\theta}} + \boldsymbol{\theta}, \tau) \,, \tag{5.8}$$

which is normalized by the total intensity $\bar{I}$,

$$\bar{I}(\bar{\boldsymbol{\theta}}, \tau) \equiv \int d^2\boldsymbol{\theta}\, I(\bar{\boldsymbol{\theta}} + \boldsymbol{\theta}, \tau) = \frac{1}{\chi^2} \int d^3\boldsymbol{y} B(\boldsymbol{x} + \boldsymbol{y}, \tau) \,. \tag{5.9}$$

Since g_i vanishes, so do I_i, satisfying $I_i(\bar{\boldsymbol{\theta}}, \tau) = 0$.

Next, we decompose $I_{i_1 \cdots i_n}$ into the spin$\pm n$ components in order to clarify the relation among physical quantities. Here, we generalize the approach of [100]. Related to our formalism, the approach to higher-order moments for gravitational lensing has been presented in Refs. [101, 102]. To clarify the below discussions, we explicitly set the coordinate of the line of sight as

$$\hat{\boldsymbol{n}} = \begin{pmatrix} \sin\iota\cos\psi \\ \sin\iota\sin\psi \\ \cos\iota \end{pmatrix}, \tag{5.10}$$

and the coordinates perpendicular to the line of sight in the right-hand system are given by

$$\boldsymbol{e}_\iota = \frac{\partial\hat{\boldsymbol{n}}}{\partial\iota} = \begin{pmatrix} \cos\iota\cos\psi \\ \cos\iota\sin\psi \\ -\sin\iota \end{pmatrix}, \qquad \boldsymbol{e}_\psi = \frac{1}{\sin\iota}\frac{\partial\hat{\boldsymbol{n}}}{\partial\psi} = \begin{pmatrix} -\sin\psi \\ \cos\psi \\ 0 \end{pmatrix}. \tag{5.11}$$

Using these orthonormal basis, $(\hat{\boldsymbol{n}},\, \boldsymbol{e}_\iota,\, \boldsymbol{e}_\psi)$, we introduce the spin±1 unit basis vectors as

$$\boldsymbol{m}_\pm \equiv \frac{1}{\sqrt{2}}\left(\boldsymbol{e}_\iota \mp i\boldsymbol{e}_\psi\right) = \frac{1}{\sqrt{2}}\begin{pmatrix} \cos\iota\cos\psi \pm i\sin\psi \\ \cos\iota\sin\psi \mp i\cos\psi \\ -\sin\iota \end{pmatrix}, \tag{5.12}$$

which satisfy

$$m^i_\pm m_{\pm\, i} = 0\,, \quad m^i_\pm m_{\mp\, i} = 1\,, \quad m^i_\pm \hat{n}_i = 0. \tag{5.13}$$

The projected nth moment tensor $I_{i_1 i_2\cdots i_n}$ can be expanded by a product of $m_{\pm i}$ as

$$m_{\pm i_1} m_{\pm i_2}\cdots m_{\pm i_n}, \quad (m_{\pm i_1} m_{\mp i_2}\cdots m_{\mp i_n} + (\text{perms})), \quad \cdots. \tag{5.14}$$

Apart from the first terms, $m_{\pm i_1} m_{\pm i_2}\cdots m_{\pm i_n}$, all other terms, which contain both $\boldsymbol{m}_+$ and $\boldsymbol{m}_-$, have trace part contributions, as one can confirm by using Eq. (5.13). Therefore, the traceless components of $I_{i_1 i_2\cdots i_n}$, $\tilde{I}_{i_1 i_2\cdots i_n}$, which satisfy, for any $p, q \in [1, n]$,

$$\tilde{I}_{i_1\cdots i_p\cdots i_q\cdots i_n} = \tilde{I}_{i_1\cdots i_q\cdots i_p\cdots i_n} \qquad \text{(symmetric condition by definition)}, \tag{5.15}$$

$$\mathcal{P}^{i_p i_q}\tilde{I}_{i_1\cdots i_p\cdots i_q\cdots i_n} = \delta^{i_p i_q}\tilde{I}_{i_1\cdots i_p\cdots i_q\cdots i_n} = 0 \qquad \text{(traceless condition)}, \tag{5.16}$$

can be expanded by the first terms of Eq. (5.14) as

$$\tilde{I}_{i_1 i_2\cdots i_n} = {}_n\gamma\, m_{+i_1} m_{+i_2}\cdots m_{+i_n} + {}_{-n}\gamma\, m_{-i_1} m_{-i_2}\cdots m_{-i_n}\,, \tag{5.17}$$

where the coefficients ${}_{\pm n}\gamma$ are given by

$${}_{\pm n}\gamma \equiv m^{i_1}_\mp m^{i_2}_\mp \cdots m^{i_n}_\mp \tilde{I}_{i_1 i_2\cdots i_n} = m^{i_1}_\mp m^{i_2}_\mp \cdots m^{i_n}_\mp I_{i_1 i_2\cdots i_n}\,. \tag{5.18}$$

In the second equality, we inserted the trace part of $I_{i_1 i_2 \cdots i_n}$, which does not contribute to ${}_{\pm n}\gamma$, satisfying $m^i_\pm m^j_\pm \delta_{ij} = m^i_\pm m^j_\pm \mathcal{P}_{ij} = 0$. Namely, even if we make $\tilde{I}_{i_1 i_2 \cdots\cdots i_n}$ operated by the *traceless* projection tensor in Eq. (5.5), instead of the projection tensor, the spin decomposition yields the same coefficients ${}_{\pm n}\gamma$. Since $\boldsymbol{m}_\pm$ transform as spin±1 vectors under a rotation by an angle β, i.e. $\boldsymbol{m}_\pm \to e^{\pm i\beta}\boldsymbol{m}_\pm$, the n products of $\boldsymbol{m}_\pm$ transform as spin$\pm n$ basis tensors, $\boldsymbol{m}_\pm \cdots \boldsymbol{m}_\pm \to e^{\pm in\beta}\boldsymbol{m}_\pm \cdots \boldsymbol{m}_\pm$, being invariant under the rotation by an angle $\beta = 2\pi N/n$ where N is an integer.

Expanding Eq. (5.18) with $I_{i_1 \cdots i_n}$, we can express the coefficents ${}_{\pm n}\gamma$ as

$$
{}_{\pm n}\gamma = \frac{1}{2^{\frac{n}{2}}} \left[\sum_{l=0}^{[\frac{n}{2}]} (-1)^l \binom{n}{2l} \underbrace{I_{\iota\iota\cdots\psi\psi\psi\psi}}_{(n-2l,2l)} \pm i \sum_{l=0}^{[\frac{n-1}{2}]} (-1)^l \binom{n}{2l+1} \underbrace{I_{\iota\iota\iota\cdots\psi\psi\psi}}_{(n-2l-1,2l+1)} \right] , \tag{5.19}
$$

where $[\cdot]$ denotes the floor function and (m, n) means the numbers of the indices ι and ψ, respectively. And we introduced

$$
I_{a_1 \cdots a_n}(\boldsymbol{x}, \tau) = e^{i_1}_{a_1} \cdots e^{i_n}_{a_n} I_{i_1 \cdots i_n}(\boldsymbol{x}, \tau) \,, \tag{5.20}
$$

where the indices a_n are the 2D coordinates on the projected plane and the indices i_n are the 3D spatial coordinates. The binomial factors are given by

$$
\binom{n}{k} \equiv \frac{n!}{k!(n-k)!} \,. \tag{5.21}
$$

Furthermore, as the same of the 3D coordinates case, using the traceless components of $I_{a_1 \cdots a_n}$, $\tilde{I}_{a_1 \cdots a_n}$, which satisfy for the any $p, q \in [1, n]$,

$$
\tilde{I}_{a_1 \cdots a_p \cdots a_q \cdots a_n} = \tilde{I}_{a_1 \cdots a_q \cdots a_p \cdots a_n} \qquad \text{(symmetric condition by definition)} \,, \tag{5.22}
$$

$$
\delta^{a_p a_q} \tilde{I}_{a_1 \cdots a_p \cdots a_q \cdots a_n} = 0 \qquad \text{(traceless condition)} \,, \tag{5.23}
$$

the coefficents ${}_{\pm n}\gamma$ can be given by a more compact expression as

$$
{}_{\pm n}\gamma = 2^{\frac{n}{2}-1} \left(\underbrace{\tilde{I}_{\iota\iota\cdots\iota\iota}}_{(n,0)} \pm i \underbrace{\tilde{I}_{\iota\iota\cdots\iota\psi}}_{(n-1,1)} \right) . \tag{5.24}
$$

We explain the derivation of Eq. (5.24) in Appendix. D.3. This resulting expression indicates that the coefficients ${}_{\pm n}\gamma$ are characterized in terms of the only two independent components of $\tilde{I}_{a_1 \cdots a_n}$. The thing that $\tilde{I}_{a_1 \cdots a_n}$ has the only two independent components can be easily checked by using the symmetric and traceless conditions and the relations among each component are given by

$$\tilde{I}_{\underbrace{\iota\iota\cdots\iota\psi\psi\cdots\psi}_{(n-2k,2k)}} = (-1)^k \tilde{I}_{\underbrace{\iota\iota\cdots\iota\iota}_{(n,0)}} \qquad (k=0,\,1,\,\cdots,[\frac{n}{2}])\,, \tag{5.25}$$

$$\tilde{I}_{\underbrace{\iota\iota\cdots\iota\psi\psi\cdots\psi}_{(n-(2k+1),2k+1)}} = (-1)^k \tilde{I}_{\underbrace{\iota\iota\cdots\iota\psi}_{(n-1,1)}} \qquad (k=0,\,1,\,\cdots,[\frac{n-1}{2}])\,. \tag{5.26}$$

Next, let us visualize the spin decomposition in order to get the picture intuitively. For this purpose, using the 2D polar coordinates $(r,\,\phi)$ with which $\theta_\iota \equiv {e_\iota}^i\theta_i$ and $\theta_\psi \equiv {e_\psi}^i\theta_i$ are given by

$$\theta_\iota = r\cos\phi\,, \qquad \theta_\psi = r\sin\phi\,, \tag{5.27}$$

we express the surface brightness $I(\theta_a)$ in the Fourier series expansion as

$$I(\theta_a) = \frac{c_0(r)}{2} + \sum_{n=1}^{\infty}\left[c_n(r)\cos(n\phi) + s_n(r)\sin(n\phi)\right]\,, \tag{5.28}$$

with

$$c_n(r) \equiv \frac{1}{\pi}\int_{-\pi}^{\pi} d\phi I(\theta_a)\cos(n\phi)\,, \qquad s_n(r) \equiv \frac{1}{\pi}\int_{-\pi}^{\pi} d\phi I(\theta_a)\sin(n\phi)\,. \tag{5.29}$$

In practice, though the surface brightness $I(\theta_a)$ depends on the conformal time τ, we abbreviate it here as it is irrelevant to this discussion. The coefficient c_0 means the amplitude of the circular distribution in the surface brightness and the coefficients satisfying for $n \geq 1$ correspond to the deviations from the circular shape. However, the coefficients c_1, s_1 ensure zero since we set the centroid as the center of coordinates, satisfying $I_a(\bar{\boldsymbol{\theta}}) = 0$.

Finally, examining the relation between the coefficients c_n, s_n in the Fourier space and $\tilde{I}_{a_1\cdots a_n}$, we can get the intuitive picture of the spin decompositions. As a simple case, we consider the $n = 2$ case, which corresponds to the usual cosmic shear. Inserting Eq. (5.28) into $\tilde{I}_{a_1a_2} = I_{a_1a_2} - \delta_{a_1a_2}I_{bb}/2$, we obtain

$$\tilde{I}_{a_1a_2} = \frac{1}{2\mathcal{C}_0}\begin{pmatrix}\mathcal{C}_2 & \mathcal{S}_2 \\ \mathcal{S}_2 & -\mathcal{C}_2\end{pmatrix}\,, \tag{5.30}$$

where we have introduced

$$\mathcal{C}_n \equiv \pi\int drr^{n+1}c_n(r)\,, \qquad \mathcal{S}_n \equiv \pi\int drr^{n+1}s_n(r)\,. \tag{5.31}$$

If we set $\gamma_+ = \mathcal{C}_2/2\mathcal{C}_0$ and $\gamma_\times = \mathcal{S}_2/2\mathcal{C}_0$, we find to reproduce the shear field, e.g., in Ref. [103].

Extending this discussion to $n \geq 3$, we obtain

$$\tilde{I}_{\iota\iota\cdots\iota\iota} = \frac{\mathcal{C}_n}{2^{n-1}\mathcal{C}_0}, \qquad \tilde{I}_{\iota\iota\cdots\iota\psi} = \frac{\mathcal{S}_n}{2^{n-1}\mathcal{C}_0}, \tag{5.32}$$

where we can avoid a messy computation by virtue of the formulae (the derivation can be found in App. D.1.1)

$$r^n \cos(n\phi) = 2^{n-1} \left[\theta_{a_1}\theta_{a_2}\cdots\theta_{a_n}\right]^{\mathrm{TL}_2} |_{a_1=\cdots=a_n=\iota}, \tag{5.33}$$

$$r^n \sin(n\phi) = 2^{n-1} \left[\theta_{a_1}\theta_{a_2}\cdots\theta_{a_n}\right]^{\mathrm{TL}_2} |_{a_1=\cdots=a_{n-1}=\iota, a_n=\psi}, \tag{5.34}$$

where TL_d denotes the d-dimentional traceless (see App. D.1.2 for the explicit expression). Thus, we find that the spin-n components of the galaxy shape function are directly related to a deviation from the circular symmetric distribution which is proportional to $\cos(n\phi)$ or $\sin(n\phi)$. As it should be, these terms remain invariant under the rotation by an angle $\Delta\phi = 2\pi N/n$ where N is an integer. Figure. 5.1 shows the deviation of $I(\boldsymbol{\theta})$ from the circular symmetric distribution, described by $c_n(r)$ and $s_n(r)$ for $n \geq 2$.

By analogy with the eliptical shape ($n = 2$) from Figure. 5.1 (see also Ref. [104] for the CMB polarization), in order to clarify the meaning about the coefficents $\tilde{I}_{\iota\iota\cdots\iota\iota}$ and $\tilde{I}_{\iota\iota\cdots\iota\psi}$, we can express $\gamma_+^{(n)}, \gamma_\times^{(n)}$ correponding to the distorted strength of the n-th moment of the galaxy shape, respectively. Thus, Eq. (5.24) can also be written as

$${}_{\pm n}\gamma = 2^{\frac{n}{2}-1}\left(\gamma_+^{(n)} \pm i\gamma_\times^{(n)}\right). \tag{5.35}$$

Under the rotation of coordianate axis by α, this is transformed as ${}_{\pm n}\gamma \to {}_{\pm n}\gamma e^{\pm in\alpha}$.

5.1.1 Angular power spectrum

In the case of CMB, the distance from the observer is not so necessary because the time of emission is roughly fixed ($z \simeq 1100$). However, in the LSS, since galaxies and clusters of galaxies exist in every redshift, the distance from the observer is an important issue in their statistical analysis.

Of course, we can extract the distance information (or spec-z) from a sample of galaxies by using spectroscopic surveys. However, this needs to be done in each galaxy, which is quite costly and time-consuming. There is a method to obtain the redshift distribution of large samples by examining the relationship between some spectroscopic samples and the brightnesses of colors of each source and examining the approximate distribution (or photo-z). It becomes equivalent to the galaxies' distribution on the sky weighted by the distribution along line-of-sight.

Here, assuming photo-z imaging surveys and that the shape fields can be written as the linear order of the matter density field $\delta(\boldsymbol{k}, \tau)$, we will provide a general expression for the shape moment of galaxy shape. On these assumption, we can write

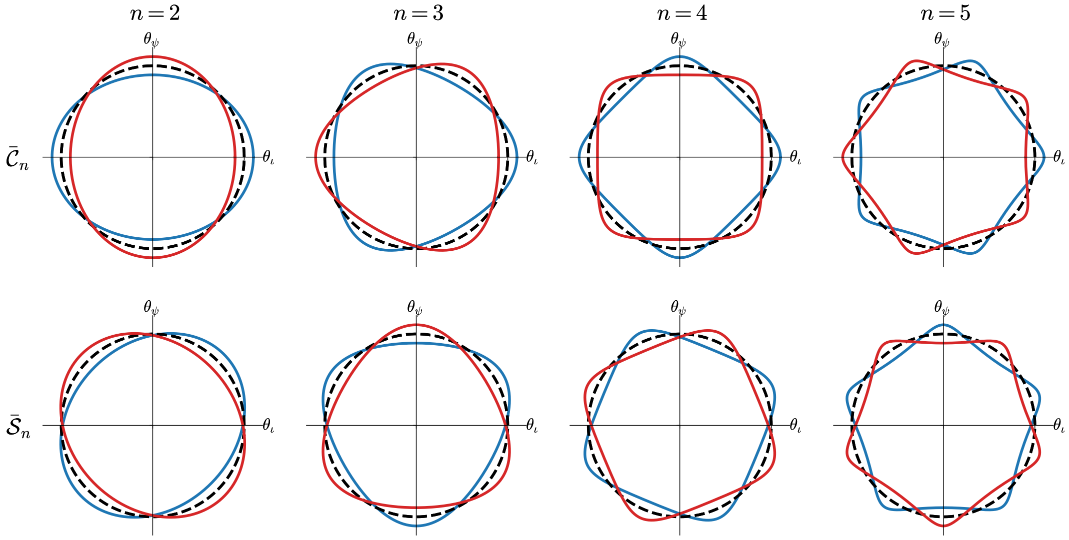

Figure 5.1: Contours of constant intensity $I(\boldsymbol{\theta})$, illustrating the distortions of galaxy images from a circularly symmetric distribution $I(\boldsymbol{\theta}) = I(|\boldsymbol{\theta}|)$ corresponding to the different moments; specifically, we show nonzero $\bar{\mathcal{C}}_n \equiv \mathcal{C}_n/(2^{n-1}\mathcal{C}_0)$ (the upper row) and $\bar{\mathcal{S}}_n \equiv \mathcal{S}_n/(2^{n-1}\mathcal{C}_0)$ (the lower row) with $n = 2, 3, 4, 5$, related to the moments via Eq. (5.32). The blue lines correspond to positive values and the red lines correspond to negative values. The dotted lines denote the unit circle. In Refs. [105, 106], the $n = 3$ component generated by the weak lensing is called "flexion." Ref. [101] refers to a very similar decomposition as "Fourier decomposition" of the image.

down to the relation between $\tilde{I}_{i_1\cdots i_n}$ and the matter density field via

$$\tilde{I}_{i_1\cdots i_n}(\hat{\boldsymbol{n}}) = \left[\mathcal{P}_{i_1}{}^{j_1}\cdots\mathcal{P}_{i_n}{}^{j_n}\right]^{\mathrm{TL}_3} i^n \int_{\boldsymbol{k}}\int dz\frac{dN}{dz}\frac{D(z)}{D(0)}\mathcal{F}^{(n)}(k,\mu,z)\hat{k}_{j_1}\cdots\hat{k}_{j_n}\delta_{\mathrm{m}0}(\boldsymbol{k})e^{ix\mu}\,, \tag{5.36}$$

where z is the redshift, dN/dz is the redshift distribution function of sources, $D(z)$ is the growth factor defined at Eq. (3.56), $\delta_{\mathrm{m}0}(\boldsymbol{k})$ is the matter density fluctuation at present, which related to be $\delta(\boldsymbol{k},z) = [D(z)/D(0)]\delta_{\mathrm{m}0}(\boldsymbol{k})$, and $\mu = \hat{\boldsymbol{k}}\cdot\hat{\boldsymbol{n}}$, $x = k\chi(z)$. The physical effects to the matter density fields are encoded in the kernel $\mathcal{F}^{(n)}(k,\mu,z)$.

Inserting Eq. (5.36) into Eq. (5.18) and acting the spin-lowering operator $\bar{\eth}$, defined as [100, 107]

$$\bar{\eth}\,{}_{+n}f(\hat{\boldsymbol{n}}) \equiv (1-\mu^2)^{\frac{1-n}{2}}\left[\partial_\mu + \frac{i}{1-\mu^2}\partial_\psi\right]\left[(1-\mu^2)^{\frac{n}{2}}{}_{+n}f(\hat{\boldsymbol{n}})\right]\,, \tag{5.37}$$

on ${}_{+n}\gamma$, we obtain a scalar quantities $\gamma^{(n)}$ as

$$\gamma^{(n)}(\hat{\boldsymbol{n}}) = \bar{\eth}^n{}_{+n}\gamma(\hat{\boldsymbol{n}}) = \int_{\boldsymbol{k}}\int dz\frac{dN}{dz}\frac{D(z)}{D(0)}\delta_{\mathrm{m}0}(\boldsymbol{k})i^n\,\bar{\eth}^n\left[\mathcal{F}^{(n)}(k,\mu,z)\left(\hat{k}_+\right)^n e^{ix\mu}\right]\,, \tag{5.38}$$

with $\hat{k}_\pm \equiv m^i_\mp \hat{k}_i$[2].

In the 3-dimensional space, the power spectrum is obtained as the correlation corresponding to the wavelength of the fluctuation by using the Fourier transform. However, since we consider the correlation on the sky, it is convenient to have the similar quantity as the wavelength of the fluctuation in the 3-dimentional space. Thus, we often use the *angular power spectrum* based on (spin-n weighted) spherical harmonics functions, defined as

$$ {}_nY_{lm}(\hat{\boldsymbol{n}}) = \sqrt{\frac{(l-|n|)!}{(l+|n|)!}} \begin{cases} \eth^n Y_{lm}(\hat{\boldsymbol{n}}) & (n \geq 0) \\ (-1)^n \bar{\eth}^{|n|} Y_{lm}(\hat{\boldsymbol{n}}) & (n < 0) \end{cases} , \tag{5.39} $$

where $Y_{lm}(\hat{\boldsymbol{n}})$ is the spherical harmonics function and the conjucate of ${}_nY_{lm}(\hat{\boldsymbol{n}})$ yields ${}_nY^*_{lm} = (-1)^{n+m}{}_{-n}Y_{l\,-m}$.

Let us expand $\gamma^{(n)}$ with the spin-n weighted sperical harmonics function as

$$ {}_{\pm n}\gamma(\hat{\boldsymbol{n}}) = \sum_{l=0}^{\infty} \sum_{m=-l}^{l} a^{(n)}_{lm}\,{}_{\pm n}Y_{lm}(\hat{\boldsymbol{n}}) , \tag{5.40} $$

and the scalar quantity $\gamma^{(n)}$ from Eq. (5.18) is given by

$$ \gamma^{(n)}(\hat{\boldsymbol{n}}) = \sum_{l=0}^{\infty} \sum_{m=-l}^{l} a^{(n)}_{lm} \bar{\eth}^n\,{}_{+n}Y_{lm}(\hat{\boldsymbol{n}}) = \sum_{l=n}^{\infty} \sum_{m=-l}^{l} a^{(n)}_{lm} \sqrt{\frac{(l+n)!}{(l-n)!}} (-1)^n Y_{lm}(\hat{\boldsymbol{n}}) , \tag{5.41} $$

and we used the following relation

$$ \eth^n \bar{\eth}^n Y_{lm} = \bar{\eth}^n \eth^n Y_{lm} = (-1)^n \frac{(l+n)!}{(l-n)!} Y_{lm} . \tag{5.42} $$

Using the orthogonality of spherical harmonic functions, we obtain the relation between the coefficients and Eq. (5.18) as

$$ a^{(n)}_{lm} = \sqrt{\frac{(l-|n|)!}{(l+|n|)!}} (-i)^n \int_{\boldsymbol{k}} \int dz \frac{dN}{dz} \frac{D(z)}{D(0)} \delta_{\mathrm{m}0}(\boldsymbol{k}) \int d\Omega_{\hat{\boldsymbol{n}}} Y^*_{lm}(\hat{\boldsymbol{n}})\, \bar{\eth}^n \left[F^{(n)}(k,\mu,z) \left(\hat{k}_+\right)^n e^{ix\mu} \right] , \tag{5.43} $$

where $d\Omega_{\hat{\boldsymbol{n}}}$ denotes solid angle element.

We define the correlation of the coefficients Eq. (5.43) as

$$ \langle a^{(n)}_{lm} a^{*(n')}_{l'm'} \rangle \equiv C^{(n,n')}_l \delta_{ll'} \delta_{mm'} , \tag{5.44} $$

where $C^{(n,n')}_l$ is the angular power spectrum between spin-n and n' quantities. Here since we used that the matter density fluctuation followed the global rotation symmetry and isotropy such as Eq. (3.31), the off-diagonal correlations disappeared.

---

[2] Applying the spin-raising operator $\eth^n$ to ${}_{-n}\gamma$, we can obtain the same quantity $\gamma^{(n)}$.

Following Refs. [108, 109, 100], we can define the E-/B- mode of the spin-n components as

$$a_{lm}^{E(n)} \equiv \frac{a_{lm}^{(n)} + a_{l\,-m}^{*(n)}(-1)^m}{2}\,, \qquad a_{lm}^{B(n)} \equiv \frac{a_{lm}^{(n)} - a_{l\,-m}^{*(n)}(-1)^m}{2i}\,. \tag{5.45}$$

The E-/B-mode distortions transform under the parity transformation ($\hat{\boldsymbol{n}} \to -\hat{\boldsymbol{n}}$) as

$$a_{lm}^{E(n)} \to (-1)^l a_{l\,m}^{E(n)}\,, \qquad a_{lm}^{B(n)} \to -(-1)^l a_{l\,m}^{B(n)}\,. \tag{5.46}$$

The auto-correlation $\langle a_{lm}^X a_{l'm'}^{*X}\rangle$ with $X = (E, B)$ transforms as parity-even for $l+l' = 2N$ and parity-odd for $l + l' = 2N + 1$, where N is an integer. Meanwhile, the cross-correlation $\langle a_{lm}^E a_{l'm'}^{*B}\rangle$ transforms as parity-even for $l+l' = 2N+1$ and parity-odd for $l + l' = 2N$.

Since we do not use $a_{lm}^{(n)}$ alone, but consider correlations such as Eq. (5.44), we finally use the matter density field $\delta_{\rm m}$ as the global rotational symmetric matter power spectrum $P_{\rm m}(k)$. This means that the contribution from each $\boldsymbol{k}$ to $a_{lm}^{(n)}$ does not depend on the angular direction of $\boldsymbol{k}$. Thus, we can compute the angular integral in $a_{lm}^{(n)}$, choosing $\boldsymbol{k} = (0, 0, k)$ as

$$\begin{aligned}\int d\Omega_{\hat{\boldsymbol{n}}} Y_{lm}^*(\hat{\boldsymbol{n}})\, \bar{\eth}^n \left[\left(\hat{k}_+\right)^n \mathcal{F}^{(n)}(k,\mu,z)e^{ix\mu}\right] \\ = \int d\Omega_{\hat{\boldsymbol{n}}} Y_{lm}^*(\hat{\boldsymbol{n}}) \frac{\partial^n}{\partial\mu^n}\left[\left(\frac{1-\mu^2}{\sqrt{2}}\right)^n \mathcal{F}^{(n)}(k,\mu,z)e^{ix\mu}\right]\,.\end{aligned} \tag{5.47}$$

Here we used that a spin-n function ${}_{+n}f$ with $n > 0$ which only depends on the polar angle μ satisfies (see. App. C.2)

$$\bar{\eth}^s {}_s f = \frac{\partial^s}{\partial\mu^s}\left[(1-\mu^2)^{s/2} {}_s f\right]\,. \tag{5.48}$$

Furthermore, we can rewrite the angular integral as follows:

$$\begin{aligned}\frac{\partial^n}{\partial\mu^n}[(1-\mu^2)^n \mathcal{F}^{(n)}(k,\mu,z)e^{ix\mu}] &= \frac{\partial^n}{\partial\mu^n}[(1+\partial_x^2)^n \mathcal{F}^{(n)}(k,-i\partial_x,z)e^{ix\mu}] \\ &= i^n (1+\partial_x^2)^n \mathcal{F}^{(n)}(k,-i\partial_x,z)[x^n e^{ix\mu}]\,,\end{aligned} \tag{5.49}$$

Here we replaced the argument μ in the kernel $\mathcal{F}^{(n)}$ with $-i\partial_x$, which means the derivative operators on all x-dependent terms. If there is no dependency of pole μ (or $-i\partial_x$) in the kernel $\mathcal{F}^{(n)}$, by using the partial wave expantion, which is given by

$$e^{ix\mu} = 4\pi \sum_{l=0}^{\infty} \sum_{m=-l}^{l} i^l j_l(x) Y_{lm}(\hat{\boldsymbol{n}}) Y_{lm}^*(\hat{\boldsymbol{k}})\,, \tag{5.50}$$

and the following relation

$$(1+\partial_x^2)^s[x^s j_l(x)] = \frac{(l+s)!}{(l-s)!}\frac{j_l(x)}{x^s} \quad (s \geq 0\,, s \in \mathbb{Z}), \tag{5.51}$$

whose derivation is summarized in App. D.2, Eq. (5.49) becomes simpler formula as

$$a_{lm}^{(n)} \sim \sqrt{\frac{2}{\pi}}\sqrt{\frac{(l+|n|)!}{(l-|n|)!}}\int dk k^2 \int dz \frac{dN}{dz}\frac{D(z)}{D(0)}\delta_{\mathrm{m}0}(\boldsymbol{k})\mathcal{F}^{(n)}(k,z)\frac{j_l(x)}{x^s}\,, \tag{5.52}$$

where we use $\sim$ instead of the equality because we have already used the global rotation symmetry of the matter power spectrum.

Finally, using Eqs. (5.52) and (5.45), we obtaion the angular power spectrum for the E-mode of the spin-n galaxy shape components as

$$C_l^{(n,n')} = \frac{2}{\pi}\sqrt{\frac{(l-|n|)!}{(l+|n|)!}\frac{(l-|n'|)!}{(l+|n'|)!}}\int dk k^2 P_{\mathrm{m}}(k)\mathcal{F}_l^{(n)}(k)\mathcal{F}_l^{(n')}(k), \tag{5.53}$$

with

$$\mathcal{F}_l^{(n)}(k) = \left(\frac{1}{2}\right)^{\frac{n}{2}}\frac{(l+|n|)!}{(l-|n|)!}\int dz \frac{dN}{dz}\frac{D(z)}{D(0)}\mathcal{F}^{(n)}(k,z)\left[\frac{j_l(x)}{x^n}\right]. \tag{5.54}$$

In general, when written as a scalar quantity with no angular dependent mode coupling on Fourier space, only the E-mode appears in the linear order of the density. In the linear order, the B-mode distortion can be generated from the primordial gravitational waves [110, 111], which is derived from the fact that the tensor perturbation mimics the tidal field on the (conformal) Fermi normal coordinate, and from a violation of the global rotation symmetry in the primordial non-Gaussianity (refer to App. B).

We dropped the index for E, since in later discussions it is sufficient to discuss only the E-mode. In order to be convenient for discussion, we introduce

$$P^{(n,n')}(k,\,z) \equiv \left[\frac{D(z)}{D(0)}\right]^2 \mathcal{F}^{(n)}(k,z)\mathcal{F}^{(n')}(k,z)P_{\mathrm{m}0}(k)\,, \tag{5.55}$$

which is useful to understand the rough behaviors of the integrand of $C_l^{(n,n')}$ at a given wavelength k and the redshift z.

5.2 Intrinsic galaxy shape

Ref. [14] pointed out that the assumption that the intrinsic elliptical galaxy shapes were uncorrelated, i.e., obeyed the random distributions, was not valid in the weak lensing analysis derived from the mass inhomogeneous distributions (see Sec. 5.3 for weak lensing effect). If the orientations of galaxy shapes obey halo shape or angular momentum, they should not be randomly distributed, but aligned under the influence

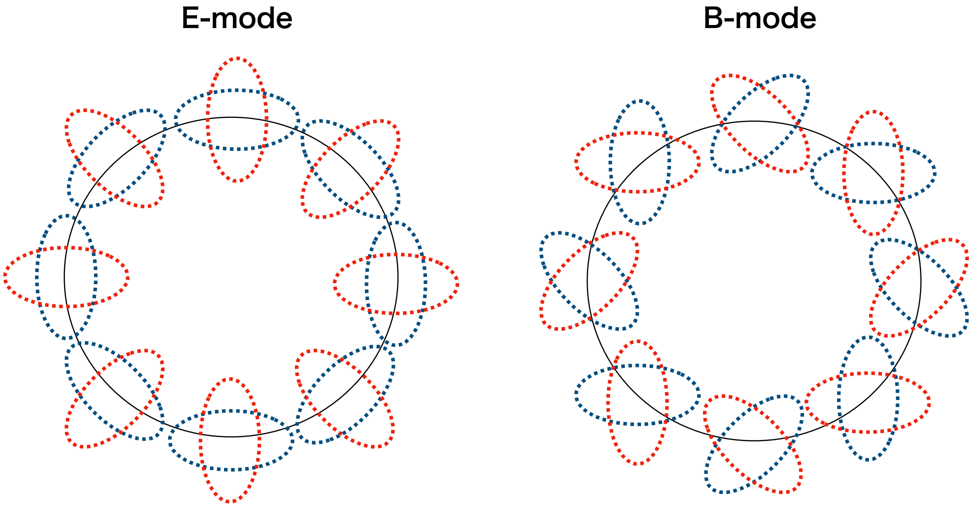

FIGURE 5.2: The E (parity-even)/B (parity-odd) modes of elliptical fields. If there exists the overdensity region in the center, we can imagine the red shape in E-mode due to the tidal force. This corresponds that $\gamma_+^{(2)}$ is negative from Fig. 5.1 and we can expect that the 2nd galaxy intrinsic shape function is proportional to the negative tidal field. On the other hand, since the cosmic shear is derived from the second partial derivative of the potential in the linear order, Eq. (5.71), this shear corresponds to the blue shape in E-mode.

of the tidal field perpendicular to the line of sight direction. Then, this might produce the distant correlation that mimics the distortions caused by weak lensing shear.

Two major models were considered as follows. First, the ellipticity of the isolated elliptical source, which leads to the elliptical galaxy (red galaxy), is determined mainly by the halo shape outside the source. This case suggests that the sources stretch along the direction of the tidal field (Fig. 5.3) and the distant correlation of ellipticities becomes proportional to the correlation of the tidal field. This is known as the linear alignment model (Fig. 5.4). Second, the orientation of the galaxy image is determined mainly by the angular momentum of the halo outside the source. This might be applied to the spiral galaxy (blue galaxy). In the simple disk formation model, the rotation axis of the disk plane turns to the direction of the angular momentum vector of the halo surrounding the source (see, e.g., Ref. [112].) The ellipticity of the spiral galaxy is determined by the disk orientation, namely the angular momentum. The angular momenta of these halos are thought to be acquired by the tidal field disturbing the collapsing galaxy to form an anisotropic momentum of inertia, which is then spun up by further coupling with the tidal field. This leads to the angular momentum vector $\boldsymbol{L}$ is given by $L_i \propto \epsilon_{ijk}\mathcal{I}_{jm}K_{km}$ with the momentum of inertia tensor $\mathcal{I}_{ij}$ and the tidal field K_{ij}. This contribution to the galaxy shapes becomes the second order of the density field because the momentum of inertia must be proportional to the tidal field in the linear order. This model is called the quadratic alignment model.

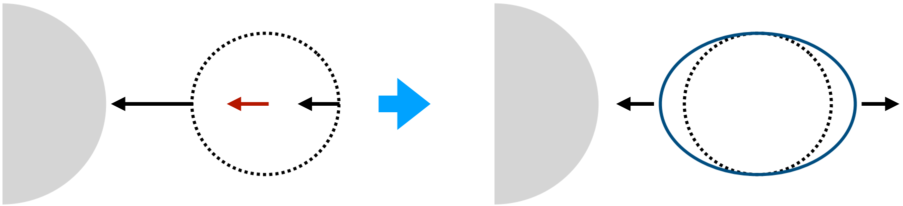

FIGURE 5.3: We show the tidal force effect. If the gray shaded region is the overdensity, the spherical object around the overdense is influenced by the gravitational force from the overdensity. In this case, the forces between at the center of gravity (red allow) and at other positions (black arrow) change slightly. The deviation force from the gravitational force on the center of gravity on the surface is called the tidal force, which causes to distort the spherical object along with the tidal force such as the right panel.

5.2.1 General bias expansion

In this section, we consider the general bias expansion of the galaxy shapes, including the galaxy number density in Sec. 4.1, to capture the effect of long-wavelength modes on these observables. In principle, by completely parametrizing this dependence with bias parameters, it is possible to describe the large-scale statistics of galaxies and their shapes strictly [113, 96], even though the formation of galaxies is extremely complicated and obeys nonlinear physics. This approach works via an expansion in perturbations and derivatives of ones, and thus applies only on scales where the matter density $\delta \ll 1$, which can be phrased as $k < k_{\rm NL}$ where $k_{\rm NL}$ is the nonlinear wavenumber, and which are larger than the length scale R_* on which galaxies form ($k < k_* \simeq 1/R_*$).

As discussed in Sec. 4.1, the position and shape of a galaxy at a given time τ depend on the trajectory of the non-linear matter density around the galaxy formation. Then, the local matter density is affected by the small-scale physics such as gas cooling, radiation pressure and star formation, and the past trajectory of matter around the focused galaxy. However, when we consider the smoothing scale Λ^{-1}, which is a much larger scale than R_*, the position, and shape of galaxies are predominantly determined by the coarse-grained gravitational potential $\Psi_{\rm L}$. Hereafter, since we always use the coarse-grained gravitational potential, we represent $\Psi_{\rm L}$ as Ψ.

Focusing on the smoothing scale Λ^{-1}, we express the number density and shape of galaxies evaluated at the Eulerian spacetime coordinates $(\boldsymbol{x}, \tau)$ as

$$\delta_{\rm n}(\boldsymbol{x},\tau) = \mathcal{N}[\delta(\boldsymbol{y},\tau'), K_{i_1 i_2}(\boldsymbol{y},\tau'), \{s_{i_1\cdots i_n}(\boldsymbol{y},\tau')\}_{n=3,4,\cdots}](\boldsymbol{x},\tau)\,, \tag{5.56}$$

$$g_{i_1\cdots i_n}(\boldsymbol{x},\tau) = \mathcal{G}_{i_1\cdots i_n}[\delta(\boldsymbol{y},\tau'), K_{i_1 i_2}(\boldsymbol{y},\tau'), \{s_{i_1\cdots i_n}(\boldsymbol{y},\tau')\}_{n=3,4,\cdots}](\boldsymbol{x},\tau)\,, \tag{5.57}$$

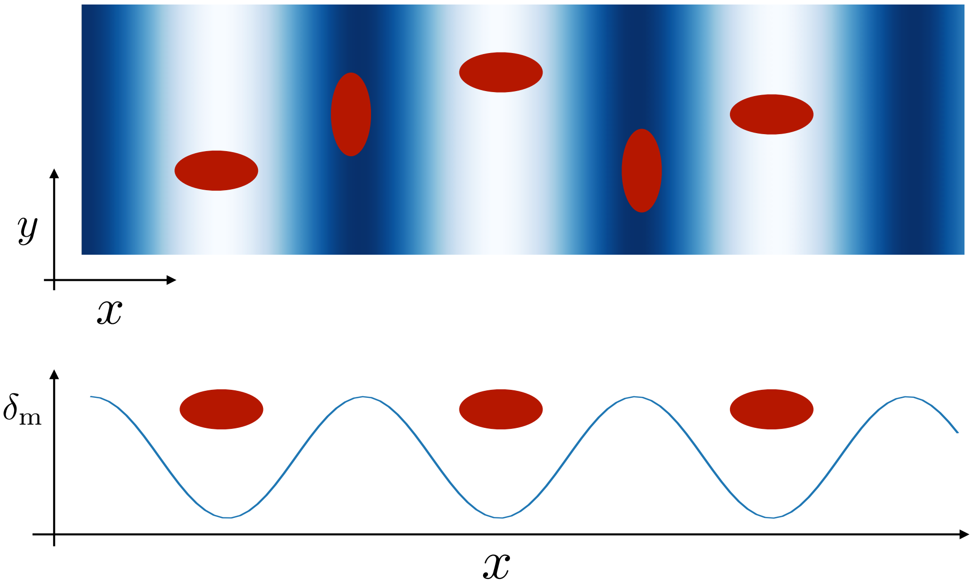

FIGURE 5.4: The schematic picture of the linear alignment model. The red ellipses show the elliptical galaxies. In the upper panel, the blue region is the high-density region and the white region is the low-density region, which corresponds to the density fluctuation on the lower panel. Since elliptical galaxies are distorted by tidal fields, At long distances, the shapes of the galaxies become correlated.

with δ and $s_{i_1\cdots i_n}$, which are defined as

$$\delta(\boldsymbol{x},\tau) \equiv \frac{\rho_{\rm m}(\boldsymbol{x},\tau)}{\bar{\rho}_{\rm m}(\tau)} - 1 = \frac{1}{4\pi G\bar{\rho}_{\rm m}(\tau)a^2}\partial^2\Psi(\boldsymbol{x},\tau)\,, \tag{5.58}$$

$$s_{i_1i_2\cdots i_n}(\boldsymbol{x},\tau) \equiv \frac{(R_*)^{n-2}}{4\pi G\bar{\rho}_{\rm m}a^2}\partial_{i_1}\partial_{i_2}\cdots\partial_{i_n}\Psi(\boldsymbol{x},\tau) \quad (n\geq 3)\,, \tag{5.59}$$

where $\bar{\rho}_{\rm m}$ denotes the background matter energy density and $K_{i_1i_2}$ is the tidal field Eq. (4.4). We used the galaxy scale R_* as the suppression factor in Eq. (5.59) since we regard the smoothing scale Λ^{-1} as roughly serveral times of R_*.

On the second equality of Eq. (5.58), we used the Poisson equation. As discussed in Sec. 4.1, the equivalence principle states that gravity can be locally eliminated, making the system equivalent to a local inertial system. This ensures that we can eliminate the gravitational potential Ψ and its derivative $\partial_i\Psi$ by performing a local coordinate transformation to choose a free-falling observer frame. Therefore, in Eqs. (5.56) and (5.57), we did not include the gravitational potential and its first derivative. As a result, the energy density δ and the tidal tensor $K_{i_1i_2}$ give the leading order local contributions.

We emphasize that the galaxy density and shape, in general, depend on the gravitational potential of their entire past history, which composes the matter density, tidal field and higher derivative terms, and so on. A key feature of the perturbative approach is that this dependence can be incorporated order by order in perturbation theory. Here, we use the fact that time and spatial dependence of the local matter density and local tidal field at each order in perturbation theory factorize. One can capture the non-locality in time by allowing for the contributions at each order to appear separately in the bias expansion. In the case of the galaxy density [114], contributions from the non-locality in time appear at third-order density perturbation as the non-locality operator $\mathcal{D}_{ij}\delta^2$. The same holds for the $n=4$ moment of galaxy shapes, while there is a contribution at second order in case of the 2nd moment [96]. Since we are interested in the leading contribution to $n=4$ moments, which is given by the second-order contribution, it is sufficient to work with the local, Eulerian density and tidal field in the bias expansion.

To determine the functional form of $\mathcal{N}$ and $\mathcal{G}_{i_1\cdots i_n}$, we need to trace the history of the galaxy formation. With the same strategy in Sec. 4.1, we expand δ_{n} and the traceless part of $g_{i_1i_2}$, using the dominant local contributions as

$$\delta_{\mathrm{n}}(\boldsymbol{x},\tau) = b^{(0)}_{\delta}(\tau)\delta(\boldsymbol{x},\tau) + \frac{1}{2}b^{(0)}_{\delta^2}(\tau)\delta^2(\boldsymbol{x},\tau) + \frac{1}{2}b^{(0)}_{K^2}(\tau)[K^2_{ij}](\boldsymbol{x},\tau) + \cdots\,, \tag{5.60}$$

$$\tilde{g}_{i_1i_2}(\boldsymbol{x},\tau) = b^{(2)}_{K}(\tau)K_{i_1i_2}(\boldsymbol{x},\tau) + \frac{1}{2}b^{(2)}_{\delta K}(\tau)[\delta K_{i_1i_2}](\boldsymbol{x},\tau) + \frac{1}{2}b^{(2)}_{K^2}(\tau)[K_{i_1j}K^{j}{}_{i_2}]^{\mathrm{TL}_3}(\boldsymbol{x},\tau) + \cdots\,, \tag{5.61}$$

where $b^{(n)}_X$ with $X=\delta,\delta^2,\cdots$ and $n=0,2$ denote the renormalized bias parameters which are defined as the response of the mean nth moment galaxy shape to the change of X. For example, the linear bias parameter for the number density, $b^{(0)}_{\delta}$, is given by the response of the mean galaxy density with respect to the background matter density as $\partial\ln\bar{n}_g/\partial\ln\bar{\rho}_{\mathrm{m}}$ and the one for the 2nd moment galaxy shape, $b^{(2)}_{K}$, is given by the response of the mean 2nd galaxy shape to the external tidal field $K_{i_1i_2}$ and so on. Here and hereafter we put a tilde to denote the symmetric traceless part of $g_{i_1\cdots i_n}$, i.e. $\tilde{g}_{i_1\cdots i_n}\equiv[g_{i_1\cdots i_n}]^{\mathrm{TL}_3,\mathrm{sym}}$. In Eqs. (5.60) and (5.61), the higher order terms in perturbation and the terms suppressed by $|R_*\partial|\sim R_*k$ with k being the Fourier mode are abbreviated.

Similarly, we can expand $\tilde{g}_{i_1\cdots i_n}$ with $n\geq 3$, using δ, $K_{i_1i_2}$, and $s_{i_1\cdots i_n}$. For example, the 4th moment $\tilde{g}_{ijkl}$ up to the quadratic order in perturbation is given by

$$\tilde{g}_{i_1i_2i_3i_4}(\boldsymbol{x},\tau) = b^{(4)}_{K^2}\left[K_{i_1i_2}(\boldsymbol{x},\tau)K_{i_3i_4}(\boldsymbol{x},\tau)\right]^{\mathrm{TL}_3,\mathrm{sym}} + \mathcal{O}\left((kR_*)^2\right)\,, \tag{5.62}$$

where the coefficient $b^{(4)}_{K^2}$ describes the response to the course-grained quadratic external tidal field[3] The terms with $s_{i_1i_2i_3i_4}$, $[\delta\, s_{i_1i_2i_3i_4}]$, and $s_{i_1i_2j}s^{j}{}_{i_3i_4}$ are all suppressed

---

[3] The explicit form of $[K_{ij}(\boldsymbol{x},\tau)K_{kl}(\boldsymbol{x},\tau)]^{\mathrm{TL}_3,\mathrm{sym}}$ is given by

$$\begin{aligned}
&3\left[K_{ij}(\boldsymbol{x},\tau)K_{kl}(\boldsymbol{x},\tau)\right]^{\mathrm{TL}_3,\mathrm{sym}}\\
=&K_{ij}K_{kl}+K_{ik}K_{jl}+K_{il}K_{jk}\\
&-\left[\frac{2}{7}\sum_{p}\left(\delta_{ij}K_{kp}K_{pl}+\delta_{ik}K_{jp}K_{pl}+\delta_{il}K_{jp}K_{pk}+\delta_{jk}K_{ip}K_{pl}+\delta_{kl}K_{ip}K_{pj}+\delta_{jl}K_{ip}K_{pk}\right)\right.\\
&\left.+\frac{2}{35}\sum_{p,q}\left(\delta_{ij}\delta_{kl}+\delta_{ik}\delta_{jl}+\delta_{il}\delta_{jk}\right)K_{pq}K_{qp}\right]\,.
\end{aligned}\tag{5.63}$$

.

by $(kR_*)^2$.

5.2.2 Linear and non-linear intrinsic alignment

We can compute the contributions of the linear and non-linear intrinsic alignment through the bias expansion. Here, we note that the linear or non-linear alignments do not mean to obey the linear density fluctuation or the non-linear one but the linear order of δ or not. In other words, if the bias expansion of nth moment galaxy shapes up to the first order of δ is given by the higher derivative operator $s_{i_1\cdots i_n}$, we call it the linear alignment.

Using $\mathcal{F}^{(n)}$, introduced in Eq. (5.54), the linear bias for general shape moments including the number density, which corresponds to the linear alignment for the shape, is given by

$$\mathcal{F}^{(n)}_{\rm LA}(k,z) = \begin{cases} b^{(0)}_\delta(z) & (n=0) \\ b^{(2)}_K(z) & (n=2) \\ b^{(n)}_s(z)\left(\dfrac{k}{k_*}\right)^{n-2} & (n\geq 3) \end{cases} , \tag{5.64}$$

with $k_* \equiv 2\pi/R_*$. Without loss of generality we left the time-dependency in the bias parameters. When doing numerical calculations below, we set k_* as $k_* = 1\,{\rm Mpc}^{-1}$, which roughly corresponds to the Lagrangian halo radius of the typical luminous red galaxy with $M_{\rm halo} \sim 3\times 10^{13}h^{-1}M_\odot$ by using Eq. (4.6). For $n\geq 3$, the leading linear alignment term is suppressed for the powers of $k \ll k_*$ and corresponds to the higher-derivative term. This implies that the most significant contribution of the intrinsic alignment for $n\geq 3$ on large scales becomes not the linear alignment but the non-linear alignment (NLA).

There are the following two cases of the non-linearity for the galaxy bias and the intrinsic galaxy alignments.

- The orignal bias expressions as the number density (5.56) and the shape function (5.57) are written by the functional including the non-locality and the bias expansions as shown in Eqs. (5.60) and (5.61) contain already non-linear terms.
- The density fluctuation δ and the tidal field K_{ij} in Eqs. (5.56) and (5.57) evolve with the non-linearity as discussion in Sec. 3.3, which corresponds to the non-linear clustering effect.

For the 2nd moment shape, the non-linearities were discussed in the detail by the simulations in Refs. [115, 116, 117], bias expansion in Refs. [118, 96] and galaxy catalogs in Ref. [119].

Hereafter, we consider a rough estimation of loop integrals from the NLA for arbitrary shape moments, which contains the non-linearities mentioned above. Ref. [120] computed the 1loop contribution to the power spectrum of the halo number density based on EFTofLSS and showed that a representative term in the limit of $k \to 0$ was given by

$$P_{\rm hh}(k) \ni 2c_2^2 \int \frac{d^3\boldsymbol{p}}{(2\pi)^3} \left[\frac{5}{7} + \frac{2}{7}\frac{[\boldsymbol{p}\cdot(\boldsymbol{k}-\boldsymbol{p})]^2}{p^2|\boldsymbol{k}-\boldsymbol{p}|^2}\right]^2 P_{\rm L}(p)P_{\rm L}(|\boldsymbol{k}-\boldsymbol{p}|)\,, \tag{5.65}$$

where $P_{\rm hh}$ is the halo-halo power spectrum, c_2 is an effective second-order bias coefficient, and the kernel, which corresponds to the square brackets, is second-order bias contributions from matter density and tidal field squared. As mentioned in Sec. 4.2 (see also Ref. [97]), this contribution behaves k^0 in the limit $k \to 0$ and while the 1loop contributions of the matter density behave $k^2 P_{\rm L}(k)$ and k^4, which was discussed in Refs. [121, 122]. These behaviors differences in the 1-loop contribution depend on whether or not the mass and momentum conservations are imposed. Therefore, the stochastic terms with $\propto k^0$ appear since the bias expansions do not impose these conservations. Though we need to consider the stochastic noise such as the Poisson noise for the auto-correlation, we evaluate this term as the stochastic noise, instead[4].

We use Eq. (5.65) to evaluate the 1loop contribution from the second-order bias expansion and noise for the shape moments. Though the shape moment functions have dimensionless tensor legs, the correlations of these tensor legs roughly modify results by an $\mathcal{O}(1)$ factor and we ignore these contributions. Then, we can use a similar expression to Eq. (5.65),

$$P^{(n,n)}_{\rm NLA}(k) = 2(b^{(n)}_{\rm NLA})^2 \int \frac{d^3\boldsymbol{p}}{(2\pi)^3} \left[\frac{5}{7} + \frac{2}{7}\frac{[\boldsymbol{p}\cdot(\boldsymbol{k}-\boldsymbol{p})]^2}{p^2|\boldsymbol{k}-\boldsymbol{p}|^2}\right]^2 P_{\rm L}(p)P_{\rm L}(|\boldsymbol{k}-\boldsymbol{p}|)\,, \tag{5.66}$$

which can be evaluated as roughly the NLA contribution to the auto-correlation for the nth shape moments and this expression matches loop computations for the 2nd moment up to a $\mathcal{O}(1)$ coefficient, previously derived in Refs. [118, 96].

This contribution is shown in Fig. 5.5 by brown dot-dashed lines. The bias parameter is set to $|b^{(n)}_{\rm NLA}| = 0.1$ both for the 2nd and 4th shape moments. Since the 1-loop contribution which appears from the linear alignment term of g_{ijkl} is suppressed by $(k/k_*)^2$ for the cross-correlation and $(k/k_*)^4$ for the auto-correlation, the above contributions only appear from K^2 type term like the one in Eq. (5.62) on the large scale.

As disscussed in Sec. 3.4, the scaling of the l-loop contribution can be estimated as

$$\left(\frac{k}{k_{\rm NL}}\right)^{(l+1)(n_{\rm L}+3)} \frac{1}{k^3} \sim \left(\frac{k}{k_{{\rm NL},z=0}}\right)^{(l+1)(n_{\rm L}+3)} \left(\frac{D(z)}{D(0)}\right)^{2(l+1)} \frac{1}{k^3}\,. \tag{5.67}$$

The 1-loop contribution shown in Fig. 5.5 or given by Eq. (5.66) follows this scaling around $k_{\rm NL}$, which explicitly corresponds to $n_{\rm L} = -1.7$ at $k_{{\rm NL},z=0} = 0.25h\,{\rm Mpc}^{-1}$.

---

[4] As discussed in Sec. 4.2, we should renormalize the loop contribution on the large scales, introducing the term $\int_{\boldsymbol{p}} P_{\rm L}^2(p)$.

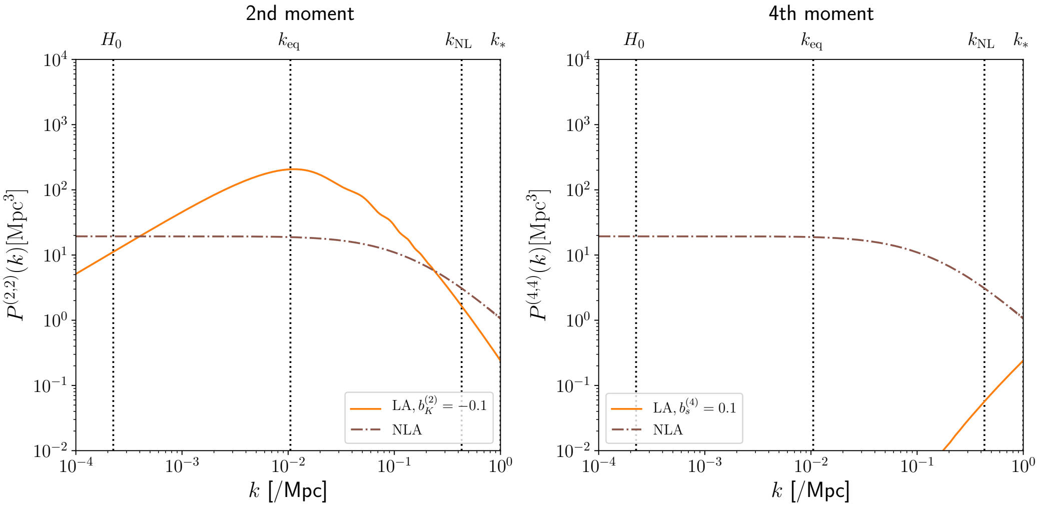

FIGURE 5.5: The 3D power spectra of each contribution at $z = 1.5$ for the 2nd moment (left) and the 4th moment galaxy shape function (right). The orange solid lines are the linear alignment and the brown dash-dotted lines are the non-linear alignment contributions. The bias parameters are set as $(b_K^{(2)}, b_K^{(4)}) = (-0.1, 0.1)$. We used $k_{{\rm NL},z=0} = 0.25[h/{\rm Mpc}]$.

Here, the time evolution is computed, considering the EdS Universe. However, according to Ref. [113], the result does not change significantly even if we consider the ΛCDM Universe. In this paper, we took into account the redshift dependence, using the linear growth factor. In Ref. [123], analyzing up to the 2loop EFTofLSS predictions for matter power spectrum, it was shown that the counter term additionally introduces tiny time dependence (see Fig. 13 in Ref. [123]). For the actual Universe, since the power spectrum does not scale with a single power, the estimation becomes more complicated (see e.g., Ref. [124]). Since $k_* > k_{\rm NL}$, these loop contributions dominate the linear alignment terms, suppressed by $(k/k_*)^2$ for the 4th moment as given in Eq. (5.64).

For the nth moment function with $n = 2m\,(m = 1,\, 2,\, \cdots)$, the leading contributions, which are not suppressed by powers of k/k_*, only appear from the non-linear bias expansion terms schematically in the form $\tilde{g}_{i_1\cdots i_{2m}} \sim (K)^m$, where the tensor indices of K_{ij} are abbreviated. For a larger n, the non-linear alignment contributions without k/k_* suppression start with higher loops. For instance, the auto-correlation of $\tilde{g}_{i_1\cdots i_6}$ starts from 2-loop contributions.

5.3 Weak lensing

The inhomogeneities in the Universe between the light emitted from the source to us distort the photon paths and this phenomenology is known as *(gravitational) lensing*. In other words, the original shapes of the source objects appear distorted when we observe these objects. To be more specific, as we will see in the process of solving the null geodesic, the lensing effect occurs via metric perturbations Φ,Ψ. If we can measure the distortions due to the lensing effect, we directly infer information on the Φ and Ψ contributions, i.e., the mass distribution in the structure.

In cosmology, the *weak lensing* is often used as one of the most important probes. This is that the intrinsic shapes of distant galaxies are *slightly* distorted by foreground overdensities between the sources and us. Roughly speaking, we use the fact that the spatial average of the 1-point function in metric perturbation on the cosmological scale is zero but the 2-point correlation remains. One powerful application of weak lensing is the calibration for galaxy bias. Since the shear due to the weak lensing is unbiased tracer, the cross-correlation between the shear and the galaxy number density provides the galaxy bias itself.

Here, since we are interested in intrinsic galaxy shapes, the weak lensing contribution becomes contamination. If we observe the shape at low redshifts, the weak lensing contribution can be negligible. However, the sample size may become small that a large-scale imaging survey would not be fully usable. Thus, evaluating the contribution of lensing distortion is of importance. In this subsection, we consider the weak lensing contribution to an arbitrary moment of the galaxy shapes. We first consider the photon path through the inhomogeneities in the Universe and then estimate how it affects the shape moment.

5.3.1 Derivation from the null geodesics

The relation between the intrinsic galaxy shape on the source plane and the apparent galaxy shape on the image plane can be computed by tracing the photon propagation in the perturbed FLRW spacetime. Using the affine parameter λ, the null geodesic equation, which describes the photon propagation, is given by

$$\frac{d^2x^\mu}{d\lambda^2} + \Gamma^\mu_{\alpha\beta}\frac{dx^\alpha}{d\lambda}\frac{dx^\beta}{d\lambda} = 0\,, \tag{5.68}$$

where $\Gamma^\mu_{\alpha\beta}$ is the Christoffel symbol of the perturbed spacetime. The Greek indices μ, α, β run from 0 to 3. Solving the geodesic equation along the orthogonal direction to $\hat{\boldsymbol{n}}$ with a use of the null condition

$$g_{\mu\nu}\frac{dx^\mu}{d\lambda}\frac{dx^\nu}{d\lambda} = 0\,, \tag{5.69}$$

we obtain the lens equation as

$$\tilde{\theta}_{\mathrm{s}\,i}(\tilde{\boldsymbol{\theta}}) = \tilde{\theta}_i + \int_0^\chi d\chi' \frac{\chi - \chi'}{\chi}\partial_{\perp i}(\Phi(\chi', \tilde{\boldsymbol{\theta}}) - \Psi(\chi', \tilde{\boldsymbol{\theta}})), \tag{5.70}$$

with $\partial_{\perp i} \equiv \mathcal{P}_i{}^j\partial_j$. Here, we have imposed the boundary condition as $\tilde{\theta}^i(\chi = 0) = \tilde{\theta}^i$ and $\tilde{\theta}^i(\chi) = \tilde{\theta}^i_{\mathrm{s}}$. The projected coordinates $\tilde{\theta}_i$ and $\tilde{\theta}_{\mathrm{s}\,i}$ correspond to those on the image plane and the source plane, respectively. A detailed computation of Eq. (5.70) can be found e.g. in Ref. [100]. We also use $\tilde{\theta}_{\mathrm{s}\,i}$ to express the mapping of a coordinate on the image plane $\tilde{\theta}_i$ to the corresponding one on the source plane as $\tilde{\theta}_{\mathrm{s}\,i}(\tilde{\boldsymbol{\theta}})$.

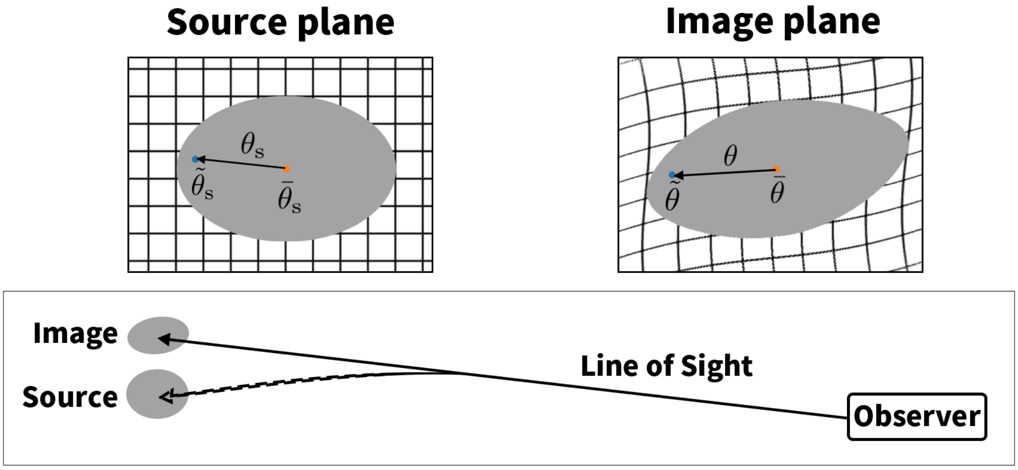

FIGURE 5.6: This figure shows the 2D coordinates on the source plane and on the image plane. The orange and blue dots denote the centroids and given points on each plane.

Taking the partial derivative of $\tilde\theta_{\mathrm{s}\,i}$ with respect to $\tilde\theta^j$, we obtain the deformation matrix A_{ij} [125] as

$$A_{ij}(\tilde{\boldsymbol{\theta}}) \equiv \frac{\partial\tilde\theta_{\mathrm{s}i}}{\partial\tilde\theta^j} = \delta_{ij} + \int_0^\chi d\chi' \frac{\chi-\chi'}{\chi}\chi'\partial_{\perp i}\partial_{\perp j}(\Phi(\chi',\,\tilde{\boldsymbol{\theta}}) - \Psi(\chi',\,\tilde{\boldsymbol{\theta}}))\,. \tag{5.71}$$

Because of the spatial inhomogeneity of Φ and Ψ, the deformation matrix A_{ij} depends on $\tilde{\boldsymbol{\theta}}$.

Now, let us compute the deviation from the centroid on the source plane, $\theta_{\mathrm{s}\,i} \equiv \tilde\theta_{\mathrm{s}\,i} - \bar\theta_{\mathrm{s}\,i}$, decomposing it into the two parts as

$$\theta_{\mathrm{s}\,i} = \left[\tilde\theta_{\mathrm{s}\,i}(\tilde{\boldsymbol{\theta}}) - \tilde\theta_{\mathrm{s}\,i}(\bar{\boldsymbol{\theta}})\right] + \left[\tilde\theta_{\mathrm{s}\,i}(\bar{\boldsymbol{\theta}}) - \bar\theta_{\mathrm{s}\,i}\right]\,. \tag{5.72}$$

These coordinates on the source plane and the image plane are visually explained in Fig. 5.6. The first square brackets describe the difference between the two coordinates on the source plane which are mapped from $\tilde\theta_i$ and $\bar\theta_i$ on the image plane, respectively. The second square brackets describe the difference between the coordinates on the source plane mapped from the apparent centroid, $\bar\theta_i$, and the actual centroid, $\bar\theta_{\mathrm{s}\,i}$. Since we cannot directly measure the source distribution, the actual centroid $\bar{\boldsymbol{\theta}}_\mathrm{s}$ is left undermined.

Using Eq. (5.70), we can compute the first square brackets in Eq. (5.72) minus θ_i as

$$\delta\theta_i \equiv \tilde\theta_{\mathrm{s}\,i}(\tilde{\boldsymbol{\theta}}) - \tilde\theta_{\mathrm{s}\,i}(\bar{\boldsymbol{\theta}}) - \theta_i = \theta_{\mathrm{s}\,i} - \theta_i - \left[\tilde\theta_{\mathrm{s}\,i}(\bar{\boldsymbol{\theta}}) - \bar\theta_{\mathrm{s}\,i}\right]\,, \tag{5.73}$$

as

$$\delta\theta_i = \int_0^\chi d\chi' \frac{\chi-\chi'}{\chi}\,\partial_{\perp i}\left[(\Phi(\chi',\,\tilde{\boldsymbol{\theta}}) - \Psi(\chi',\,\tilde{\boldsymbol{\theta}})) - (\Phi(\chi',\,\bar{\boldsymbol{\theta}}) - \Psi(\chi',\,\bar{\boldsymbol{\theta}}))\right]\,. \tag{5.74}$$

Here we are evaluating Φ and Ψ along the unperturbed photon path. This is only correct in linear order in the deflection. If one includes the lower-order deflection in the argument of these metric perturbations and expands this effect as well, one obtains additional contributions which involve the integral over products of $\partial_k\partial_l\Phi$ and $\partial_k\partial_l\Psi$. These contributions, which are known as "post-Born corrections" (e.g., [126]), to the nth moment can be roughly approximated as being of order $(\delta A^{(2)})^m$, with $m = n$ if n is even and $m = (2n+1)/2$ if n is odd. This means that they are of the same order as the nonlinear lensing contribution we will discuss below, and hence we will not derive them in detail here.

Expanding $\delta\theta_i$ with respect to $\theta_i = \tilde{\theta}_i - \bar{\theta}_i$, we obtain

$$\delta\theta_i(\boldsymbol{\theta}) = \sum_{n=2}^{\infty} \frac{1}{(n-1)!}\, \delta A^{(n)}_{ii_1\cdots i_{n-1}} \theta^{i_1}\cdots\theta^{i_{n-1}}\,, \tag{5.75}$$

with

$$\delta A^{(n)}_{ii_1\cdots i_{n-1}} = \int_0^{\chi} d\chi' \frac{\chi-\chi'}{\chi}\left[\prod_{k=1}^{n-1}(\chi'\partial)_{\perp i_k}\right]\partial_{\perp i}(\Phi(\chi',\bar{\boldsymbol{\theta}}) - \Psi(\chi',\bar{\boldsymbol{\theta}}))\,. \tag{5.76}$$

The spatial variation of A_{ij} yields the higher order terms of θ_i, characterized by $\delta A^{(n)}_{ii_1\cdots i_{n-1}}$ with $n \geq 3$. For $n = 2$, $\delta A^{(2)}_{ij}$ is nothing but the deviation of the deformation matrix from the unit matrix. The traceless part of $\delta A^{(n)}_{ii_1\cdots i_{n-1}}$ describes the spin-n deformation due to the gravitational lensing, whose visual image is discussed in Sec. 5.1.

5.3.2 Estimation of weak lensing effect

Using the formula derived in the previous subsection, let us compute the weak lensing contribution in Eq. (5.3), which can be rewritten as

$$I^{\rm WL}_{i_1i_2\cdots i_n}(\bar{\boldsymbol{\theta}}) = \left[I_{i_1i_2\cdots i_n}(\bar{\boldsymbol{\theta}}) - I^{\rm int}_{i_1i_2\cdots i_n}(\bar{\boldsymbol{\theta}}_{\rm s})\right] + \left[I^{\rm int}_{i_1i_2\cdots i_n}(\bar{\boldsymbol{\theta}}_{\rm s}) - I^{\rm int}_{i_1i_2\cdots i_n}(\boldsymbol{\theta}_{\rm s}(\bar{\boldsymbol{\theta}}))\right]\,. \tag{5.77}$$

Similarly to Eq. (5.8), using the projected coordinates on the source plane, $\theta_{{\rm s}\,i}$, the n-th moment intrinsic galaxy shape function is defined as

$$I^{\rm int}_{i_1i_2\cdots i_n}(\bar{\boldsymbol{\theta}}_{\rm s},\,\tau) = \frac{\chi^n}{\bar{I}^{\rm int}(\bar{\boldsymbol{\theta}}_{\rm s})R_*^n}\int d^2\boldsymbol{\theta}_{\rm s}\prod_{m=1}^{n}\theta_{{\rm s}\,i_m} I^{\rm int}(\bar{\boldsymbol{\theta}}_{\rm s}+\boldsymbol{\theta}_{\rm s},\,\tau)\,, \tag{5.78}$$

with the normalization

$$\bar{I}^{\rm int}(\bar{\boldsymbol{\theta}}_{\rm s},\,\tau) \equiv \int d^2\boldsymbol{\theta}_{\rm s}\, I^{\rm int}(\bar{\boldsymbol{\theta}}_{\rm s}+\boldsymbol{\theta}_{\rm s},\,\tau)\,. \tag{5.79}$$

The brightness theorem, which states that the lensing does not change the surface brightness, relates the apparent surface brightness $I(\tilde{\boldsymbol{\theta}})$ to the intrinsic surface brightness $I^{\rm int}(\tilde{\boldsymbol{\theta}}_{\rm s})$ as $I^{\rm int}(\tilde{\boldsymbol{\theta}}_{\rm s}) = I(\tilde{\boldsymbol{\theta}})$ or equivalently in our notation,

$$I^{\rm int}(\bar{\boldsymbol{\theta}}_{\rm s} + \boldsymbol{\theta}_{\rm s},\, \tau) = I(\bar{\boldsymbol{\theta}} + \boldsymbol{\theta},\, \tau)\,. \tag{5.80}$$

First, let us compute the first square brackets of Eq. (5.77) by using θ_i expressed in terms of $\theta_{{\rm s}\,i}$. In the previous subsection, we derived the expression of $\delta\theta_i(\boldsymbol{\theta})$, solving the null geodesics. Using this expression, $\theta_{{\rm s}\,i}$ in the left hand side of Eq. (5.72) can be expressed in terms of θ_i and the global shift between the apparent and actual centroids. Solving Eq. (5.72) recursively, we can express θ_i in terms of $\theta_{{\rm s}\,i}$ and the contribution due to the global shift of the centroid as

$$\theta_i = \theta_{{\rm s}\,i} + \sum_{n=2}^{\infty} \frac{1}{(n-1)!}\, \delta B^{(n)}_{i i_1 \cdots i_{n-1}} \theta_{\rm s}^{i_1} \cdots \theta_{\rm s}^{i_{n-1}} + \mathcal{F}_i(\tilde{\boldsymbol{\theta}}_{\rm s}(\bar{\boldsymbol{\theta}}) - \bar{\boldsymbol{\theta}}_{\rm s})\,, \tag{5.81}$$

where, e.g., the leading contributions of $\delta B^{(2)}_{i_1 i_2}$ and $\mathcal{F}_i$, which is a function of $\tilde{\boldsymbol{\theta}}_{\rm s}(\bar{\boldsymbol{\theta}}) - \bar{\boldsymbol{\theta}}_{\rm s}$, are given by

$$\begin{aligned} \delta B^{(2)}_{i_1 i_2} &= -\delta A^{(2)}_{i_1 i_2} + \delta A^{(2)}_{i_1 j} \delta A^{(2)j}{}_{i_2} + \cdots\,, \\ \mathcal{F}_i(\tilde{\boldsymbol{\theta}}_{\rm s}(\bar{\boldsymbol{\theta}}) - \bar{\boldsymbol{\theta}}_{\rm s}) &= \left[-\delta_i{}^j + \delta A^{(2)j}_i + \cdots\right] \left(\tilde{\theta}_{{\rm s}\,j}(\bar{\boldsymbol{\theta}}) - \bar{\theta}_{{\rm s}\,j}\right) + \cdots\,. \end{aligned} \tag{5.82}$$

Since $\delta A^{(n)}_{i_1 \cdots i_n}$ are the functions of $\bar{\boldsymbol{\theta}}$, so are $\delta B^{(n)}_{i_1 \cdots i_n}$. Inserting Eq. (5.81) into Eq. (5.8), we can expand $I_{i_1 i_2 \cdots i_n}(\bar{\boldsymbol{\theta}})$ in terms of $I^{\rm int}_{i_1 i_2 \cdots i_n}(\bar{\boldsymbol{\theta}}_{\rm s})$, where the coefficients are given by products of $\delta B^{(n)}_{i_1 \cdots i_n}$ and $\mathcal{F}_i$.

The leading lensing effect on the nth moment of a galaxy image can be computed by making the lensing operators derived above act on a perfectly symmetric (spherical) intrinsic image, whose moments are given by

$$I^{\rm int}_{i_1 i_2 \cdots i_n}(\bar{\boldsymbol{\theta}}_{\rm s}) = \begin{cases} C_{2N}[\mathcal{P}_{i_1 i_2} \mathcal{P}_{i_3 i_4} \cdots \mathcal{P}_{i_{2N-1} i_{2N}} + \text{perms.}] & n = 2N\,, \\ 0 & n = 2N-1\,, \end{cases} \tag{5.83}$$

where N is a natural number and C_{2N} is of order the angular size of the image to the nth power; Ref. [101] also presents the effects of non-symmetric intrinsic images. In the following, we calculate the terms in the first brackets of Eq. (5.77) for $n = 2N$. For the moment, let us ignore the contributions due to the shift of the centroid, which turns out to be sub-leading. Inserting Eq. (5.81) into Eq. (5.8) and using Eq. (5.83), we obtain

$$\begin{aligned} \text{1st brackets of Eq.(5.77)} \ni \left(\frac{R_*}{\chi}\right)^{2(M-1)} & \delta A^{(2M)}_{i_1 \cdots i_m}, \\ & \delta A^{(2)}_{i_1 j_1} \delta A^{(2)j_1}{}_{i_2} \cdots \delta A^{(2)}_{i_{2N-1} j_N} \delta A^{(2)j_N}{}_{i_{2N}}\,,\ (\text{perms})\,, \\ & \cdots\,, \end{aligned} \tag{5.84}$$

with $M = 1, 2, \cdots$. The factor $(R_*/\chi)^{2(M-1)}$ of the first contribution appears, since $I_{i_1\cdots i_{2N}}$ and $I^{\rm int}_{i_1\cdots i_{2(N+M-1)}}$ carry different powers of R_*/χ. In computing the terms in the second line, which is given by $2N$ product of $\delta A^{(2)}$, we used $\delta A^{(2)}_{i_pj}\delta A^{(2)}{}_{i_qj'}\mathcal{P}^{jj'} = \delta A^{(2)}_{i_pj}\delta A^{(2)j}{}_{i_q}$. The ellipses stand for the trace part and other non-linear terms in perturbations. As discussed above, these include post-Born corrections which are of similar order of magnitude. While we did not write it explicitly, for $M < N$, the lacking indices should be supplied by the projection tensor $\mathcal{P}_{ij}$. Therefore, such terms do not contribute to the traceless component. Since the order of $\delta A^{(2M)}_{i_1\cdots i_{2M}}$ is given by

$$\left|\delta A^{(2M)}_{i_1\cdots i_{2M}}\right| = \mathcal{O}\left((k\chi')^{2(M-1)}\right) \times |\delta A^{(2)}|\,, \tag{5.85}$$

the first contribution in Eq. (5.84) amounts to

$$\left|\left(\frac{R_*}{\chi}\right)^{2(M-1)} \times \delta A^{(2M)}_{i_1\cdots i_{2M}}\right| = \mathcal{O}\left((kR_*)^{2(M-1)}\right) \times |\delta A^{(2)}|\,. \tag{5.86}$$

In Eq. (5.85), we have replaced $\partial/\partial\bar{\theta}^i$ with $k\chi'$, where k is the Fourier mode of the 3D coordinates of the centroid on the image plane. Equation (5.86) indicates that at the linear order of the perturbation, the traceless component of the first brackets of Eq. (5.77) with $n = 2N \geq 4$ is suppressed at least by $(kR_*)^{n-2}$, which is much smaller than 1 since we only consider larger scales than the typical size of galaxies. To be precise, the integrand of $\delta A^{(2)}$ in Eq. (5.86) is further suppressed by $(\chi'/\chi)^{2(M-1)}$. For example, for the 4th moment, the tree-level diagram which appears by contracting the first contribution in Eq. (5.84) roughly scales as

$$(kR_*)^4 \times P_{\rm L}(k)\,. \tag{5.87}$$

Meanwhile, for the 2nd moment with $N = 1$, the linear contribution simply gives the deformation matrix $\delta A^{(2)}_{i_1i_2}$.

Similarly, all the non-linear contributions which include $\delta A^{(n)}_{i_1\cdots i_n}$ with $n \geq 3$ are suppressed by positive powers of kR_*. Therefore, the only contributions which are not suppressed by $kR_* \ll 1$ are products of $\delta A^{(2)}$, i.e. the second contribution in Eq. (5.84). In the end of this subsection we will discuss the loop contributions from the products of $\delta A^{(2)}$.

So far, we have not considered the contribution from the shift of the centroid. According to Ref. [106], the centroid shift can be estimated by (see also Ref. [127])

$$|\theta_{\rm si}(\bar{\boldsymbol{\theta}}) - \bar{\theta}_{\rm si}| \sim \mathcal{O}(\Delta\theta^j\partial\delta A^{(2)}/\partial\theta^j) \times \Delta\theta_i\,. \tag{5.88}$$

Repeating a similar argument, we find that the leading contribution of the centroid shift has more (kR_*) than the leading contribution and is suppressed more on the large scale. For this reason, we do not consider the contribution of the centroid shift.

Next, let us discuss the first brackets of Eq. (5.77) for an odd number n. Repeating the same argument, we find that the odd nth moment is always suppressed by kR_*, since the intrinsic nth moment of the galaxy shape function $I^{\rm int}_{i_1 i_2\cdots i_n}(\bar{\boldsymbol{\theta}}_{\rm s})$ vanishes for an odd n under the assumption of Eq. (5.83). In particular, the first brackets of Eq. (5.77) is suppressed at least by $(kR_*)^{n-2}$ at the linear perturbation.

In summary, we showed that the only contributions that are not suppressed by $kR_*(\ll 1)$ are the products of $\delta A^{(2)}$. A contraction of $\delta A^{(2)}$ yields weak lensing loops, computed in the projected 2D plane. As emphasized in Sec. 5.2.2, these 2D loops are qualitatively different from 3D loop contributions to the galaxy shape moments, which are projected into 2D after computing loop contributions in 3D (see, e.g. Eq. (5.66)). The 3D loop contributions are included as the non-linear alignment effect. For a comparison of 2D and 3D loops, here we estimate their contributions to the angular power spectrum of the 4th shape moment, $C_l^{(4,4)}$. Taking the flat-sky limit, the 2D weak lensing loops in $C_l^{(4,4)}$ is roughly estimated as,

$$C_l^{(4,4){\rm 2D\text{-}1L}} \sim \langle (\delta A^{(2)}\delta A^{(2)})(\boldsymbol{l})(\delta A^{(2)}\delta A^{(2)})(\boldsymbol{l}')\rangle \sim 2\int \frac{d^2 l_1}{(2\pi)^2} C_\gamma(l_1) C_\gamma(|\boldsymbol{l}-\boldsymbol{l}_1|)\,, \tag{5.89}$$

where $C_\gamma(l)$ is the lensing shear for 2nd moment and $\boldsymbol{l}$ is a 2D vector on the Cartesian coordinate. We find that the contribution of 2D lensing 1-loop, given by Eq. (5.89), is much smaller than the one of the 3D 1-loop(NLA). Therefore, evaluating the forecast in this paper, we neglect the weak lensing contribution, whose linear contribution is suppressed by kR_* and whose loop contributions are much smaller than the 3D loops, included in non-linear alignment effects.

Assuming the absence of the intrinsic deformation, i.e. assuming a circular intrinsic image, we have estimated the nth moment deformation of the galaxy shape due to the weak lensing. To estimate the weak lensing contribution more accurately by taking into account the intrinsic deformation, the assumption, (5.83), should be abandoned.

5.3.3 Summary

The weak lensing contribution to the nth moment function, $\tilde{I}^{\rm WL}_{i_1\cdots i_n}$, should have n tensor indices which are projected to the 2D plane. For the 2nd moment, the lensing contribution, $\tilde{I}^{\rm WL}_{ij}$ is nothing but the deformation matrix A_{ij}. Meanwhile, for $n \geq 3$, the additional tensor indices are supplied either by acting with angular derivatives or by multiplying several A_{ij}s. The former yields a suppression by powers of k/k_*, while the latter contributes as two-dimensional loop integrals.

The linear weak lensing (LWL) contribution, whose indices can thus only be supplied by operating with the spatial derivative operator, are suppressed as

$$F^{(n)}_{\rm LWL}(k,z) \propto \left(\frac{k}{k_*}\right)^{n-2} \qquad (n \geq 2)\,, \tag{5.90}$$

where we have dropped the redshift dependence. This result is in agreement with Eq. (84) of [101]. Therefore, similarly to the intrinsic alignment, for $n > 2$, the leading contribution for $k \ll k_*$ stems from the loop contributions. Notice that since A_{ij}, which is given by integrating along the line of sight, is a 2D object, loop integrals of the weak lensing, expressed by non-linear terms of A_{ij}, should be performed in the projected 2D space. Therefore, weak lensing loops are qualitatively different from the loop contributions in the intrinsic alignment, which are given by first computing loop integrals in 3D space and subsequently projecting it to the 2D space. The lensing loops obtained after projection are much smaller than the latter for the auto-correlation of the 4th moment.

5.4 Intrinsic galaxy shape with PNGs

As discussed in Sec. 5.2.2, we found that the intrinsic shapes on the large scale could respond to the density contrast and the external tidal fields at each time. In this section, when there exist the primordial non-Gaussianities, especially for the primordial bispectrum, we investigate how to modify the bias expansion of the intrinsic shapes.

5.4.1 Imprint of spin-2 particles on 2nd moment shape

Before the discussion on the 4th shape moment, we summarize the contribution of the PNGs in the second shape moment. Ref. [41] showed that the contribution of the PNG (2.57) in the second shape moment $\tilde{g}_{i_1 i_2}$ at first, and here we brief the derivation along the line with Ref. [41].

First, we consider the cross-correlation the matter density field on the large scale with the second moment galaxy shape function Eq. (5.61), which is written as

$$\begin{aligned}\langle \delta(\boldsymbol{x}) \tilde{g}_{i_1 i_2}(\boldsymbol{y}) \rangle = b_K^{(2)} \langle \delta(\boldsymbol{x}) K_{i_1 i_2}(\boldsymbol{y}) \rangle + \frac{1}{2} b_{\delta K}^{(2)} \langle \delta(\boldsymbol{x}) [\delta K_{i_1 i_2}](\boldsymbol{y}) \rangle \\ + \frac{1}{2} b_{K^2}^{(2)} \langle \delta(\boldsymbol{x}) [K_{i_1 j} K^{j}_{\ i_2}]^{\mathrm{TL}_3}(\boldsymbol{y}) \rangle + \cdots \,,\end{aligned} \tag{5.91}$$

where we drop the time argument due to the evaluation at the same time. In the initial Gaussian condition, the terms corresponding to the 3-point correlation vanish on the large scale and contribute only to the nonlinear evolution on small scale. On the other hand, in the initial non-Gaussian condition, the 3-point correlation terms are sensitive to the squeezed-limit bispectrum since the 2-point fields are evaluated at the same position. The same will be done later in the case of the 4th moment, then here we omit the specific calculations, but for example, the second term corespoinding to the 3-point functions on the squeezed primoridal bispectrum, given by the case of $\Delta_2 = 0$ in Eq. (2.64), becomes in Fourier space

$$\langle \delta(\boldsymbol{k}) [\delta K_{i_1 i_2}](\boldsymbol{k}') \rangle = \frac{2}{5} A_2 [\hat{k}_{i_1} \hat{k}_{i_2}]^{\mathrm{TL}_3} \mathcal{M}^{-1}(k, z) P_{\mathrm{m}}(k) \langle \delta^2 \rangle (2\pi)^3 \delta_{\mathrm{D}}(\boldsymbol{k} + \boldsymbol{k}') \,. \tag{5.92}$$

This means that the 2nd moment galaxy shape has the non-Gaussian contribution of the primordial squeezed anisotropic bispectrum corresponding to A_2 since $[\hat{k}_{i_1} \hat{k}_{i_2}]^{\mathrm{TL}_3}$ leads to the quadrupole mode $\mathcal{P}_2$.

However, the 3-point functions such as Eq. (5.92) contain the matter density variance $\langle\delta^2\rangle$, which leads to the logarithmic divergence if the cutoff scale $\Lambda^{-1} \to 0$. This is also read as the unphysical dependence of the arbitrary cutoff scale. Then, we need to introduce the counter-term in the bias expansion such as $\mathcal{D}_{i_1i_2}\Phi$. As discussed in Sec. 4.1, the need for the counter-term is natural since the bias expansion Eq. (5.61) is implicitly assumed the statistics of the initial short-modes which influence local galaxy formation are the same regardless of positions, which means that the short-modes uncorrelated the long-modes. In this situation, the small-scale matter power spectrum is modulated by the long-mode potential perturbation such as Eq. (4.24). Then, we must consider the dependence of galaxy shapes on the amplitude and anisotropy of small-scale fluctuations.

After renormalization, we obtain

$$\langle\delta(\boldsymbol{x})\tilde{g}_{i_1i_2}(\boldsymbol{y})\rangle = b_K^{(2)}\mathcal{D}_{i_1i_2}\xi(|\boldsymbol{x}-\boldsymbol{y}|) + 3b_{\rm NG}^{(2)}A_2\mathcal{D}_{i_1i_2}\xi_{\delta\Phi}(|\boldsymbol{x}-\boldsymbol{y}|)\,, \tag{5.93}$$

and in Fourier space

$$\langle\delta(\boldsymbol{k})\tilde{g}_{i_1i_2}(\boldsymbol{k}')\rangle = \left[\hat{k}_{i_1}\hat{k}_{i_2}\right]^{\rm TL_3}[b_K^{(2)} + 3b_{\rm NG}^{(2)}A_2\mathcal{M}^{-1}(k)]P_{\rm m}(k)(2\pi)^3\delta_{\rm D}(\boldsymbol{k}+\boldsymbol{k}')\,. \tag{5.94}$$

In the case of the scale dependence in the primoridal bispectrum, we can extend

$$\begin{aligned}\langle\delta(\boldsymbol{k})\tilde{g}_{i_1i_2}(\boldsymbol{k}')\rangle = \left[\hat{k}_{i_1}\hat{k}_{i_2}\right]^{\rm TL_3}[b_K^{(2)} + 3b_{\rm NG}^{(2)}\left(\frac{k}{k_*}\right)^{3/2}A_2\mathcal{M}^{-1}(k)\cos\left[\nu_2\ln\left(\frac{k}{k_*}\right)+\Theta_2\right]]\\ \times P_{\rm m}(k)(2\pi)^3\delta_{\rm D}(\boldsymbol{k}+\boldsymbol{k}')\,,\end{aligned} \tag{5.95}$$

where k_* is the pivot scale and the Θ_2 is the phase depending on the halo model.

5.4.2 Imprint of spin-4 particles on 4th moment shape

We will show that similarly only the PNG generated by the spin-4 particle contributes to the 4th shape moment, $\tilde{g}_{i_1i_2i_3i_4}$. Along the line with Sec. 5.4.1, we compute the contribution of the PNG to $\tilde{g}_{i_1i_2i_3i_4}$ by evaluating the correlation between δ and $\tilde{g}_{i_1i_2i_3i_4}$.

In Sec. 5.2.1, various contributions to the 4th shape moment for the Gaussian initial condition were computed. The angular dependent PNG leads to an additional contribution to the correlation $\langle\delta(\boldsymbol{x})\tilde{g}_{i_1i_2i_3i_4}(\boldsymbol{y})\rangle$. For example, when the PNG is given by Eq. (2.57) with $\Delta_4 = 0$, we obtain

$$\langle\delta(\boldsymbol{x})\tilde{g}_{i_1i_2i_3i_4}(\boldsymbol{y})\rangle = \frac{2}{9}b_{K^2}^{(4)}A_4\mathcal{D}_{i_1i_2i_3i_4}\xi_{\delta\Phi}(|\boldsymbol{x}-\boldsymbol{y}|)\langle\delta^2\rangle\,, \tag{5.96}$$

with $\mathcal{D}_{i_1i_2i_3i_4} \equiv [\mathcal{D}_{i_1i_2}\mathcal{D}_{i_3i_4}]^{\rm TL_3,sym}$ and $\xi_{\delta\Phi}$ being the cross-correlation between the linear δ and Φ. A more detailed computation of Eq. (5.96) can be found in App. D.4.

Performing the Fourier transformation, we obtain

$$\langle\delta(\boldsymbol{k})\tilde{g}_{i_1i_2i_3i_4}(\boldsymbol{k}')\rangle = \frac{2}{9}b^{(4)}_{K^2}A_4[\hat{k}_{i_1}\hat{k}_{i_2}\hat{k}_{i_3}\hat{k}_{i_4}]^{\mathrm{TL}_3}(2\pi)^3\mathcal{M}^{-1}(k,z)P_{\mathrm{m}}(k,z)\langle\delta^2\rangle\delta_{\mathrm{D}}(\boldsymbol{k}+\boldsymbol{k}')\,, \tag{5.97}$$

where $P_{\mathrm{m}}(k,z)$ is the linear matter power spectrum at z and $\mathcal{M}(k,z)$ is defined at Eq. (3.28).

As the same in Sec. 5.4.1, since Eq. (5.97) depends on $\langle\delta^2\rangle$, which diverges when we send the UV cutoff to the infinity, we need to perform the renormalization to compute the observable effect. The renormalization proceeds analogously to the one for the PNG generated by the spin-0 and spin-2 particles discussed in Refs. [41, 67, 68]. As one can see in Eq. (2.61), the counter term for the contribution of the PNG generated by the spin-4 particle should be in the form, $\mathcal{D}_{i_1i_2i_3i_4}\Phi$. In the presence of the PNG generated by the spin-4 particle, the local matter density for the short mode $\boldsymbol{k}$ is modified as

$$\delta^{\mathrm{loc}}(\boldsymbol{k};\boldsymbol{x}) = \left(1+\frac{1}{2}\alpha_{\mathrm{L}\,i_1i_2i_3i_4}(\boldsymbol{x})[\hat{k}^{i_1}\hat{k}^{i_2}\hat{k}^{i_3}\hat{k}^{i_4}]^{\mathrm{TL}_3}\right)\delta^{\mathrm{iso}}(\boldsymbol{k})\,, \tag{5.98}$$

with

$$\alpha_{\mathrm{L}\,i_1i_2i_3i_4}(\boldsymbol{x}) \equiv \int\frac{d^3\boldsymbol{k}_{\mathrm{L}}}{(2\pi)^3}\frac{35}{8}A_4[\hat{k}_{\mathrm{L},i_1}\hat{k}_{\mathrm{L},i_2}\hat{k}_{\mathrm{L},i_3}\hat{k}_{\mathrm{L},i_4}]^{\mathrm{TL}_3}\Phi(\boldsymbol{k}_{\mathrm{L}})e^{i\boldsymbol{k}_{\mathrm{L}}\cdot\boldsymbol{x}}\,. \tag{5.99}$$

The renormalized bias is then defined through the response of 4th moment to α

$$b^{(4)}_{\mathrm{NG}} \equiv \left.\frac{\partial\langle\tilde{g}_{i_1i_2i_3i_4}\rangle_{\alpha_{\mathrm{L}}}}{\partial\alpha_{\mathrm{L}\,i_1i_2i_3i_4}}\right|_{\alpha_{\mathrm{L}}=0}, \tag{5.100}$$

which leads to

$$\langle\delta(\boldsymbol{k})\tilde{g}_{i_1i_2i_3i_4}(\boldsymbol{k}')\rangle = \frac{35}{4}b^{(4)}_{\mathrm{NG}}A_4[\hat{k}_{i_1}\hat{k}_{i_2}\hat{k}_{i_3}\hat{k}_{i_4}]^{\mathrm{TL}_3}(2\pi)^3\mathcal{M}^{-1}(k,z)P_{\mathrm{m}}(k,z)\delta_{\mathrm{D}}(\boldsymbol{k}+\boldsymbol{k}')\,. \tag{5.101}$$

The detailed computation is summarized in App. D.4.2. As the same of the second moment galaxy shape function, this result can be straightforwardly extended to the PNG with $\Delta_4 = 3/2 \pm i\nu_4$ as

$$\begin{aligned}\langle\delta(\boldsymbol{k})\tilde{g}_{i_1i_2i_3i_4}(\boldsymbol{k}')\rangle = {}&\frac{35}{4}b^{(4)}_{\mathrm{NG}}A_4\left(\frac{k}{k_*}\right)^{3/2}[\hat{k}_{i_1}\hat{k}_{i_2}\hat{k}_{i_3}\hat{k}_{i_4}]^{\mathrm{TL}_3}\cos\left[\nu_4\ln\left(\frac{k}{k_*}\right)+\Theta_4\right]\\ &\times(2\pi)^3\mathcal{M}^{-1}(k,z)P_{\mathrm{m}}(k,z)\delta_{\mathrm{D}}(\boldsymbol{k}+\boldsymbol{k}')\,.\end{aligned} \tag{5.102}$$

Here and hereafter, we set the pivot scale k_{p} to k_*. For a different choice of k_*, the corresponding $b^{(4)}_{\mathrm{NG}}$ and Θ_4 differ.

5.4.3 Imprint of particle with a general integer spin

We can also evaluate the imprint of the PNG generated by the spin-n particle with a general integer n, encoded in $\langle \delta(\boldsymbol{x}) \tilde{g}_{i_1 \cdots i_n}(\boldsymbol{y}) \rangle$. The PNG from the spin-$n$ particle selectively appears in the traceless part of the nth shape moment, $\tilde{g}_{i_1 \cdots i_n}$. Therefore, even if A_0, which corresponds to $f_{\rm NL}$, is much larger than A_s with $s \geq 2$, the contribution of A_0 does not contaminate $\tilde{g}_{i_1 \cdots i_n}$ with $n \geq 2$ in the linear regime.

Repeating a similar computation to App. D.4, we find that the spin-n contribution in the squeezed PNG (2.57) yields the additional intrinsic alignment contribution given by

$$\mathcal{F}^{(n)}_{\rm PNG}(k,z) = C_n b^{(n)}_{\rm NG} A_n \left(\frac{k}{k_*}\right)^{{\rm Re}[\Delta_n]} \mathcal{M}^{-1}(k,z) \cos\left[{\rm Im}[\Delta_n] \ln\left(\frac{k}{k_*}\right) + \Theta_n\right] \, , \quad (5.103)$$

where $\mathcal{F}^{(n)}_{\rm PNG}$ denotes the PNG contribution in Eq. (5.54) and Θ_n is the phase determined for a given halo model, i.e. it is a function of k_*. Hereafter, we denote ${\rm Im}[\Delta_n]$ as ν_n. The leading PNG contribution appears from the quadratic terms in the bias expansion of the nth shape moment, which are accompanied with additional spatial gradient for $n > 4$. However, the spatial gradient does not yield an additional suppression by k/k_* in Eq. (5.103), since it is replaced with $(k_{\rm S}/k_*)^{n-4}$, where $k_{\rm S}$ is the short mode. Therefore, as written in Eq. (5.103), the leading PNG contribution scales as $\propto k^{{\rm Re}[\Delta_n]} \mathcal{M}^{-1}(k,z)$ for a general integer n. The coefficient C_n is determined by conducting the renormalization. The counter term needed for the renormalization differs for a different n. For $n = 0, 2, 4$, C_n is given by $C_0 = 1/2$, $C_2 = 3$ ([41]) and $C_4 = 35/4$ (Sec. 5.4.2).

Let us emphasize that the separability of the PNG contributions from different spins no longer holds, once the loop contributions become important because the kernel functions also induce the angular dependence. Then, the PNG generated by the spin-s particles can contribute to the nth moment of the galaxy shape function only for $n = s$. Having considered this, in the next section, we explore whether there is a scale where the contribution from the PNG becomes dominant, keeping the late-time non-linear contributions subdominant.

5.5 Forecast for future surveys

We have computed the contribution of the PNG generated by a spin-n particle, to the nth moment galaxy shape function, $\tilde{I}_{i_1 \cdots i_n}$. In this section, comparing it to other contributions predicted in ΛCDM cosmology with the adiabatic Gaussian initial condition, let us discuss whether we can observe the imprint of the higher spin particles from future observations.

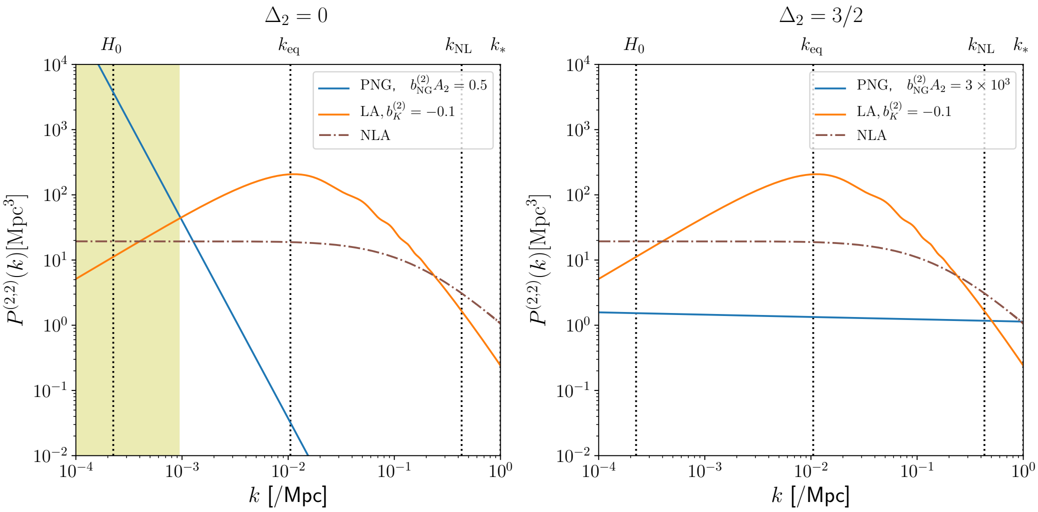

FIGURE 5.7: The k-dependence of each contribution at $z = 1.5$ for the 2nd moment galaxy shape function. The LA and NLA are the same as Fig. 5.5. The left and right panels additionally include the PNG contribution, given in Eq. (5.103), for $\Delta_2 = 0$ and $b^{(2)}_{\rm NG}A_2 = 0.5$ (left) and for $\Delta_2 = 3/2$ and $b^{(2)}_{\rm NG}A_2 = 3\times10^3$ (right), respectively. The yellow shade shows the range of k at which the PNG contribution exceeds those of LA and NLA.

5.5.1 Dominant contribution at different scales

Combining the results obtained in Sec. 5.2.1 and Sec. 5.3, we can evaluate which effect is dominant at each scale or at each multipole moment. Figure 5.7 compares the contributions of the PNG from the spin-2 particle to LA and NLA for the 2nd galaxy moment. Here, considering the ΛCDM Universe, we set $n_{\rm L} \sim -1.7$ and $k_{{\rm NL},z=0} = 0.25h/{\rm Mpc}$ [113]. For $\Delta_2 = 0$, the contribution of the PNG dominates at the large scales as pointed out in Ref. [41] (see also Ref. [42] for N-body simulation). The colored region shows the range of k at which the PNG dominates the other contributions. Meanwhile, for ${\rm Re}[\Delta_2] = 3/2$ (only scaling), the contribution of the PNG is dominated by NLA at all scales with $k < k_{\rm eq}$, where the galaxy imaging surveys work as a spin-sensitive detector. When the perturbative expansion holds, satisfying $b^{(2)}_{\rm NG}A_2 \ll 10^4$ (assuming $b^{(2)}_{\rm NG} = 0.1$), there is no range of k where the PNG generated from the massive spin-2 particle with ${\rm Re}[\Delta_2] = 3/2$ dominates the 2nd moment of the galaxy shape function. The PNG from the spin-2 particle in the principle mass series, which is suppressed by the dilution, ${\rm Re}[\Delta_2] = 3/2$, exhibits the oscillatory resonance feature as shown in Eqs. (2.57) and (2.58). Since our purpose here is to compare the amplitudes of different contributions, for the illustrative purpose, the oscillatory contribution in Eq. (5.103) is ignored.

The situation is different for the PNG generated from the spin-n particle with $n > 2$, because the linear alignment and the linear weak lensing for $\tilde{I}_{i_1 i_2 \cdots i_n}$ are both suppressed by $(k/k_*)^{n-2}$. Meanwhile, as shown in Eq. (5.103), the PNG can contribute to $\tilde{I}_{i_1 i_2 \cdots i_n}$ without being suppressed at large scales, especially for $\Delta_s = 0$.

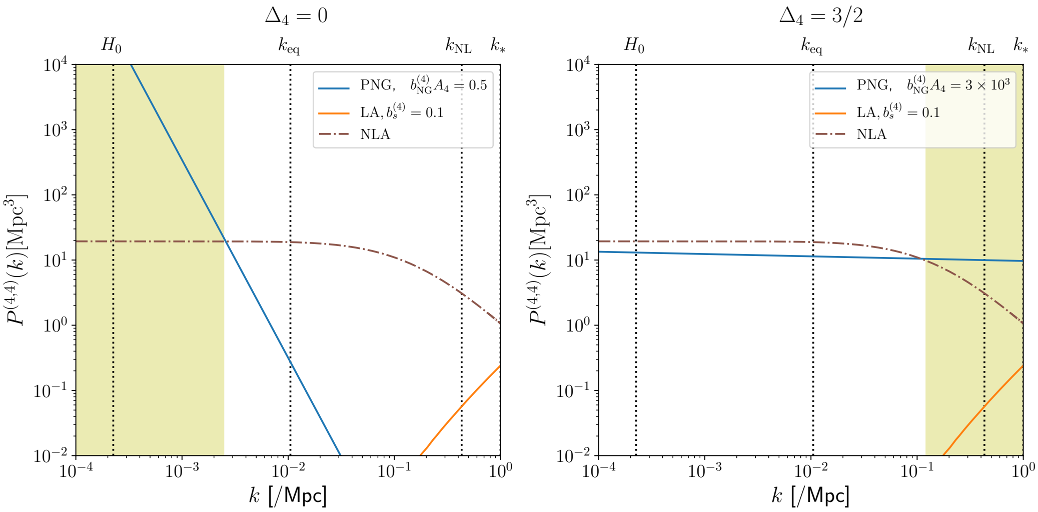

FIGURE 5.8: The k-dependence of each contribution at $z = 1.5$ for the 4th moment galaxy shape function. The LA and NLA are the same as Fig. 5.5. The left and right panels additionally include the PNG contribution, given in Eq. (5.103), for $\Delta_4 = 0$ and $b^{(4)}_{\rm NG}A_4 = 0.5$ (left) and for $\Delta_4 = 3/2$ and $b^{(4)}_{\rm NG}A_4 = 3 \times 10^3$ (right), respectively. The yellow shades show the range of k at which the PNG contribution exceeds those of LA and NLA.

Figure 5.8 compares the different contributions to the auto-correlation of $\tilde{I}_{i_1i_2i_3i_4}$. Since the dominant contamination of the 4th shape moment comes from NLA, i.e. the 3D loops under the Gaussian initial condition (even if we include the lensing contribution), here let us compare it to the PNG contribution. Around $k_{\rm NL}$, where the 1-loop NLA acquires the additional factor $(k/k_{\rm NL})^{n_{\rm L}+3}$, the PNG contribution dominates the NLA contribution in the range of k which satisfies

$$(C_4 b^{(4)}_{\rm NG}A_4)^2 \left(\frac{k}{k_*}\right)^{2{\rm Re}[\Delta_4]} \mathcal{M}^{-2}(k) > \left(\frac{k}{k_{\rm NL}}\right)^{n_{\rm L}+3} . \tag{5.104}$$

Here, focusing on the amplitude, the oscillatory contribution (if any) is again ignored. On the other hand, for $k < k_{\rm eq}$, the leading contribution of NLA, which corresponds to the stochastic term, is roughly given by

$$P_{\rm NLA}(k < k_{\rm eq}, z) \sim b^2_{\rm NLA}\left[\frac{D(z)}{D(0)}\right]^4 \int_k^\infty dp p^2 [P_{\rm L}(p)]^2 \sim b^2_{\rm NLA}\left[\frac{D(z)}{D(0)}\right]^4 [P_{\rm L}(k_{\rm eq})]^2 k^3_{\rm eq} , \tag{5.105}$$

which is almost scale independent like the white noise. In practice, this contribution would be absorbed by the amplitude of the noise in the 4th moment, for which we do not have a reliable estimate. In our idealized setting then, the PNG contribution should exceed this to be detectable.

The PNG contribution is z-independent while the linear alignment contribution varies as $\sim (1+z)^{-2}$ and the NLA contribution depends on $\sim (1+z)^{-4}$. Therefore, a smaller amplitude of PNG can be detected for a deeper survey. This point is

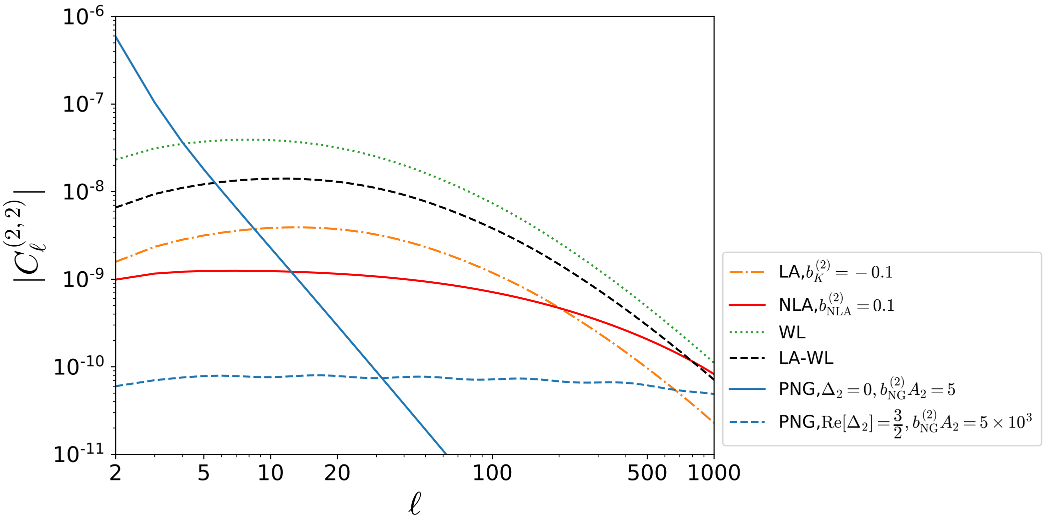

FIGURE 5.9: This plot shows the contributions of LA (orange dash-dotted), NLA (red solid), linear WL (green dotted), and PNG (blue), to the angular power spectrum of the second shape moment $C_l^{(2,2)}$ for LSST-like survey, whose dN/dz is given by Eq. (5.106). The black dashed curve shows the cross-correlation between LA and linear WL, which becomes negative, and the other curves show the auto-correlations of each contribution. The blue solid line corresponds to $\Delta_2 = 0$ and the blue dashed line corresponds to ${\rm Re}[\Delta_2] = 3/2$, $\nu_2 = 3$, $\Theta_2 = 0$.

quantitatively analyzed in Fig. 5.14.

5.5.2 Angular power spectrum

Using Eq. (5.53), we can compute the angular power spectrum. Here, we focus on $C_l^{(2,2)}$ and $C_l^{(4,4)}$, by which we can explore the imprint of the spin-2 and spin-4 particles, respectively. In conducting the numerical computation, the Limber approximation is employed for $l > 20$.

Inserting Eq. (5.103) into Eq. (5.53), we can compute the contribution of the PNG from spin-s particle to the angular power spectrum $C_l^{(n,n')}$, where n and (or) n' are (is) equal to s. The PNG contribution from the spin-2 particle was addressed in Ref. [41] ($\Delta_2 = 0$). In Fig. 5.9, we show the contributions of LA, NLA, WL, and PNG to $C_l^{(2,2)}$, including NLA, which was not taken into account in Refs. [41, 43]. (and we show also more realistic estimation expect for NLA in Appendix. A).Assuming an LSST like lensing survey [8, 128], we have used the function dN/dz given by

$$\frac{dN}{dz} \propto \left(\frac{z}{z_*}\right)^{1.24} \exp\left[-\left(\frac{z}{z_*}\right)^{1.01}\right], \tag{5.106}$$

which is normalized as $\int dz(dN/dz) = 1$ and $z_* = 0.51$. In Fig. 5.9, we show the auto-correlations of each contribution and the cross-correlations between the LA and the linear WL.

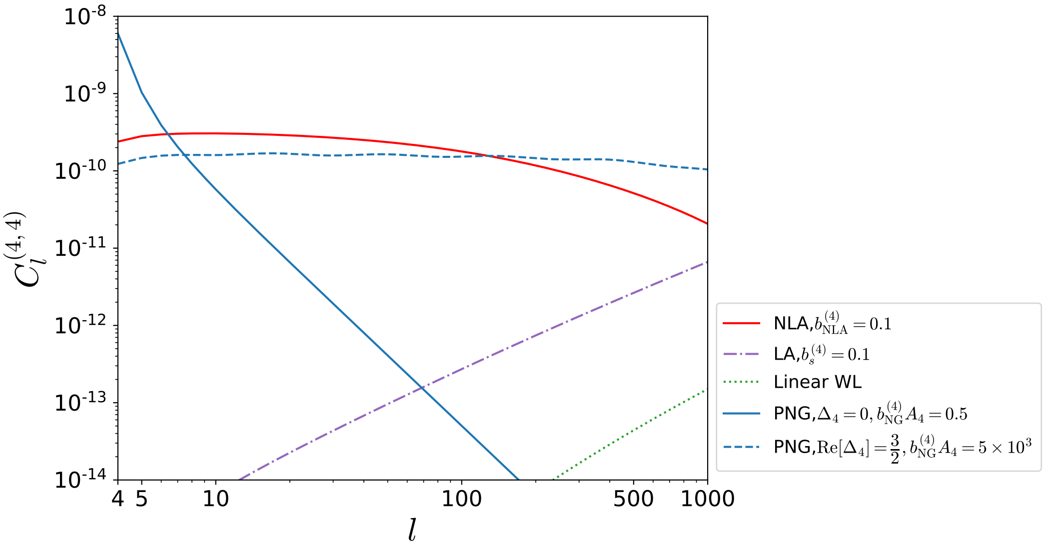

FIGURE 5.10: This plot shows each contribution in the auto-correlation of 4th shape moment for LSST-like survey. The blue solid line corresponds to $\Delta_4 = 0$ and the blue dashed line corresponds to $\mathrm{Re}[\Delta_4] = 3/2$, $\nu_4 = 3$, $\Theta_4 = 0$ in Eq. (5.103). The purple dash-dotted line is the LA contribution. The red solid line shows the 1-loop NLA contribution evaluated by using Eq. (5.66). The green dotted line corresponds to the linear WL.

Similarly, using Eqs. (5.53), (5.64), and (5.103), we can compute the auto-correlation of each contribution in the angular power spectra for $n = 4$ as

$$C_l^{(4,4)X} = \frac{2}{\pi}\frac{(l-4)!}{(l+4)!}\int k^2 dk P_{\rm m}(k)|F_l^X(k)|^2 \qquad (X = \mathrm{LA}, \mathrm{PNG}, \mathrm{LWL}), \tag{5.107}$$

with

$$F_l^Y(k) = \frac{1}{4}\frac{(l+4)!}{(l-4)!}\int dz \frac{dN}{dz} F_Y^{(4)}(k,z)\frac{D(z)}{D(0)}\left[\frac{j_l(x)}{x^4}\right]_{x=k\chi(z)} \qquad (Y = \mathrm{LA}, \mathrm{PNG}), \tag{5.108}$$

$$\begin{aligned} F_l^{\rm LWL}(k) = \frac{1}{4}\frac{(l+4)!}{(l-4)!}\int_0^{\chi_{\rm max}} & d\chi' \chi' D_\Phi(z(\chi'))\left(\frac{k}{k_*}\right)^2\left[\frac{j_l(k\chi')}{(k\chi')^4}\right] \\ & \times \int_{\chi'}^{\chi_{\rm max}} d\chi H(\chi)\frac{dN}{dz}\left(\frac{\chi'}{\chi}\right)^2\frac{\chi-\chi'}{\chi}, \end{aligned} \tag{5.109}$$

and

$$D_\Phi(z) \equiv 3H_0^2\Omega_{\rm m0}\frac{(1+z)D(z)}{D(0)}. \tag{5.110}$$

Equation (5.109) can be derived by operating the source distribution function on the expression for a source at fixed redshift given by Eq. (5.71)[5].

Figure 5.10 compares different contributions to $C_l^{(4,4)}$. The purple dash-dotted

---

[5] Since we estimated only the scaling of the linear WL for $(kR_*\chi'/\chi) \ll 1$, our Eq. (5.109) should be additionally multiplied by 1/12 to match with Eq. (84) in Ref. [101].

line shows the contribution of the LA, which is suppressed by $(k/k_*)^4$. The green dotted line shows the contribution of the linear weak lensing. The contribution of the weak lensing 1-loop in the projected 2D space (2D 1LOOP), which is given by Eq. (5.89), is much smaller and below the shown range in the figure, under the assumption of this bias parameter values. The blue solid line shows the contribution of the PNG with $\Delta_4 = 0$ and the blue dashed line shows the one of the PNG with $\Delta_4 = 3/2 + i\nu_4$, which corresponds to the PNG from a spin-4 particle in the principle mass series. For a larger ν_4, the net contribution of the PNG to $C_l^{(4,4)\mathrm{PNG}}$ becomes smaller, being smoothed out by the integration over k. This aspect is common with massive particles in the principal mass series with other spins, as discussed in Ref. [43] (see also Appendix. A).

Since the PNG contribution with $\mathrm{Re}[\Delta_s] = 3/2$ is almost constant, being independent of l, one may think it can be detected at high ls even if it is subdominant at lower ls. However, at high ls, because of the mixing due to the non-linear evolution, we cannot separately pick up the PNG contributions from particles with different spins. (Roughly speaking, using the redshift of the peak of dN/dz, we can estimate $l_{\mathrm{NL}} \sim k_{\mathrm{NL},z=0.5}\chi(z = 0.5) \sim 470$ as the non-linear angular scale.) In the range where the non-linear evolution is negligible, while the PNG contribution does not become dominant for $n = 2$, it can be dominant for $n = 4$ in $l \gtrsim 200$[6].

5.5.3 Forecast for future imaging survey

We investigate the detectability of the PNG generated by higher spin particles, considering the future galaxy survey, LSST. As discussed in Sec. 5.5.1, on large scales the PNG from each particle with spin-s only contributes to the sth galaxy moment of the galaxy shape function, leaving an imprint in the auto-correlation $C_l^{(n,n)}$ with $n = s$ and the cross-correlations $C_l^{(n,n')}$ with $n = s$ or $n' = s$. Therefore, no matter how large the angular independent PNG f_{NL} is, this does not disturb probing the signal of the higher spin particle encoded in $\tilde{I}_{i_1\cdots i_n}$ with the corresponding value of n (see [129] for a demonstration including f_{NL} and $\mathcal{A}_2$). Furthermore, even if there exists an infinite tower of higher spin particles as predicted in string theory, we can single out the contribution of the spin-s particle by looking at the sth galaxy shape moment.

On the other hand, when the contribution of the loops becomes important, the non-trivial momentum dependence in the kernel functions allows the contribution of the PNG from the spin-n' particle to contaminate $\tilde{I}_{i_1\cdots i_n}$ with $n' \neq n$. Therefore, in what follows, we focus on $k < k_{\mathrm{NL}}$, where the loop contribution remains subdominant.

In the 2nd moment induced by the spin-2 particles, since the noise estimation for the galaxy shape was estimated, we investigate the forecast by using a Fisher analysis.

---

[6] The coefficients C_2, C_4, which are determined by renormarization in Eq. (5.103), are different between the 2nd moment and the 4th moment. Therefore, even if $b_{\mathrm{NG}}^{(2)} A_2 = b_{\mathrm{NG}}^{(4)} A_4$, the corresponding contribution of the PNG for $n = 4$ is larger than the one for $n = 2$ by the factor $(C_4/C_2)^2 = (35/12)^2 \sim 9$.

On the other hand, in the 4th moment induced by the spin-4 particles, since the shape noise for the 4th moment shape is unknown, we study a rough forecast by estimating the signal-to-noise ratio when the NLA is used as noise term up to the scale where the non-linear is negligible.

Spin-2 case

We study how well future observations will be able to constrain the model parameters by using the Fisher matrix formalism (see e.g., Refs. [130, 131, 132]). The Fisher information matrix is given by

$$F_{ij} = \sum_l \frac{(2l+1)f_{\mathrm{sky}}}{2} \mathrm{Tr}\left(\mathbf{C}^{-1}\frac{\partial \mathbf{C}}{\partial p_i}\mathbf{C}^{-1}\frac{\partial \mathbf{C}}{\partial p_j}\right) , \tag{5.111}$$

with the covariance matrix

$$\mathbf{C}(l) \equiv \begin{pmatrix} C_l^{(0,0)} & C_l^{(0,2)} \\ C_l^{(0,2)} & C_l^{(2,2)} \end{pmatrix} . \tag{5.112}$$

Here, p_i is a model parameter. Recall that in this section, we consider the case with the parity symmetry and the global rotational symmetry, which lead to the absence of the B-mode and correlations among different multipoles under the consideration on the large scale.

As a noise effect, here we consider the shot noise which we assume to be white spectrum as

$$N^{(2,2)} = \frac{\sigma_\gamma^2}{\bar{n}_{\mathrm{G}}} , \qquad N^{(0,0)} = \frac{1}{\bar{n}_{\mathrm{n}}} , \qquad N^{(0,2)} = 0 , \tag{5.113}$$

where σ_γ^2 is the dispersion of the intrinsic shape with instrumental noise per component, $\bar{n}_{\mathrm{G}}$ is the projected surface density of galaxies with shapes per steradian, and $\bar{n}_{\mathrm{n}}$ is the galaxies clustering density per steradian. We include this noise effect, changing the angular power spectra in Eq. (5.112) as

$$C_l^\alpha \to C_l^\alpha + N_l^\alpha , \qquad (\alpha = (0,0), (0,2), (2,2)) . \tag{5.114}$$

In the following, considering a noise estimation for an LSST-like measurement [8, 128], we use $f_{\mathrm{sky}} = 0.5$, $\bar{n}_{\mathrm{G}} = 37/\mathrm{arcmin}^2$, $\bar{n}_{\mathrm{n}} = 46/\mathrm{arcmin}^2$, and $\sigma_\gamma = 0.25$. Furthermore, we use the function dN_n/dz for the number density given by

$$\frac{dN_n}{dz} \propto \left(\frac{z}{1.0}\right)^{1.25} \exp\left[-\left(\frac{z}{1.0}\right)^{1.26}\right] , \tag{5.115}$$

and the function dN/dz for the 2nd moment galaxy shape as Eq. (5.106) with $z_* = 0.51$. For simplicity, though we use the same distribution of the intrinsic shape and the weak lensing, actually, the distribution of the intrinsic shape and the weak lensing are different because The former targets the only red galaxy, while the latter is all samples. To study how the forecast on parameter uncertainties changes, depending on the galaxy redshift distribution, we leave $z_{*\rm I}$ for the intrinsic shape, which we assume to be equal to $z_{*\rm G}$ for the weak lensing, as a free parameter.

For a simple halo model, the non-linear bias parameter for the number density $b_{\rm NG}^{(0)}$ is given by [22, 133, 134] (see also Ref. [135])

$$b_{\rm NG}^{(0)} = (b_\delta^{(0)} - 1)\delta_{\rm c}\,, \tag{5.116}$$

where $\delta_{\rm c}$ $(= 1.686)$ denotes the critical density for spherical collapse. Along the line with the convention of the tidal alignment [136], we set the linear bias parameter $b_K^{(2)}$ as

$$b_K^{(2)}(z) = \bar{b}_1^{\rm I}\Omega_{\rm m0}\frac{D(0)}{D(z)}\,, \tag{5.117}$$

which is consistent with observations of luminous red galaxies. Meanwhile, the non-linear bias parameter for the galaxy shape $b_{\rm NG}^{(2)}$ is not very well known. Assuming that $b_{\rm NG}^{(2)}$ is a constant parameter which is comparable to $b_K^{(2)}$ [41], we parametrize $b_{\rm NG}^{(2)}$ as

$$b_{\rm NG}^{(2)} = \bar{b}_{\rm NG}^{\rm I}\,\bar{b}_1^{\rm I}\,\Omega_{\rm m0} = \bar{b}_{\rm NG}^{\rm I}\,b_K^{(2)}(z)\frac{D(z)}{D(0)}\,. \tag{5.118}$$

Here, $\bar{b}_{\rm NG}^{\rm I}$ is another constant parameter.

The present setup includes the parameters

$$\{b_\delta^{(0)},\, \bar{b}_1^{\rm I},\, A_0,\, \bar{b}_{\rm NG}^{\rm I}A_2,\, A_s\}, \tag{5.119}$$

where A_s is the amplitude of the scalar power spectrum at the pivot scale $k_{\rm p} = 0.05{\rm Mpc}^{-1}$, and the parameters

$$\{{\rm Re}[\Delta_0],\, \nu_0,\, \Theta_0,\, {\rm Re}[\Delta_2],\, \nu_2,\, \Theta_2\}, \tag{5.120}$$

which characterize the scale dependence of $C_l^{(0,0)}$ and $C_l^{(2,2)}$. Since $\bar{b}_{\rm NG}^{\rm I}$ and A_2 entirely degenerate, here we take $\bar{b}_{\rm NG}^{\rm I}A_2$ as a single parameter. In the following, considering a certain model of inflation, we fix the parameters (5.120) to specific values. In particular, we consider the PNGs which are generated in two different inflation models:

1. Inflation model with multi-light scalar fields and a massive spin-2 field in the principal series coupled with the inflaton, where the PNG with A_0, A_2, $\nu_2 \neq 0$ and $\Delta_0 = \nu_0 = \Theta_0 = 0$ and ${\rm Re}[\Delta_2] = 3/2$ can be generated.
2. Inflation model with a massive scalar field and a massive spin-2 field which are both in the principal series and are both coupled with the inflaton, where the PNG with A_0, A_2, ν_0, ν_2, $\neq 0$ and ${\rm Re}[\Delta_0] = {\rm Re}[\Delta_2] = 3/2$ can be generated.

Here, marginalizing over other parameters, we discuss a possible constraint on the parameters $p_1 \equiv A_0$ and $p_2 \equiv \bar{b}^{\rm I}_{\rm NG} A_2$. When all other parameters, leaving aside either of p_1 or p_2, are fully marginalized, the 1σ bound on p_i is given by $\sigma(p_i) = \sqrt{(\mathbf{F}^{-1})_{ii}}$ (see e.g., Ref. [130]). Here, we choose the fiducial values of the parameters (5.119) as

$$(b^{(0)}_\delta,\, \bar{b}^{\rm I}_1,\, A_0,\, \bar{b}^{\rm I}_{\rm NG} A_2,\, A_s) = (2,\, -0.1,\, 0,\, 0\,,\, 2.2 \times 10^{-9})\,,$$

where the fiducial value of A_s is set to the best fit value of Planck 15 [137]. For the Fisher analysis, we use the angular power spectra with $3 \leq l \leq 600$. Table 5.1 and Table 5.2 show the 1-σ uncertainties of p_i ($i = 1,\, 2$) for the model 1 and the model 2, respectively.

$\nu_2 = 3$	$\sigma(f^{\rm loc}_{\rm NL})$	$\sigma(\bar{b}^{\rm I}_{\rm NG} A_2)$	$\nu_2 = 6$	$\sigma(f^{\rm loc}_{\rm NL})$	$\sigma(\bar{b}^{\rm I}_{\rm NG} A_2)$
$\Theta_2 = 0$	1.9	7.5×10^3	$\Theta_2 = 0$	1.9	2.1×10^4
$\Theta_2 = \pi/2$	1.9	7.1×10^3	$\Theta_2 = \pi/2$	1.9	2.5×10^4

TABLE 5.1: 1-σ uncertainties of the non-Gaussian parameters A_0 and $\bar{b}^{\rm I}_{\rm NG} A_2$ for the model 1 with the other parameters fully marginalized. The parameter ν_2 was set to $\nu_2 = 3$ (Left) and $\nu_2 = 6$ (Right). Here, considering an LSST-like measurement, we set $z_{*\,a}$ with $a = {\rm I},\, {\rm G}$ as $z_{*\,{\rm I}} = z_{*\,{\rm G}} = 0.51$. Adjusting to the convention, we used $f^{\rm loc}_{\rm NL}$, which is related to A_0 as $f^{\rm loc}_{\rm NL} = A_0/4$.

$\nu_{0,2} = 3$	$\sigma(A_0)$	$\sigma(\bar{b}^{\rm I}_{\rm NG} A_2)$	$\nu_{0,2} = 6$	$\sigma(A_0)$	$\sigma(\bar{b}^{\rm I}_{\rm NG} A_2)$
$\Theta_{0,2} = 0$	3.5×10^3	1.0×10^4	$\Theta_{0,2} = 0$	7.4×10^3	3.1×10^4
$\Theta_{0,2} = \pi/2$	4.3×10^3	1.0×10^4	$\Theta_{0,2} = \pi/2$	8.7×10^3	3.7×10^4

TABLE 5.2: The same as Table 5.1 for the model 2. The parameter ν_0 and ν_2 were set to $\nu_0 = \nu_2 = 3$ (Left) and $\nu_0 = \nu_2 = 6$ (Right). For simplicity, we choose the same value for the phases Θ_0 and Θ_2.

In order to examine a possible degeneracy among the non-Gaussian parameters, we also compute a partially marginalized bound on the parameters $p_i (i = 1,\, 2)$, using the submatrix $(\mathbf{F}^{-1})_{i=[1,2],j=[1,2]}$. Here, we marginalize only over the parameters $\{b^{(0)}_\delta,\, \bar{b}^{\rm I}_1,\, A_s\}$. The result is in Fig. 5.11. As is shown in the left panel, there is almost no degeneracy between $f^{\rm loc}_{\rm NL}$ and $\bar{b}^{\rm I}_{\rm NG} A_2$. This is because $f^{\rm loc}_{\rm NL}$ contributes to low ls, but $\bar{b}^{\rm I}_{\rm NG} A_2$ contributes to high ls. On the other hand, as is shown in the right panel, there is some degeneracy between A_0 and $\bar{b}^{\rm I}_{\rm NG} A_2$, because both of them contribute to high ls[7].(A correlation between the PNGs from fields with different spins was discussed in Ref. [139].)

The constraint on A_0 with $\nu_0 = \Theta_0 = 0$, so no oscillatory feature, was discussed in Ref. [140], including also the non-linear loop corrections. As is shown in Fig. A.2, the enhancement due to the PNG becomes less significant for a larger value of ν_s, since

---

[7] Our constraint on $f^{\rm loc}_{\rm NL}$ is much tighter than the one in Ref. [41]. This is mainly because our redshift distribution $dN_{\rm n}/dz$ extends to higher redshift region than the one used in Ref. [41]. In fact, when we use the redshift distribution for LSST red samples [138] and set $\bar{n}_{\rm I}$, $\bar{n}_{\rm G}$ and $\bar{n}_{\rm n}$ to the values used in Ref. [41], i.e., $\bar{n}_{\rm I} = \bar{n}_{\rm G} = 3$ and $\bar{n}_{\rm n} = 26$, we obtain $\sigma(f^{\rm loc}_{\rm NL}) = 8.3$, $\sigma(\bar{b}^{\rm I}_{\rm NG} A_2) = 3.0 \times 10^3$ for $\nu_2 = 3$ and $\Theta_2 = 0$. Now, $\sigma(f^{\rm loc}_{\rm NL}) = 8.3$ is almost same as the one in Ref. [41].

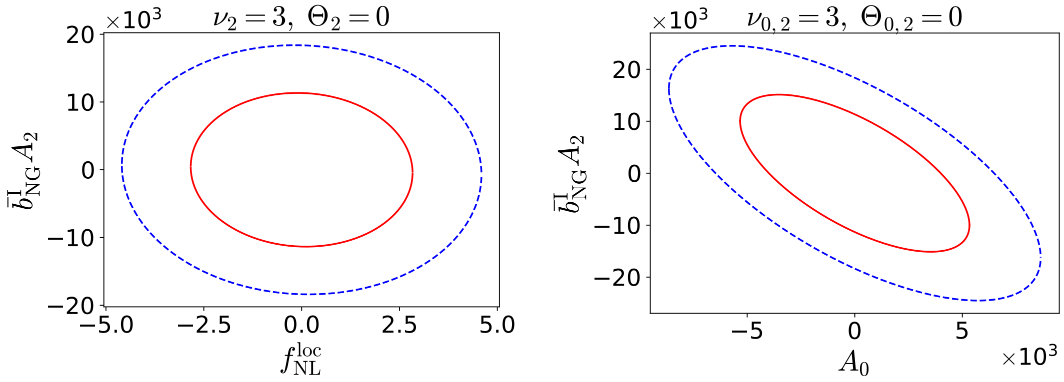

FIGURE 5.11: These plots show 1-σ and 2-σ uncertainties in the non-Gaussian parameters A_0 and $\bar{b}^{\rm I}_{\rm NG}A_2$, when we marginalize over $\{b_\delta^{(0)}, \bar{b}^{\rm I}_1, A_s\}$. The red solid lines show the 1-σ contours and the blue dotted lines show the 2-σ contours. The left panel is the model 1 (with $\Delta_0 = \nu_0 = \Theta_0 = 0$ and the right one is the model 2 (with $\mathrm{Re}[\Delta_0] = 3/2$). Other parameters are set to $\mathrm{Re}[\Delta_2] = 3/2$, $\nu_2 = 3$, $\Theta_2 = 0$ (Left) and $\mathrm{Re}[\Delta_0] = \mathrm{Re}[\Delta_2] = 3/2$, $\nu_0 = \nu_2 = 3$, $\Theta_0 = \Theta_2 = 0$ (Right).

the oscillatory contribution is more smoothed out by integrating over k. Because of that, constraints for $\nu_0 = \nu_2 = 6$ become weaker than those for $\nu_0 = \nu_2 = 3$.

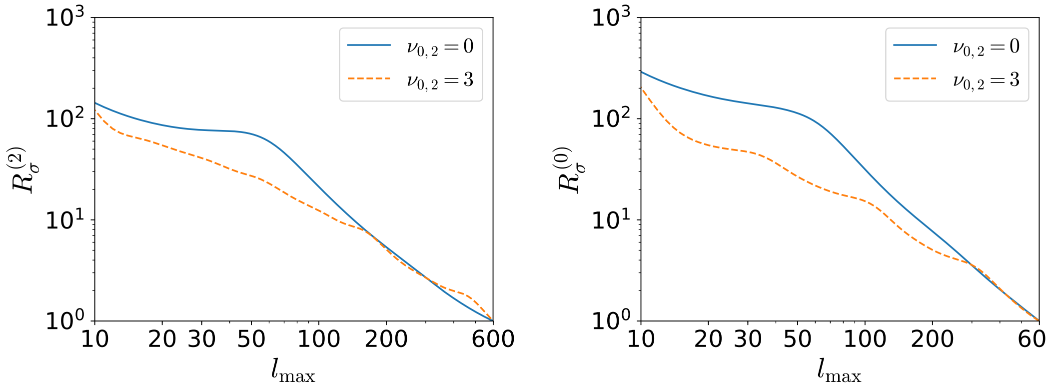

FIGURE 5.12: The left and right panels show $R_\sigma^{(2)}$ and $R_\sigma^{(0)}$, respectively, which are defined in Eq. (5.121). The blue solid lines show the case with $\nu_0 = \nu_2 = 0$ and the orange dotted lines show the case with $\nu_0 = \nu_2 = 3$. For both cases, we set $\Theta_0 = \Theta_2 = 0$.

When $\mathrm{Re}[\Delta_s]$ with $s = 0, 2$ are $3/2$, the dominant signals of the PNG come from the small scales with $k > k_{\rm eq}$. Therefore, the possible constraints on the non-Gaussian parameters are highly sensitive to $k_{\rm max}$ or $l_{\rm max}$. In Fig. 5.12, to see the $l_{\rm max}$ dependence of 1-σ uncertainty, we plotted

$$R_\sigma^{(s)} \equiv \frac{\sigma_{3\le l\le l_{\rm max}}(x_s)}{\sigma(x_s)} \qquad s = 0,\, 2\,, \tag{5.121}$$

with $x_0 = A_0$ and $x_2 \equiv \bar{b}^{\mathrm{I}}_{\mathrm{NG}} A_2$. Here, $\sigma_{3 \le l \le l_{\max}}(x_s)$ denotes the 1-σ uncertainty when we only use $3 \le l \le l_{\max}$, i.e., $\sigma(x_s) = \sigma_{3 \le l \le 600}(x_s)$. For both $s = 0$ and $s = 2$, $R^{(s)}_{\sigma,\max}$ does not change much until around $l_{\max} = 100$ and it significantly drops for $l_{\max} \gtrsim 100$, approaching to 1.

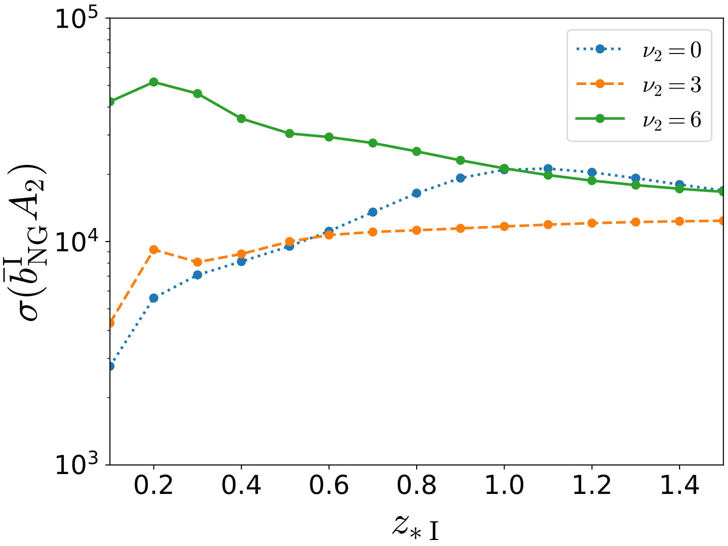

FIGURE 5.13: This plot shows how the 1-σ uncertainty of $\bar{b}^{\mathrm{I}}_{\mathrm{NG}} A_2$ changes under a variation of $z_{*\mathrm{I}} = z_{*\mathrm{G}}$ for different values of ν_2. Here, we chose $\Theta_2 = 0$.

The forecast of 1-σ uncertainties in the non-Gaussian parameters also depends on the redshift distribution of galaxies dN/dz.

Figure 5.13 shows a change of the 1-σ uncertainty for the parameter $\bar{b}^{\mathrm{I}}_{\mathrm{NG}} A_2$ under a variation of $z_{*\mathrm{I}}(= z_{*\mathrm{G}})$. As we change $z_{*\mathrm{I}}$ to a smaller value, the peaks of the linear spectra shift to lower multipoles, leaving more spaces for the PNG with $\mathrm{Re}[\Delta_s] > 0$ to exhibit the signal at the high multipoles. Because of that, a galaxy survey that explores lower redshift tends to give a tighter constraint if it were to be no oscillation (see the plot with $\nu_2 = 0$). Notice however that $\sigma(\bar{b}^{\mathrm{I}}_{\mathrm{NG}} A_2)$ does not monotonically decrease as we decrease $z_{*\mathrm{I}}$ in the presence of the oscillation, i.e., $\nu_2 \neq 0$. It is because depending on the phase Θ_2, the oscillation can reduce the signal of the PNG at the high multipoles at which the contribution from the PNG can dominate the linear contributions.

In the present analysis, we only considered a single tracer and integrated over the whole redshift distribution of galaxies, losing the information about modes along the line of sight (see also the discussion in Ref. [41]). Therefore, using tomographic information for multi tracers will improve our constraints on the non-Gaussian parameters. (For a multi-tracer analysis with $\Delta_2 = \nu_2 = 0$, see [129]. See also Ref. [83].)

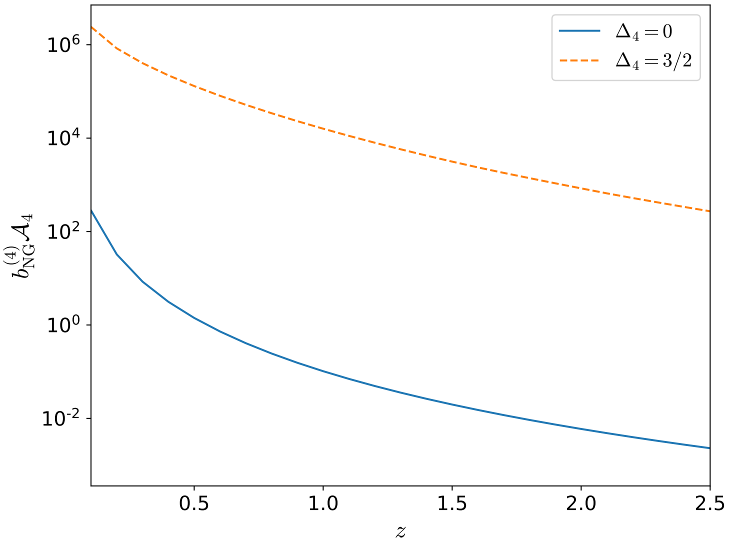

FIGURE 5.14: This plot shows the amplitude of the PNG $b_{\rm NG}^{(4)} A_4$ which is required for a detection with S/N $= 5$ by a survey covering a fraction $f_{\rm sky} = 0.5$ of the sky when including scales up to $l_{\rm max} = k_{\rm NL}(z)\chi(z)$. The blue solid line corresponds to $\Delta_4 = 0$ and the orange dotted line corresponds to $\Delta_4 = 3/2$.

Spin-4 case

As discussed in Sec. 5.2.2, since the dominant contamination to the $s = 4$ signal at $k < k_{\rm NL}$ comes from NLA, in the following, we ignore the contributions of the linear alignment and weak lensing. The signal to noise ratio (S/N) for each redshift, which is not cumulative, is expressed by

$$[{\rm S/N}]^2(z) \sim f_{\rm sky} \sum_{l=4}^{l_{\rm max}} (2l+1) \left[\frac{C^{(4,4){\rm PNG}}(l,z)}{C^{(4,4){\rm PNG}}(l,z) + C^{(4,4){\rm NLA}}(l,z)} \right]^2 , \qquad (5.122)$$

where $f_{\rm sky}$ is the sky fraction to the galaxy imaging survey and $C^{(4,4){\rm NLA}}(l,z)$ denotes the NLA contribution which is crudely estimated by using Eq. (5.66). Here, we have discarded the contribution from the non-linear scales, setting $l_{\rm max} = k_{\rm NL}(z)\chi(z)$.

For $\Delta_4 = 0$ (without dilution), S/N becomes independent of $l_{\rm max}$ when we choose a sufficiently large $l_{\rm max}$, since the shape signal of PNG is significant at the large scales. On the other hand, for ${\rm Re}[\Delta_4] = 3/2$ (with dilution), since the signal dominates the shape noise only at the small scales, S/N depends on the choice of $l_{\rm max}$. However, since we cannot selectively single out the contribution of the spin-4 particle, we expect that increasing $l_{\rm max}$ will not improve the actual S/N very much. Meanwhile, the forecast depends on $k_{\rm NL}$, which determines the scales at which the PNG can be selectively detected. The amplitude of the PNG $b_{\rm NG}^{(4)} A_4$ needs to be roughly factor 4 larger for a detection, when we choose $k_{{\rm NL},z=0} = 0.1h/{\rm Mpc}$.

Using Eq. (5.122) we can compute the corresponding amplitude of the PNG which can be detected for a given S/N. Figure 5.14 shows the amplitude of $b_{\rm NG}^{(4)} A_4$ which is detectable with S/N $= 5$ for a survey covering a fraction $f_{\rm sky} = 0.5$ of the sky up to redshift z. The increasing volume and number of modes available at higher redshift lead to improved constraints. Further, as discussed in Sec. 5.5.1, since the NLA contribution is smaller at higher redshifts while the PNG contribution remains constant, we find that the high redshift survey works in favor of PNG detection.

Chapter 6

Conclusion

We have investigated the contributions of the PNGs on the galaxy shape correlations for future galaxy imaging surveys, focusing specifically on the angular-dependent PNGs. First, we have prepared galaxy shape functions for arbitrary moments through the shape moment decomposition of the galaxy shapes. Moreover, for the observational analysis, we have generalized the angular power spectrum by using the conventional cosmic shear analysis to arbitrary spin components of galaxy shape functions, assuming that the leading term for shape functions is the matter density fluctuation. Under this assumption, only the E-mode is generated since we perform the spin-decomposition on a linear scalar field as a matter density field. This is useful for shape analysis on the sky by using the photo-z samples.

In order to distinguish between a signal of new physics through PNGs and other contributions, we need to understand the predictions of the galaxy shape correlations in the concordance cosmology. Assuming ΛCDM cosmology with the Gaussian initial condition, which is a representative model of our Universe, we have estimated the contributions of the linear and non-linear alignments, derived from the external tidal fields, and the contributions of the linear and non-linear weak lensing to the nth shape moment. The estimation of these contributions is necessary to test whether the contribution of PNGs produces significant changes compared to these potentially emerging signals. In the case of the 2nd moment galaxy shape, which corresponds to the usual cosmic shear, the contributions both of the linear weak lensing and the linear alignment mainly contaminate the signals of the new physics. Meanwhile, in the case of the higher galaxy shape moment with $n > 2$, the linear contributions, including the weak lensing distortion, are suppressed by a positive power of $k/k_* \ll 1$, where k_* is the reference scale. These suppressions lead to the dominant contaminations from loop contributions through the non-linear alignment. We have investigated the contributions of the non-linear alignments by the estimation of these loop contributions with the self-similarity solutions.

This thesis focuses on the angular-dependent PNGs generated through the integer spin particles during inflation. We have found that under an ideal galaxy imaging survey, the different galaxy shape moments can supply the imprints of new particles with different spins separately. However, the detection of the separate imprints of spin particles only works on the larger scales than the non-linear scale $k_{\rm NL}$. This is because the contamination from the loop contributions contains the angular dependence by different spins through the kernel functions.

Specifically, we have investigated the effects of the angular-dependent PNGs, including the different scalings as $\Delta_s = 0$ and $\mathrm{Re}[\Delta_s] = 3/2$, for the 2nd moment and the 4th moment shapes. As mentioned above, the 2nd moment shape is greatly affected by the linear alignment and the weak lensing, while the 4th moment shape is influenced by non-linearity effects. The effects of angular-dependent PNGs are the same in both cases. The contribution of $\Delta_s = 0$ appears on a large scale while that of $\mathrm{Re}[\Delta_s] = 3/2$ appears on a small scale. In the former case, the cosmic variance can be problematic for its detection of the PNGs. However, as one possible solution, the multi-tracers technique, which uses not only red galaxies responding to the external tidal fields but also blue galaxies, has the potential to improve the cosmic variance [129]. On the other hand, in the case of $\mathrm{Re}[\Delta_s] = 3/2$, though the cosmic variance is not an essential issue of the detection of the signal of PNGs, the non-linearity contamination from the loop contributions appears. It leads to mixing the contributions of the different spins and the contamination from the Gaussian perturbation due to the time-evolution. However, the imprints of the oscillatory feature not just scaling may allow us to distinguish other contributions.

We also have studied the forecast of the constraints on the amplitude of PNGs assuming an LSST-like survey. For practical forecasts, we need to consider the shape noise. Although the shape noise for the 2nd moment shape was estimated based on LSST, the shape noise for the 4th moment is still unknown. Instead, for rough estimation, we have used the contribution of k^0 from the large scale limit ($k \to 0$) of the loop contribution of the non-linear alignment[1]. As a result, we have found that the deeper galaxy imaging survey can detect the $\mathcal{O}(1)$ amplitude of the PNGs with the scaling of $\Delta_s = 0$. Meanwhile, detecting the PNGs with $\mathrm{Re}[\Delta_s] = 3/2$ is rather challenging. This is because the PNGs contribution appears at smaller scales.

We have considered another case of angular-dependent PNGs with global anisotropy. Examining this case gives us whether the signal from the angular-dependent PNGs generated by spin-particles, which have the property of the global rotational symmetry, is unique or not. We have found that the distinctive contributions of the angular dependent PNGs which violates the global rotational symmetry to galaxy shapes are as follows; i) Non-zero B-mode signal, ii) Correlations between different multipoles l, iii) Azimuthal dependence of angular spectra. These differences help distinguish the PNGs with the global anisotropy and the one with global isotropy.

As for future works, the use of the biased tracers such as the galaxy density and the galaxy shapes causes the bias from the long-wavelength mode perturbation and the amplitude of the PNGs to degenerate. For the galaxy bias, though we can solve the degeneracy of bias analytically by using the peak theory, there is no such theory for the galaxy shapes. In order to extract the actual amplitude of the PNGs, we also need to solve these degeneracies through a theoretical approach for the galaxy

---

[1] Note that we need to renormalize the loop contribution on the large scales with the noise terms.

shape bias. The degeneracy in the 2nd moment has recently been approached from N-body simulation [42]. A similar method may be useful for the 4th moment. In addition, it may be beneficial to estimate the more realistic shape noise of higher-order shape moments. However, it may be challenging to investigate the PNGs induced by spin-4 in N-body simulations using the commonly used TreePM method. This is because even if the spin-4 contribution is implemented in the initial conditions, it may not reflect the effects of contributions above the third-order derivative as long as the Poisson equation is used. This requires either ingenious calculations or direct gravitational interaction calculations.

Appendix A

Angular power spectra for number density and 2nd moment shape

In this appendix, using Eqs. (5.64) and (5.103), we numerically compute the angular power spectra for the perturbation of the number density and the 2nd moment shape (cosmic shear). Here, we adopt the Limber approximation [141, 142] for $l \geq 60$.

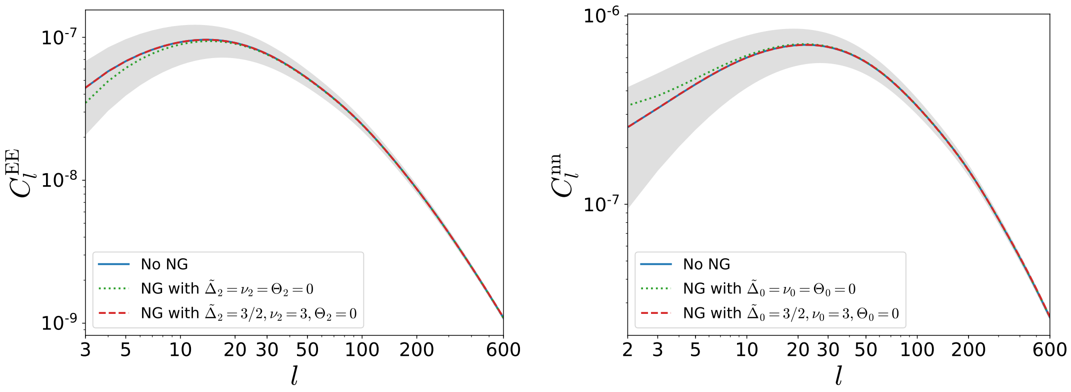

FIGURE A.1: These plots show the angular auto-power spectra $C_l^{\mathrm{EE}}(C_l^{(2,2)})$ (Left) and $C_l^{\mathrm{nn}}(C_l^{(0,0)})$ (Right) for initial conditions with different PNGs. The blue solid lines show the case with $\bar{b}^{\mathrm{I}}_{\mathrm{NG}}A_2 = 0$ (Left) and $A_0 = 0$ (Right), including the Gaussian initial condition. In the left panel, the green dotted line shows the case with $\bar{b}^{\mathrm{I}}_{\mathrm{NG}}A_2 = 100$ and $\Delta_2 = \nu_2 = \Theta_2 = 0$ and the red dashed line shows the case with $\bar{b}^{\mathrm{I}}_{\mathrm{NG}}A_2 = 8 \times 10^3$, $\mathrm{Re}[\Delta_2] = 3/2$, $\nu_2 = 3$, and $\Theta_2 = 0$. In the right panel, the green dotted line shows the case with $A_0 = 10$ and $\Delta_0 = \nu_0 = \Theta_0 = 0$ and the red dashed line shows the case with $A_0 = 8 \times 10^3$, $\mathrm{Re}[\Delta_0] = 3/2$, $\nu_0 = 3$, and $\Theta_0 = 0$. The shaded regions show the noise due to the cosmic variance computed for the Gaussian initial condition. Here, we set $z_{*\,\mathrm{I}} = z_{*\,\mathrm{G}} = 0.3$.

The left panel of Fig. A.1 shows the angular spectrum of the E-mode cosmic shear (the 2nd moment shape), given in Eq. (5.103) for three different initial conditions. The blue line shows the case with $A_2 = 0$, which includes the case with the Gaussian initial condition. The green dotted line shows the case with $\bar{b}^{\mathrm{I}}_{\mathrm{NG}}A_2 = 100$ and $\Delta_2 =$

$\nu_2 = \Theta_2 = 0$, which was studied in Ref. [41]. The red dashed line shows the case with $\bar{b}^{\rm I}_{\rm NG} A_2 = 8000$, $\mathrm{Re}[\Delta_2] = 3/2$, $\nu_2 = 3$, and $\Theta_2 = 0$, which can be generated from the massive spin 2 field. Here, we set the (remaining) bias parameters as $b^{(0)}_\delta = 2$, $\bar{b}^{\rm I}_1 = -0.1$, and $\bar{b}^{\rm I}_{\rm NG} = 1$ [41] and the shape distribution as $z_{*\rm I} = z_{*\rm G} = 0.3$. The right panel of Fig. A.1 shows the angular power spectrum of $\delta_{\rm n}$ for the three different initial conditions: $A_0 = 0$ (Blue), $A_0 = 10$, $\tilde{\Delta}_0 = \nu_0 = \Theta_0 = 0$ (Green dotted), and $A_0 = 8000$, $\mathrm{Re}[\Delta_0] = 3/2$, $\nu_0 = 3$, $\Theta_0 = 0$ (Red dashed). The imprint of the PNG with $A_0 \neq 0$ on $C^{\rm nn}_l$ appears in a similar way to the one of the PNG with $A_2 \neq 0$ on $C^{\rm EE}_l$. In Fig. A.1, we set the non-Gaussian parameters $\bar{b}^{\rm I}_{\rm NG} A_2$ and A_0 to those which roughly amount to the 1σ uncertainties obtained in Sec. 5.5.3. The deviations of the cases with $\mathrm{Re}[\Delta_s] = 3/2$ (the red dashed lines) from the Gaussian case (the blue solid lines), which are not visible in Fig. A.1, are manifestly shown in Fig. A.2.

Since $\mathcal{M}(k,\, z)$ scales as k^2 in the limit $k \to 0$, for $\Delta_2 = 0$, the contribution of PNGs becomes larger at larger scales, leading the relative enhancement for small ls. On the other hand, for $\mathrm{Re}[\Delta_2] = 3/2$, the enhancement at the low multipoles are not significant. Instead, the imprint of the PNG becomes more and more significant at higher multipoles. This can be understood as follows. For $k \gg k_{\rm eq}$, where $k_{\rm eq}$ denotes the comoving Hubble scale at the matter-radiation equality and is given by $k_{\rm eq} \simeq 1.6 \times 10^{-2} h/\mathrm{Mpc}$, $\mathcal{M}(z,\, k)$ ceases to depend on k. Therefore, in the range $k \gg k_{\rm eq}$, the PNG contribution (5.103) can dominate the linear term (5.64) for $\mathrm{Re}[\Delta_2] > 0$ and $\mathrm{Re}[\Delta_0] > 0$, respectively. For the higher multipoles on which the information of the modes $k > k_{\rm eq}$ is encoded, using the Limber approximation, we find that the auto-correlations of the contributions from the PNG scale as

$$C^{(2,2),\rm PNG}_l \propto l^{2\mathrm{Re}[\Delta_2]-3+n_{\rm s}-1}\,, \qquad C^{(0,0),\rm PNG}_l \propto l^{2\mathrm{Re}[\Delta_0]-3+n_{\rm s}-1}\,, \tag{A.1}$$

where $n_{\rm s}$ is the spectral index for the adiabatic perturbation. (Here, dropping the oscillatory contributions, we only picked up the powers of l.) Therefore, especially for $\mathrm{Re}[\Delta_s] \simeq 3/2$ with $s = 0, 2$, the contributions from the PNG in the angular spectra stay almost constant at the higher multipoles in contrast to the linear contributions which are suppressed.

To exhibit the enhancements of the contribution from the PNG at the high multipoles more clearly, in Fig. A.2, we plot the fractional changes of $C^{\rm EE}_l$ and $C^{\rm nn}_l$ which quantify the contributions from the PNG as

$$\Delta^\alpha_l \equiv \frac{|C^\alpha_l - C^\alpha_{l,\rm Gauss}|}{C^\alpha_{l,\rm Gauss}} \qquad (\alpha = \mathrm{EE},\, \mathrm{nn})\,, \tag{A.2}$$

where $C^\alpha_{l,\rm Gauss}$ denotes the angular power spectrum computed for the Gaussian initial condition. The different lines show the PNG with the different periodic oscillations and the phases. Notice that there is a phase difference between $\Delta^{\rm EE}_l$ and $\Delta^{\rm nn}_l$ with the same oscillatory period, i.e., $\nu_2 = \nu_0$, and the phase, i.e., $\Theta_2 = \Theta_0$.

In Ref. [140], the modification of the halo bias due to the presence of the PNG

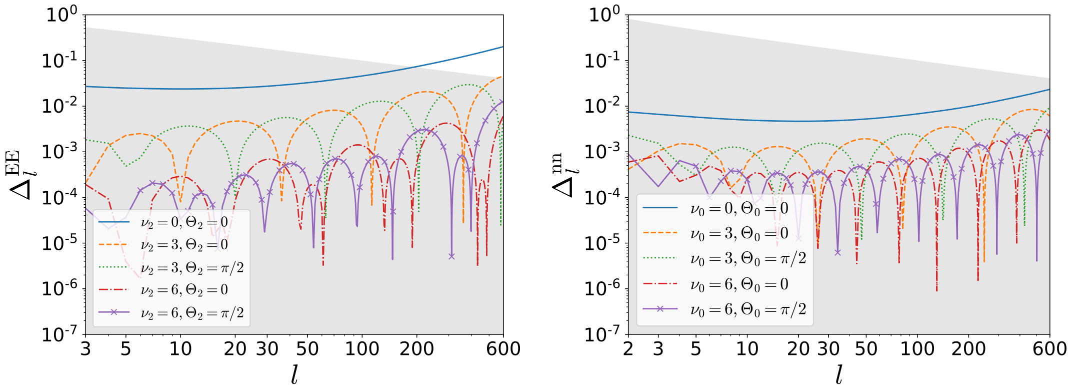

FIGURE A.2: These plots show the fractional changes Δ_l^α, defined in Eq. (A.2), for $\alpha = \text{EE}$ (left) and for $\alpha = \text{nn}$ (Right). The parameters $\text{Re}[\Delta_0]$ and $\text{Re}[\Delta_2]$ are both chosen to be 3/2. In the left panel, $\bar{b}^{\rm I}_{\rm NG} A_2$ is set to $\bar{b}^{\rm I}_{\rm NG} A_2 = 8000$ and in the right panel, A_0 is set to $A_0 = 8000$. The shaded regions show the variance computed by taking into account the cosmic variance. Here, we set $z_{*\,\rm I} = z_{*\,\rm G} = 0.3$.

with $A_0 \neq 0$ and $0 \leq \text{Re}[\Delta_0] \leq 2$ was computed. It was shown that for a larger $\text{Re}[\Delta_0]$, the signal of the PNG appears in the small scales (see also Ref. [143]). Here, we have shown that the signal of the PNG with $A_2 \neq 0$ and $\text{Re}[\Delta_2] = 3/2$ also becomes more prominent at higher multipoles which capture the contributions of the modes $k > k_{\rm eq}$.

For $\Delta_s = 0$, the information of the PNG is encoded in large-scale fluctuations. Therefore, the detection of such a PNG is usually limited by the cosmic variance. On the other hand, for a larger value of $\text{Re}[\Delta_s]$, the situation becomes very different, since the signal of the PNG appears in small scales. For an accurate computation, we need to include non-linear evolution.

Appendix B

Angular dependent PNG with global anisotropy

In this appendix, we discuss the influence of the PNG with global anisotropy to the galaxy shape. Similarly to the case with the angular dependent PNG with the global isotropy (2.64), the angular dependent PNG without the global isotropy, which will be introduced in Sec. B.1, also can deform intrinsic shapes of galaxies. Given that these two different cases are not distinguishable from the power spectrum but the difference shows up only from non-Gaussian correlators such as the bispectrum, can we observationally distinguish these two cases? If this is not possible, the enhanced cosmic shear due to the intrinsic alignment cannot be a unique signal which shows the presence of massive fields with the spin $s \geq 2$ in the early universe. We will address this question in the succeeding sections.

B.1 PNG with global anisotropy

In order to assert that the enhanced intrinsic alignment is a unique signal of such spinning fields, the signal has to be distinguishable from those generated by other sources. As an example, let us consider a PNG given by

$$\bar{B}_\Psi(\boldsymbol{k}_\mathrm{L},\, \boldsymbol{k}_\mathrm{S};\, \hat{\boldsymbol{p}}) = \sum_{l=0}^{\infty} \left[\bar{A}_l + \bar{B}_l\, \hat{\boldsymbol{k}}_\mathrm{L} \cdot \hat{\boldsymbol{k}}_\mathrm{S} + \cdots\right] i^{\frac{1-(-1)^l}{2}}\, \mathcal{P}_l(\hat{\boldsymbol{p}} \cdot \hat{\boldsymbol{k}}_\mathrm{S}) P_\Psi(k_\mathrm{L}) P_\Psi(k_\mathrm{S})\,, \quad \text{(B.1)}$$

where l sums over all non-negative integers. In addition to the terms which depend on the angle between $\boldsymbol{k}_\mathrm{L}$ and $\boldsymbol{k}_\mathrm{S}$, the bispectrum $\bar{B}_\Psi$ also contains the terms which depend on the constant unit vector $\hat{\boldsymbol{p}}$. While the global rotational symmetry is preserved in Eq. (2.64), it is not the case for $\bar{B}_\Psi$. In the square brackets, we abbreviated terms with more powers of $\hat{\boldsymbol{k}}_\mathrm{L} \cdot \hat{\boldsymbol{k}}_\mathrm{S}$. The coefficients $\bar{A}_l$ and $\bar{B}_l$ do not depend on $\hat{\boldsymbol{k}}_\mathrm{S}$, but can depend on k_L, k_S, and $\hat{\boldsymbol{k}}_\mathrm{L} \cdot \hat{\boldsymbol{p}}$.

The PNG (B.1), which depends on the constant vector can be generated, when the primordial curvature perturbation is also sourced by a vector field (see e.g., Refs. [99, 144]). Even if the contribution from the vector field, which breaks the global rotational symmetry, is suppressed in the power spectrum, being compatible with the current CMB observations [3, 145], it is not necessarily suppressed also in the higher-point functions. (The global anisotropy in the galaxy and CMB spectra was studied e.g., in Refs. [146, 147, 148].) This possibility was explored in Ref. [99] and claimed that this is in fact possible in the presence of an enhanced cubic interaction. (See also Refs. [78, 149].)

B.2 PNG contribution to galaxy shape function

We consider the PNG (B.1) with a violation of the global rotational symmetry, which may be sourced from a vector field during inflation. Repeating a similar computation in Sec. 5.4.1, we find that the PNG (B.1) yields the following contributions in the galaxy shape function $\tilde{g}_{ij}$:

$$\tilde{g}_{ij} \propto \left(\hat{p}_i\hat{p}_j - \frac{1}{3}\delta_{ij}\right)\Psi\,, \quad \left(\hat{p}_i\partial_j + \hat{p}_j\partial_i - \frac{2}{3}\delta_{ij}\hat{p}^k\partial_k\right)\Psi\,, \quad \cdots\,, \tag{B.2}$$

which breaks the global rotational symmetry. The computation becomes somewhat lengthy and is summarized in Appendix D.5.1.

Including a typical contribution of the intrinsic alignment in the presence of the global anisotropy, here, we consider the case where the galaxy shape function is given by

$$\begin{aligned}\tilde{g}_{ij}(\boldsymbol{x}, z) = \int \frac{d^3\boldsymbol{k}}{(2\pi)^3}\, e^{i\boldsymbol{k}\cdot\boldsymbol{x}} \Bigg[& b_K^{(2)}\left(\hat{k}_i\hat{k}_i - \frac{1}{3}\delta_{ij}\right)\delta(z,\, \boldsymbol{k}) \\ & + 3b^p_{\rm NG}\bar{A}_2\left(\frac{k}{k_*}\right)^{\Delta_p}\left(\hat{p}_i\hat{p}_j - \frac{1}{3}\delta_{ij}\right)\Psi(\boldsymbol{k})\Bigg]\,,\end{aligned} \tag{B.3}$$

where $b^p_{\rm NG}$ denotes the bias parameter after the renormalization. (Here, we introduced the factor 3 for the non-Gaussian contribution, adjusting to the notation in Sec. 5.4.1) For instance, when the primordial bispectrum is given by Eq. (B.1) with $\bar{A}_2 \neq 0$ and $\bar{B}_2 = \mathcal{O}((k_{\rm L}/k_{\rm S}))$, the leading contribution of $\tilde{g}_{ij}$ takes the form of Eq. (B.3).

Meanwhile, any galaxy surveys can probe only a finite spatial region in the universe. Because of that, even if the primordial bispectrum preserves the global isotropy, the limitation of the survey region can lead to an apparent anisotropic clustering of galaxy distributions, depending on the shape of the survey region [150] (see also Ref. [151]).

In the following, considering $\tilde{g}_{ij}$ given by Eq. (B.3) without specifying the origin of the global anisotropy therein, we consider its observable imprints on the cosmic shear. We assume the power spectrum of Ψ with the global isotropy. (According to Ref. [99], the global anisotropy appears only from the bispectrum in a certain parameter range of the model.)

Following Sec. 5.1, we obtain the coefficient $a^{\rm IA}_{lm}$ for the expansion series of the intrinsic galaxy shear in terms of the spin weighted spherical harmonics as

$$a^{\rm IA}_{lm} = 2\pi\sqrt{\frac{(l+2)!}{(l-2)!}}\int\frac{d^3\boldsymbol{k}}{(2\pi)^3}\delta(\boldsymbol{k})\sum_{s=-2}^{2}F^{{\rm IA},(s)}_{l,m}(k)i^{l+s}Y^{*}_{l+s,\,m}(\hat{\boldsymbol{k}})\,, \tag{B.4}$$

where $\delta(\boldsymbol{k})$ is the matter perturbation at present and $F^{{\rm IA},(s)}_{l,m}(k)$ is given by

$$F^{{\rm IA},(s)}_{l,m}(k) \equiv \int dz\frac{dN_{\rm I}}{dz}\frac{D(z)}{D(0)}j_{l+s}(x) \times\left[-\frac{b^{(2)}_K}{x^2}\delta_{s,0}+3b^{p}_{\rm NG}\bar{A}_2\left(\frac{k}{k_*}\right)^{\Delta_p}\mathcal{M}^{-1}(z,\,k)\frac{(l-2)!}{(l+2)!}\alpha^{(s)}_{l,m}\right]. \tag{B.5}$$

The detailed computation and the expression of $\alpha^{(s)}_{l,m}$ are summarized in Appendix D.5.2. Notice that the violation of the global rotational symmetry leads to the contamination of the different multipoles $l+s$ with $s=\pm1,\,\pm2$. The first term in the square brackets of Eq. (B.5) is the contribution which preserves the global rotational symmetry and the second term is the one which does not. The overall factor of the second term has the typical form of the scale dependent bias.

Notice that for the present pattern of the symmetry breaking, all of $\alpha^{(s)}_{l,\,m}$ vanish for $l=0$ and $l=1$. Therefore, the lowest multipole of the cosmic shear is still $l=2$. Also notice that $\alpha_{l,\,m}$ takes a different value, depending on the value of m, and in particular, we find

$$\alpha^{(s)}_{l,\,-m}=\alpha^{(s)}_{l,m}\quad(s=0,\,\pm2)\,,\qquad \alpha^{(s)}_{l,\,-m}=-\alpha^{(s)}_{l,m}\quad(s=\pm1)\,. \tag{B.6}$$

In doing the harmonic expansion, we defined the z axis (with the colatitude angle $\theta=0$) to be along the constant vector $\hat{\boldsymbol{p}}$. Some of the properties described here are specific for this coordinate choice (see Appendix D.5.2).

B.3 Angular power spectrum

Using $a^{\rm IA}_{lm}$, given in Eq. (B.4), now we can compute the angular power spectrum of the cosmic shear. The second term in the left-hand side of Eq. (B.3) only contributes to the intrinsic alignment, leaving the perturbation of the number density and the gravitational lensing shear intact. Therefore, simply changing the contribution of the galaxy alignment into Eq. (B.4) in the computation of the previous section, we can obtain the angular power spectra as

$$\langle a^{X}_{lm}a^{Y\,*}_{l'm'}\rangle = C^{XY}_{l,l';m}\delta_{m,\,m'}\,, \tag{B.7}$$

where $X,\,Y={\rm n,\,E,\,B}$. Since the galaxy alignment has sensitivity to the direction of the constant vector field $\boldsymbol{p}$, the B-mode cosmic shear takes a non-vanishing value.

For instance, the auto-correlation of the B-mode is given by

$$C^{\rm BB}_{l,l';m} = \frac{1}{2\pi}\sqrt{\frac{(l-2)!}{(l+2)!}}\sqrt{\frac{(l'-2)!}{(l'+2)!}}\,(3b^{p}_{\rm NG}\bar{A}_2)^2 \sum_{s=\pm1}\sum_{s'=\pm1}\delta_{l+s,\,l'+s'}\alpha^{(s)}_{l,m}\alpha^{(s')}_{l',m}$$
$$\times\int dz\frac{dN_{\rm I}}{dz}\int dz'\frac{dN_{\rm I}}{dz'}\int dk k^2\, j_{l+s}(k\chi(z))j_{l'+s'}(k\chi(z'))\left(\frac{k}{k_*}\right)^{2\Delta_p}P_\phi(k). \quad \text{(B.8)}$$

Since the weak lensing contribution disappears at linear order, the B-mode cosmic shear only appears from the intrinsic galaxy alignment. (The weak lensing effect beyond Born approximation generates the BB correlation [152].)

Except for $X = Y = {\rm n}$, on which the violation of the global rotational symmetry does not affect, $C_{l,l';m}$ has non-diagonal components on l. This is summarized in Table B.1. We find that the auto-correlations $C^{\rm EE}_{l,l';m}$ and $C^{\rm BB}_{l,l';m}$ and the cross-correlation $C^{\rm nE}_{l,l';m}$ take non-vanishing values, when $l-l'$ are even numbers. On the other hand, the cross-correlations $C^{\rm EB}_{l,l';m}$ and $C^{\rm nB}_{l,l';m}$ take non-vanishing values, when $l-l'$ are odd numbers. This is because $a^{\rm E}_{lm}$ consists of the density perturbation with l, $l\pm2$ and $a^{\rm B}_{lm}$ consists of the one with $l\pm1$. As discussed in Sec. 5.1.1, even if there exists off-diagonal component, the parity of these correlations is conserved. For $a^{\rm n}_{lm}$, there is no mode coupling between different multipoles.

l'	$l-4$	$l-3$	$l-2$	$l-1$	l	$l+1$	$l+2$	$l+3$	$l+4$
$C^{\rm EE}_{l,l';m}$	Red (solid)	0	Green (dashed)	0	Blue (dotted)	0	Red (dot-dashed)	0	Green (cross)
$C^{\rm EB}_{l,l';m}$	0		0		0		0		0
$C^{\rm BB}_{l,l';m}$	0	0	Red (solid)	0	Green (dashed)	0	Blue (dotted)	0	0
$C^{\rm nE}_{l,l';m}$	0	0		0		0		0	0
$C^{\rm nB}_{l,l';m}$	0	0	0		0		0	0	0

TABLE B.1: For the components which identically vanish, we put 0, otherwise non-zero. The modes with colour descriptions are shown in those colours in Fig. B.2, which shows the auto-correlations of the E-mode and the B-mode.

Figure B.1 shows the auto-correlations of the E-mode and the B-mode, when the PNG is given by Eq. (2.64) with $\bar{A}_2 \neq 0$ and $\bar{B}_2 = \Delta_p = 0$. In this case, the galaxy shape function is given by Eq. (B.3) with $\Delta_p = 0$. For a comparison, we also plotted the angular spectra for the Gaussian initial condition and also for the PNG (2.64), which preserves the global rotation symmetry, with $A_2 \neq 0$ and $\Delta_2 = \nu_2 = \Theta_2 = 0$. In this computation, we choose the bias parameters as Eq. (5.117) and $b^p_{\rm NG} = \bar{b}^p_{\rm NG}\,\bar{b}^{\rm I}_1\,\Omega_{\rm m0}$ with $\bar{b}^{\rm I}_1 = -0.1$. Here, other bias parameters are irrelevant. The PNG (B.1) leads to the enhancement of the E-mode at large scales likewise the PNG (2.64) with $\Delta_2 = 0$. Because of the parity violation in the galaxy alignment, the B-mode takes a non-vanishing value and is enhanced especially at low multipoles.

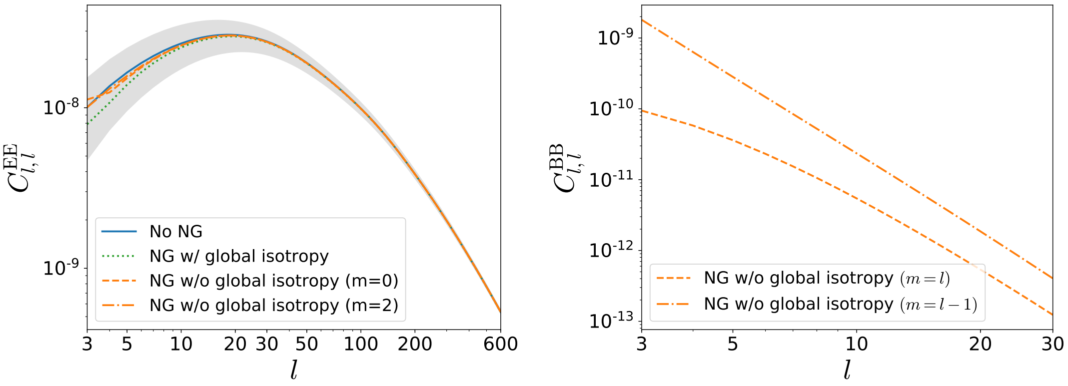

Figure B.1: The left panel shows the E-mode cosmic shear and the right panel shows the B-mode cosmic shear for three cases; the blue solid line shows the case with the Gaussian initial condition, the green dotted line shows the case with the PNG (2.64) with $A_2 \neq 0$ and $\Delta_2 = \nu_2 = \Theta_2 = 0$, and finally the orange dashed and dot-dashed lines show the case with the PNG (B.1) with $\bar{A}_2 \neq 0$ and $\bar{B}_2 = \Delta_p = 0$. The non-Gaussian parameters are set to $\bar{b}^{\rm I}_{\rm NG} A_2 = \bar{b}^{p}_{\rm NG} \bar{A}_2 = 100$. In the first two cases, the global rotational symmetry is preserved, while it is broken in the last one. The angular power spectra for the PNG (B.1) has the non-diagonal components of l and the azimuthal dependence. Here, we only plot the power spectra with $l = l'$. We plotted $m = 0$ and $m = 2$ for the E-mode and $m = l$ and $m = l - 1$ for the B-mode. Here, we set $z_{*\rm I} = z_{*\rm G} = 0.51$.

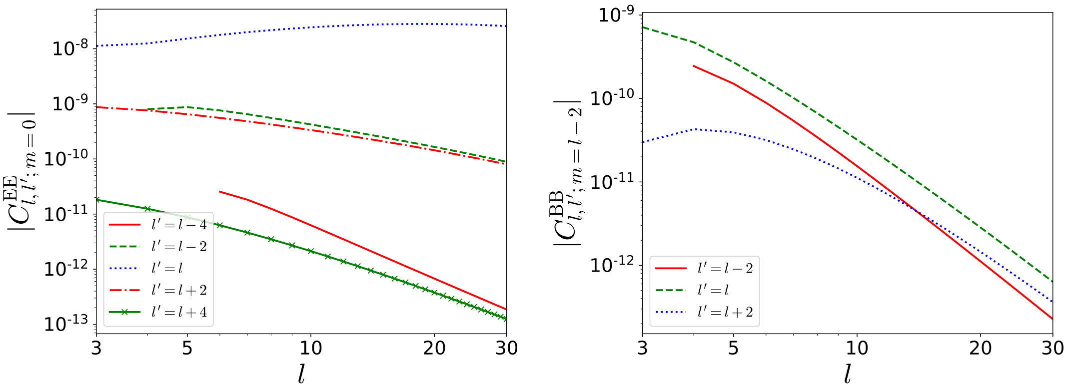

Figure B.2: The angular power spectra of the E-mode (Left) and the B-mode (Right) for the diagonal and non-diagonal components. The left panel is the E mode auto-correlation with $m = m' = 0$. The right one is the B mode auto-correlation with $m = m' = l - 2$. The non-Gaussian parameters are set to $\bar{b}^{\rm I}_{\rm NG} A_2 = \bar{b}^{p}_{\rm NG} \bar{A}_2 = 100$. Here, we set $z_{\rm I} = z_{*\rm G} = 0.51$.

Figure B.2 shows the angular power spectra of the E-mode and the B-mode for the diagonal and non-diagonal components of ls. For the E-mode, we find that the diagonal component with $l = l'$ takes a larger amplitude than the non-diagonal components with $l - l' = \pm 2$ and $l - l' = \pm 4$ and among the non-diagonal components, the former takes a larger amplitude than the latter. This can be understood by focusing on the contributions of the linear alignment term and the lensing term. They do not contribute to $C^{\rm EE}_{l,l';m}$ with $l - l' = \pm 4$ and contribute to the one with $l - l' = \pm 2$ only as the cross-correlation with the term from the PNG.

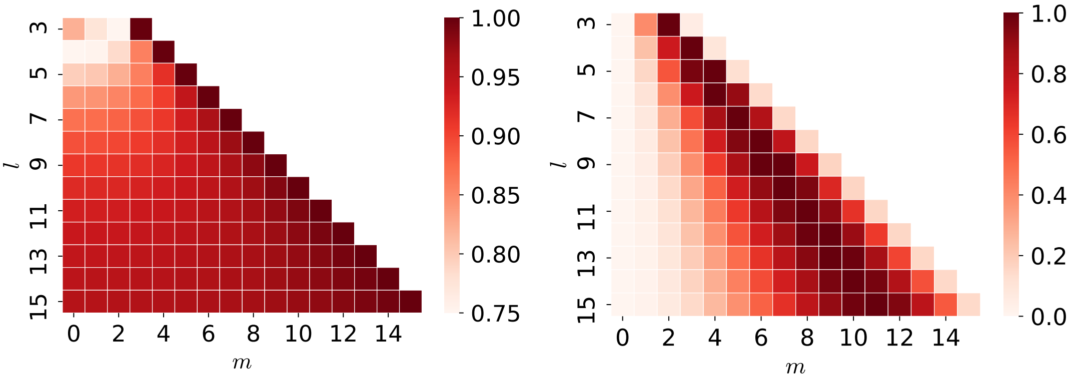

FIGURE B.3: The left panel shows the azimuthal dependence for $C^{\rm EE}_{l,l;m'}$ and the right one shows the same for $C^{\rm BB}_{l,l;m'}$. Here, the angular power spectra are normalized by the maximum values for each l. Here, we set $z_{*{\rm I}} = z_{*{\rm G}} = 0.51$.

As another consequence of the violation of the global rotational symmetry, the angular power spectra (other than $C^{\rm nn}$) take different values for different ms. This is summarized in Fig. B.3, which shows the azimuthal dependence of $C^{\rm EE}_{l,l';m}$ and $C^{\rm BB}_{l,l';m}$ with $l = l'$. Notice that the azimuthal modes m which are highly asymmetric lead to the larger global rotational symmetry violation, generating larger values of $C^{\rm BB}_{l,l';m}$. In fact, $C^{\rm BB}_{l,l';m}$ vanishes for $m = 0$. In contrast, $C^{\rm EE}_{l,l';m}$ takes non-vanishing values for all azimuthal modes and the amplitude does not change as much as $C^{\rm BB}_{l,l';m}$ does.

Appendix C

Convenient formualae

C.1 Covolution integral

A general function $f(\boldsymbol{x})$ in real space is transformed into the Fourier space by

$$f(\boldsymbol{x}) = \int \frac{d^3k}{(2\pi)^3} e^{-i\boldsymbol{k}\cdot\boldsymbol{x}} f(\boldsymbol{k})\,. \tag{C.1}$$

We note that the difference between the Fourier space and the real space is expressed by the argument in the function. And the inverse Fourier transformation is given by

$$f(\boldsymbol{k}) = \int d^3x\, e^{i\boldsymbol{k}\cdot\boldsymbol{x}} f(\boldsymbol{x})\,. \tag{C.2}$$

When we want to transform the multiple function $f^n(\boldsymbol{x})$ in real space into the Fourier space, this can be given by the convolution integral calculation.

$$f^n(\boldsymbol{x}) = \int \frac{d^3k}{(2\pi)^3} \int \frac{d^3k_1}{(2\pi)^3} \cdots \int \frac{d^3k_n}{(2\pi)^3} e^{-i\boldsymbol{k}\cdot\boldsymbol{x}} (2\pi)^3 \delta_{\rm D}(\boldsymbol{k} - \boldsymbol{k}_1 - \cdots - \boldsymbol{k}_n) f(\boldsymbol{k}_1) \cdots f(\boldsymbol{k}_n) \tag{C.3}$$

C.2 Spherical harmonics function

The shperical harmonics function on 3D spherical coordinates is given by

$$Y_{\ell m}(\theta, \psi) = \epsilon_m \sqrt{\frac{2\ell+1}{4\pi} \frac{(\ell-|m|)!}{(\ell+|m|)!}} \mathcal{P}_\ell^{|m|}(\cos\theta) e^{im\psi}\ ;\ \epsilon_m = \begin{cases} 1 & (m > 0) \\ (-1)^m & (m \leq 0) \end{cases}\,, \tag{C.4}$$

where $\mathcal{P}_\ell^{|m|}$ is the associated Legendre function, which for $m \geq 0$ satisfies

$$\mathcal{P}_\ell^m(\mu) = (-1)^m (1-\mu^2)^{m/2} \frac{d^m}{d\mu^m} \mathcal{P}_\ell(\mu), \quad \mathcal{P}_\ell^{-m}(\mu) = (-1)^m \frac{(\ell-m)!}{(\ell+m)!} \mathcal{P}_\ell^m(\mu)\,. \tag{C.5}$$

We summarize the property of the spherical harmonics function.

Complex Conjugate $Y^*_{\ell m} = (-1)^m Y_{\ell -m}$

Orthogonal $\int d\Omega\, Y^*_{\ell m}\, Y_{\ell' m'} = \delta_{\ell\ell'} \delta_{mm'}$

Parity transformation $Y_{\ell m}(\theta,\psi)\rightarrow Y_{\ell m}(\pi-\theta,\pi+\psi)=(-1)^{\ell}Y_{\ell m}(\theta,\psi)$

Trigonometric addition formula For the angle θ between $(\theta_1,\psi_1),(\theta_2,\psi_2)$ points,

$$\frac{4\pi}{2\ell+1}\sum_m Y^*_{\ell m}(\theta_1,\psi_1)Y_{\ell m}(\theta_2,\psi_2)=\mathcal{P}_\ell(\cos\theta)$$

Recurrence formula

$$\begin{aligned}\frac{\partial}{\partial\theta}Y_{\ell m}&=\frac{\sqrt{(\ell-m)(\ell+m+1)}}{2}Y_{\ell m+1}e^{-i\psi}-\frac{\sqrt{(\ell+m)(\ell-m+1)}}{2}Y_{\ell m-1}e^{i\psi}\\ \cos\theta\;Y_{\ell m}&=\sqrt{\frac{(\ell-m+1)(\ell+m+1)}{(2\ell+1)(2\ell+3)}}Y_{\ell+1\,m}+\sqrt{\frac{(\ell-m)(\ell+m)}{(2\ell-1)(2\ell+1)}}Y_{\ell-1\,m}\\ \sin\theta e^{\pm i\psi}Y_{\ell m}&=\mp\sqrt{\frac{(\ell\pm m+1)(\ell\pm m+2)}{(2\ell+1)(2\ell+3)}}Y_{\ell+1m\pm1}\pm\sqrt{\frac{(\ell\mp m)(\ell\mp m-1)}{(2\ell-1)(2\ell+1)}}Y_{\ell-1m\pm1}\end{aligned}$$

Integration of the 3-products of the spherical harmonics function

$$\begin{aligned}&\int \mathrm{d}\Omega Y_{\ell_1 m_1}(\theta,\psi)Y_{\ell_2 m_2}(\theta,\psi)Y_{\ell_3 m_3}(\theta,\psi)\\ =&\sqrt{\frac{(2\ell_1+1)(2\ell_2+1)(2\ell_3+1)}{4\pi}}\begin{pmatrix}\ell_1&\ell_2&\ell_3\\0&0&0\end{pmatrix}\begin{pmatrix}\ell_1&\ell_2&\ell_3\\m_1&m_2&m_3\end{pmatrix}\end{aligned}$$

This is used by Wigner 3j-Symbol.

The basis for the spin-function is used by the spin-weighted Spherical harmonics fucntion, which is defined as

$${}_sY_{\ell m}=\sqrt{\frac{(\ell-|s|)!}{(\ell+|s|)!}}\begin{cases}\eth^s Y_{\ell m} & (s\geq 0)\\ (-1)^s\bar{\eth}^{|s|}Y_{\ell m} & (s<0)\end{cases}, \tag{C.6}$$

where $\eth$ is the ladder operator.

Ladder Operator When ${}_sf(\theta,\psi)$ means the spin-s function on the sky,

$$\begin{aligned}{}_{s+1}f&=\eth_s f=-\sin^s\theta\left(\frac{\partial}{\partial\theta}+\frac{i}{\sin\theta}\frac{\partial}{\partial\psi}\right)\left(\frac{{}_sf}{\sin^s\theta}\right)\\ {}_{s-1}f&=\bar{\eth}_s f=-\frac{1}{\sin^s\theta}\left(\frac{\partial}{\partial\theta}-\frac{i}{\sin\theta}\frac{\partial}{\partial\psi}\right)({}_sf\sin^s\theta)\end{aligned}$$

And when you can separate variables as ${}_sf(\theta,\psi)=e^{im\psi}{}_s\tilde{f}(\mu)$; $\mu=\cos\theta$,

$$\begin{aligned}{}_{s+1}f&=\eth_s f=-(1-\mu^2)^{\frac{1+s}{2}}\left(-\frac{\partial}{\partial\mu}-\frac{m}{1-\mu^2}\right)(1-\mu^2)^{-\frac{s}{2}}{}_sf\\ {}_{s-1}f&=\bar{\eth}_s f=-(1-\mu^2)^{\frac{1-s}{2}}\left(-\frac{\partial}{\partial\mu}+\frac{m}{1-\mu^2}\right)(1-\mu^2)^{\frac{s}{2}}{}_sf\end{aligned}$$

Furthermore, you can convert spin-s functions into scalar functions as

$$f = \begin{cases} \bar{ð}^{s}{}_{s}f = (-1)^{s}\left(-\dfrac{\partial}{\partial\mu} + \dfrac{m}{1-\mu^{2}}\right)^{s}(1-\mu^{2})^{\frac{s}{2}}{}_{s}f & (s > 0) \\ ð^{|s|}{}_{s}f = (-1)^{|s|}\left(-\dfrac{\partial}{\partial\mu} - \dfrac{m}{1-\mu^{2}}\right)^{|s|}(1-\mu^{2})^{\frac{|s|}{2}}{}_{s}f & (s < 0) \end{cases} \tag{C.7}$$

Parity transformation ${}_{s}Y_{\ell m}(-\hat{\mathbf{n}}) = (-1)^{l}\ {}_{-s}Y_{\ell m}(\hat{\mathbf{n}})$

Complex Conjugate ${}_{s}Y^{*}_{\ell m} = (-1)^{s+m}\ {}_{-s}Y_{\ell -m}$

Orthogonal $\int d\Omega\ {}_{s}Y^{*}_{\ell m}\ {}_{s}Y_{\ell' m'} = \delta_{\ell\ell'}\delta_{mm'}$

Appendix D

Derivations

D.1 Symmetric traceless tensor

D.1.1 2-dimensional relation

We show the following identities by mathematical induction;

$$\begin{aligned} \cos(n\phi) =& 2^{n-1}\left[\theta_{a_1}\cdots\theta_{a_n}\right]^{\mathrm{TL}_2}|_{a_\iota=\cdots=a_n=\iota}, && \text{(D.1)} \\ \sin(n\phi) =& 2^{n-1}\left[\theta_{a_1}\cdots\theta_{a_n}\right]^{\mathrm{TL}_2}|_{a_\iota=\cdots=a_{n-1}=\iota, a_n=\psi}, && \text{(D.2)} \end{aligned}$$

with $(\theta_\iota, \theta_\psi) = (\cos\phi, \sin\phi)$. For $n = 2$, it is straightforward to show

$$\left[\theta_{a_1}\theta_{a_2}\right]^{\mathrm{TL}_2} = \frac{1}{2}\begin{pmatrix} \cos^2\phi - \sin^2\phi & 2\cos\phi\sin\phi \\ 2\sin\phi\cos\phi & -(\cos^2\phi - \sin^2\phi) \end{pmatrix}, \tag{D.3}$$

and hence (no summation) $\left[\theta_\iota\theta_\iota\right]^{\mathrm{TL}_2} = \cos(2\phi)/2$ and $\left[\theta_\iota\theta_\psi\right]^{\mathrm{TL}_2} = \sin(2\phi)/2$.

Let us assume that for $n = k$ Eq. (D.1) and (D.2) hold. A symmetric traceless $(k+1)$-rank tensor is related to a symmetric traceless k-rank tensor [1]

$$\begin{aligned} \left[\theta_{a_1}\cdots\theta_{a_k}\theta_{a_{k+1}}\right]^{\mathrm{TL}_2} =& \frac{1}{k+1}\left(\left[\theta_{a_1}\cdots\theta_{a_k}\right]^{\mathrm{TL}_2}\theta_{a_{k+1}} + \text{perms.}\right) \\ & - \frac{1}{k(k+1)}\sum_{i=1,2}\left(\delta^{a_1a_2}\left[\theta_{a_3}\cdots\theta_{a_{k+1}}\theta_a\right]^{\mathrm{TL}_2}\theta_a + \text{perms.}\right). \end{aligned} \tag{D.4}$$

---

[1] This relation can be shown as follows: We can assume a symmetric traceless $(k+1)$-rank tensor to be of the form; $\left[\theta_{a_1}\cdots\theta_{a_k}\theta_{a_{k+1}}\right]^{\mathrm{TL}_2} = \frac{1}{k+1}\left(\left[\theta_{a_1}\cdots\theta_{a_k}\right]^{\mathrm{TL}_2}\theta_{a_{k+1}} + \text{perms.}\right) - c_k\sum_{a=\iota,\psi}\left(\delta^{a_1a_2}\left[\theta_{a_3}\cdots\theta_{a_{k+1}}\theta_a\right]^{\mathrm{TL}_2}\theta_a + \text{perms.}\right)$, where c_k is a k-dependent constant. The traceless condition $\delta^{a_1a_2}\left[\theta_{a_1}\cdots\theta_{a_k}\theta_{a_{k+1}}\right]^{\mathrm{TL}_2} = 0$ gives $c_k = 1/k(k+1)$.

Notice that with the assumption we have

$$\sum_{a=\iota,\psi} \left[\theta_{a_1}\cdots\theta_{a_{k-1}}\theta_a\right]^{\mathrm{TL}_2} \theta_a|_{a_1=\cdots=a_{k-1}=\iota} = \frac{1}{2^{k-1}}\left(\cos(k\phi)\cos\phi+\sin(k\phi)\sin\phi\right), \tag{D.5}$$

$$\sum_{a=\iota,\psi} \left[\theta_{a_1}\cdots\theta_{a_{k-1}}\theta_a\right]^{\mathrm{TL}_2} \theta_a|_{a_1=\cdots=a_{k-2}=\iota,a_{k-1}=\psi} = \frac{1}{2^{k-1}}\left(\sin(k\phi)\cos\phi-\cos(k\phi)\sin\phi\right). \tag{D.6}$$

Then, we get

$$\begin{aligned}
&\left[\theta_{a_1}\cdots\theta_{a_k}\theta_{a_{k+1}}\right]^{\mathrm{TL}_2}|_{a_1=\cdots=a_{k+1}=\iota}\\
&\quad=\frac{1}{2^{k-1}}\cos(k\phi)\cos\phi-\frac{1}{k(k+1)}\cdot\binom{k+1}{2}\cdot\frac{1}{2^{k-1}}\left(\cos(k\phi)\cos\phi+\sin(k\phi)\sin\phi\right)\\
&\quad=\frac{1}{2^k}\left(\cos(k\phi)\cos\phi-\sin(k\phi)\sin\phi\right)\\
&\quad=\frac{1}{2^k}\left(\cos(k+1)\phi\right), \qquad\qquad (\text{D.7})\\
&\left[\theta_{a_1}\cdots\theta_{a_k}\theta_{a_{k+1}}\right]^{\mathrm{TL}_2}|_{a_1=\cdots=a_k=\iota,a_{k+1}=\psi}\\
&\quad=\frac{1}{k+1}\cdot\frac{1}{2^{k-1}}\left(\cos(k\phi)\sin\phi+k\sin(k\phi)\cos\phi\right)\\
&\qquad\quad-\frac{1}{k(k+1)}\cdot\binom{k}{2}\cdot\frac{1}{2^{k-1}}\left(\sin(k\phi)\cos\phi-\cos(k\phi)\sin\phi\right)\\
&\quad=\frac{1}{2^k}\left(\sin(k\phi)\cos\phi+\cos(k\phi)\sin\phi\right)\\
&\quad=\frac{1}{2^k}\left(\sin(k+1)\phi\right), \qquad\qquad (\text{D.8})
\end{aligned}$$

which indicates that Eq. (D.1) and Eq. (D.2) are true for $n = k+1$. Therefore, Eq. (D.1) and Eq. (D.2) hold for all $n \geq 2$.

D.1.2 Arbitrary dimension

We consider an nth symmetric traceless tensor in d-dimension, expressing it as

$$\tilde{I}_{i_1i_2\cdots i_n} = I_{i_1i_2\cdots i_n} + \sum_{k=1}^{[n/2]} \tilde{C}_k \left[I_{\tilde{i}_1\tilde{i}_1\cdots\tilde{i}_k\tilde{i}_k i_{2k+1}\cdots i_n}\delta_{i_1,i_2}\cdots\delta_{i_{2k-1},i_{2k}} + (\text{perms.})\right], \tag{D.9}$$

where $I_{i_1i_2\cdots i_n}$ is an arbitrary rank-n symmetric tensor and $\tilde{I}_{i_1i_2\cdots i_n}$ is its traceless part. In the square brackets of the right hand side, the indices $I_{i_1i_2\cdots i_n}$ are replaced with the contraction by $\tilde{i}_m$ ($m = 1, \cdots, k$) and the replaced indices appear as the indices of the Kronecker delta. Imposing the traceless condition, we obtain

$$\tilde{C}_k = \tilde{C}_{k+1}[2k-(d+2n-4)]\,. \tag{D.10}$$

For $n \geq 2, d \geq 2$ and $0 \leq k \leq [n/2]$, $2k-(d+2n-4) \leq 0$. Then, we can obtain

$$\tilde{C}_k = \left(-\frac{1}{2}\right)^k \frac{\Gamma(n-k-1+d/2)}{\Gamma(n-1+d/2)!}\,. \tag{D.11}$$

For example, the coefficient for $d=2$ is given by

$$\tilde{C}_k = \left(-\frac{1}{2}\right)^k \frac{(n-k-1)!}{(n-1)!}\,, \tag{D.12}$$

and the one for $d=3$ is given by

$$\tilde{C}_k = (-1)^k \frac{(2n-2k-1)!!}{(2n-1)!!}\,. \tag{D.13}$$

The number of permutation in Eq. (D.9) is determined by counting the possible number of this replacement as

$$\frac{1}{k!}\binom{n}{2}\binom{n-2}{2}\cdots\binom{n-2(k-1)}{2} = \frac{1}{2^k k!}\frac{n!}{(n-2k)!}\,. \tag{D.14}$$

For instance, for $n=2$, Eq. (D.9) simply gives the familiar expression as

$$\tilde{I}_{i_1 i_2} = I_{i_1 i_2} + \tilde{C}_1 I_{\tilde{i}_1 \tilde{i}_1}\delta_{i_1,i_2} = I_{i_1 i_2} - \frac{I_{\tilde{i}_1 \tilde{i}_1}}{d}\delta_{i_1,i_2}\,. \tag{D.15}$$

D.2 The derivative of spherical Bessel function

In this seciton, we describe the derivation of Eq. (5.51) for all integers $s \geq 0$ by using mathematical induction:

$$P(s) : (1+\partial_x^2)^s[x^s j_l(x)] = \frac{(l+s)!}{(l-s)!}\frac{j_l(x)}{x^s}.$$

We can explicitly confirm $P(s)$ for $s = 0,1,2$. Given that $P(s)$ is true for $s = k, k-1\,(k \geq 2)$, taking the derivative of $P(k)$ with respect to x, we obtain

$$(1+\partial_x^2)^k[x^k j_l'(x)] = \frac{(l+k)!}{(l-k)!}\left[\frac{j_l'(x)}{x^k} - k\frac{j_l(x)}{x^{k+1}}\right] - (1+\partial_x^2)\left[k\frac{(l+k-1)!}{(l-k+1)!}\frac{j_l(x)}{x^{k-1}}\right], \tag{D.16}$$

where we used

$$(1+\partial_x^2)^k[kx^{k-1}j_l(x) + x^k j_x'(x)] = (1+\partial_x^2)\left[k\frac{(l+k-1)!}{(l-k+1)!}\frac{j_l(x)}{x^{k-1}}\right] + (1+\partial_x^2)^k[x^k j_l'(x)].$$

The left hand side of $P(k+1)$ is given by

$$\begin{aligned}&(1+\partial_x^2)^{k+1}[x^{k+1}j_l(x)]\\ =&(1+\partial_x^2)^k[\{x^{k+1}+k(k+1)x^{k-1}\}j_l(x) + 2(k+1)x^k j_l'(x) + x^{k+1}j_l''(x)].\end{aligned} \tag{D.17}$$

Using $P(k)$, Eq. (D.16) and the Bessel differential equation:

$$x^2 j_l''(x) + 2x j_l'(x) + [x^2 - l(l+1)] j_l(x) = 0,$$

we obtain

$$\begin{aligned}(\text{D.17}) &= 2k\frac{(l+k)!}{(l-k)!}\left[\frac{j_l'(x)}{x^k} - k\frac{j_l(x)}{x^{k+1}}\right] + \frac{(l+k-1)!}{(l-k+1)!}[l(l+1) - k(k-1)](1+\partial_x^2)\frac{j_l(x)}{x^{k-1}} \\ &= \frac{\{l+(k+1)\}!}{\{l-(k+1)\}!}\frac{j_l(x)}{x^{k+1}}\,.\end{aligned}$$

Thus, $P(k+1)$ is true, whenever $P(k)$ and $P(k-1)$ are true. Hence, by the Principle of Mathematical Induction, $P(s)$ is true for all integers $s \geq 0$.

D.3 Rewriting Eq. (5.19) into Eq. (5.24)

We show the following formulae

$$\tilde{I}_{\underbrace{\iota\iota\cdots\iota\iota}_{(n,0)}} = \frac{1}{2^{n-1}}\sum_{l=0}^{[n/2]}(-1)^l\binom{n}{2l} I_{\underbrace{\iota\iota\cdots\psi\psi}_{(n-2l,2l)}}\,, \tag{D.18}$$

$$\tilde{I}_{\underbrace{\iota\iota\cdots\iota\psi}_{(n-1,1)}} = \frac{1}{2^{n-1}}\sum_{l=0}^{[(n-1)/2]}(-1)^l\binom{n}{2l+1} I_{\underbrace{\iota\iota\cdots\psi\psi}_{(n-2l-1,2l+1)}}\,, \tag{D.19}$$

with which we can rewrite Eq. (5.19) into Eq. (5.24).

Let us start with expressing $\tilde{I}_{\iota\iota\cdots\iota\iota}$ and $\tilde{I}_{\iota\iota\cdots\iota\psi}$, using Eq. (D.9). Counting the numbers of $I_{i_1\cdots i_n}$ with $2l$ indices being ψ and $(n-2l)$ indices being ι for $l = 1, \cdots [n/2]$, we obtain

$$\begin{aligned}\tilde{I}_{\iota\iota\cdots\iota} &= \sum_{k=0}^{[n/2]}(-1)^k 2^{-2k}\frac{(n-k-1)!}{(n-1)!}\frac{n!}{k!(n-2k)!}\sum_{q=0}^{k}\binom{k}{q} I_{\underbrace{\iota\iota\cdots\psi\psi}_{(n-2k+2q,2k-2q)}} \\ &= \sum_{k=0}^{[n/2]}\sum_{l=0}^{k}(-1)^k 2^{-2k}\frac{n}{l}\binom{n-k-1}{k-1}\binom{k-1}{k-l} I_{\underbrace{\iota\iota\cdots\psi\psi}_{(n-2l,2l)}},\end{aligned} \tag{D.20}$$

where the summation over q counts the number of indices with $\tilde{a}_{i_1} = \cdots = \tilde{a}_{i_q} = \iota$ among the k contracted indices of $I_{\tilde{a}_1\tilde{a}_1\cdots\tilde{a}_k\tilde{a}_k a_{2k+1}\cdots a_n}$ (then the total number of index ι becomes $(2n-2k)+2q$ and the one of index ψ becomes $2k-2q$) and the numerical factor, $n!/(2^k k!(n-2k)!)$ comes from the number of permutation, given in Eq. (D.14). In the second equality, we have changed $k - q \to l$. Similarly, we obtain

$$\tilde{I}_{\iota\iota\cdots\psi} = \sum_{k=0}^{[(n-1)/2]}\sum_{l=0}^{k}(-1)^k 2^{-2k}\binom{n-k-1}{k}\binom{k}{k-l} I_{\underbrace{\iota\iota\cdots\iota\psi}_{(n-2l-1,2l+1)}}\,, \tag{D.21}$$

where the number of permutation is now given by

$$\frac{1}{k!}\binom{n-1}{2}\binom{n-3}{2}\cdots\binom{n-2(k-1)-1}{2}=\frac{1}{2^k k!}\frac{(n-1)!}{(n-2k-1)!}\,, \tag{D.22}$$

since the terms including $\delta_{\iota\psi}$ vanish.

Changing the summation from $0\leq k\leq[n/2]$ and $0\leq l\leq k$ to $0\leq l\leq[n/2]$ and $l\leq k\leq[n/2]$, we can further rewrite Eq. (D.20) and Eq. (D.21) as

$$\tilde{I}_{\iota\iota\cdots\iota}=\sum_{l=0}^{[n/2]}\frac{n}{l}\left(-\frac{1}{4}\right)^l\sum_{k=0}^{[n/2]-l}\left(-\frac{1}{4}\right)^k\binom{n-k-l-1}{k+l-1}\binom{k+l-1}{k}I_{\underbrace{\iota\iota\cdots\iota\psi}_{(n-2l,2l)}}\,, \tag{D.23}$$

$$\tilde{I}_{\iota\iota\cdots\psi}=\sum_{l=0}^{[(n-1)/2]}\left(-\frac{1}{4}\right)^l\sum_{k=0}^{[(n-1)/2]-l}\left(-\frac{1}{4}\right)^k\binom{n-k-l-1}{k+l}\binom{k+l}{k}I_{\underbrace{\iota\iota\cdots\iota\psi}_{(n-2l,2l)}}\,, \tag{D.24}$$

where we have changed $k-l\to k$. Rewriting the summation over k by using the following formulae:

$$\sum_{k=0}^{[n/2]}\left(-\frac{1}{4}\right)^k\binom{n-k+l-1}{k+l-1}\binom{k+l-1}{k}=\frac{1}{2^n}\frac{(n+2l-1)!}{n!(2l-1)!}\,, \tag{D.25}$$

$$\sum_{k=0}^{[n/2]}\left(-\frac{1}{4}\right)^k\binom{n-k+l}{k+l}\binom{k+l}{k}=\frac{1}{2^n}\frac{(n+2l+1)!}{n!(2l+1)!}\,, \tag{D.26}$$

we arrive at Eqs. (D.18) and (D.19).

D.4 Contribution of PNG with spin-4

We compute the contribution of the PNG generated by a spin-4 particle, given in Eq. (2.57), to the 4th moment galaxy shape function.

D.4.1 Contributions to galaxy shape function

From Eq. (5.62), the cross-correlation of the matter density field with $\tilde{g}_{ijkl}$ is

$$\langle\delta(\boldsymbol{x})\tilde{g}_{ijkl}(\boldsymbol{y})\rangle=b_{K^2}^{(4)}\left\langle\delta(\boldsymbol{x})\left[K_{ij}(\boldsymbol{y})K_{kl}(\boldsymbol{y})\right]^{\mathrm{TL}_3,\,\mathrm{sym}}\right\rangle+\mathcal{O}((kR_*)^2). \tag{D.27}$$

Let us compute $\left\langle \delta(\boldsymbol{x})\,[K_{ij}(\boldsymbol{y})K_{kl}(\boldsymbol{y})]^{\mathrm{TL}_3,\,\mathrm{sym}}\right\rangle$ term in the presence of the non-Gaussian initial condition such as Eq. (2.57).

$$\begin{aligned}&\left\langle \delta(\boldsymbol{x})\,[K_{ij}(\boldsymbol{y})K_{kl}(\boldsymbol{y})]^{\mathrm{TL}_3,\,\mathrm{sym}}\right\rangle\\ &=\int\frac{d^3\boldsymbol{k}}{(2\pi)^3}e^{i\boldsymbol{k}\cdot\boldsymbol{r}}\mathcal{M}(k)\int\frac{d^3\boldsymbol{p}}{(2\pi)^3}\,[\hat{p}_i\hat{p}_j\hat{p}'_k\hat{p}'_l]^{\mathrm{TL}_3}\mathcal{M}(p)\mathcal{M}(|\boldsymbol{k}+\boldsymbol{p}|)B_\Psi(k,p,|\boldsymbol{k}+\boldsymbol{p}|)\end{aligned} \tag{D.28}$$

$$\begin{aligned}&=\int\frac{d^3\boldsymbol{k}}{(2\pi)^3}e^{i\boldsymbol{k}\cdot\boldsymbol{r}}\mathcal{M}(k)P_\Psi(k)\int\frac{p^2dp}{(2\pi)^2}\mathcal{M}^2(p)P_\Psi(p)\\ &\qquad\int d\mu\int\frac{d\varphi}{2\pi}\,[\hat{p}_i\hat{p}_j\hat{p}'_k\hat{p}'_l]^{\mathrm{TL}_3}\sum_\ell A_\ell\mathcal{P}_\ell(\mu)[2+2q\mu\{n_\Psi+n_{\mathcal{M}}(p)\}+\mathcal{O}(q^2)]\end{aligned} \tag{D.29}$$

with $\boldsymbol{r}=\boldsymbol{x}-\boldsymbol{y}$, $\hat{\boldsymbol{p}}'=-(\widehat{\boldsymbol{k}+\boldsymbol{p}})$, $q=k/p$, $\mu=\hat{\boldsymbol{k}}\cdot\hat{\boldsymbol{p}}$, $n_\Psi=n_s-4$, $n_{\mathcal{M}}(p)\equiv\partial\ln\mathcal{M}(p)/\partial\ln p$. In the first line, we used the symmetric tensor property and in the second line, we used Eq.(2.57) and expanded $B_\Psi(k,p,|\boldsymbol{k}+\boldsymbol{p}|)$ and $\mathcal{M}(|\boldsymbol{k}+\boldsymbol{p}|)$ in the powers of $q\ll 1$.

We also apply $\hat{\boldsymbol{p}}'\sim\hat{\boldsymbol{p}}$ in the powers of $q\ll 1$. Choosing the z direction of the polar coordinates along the direction of $\hat{\boldsymbol{k}}$ and integrating over the azimuthal angle φ, we obtain

$$\int\frac{d\varphi}{2\pi}[\hat{p}_{i_1}\cdots\hat{p}_{i_n}]^{\mathrm{TL}_3}\propto[\hat{k}_{i_1}\cdots\hat{k}_{i_n}]^{\mathrm{TL}_3}. \tag{D.30}$$

This can be understood by noticing that since the left-hand side of Eq. (D.30) should be independent of φ, all the tensor indices should be along the direction of $\hat{\boldsymbol{k}}$, satisfying the symmetric traceless condition.

The amplitude of the left hand side of Eq. (D.30) can be determined as follows. As shown in Ref. [153] (in this paper, the spatial dimension is d, so here we set $d=3$), the contraction between $[\hat{p}_{i_1}\cdots\hat{p}_{i_n}]^{\mathrm{TL}_3}$ and $[\hat{k}_{i_1}\cdots\hat{k}_{i_n}]^{\mathrm{TL}_3}$ is given by

$$[\hat{p}^{i_1}\cdots\hat{p}^{i_n}]^{\mathrm{TL}_3}[\hat{k}_{i_1}\cdots\hat{k}_{i_n}]^{\mathrm{TL}_3}=\frac{n!}{(2n-1)!!}\mathcal{P}_n(\mu). \tag{D.31}$$

Operating $[\hat{k}^{i_1}\cdots\hat{k}^{i_n}]^{\mathrm{TL}_3}$ on the left hand side of Eq. (D.30) and using Eq. (D.31), we find that the amplitude of the left hand side of Eq. (D.30) should be $\mathcal{P}_n(\mu)$, i.e.

$$\int\frac{d\varphi}{2\pi}[\hat{p}_{i_1}\cdots\hat{p}_{i_n}]^{\mathrm{TL}_3}=\mathcal{P}_n(\mu)[\hat{k}_{i_1}\cdots\hat{k}_{i_n}]^{\mathrm{TL}_3}. \tag{D.32}$$

Here, we used

$$[\hat{k}^{i_1}\cdots\hat{k}^{i_n}]^{\mathrm{TL}_3}[\hat{k}_{i_1}\cdots\hat{k}_{i_n}]^{\mathrm{TL}_3}=\frac{n!}{(2n-1)!!}\mathcal{P}_n(\hat{\boldsymbol{k}}\cdot\hat{\boldsymbol{k}}=1)=\frac{n!}{(2n-1)!!}\,. \tag{D.33}$$

Using Eq. (D.32) in Eq. (D.29), we obtain

$$\langle\delta(\boldsymbol{x})\,\{K_{ij}(\boldsymbol{y})K_{kl}(\boldsymbol{y})\}\rangle=\frac{2}{9}A_4\int\frac{d^3k}{(2\pi)^3}e^{i\boldsymbol{k}\cdot\boldsymbol{r}}\mathcal{M}(k)P_\Psi(k)\,[\hat{k}_i\hat{k}_j\hat{k}_k\hat{k}_l]^{\mathrm{TL}_3}\int\frac{p^2dp}{2\pi^2}\mathcal{M}^2(p)P_\Psi(p)\,, \tag{D.34}$$

where we haved used the orthonormality of the Legendre polynomials.

D.4.2 Renormalization

Next, we define the renormalized bias parameter $b_{\mathrm{NG}}^{(4)}$ following the discussions in Refs. [98, 41].

Gaussian initial conditions

First, we consider the case of Gaussian initial conditions. Let us introduce the coarse-grained density field δ_{L} and tidal field $K_{\mathrm{L},ij}$ with a coarse-graining scale R_{L}. Then, using a functional $F_{\mathrm{L},ijkl}$, we can formally express $\tilde{g}_{ijkl}(\boldsymbol{x})$ as

$$\tilde{g}_{ijkl}(\boldsymbol{x})=F_{\mathrm{L},ijkl}(\delta_{\mathrm{L}}(\boldsymbol{x});K_{\mathrm{L},pq}(\boldsymbol{x});\delta_{\mathrm{s}}(\boldsymbol{x})), \tag{D.35}$$

with $\delta_{\mathrm{s}}(\boldsymbol{x})\equiv\delta(\boldsymbol{x})-\delta_{\mathrm{L}}(\boldsymbol{x})$ being the small-scale fluctuations on which in principle the 4th moment depends other than δ_{L} and $K_{\mathrm{L},ij}$. A formal Taylor expansion of $F_{\mathrm{L},ijkl}$ in δ_{L} and $K_{\mathrm{L},ij}$ leads to

$$\tilde{g}_{ijkl}(\boldsymbol{x})=c_{K^2}^{(4)}(R_{\mathrm{L}};\delta_s(\boldsymbol{x}))\,[K_{\mathrm{L},ij}K_{\mathrm{L},kl}]^{\mathrm{TL}_3,\,\mathrm{sym}}(\boldsymbol{x})+\mathcal{O}(\delta_{\mathrm{L}}^3,\nabla^2\delta_{\mathrm{L}}), \tag{D.36}$$

In general, the coefficient $c_{K^2}^{(4)}$ depend on on the short modes δ_{s} and the coarse-graining scale R_{L} [2]. In the Gaussian case, however, the short modes and long modes are uncorrelated, so the $c_{K^2}^{(4)}$ can be regarded as an effective constant.

The spherical symmetry requires the expectation value of $\tilde{g}_{ijkl}(\boldsymbol{x})$ to vanish. Let us consider the following modification of the tidal field:

$$K_{\mathrm{L},ij}(\boldsymbol{x},\tau)\to K_{\mathrm{L},ij}(\boldsymbol{x},\tau)+D(\tau)\beta_{ij};\quad\delta_{\mathrm{L}}(\boldsymbol{x},\tau)\to\delta_{\mathrm{L}}(\boldsymbol{x},\tau), \tag{D.37}$$

or equivalently the modification of the Newtonian potential,

$$\Psi_{\mathrm{N}}(\boldsymbol{x})\to\Psi_{\mathrm{N}}(\boldsymbol{x})+\frac{3}{4}\Omega_{\mathrm{m0}}H_0^2(1+z)D(z)\beta_{ij}x^ix^j, \tag{D.38}$$

where β_{ij} is a constant symmetric traceless tensor. One can interpret this as the leading observable effect of a potential perturbation in the $k\to0$ limit, as constant and pure-gradient potential perturbations can be removed by coordinate transformations. Alternatively, this effect can be realized in simulations by implementing an anisotropic expansion, roughly resembling a Bianchi I spacetime [154, 155, 156].

---

[2] R_{L} is an arbitrary coarse-graining scale, while R_{L} should satisfy $R_{\mathrm{L}}>R_*$, where R_* corresponds to the physical size of galaxies/halos.

Under this modification, the expectation value of $\tilde{g}_{ijkl}$ changes to

$$\langle \tilde{g}_{ijkl}(\boldsymbol{x}) \rangle_\beta = c^{(4)}_{K^2} \left[\beta_{ij}\beta_{kl}\right]^{\mathrm{TL}_3,\,\mathrm{sym}} + \mathcal{O}(\delta_{\mathrm{L}}^3, \nabla^2\delta_{\mathrm{L}}). \tag{D.39}$$

Notice that $\langle \tilde{g}_{ijkl}(\boldsymbol{x}) \rangle$ does not vanish owing to the presence the preferred direction β_{ij}. Then, the renormalized bias parameters are introduced via

$$b^{(4)}_{K^2} \equiv \left[\frac{\partial^2}{\partial\beta_{ij}\partial\beta_{kl}}\right]^{\mathrm{TL}_3,\,\mathrm{sym}} \langle \tilde{g}_{ijkl} \rangle_\beta \Bigg|_{\beta=0} = c^{(4)}_{K^2} + \mathcal{O}([\delta_{\mathrm{L}}, K_{\mathrm{L},ij}]^2). \tag{D.40}$$

Note that here the summation is not taken. This definition of the bias parameter $b^{(4)}_{K^2}$ is independent of R_{L} by construction. The point is that the renormalized bias is defined as the response to the locally uniform transformation of the tidal field (second derivatives of the potential).

Finally we get

$$\langle \delta(\boldsymbol{x}) \tilde{g}_{ijkl}(\boldsymbol{y}) \rangle = b^{(4)}_{K^2} \left\langle \delta(\boldsymbol{x}) \left[K_{ij}K_{kl}\right]^{\mathrm{TL}_3,\,\mathrm{sym}} (\boldsymbol{y}) \right\rangle + \cdots . \tag{D.41}$$

For Gaussian initial conditions, the three-point function in Eq. (D.41) only arises from non-linear evolution, therefore is relevant only on small scales.

Non-Gaussian initial conditions with no scaling (local-type)

In the presence of the primordial non-Gaussianity (2.57), Eq. (D.34) yields

$$\left\langle \delta(\boldsymbol{x}) \left[K_{ij}K_{kl}\right]^{\mathrm{TL}_3,\,\mathrm{sym}} (\boldsymbol{y}) \right\rangle = \frac{2}{9} A_4 \mathcal{D}_{ijkl} \xi_{\delta\Psi}(|\boldsymbol{x}-\boldsymbol{y}|) \langle \delta_{\mathrm{L}}^2 \rangle. \tag{D.42}$$

This expression strongly depends on the coarse-graining scale through $\langle \delta_{\mathrm{L}}^2 \rangle$, so the bias expansion Eq. (D.41) is not sufficient for non-Gaussian initial conditions. In this case, we have to take into account the dependence of g_{ijkl} on the small-scale fluctuations δ_{s} explicitly, since the primordial non-Gaussianity couples the long-modes with short-modes. To do this, let us introduce the parameter y_{s}^{ijkl} as the hexadecapole anisotropy of the local small-scale correlation function within a region of size R_{L},

$$y_{\mathrm{s}}^{ijkl}(\boldsymbol{x}) = \frac{1}{\sigma_y^2} \int d^3\boldsymbol{r}\; W_{\mathrm{L}}(|\boldsymbol{r}|) \left[K_{\mathrm{s}}^{ij}\left(\boldsymbol{x}-\frac{\boldsymbol{r}}{2}\right) K_{\mathrm{s}}^{kl}\left(\boldsymbol{x}+\frac{\boldsymbol{r}}{2}\right)\right]^{\mathrm{TL}_3,\,\mathrm{sym}}, \tag{D.43}$$

$$\sigma_y^2 = \int \frac{d^3\boldsymbol{k}}{(2\pi)^3} \widetilde{W}_{\mathrm{L}}(k) \widetilde{W}_{\mathrm{s}}^2(k) P_{\mathrm{m}}(k), \tag{D.44}$$

where W_{L} is an isotropic window function of the scale R_{L}, $K_{\mathrm{s}}^{ij}(\boldsymbol{x} \pm \boldsymbol{r}/2) \equiv \mathcal{D}_r^{ij} \delta_{\mathrm{s}}(\boldsymbol{x} \pm \boldsymbol{r}/2)$ with $\mathcal{D}_r^{ij}$ being the derivative operator acting on $\boldsymbol{r}$ and $\widetilde{W}_{\mathrm{s}}(k) \equiv 1 - \widetilde{W}_{\mathrm{L}}(k)$. We now introduce explicitly the dependence of $g_{ijkl}(\boldsymbol{x})$ on $y_{\mathrm{s}}^{ijkl}(\boldsymbol{x})$:

$$\tilde{g}_{ijkl}(\boldsymbol{x}) = F_{\mathrm{L},ijkl}(\delta_{\mathrm{L}}(\boldsymbol{x}); K_{\mathrm{L},pq}(\boldsymbol{x}); y_{\mathrm{s}}^{pqrs}(\boldsymbol{x})). \tag{D.45}$$

Expanding $F_{\mathrm{L},ijkl}$ to linear order in y_{s}^{pqrs} leads to adding a term

$$c_{\mathrm{NG}}^{(4)} y_{\mathrm{s}}^{ijkl}(\boldsymbol{x}) \tag{D.46}$$

to the expansion on the r.h.s. of Eq. (D.36). Then, we have additional contribution to matter-shape correlation,

$$\langle \delta(\boldsymbol{x}) \tilde{g}_{ijkl}(\boldsymbol{y}) \rangle = b_{K^2}^{(4)} \left\langle \delta(\boldsymbol{x}) \left[K_{\mathrm{L},ij} K_{\mathrm{L},kl} \right]^{\mathrm{TL}_3,\,\mathrm{sym}} (\boldsymbol{y}) \right\rangle + c_{\mathrm{NG}}^{(4)} \langle \delta(\boldsymbol{x}) y_{\mathrm{s}}^{ijkl}(\boldsymbol{y}) \rangle + \cdots . \tag{D.47}$$

The Fourier transform of Eq. (D.43) is given by

$$y_{\mathrm{s}}^{ijkl}(\boldsymbol{k}) = \frac{1}{\sigma_y^2} \int \frac{d^3\boldsymbol{p}_1}{(2\pi)^3} \left[\hat{p}_1^i \hat{p}_1^j \hat{p}_2^k \hat{p}_2^l \right]^{\mathrm{TL}_3,\,\mathrm{sym}} \widetilde{W}_{\mathrm{L}} \left(\left| -\boldsymbol{p}_1 + \frac{1}{2}\boldsymbol{k} \right| \right) \delta_{\mathrm{s}}(\boldsymbol{p}_1) \delta_{\mathrm{s}}(\boldsymbol{p}_2), \tag{D.48}$$

where we introduced $\boldsymbol{p}_1$ and $\boldsymbol{p}_2$ satisfying $\boldsymbol{p}_1 + \boldsymbol{p}_2 = \boldsymbol{k}$. We then obtain

$$\begin{aligned} \langle \delta(\boldsymbol{x}) y_{\mathrm{s}}^{ijkl}(\boldsymbol{y}) \rangle = & \frac{1}{\sigma_y^2} \int \frac{d^3\boldsymbol{k}}{(2\pi)^3} e^{-i\boldsymbol{k}\cdot\boldsymbol{r}} \mathcal{M}(k) \int \frac{d^3\boldsymbol{p}_1}{(2\pi)^3} \widetilde{W}_{\mathrm{L}} \left(\left| -\boldsymbol{p}_1 + \frac{1}{2}\boldsymbol{k} \right| \right) \left[\hat{p}_1^i \hat{p}_1^j \hat{p}_2^k \hat{p}_2^l \right]^{\mathrm{TL}_3,\,\mathrm{sym}} \\ & \times \mathcal{M}_{\mathrm{s}}(p_1) \mathcal{M}_{\mathrm{s}}(|\boldsymbol{k} + \boldsymbol{p}_1|) B_\Psi(k, p_1, |\boldsymbol{k} + \boldsymbol{p}_1|) \end{aligned} \tag{D.49}$$

with $\boldsymbol{r} \equiv \boldsymbol{x} - \boldsymbol{y}$ and $\mathcal{M}_{\mathrm{s}}(k) \equiv \mathcal{M}(k) \widetilde{W}_{\mathrm{s}}(k)$. Expanding this integrand in power of $q_1 = k/p_1$ and performing the angle integral with respect to $\boldsymbol{p}_1$, we have

$$\begin{aligned} \langle \delta(\boldsymbol{x}) y_{\mathrm{s}}^{ijkl}(\boldsymbol{y}) \rangle = & \frac{1}{\sigma_y^2} \int \frac{d^3\boldsymbol{k}}{(2\pi)^3} e^{i\boldsymbol{k}\cdot\boldsymbol{r}} \mathcal{M}(k) P_\Psi(k) \left[\hat{k}^i \hat{k}^j \hat{k}^k \hat{k}^l \right]^{\mathrm{TL}_3} \int \frac{p_1^2 dp_1}{(2\pi)^2} \widetilde{W}_{\mathrm{L}}(p_1) \mathcal{M}_{\mathrm{s}}^2(p_1) P_\Psi(p_1) \\ & \times \int_{-1}^{1} d\mu_1 \mathcal{P}_4(\mu_1) \sum_\ell A_\ell \mathcal{P}_\ell(\mu_1) \left[2 + \mathcal{O}(q_1) \right] , \end{aligned} \tag{D.50}$$

where we have used $\widetilde{W}_{\mathrm{L}} \left(\left| -\boldsymbol{p}_1 + \frac{1}{2}\boldsymbol{k} \right| \right) = \widetilde{W}_{\mathrm{L}}(p_1) + \mathcal{O}(q_1)$ and $\hat{p}_2 = -\hat{p}_1 + \mathcal{O}(q_1)$. Following the same strategy of the calculation of Eq. (D.34), we obtain

$$\langle \delta(\boldsymbol{x}) y_s^{ijkl}(\boldsymbol{y}) \rangle = \frac{2}{9} A_4 \mathcal{D}_{ijkl} \xi_{\Psi\delta}(|\boldsymbol{x} - \boldsymbol{y}|). \tag{D.51}$$

Thus, there are two non-Gaussian terms which are proportional to $A_4 \mathcal{D}_{ijkl} \xi_{\Phi\delta}$, one of which explicitly depends on R_{L}. A renormalized bias $b_{\mathrm{NG}}^{(4)}$ should consist of R_{L}-independent combination of these contributions. In other words, physically, $b_{\mathrm{NG}}^{(4)}$ should correspond to the response of the 4th moment to a specific (R_{L}-independent) transformation of the density field as implied in the previous subsection.

In fact, under the initial condition given by Eq. (2.57) the local power spectrum is modulated like Eq. (2.61), which means that the long-wavelength potential perturbation leads an anisotropic modulation of the local initial matter power spectrum described by

$$P_{\mathrm{m},\alpha}^{\mathrm{ini}}(\boldsymbol{k}_{\mathrm{S}}; \boldsymbol{x}) = \left[1 + \alpha_{\mathrm{L}\,pqrs}(\boldsymbol{x}) \left[\hat{k}_{\mathrm{S}}^p \hat{k}_{\mathrm{S}}^q \hat{k}_{\mathrm{S}}^r \hat{k}_{\mathrm{S}}^s \right]^{\mathrm{TL}_3} \right] P_{\mathrm{m,iso}}^{\mathrm{ini}}(k_{\mathrm{S}}), \tag{D.52}$$

with

$$\alpha_{\mathrm{L}\,pqrs}(\boldsymbol{x}) \equiv \frac{35}{8}\int \frac{d^3\boldsymbol{k}_\mathrm{L}}{(2\pi)^3} A_4 \left[\hat{k}_{\mathrm{L},p}\hat{k}_{\mathrm{L},q}\hat{k}_{\mathrm{L},r}\hat{k}_{\mathrm{L},s}\right]^{\mathrm{TL}_3} \Psi(\boldsymbol{k}_\mathrm{L}) e^{i\boldsymbol{k}_\mathrm{L}\cdot\boldsymbol{x}}. \tag{D.53}$$

Note that we treat $\alpha_{\mathrm{L},pqrs}$ as a locally constant number. Here, we assumed $f_4(k_\mathrm{L}/k_\mathrm{S}) \simeq 1$. This implies that in terms of the density field the presence of the anisotropic non-Gaussianity alters the local density field such that

$$\delta_\alpha(\boldsymbol{k}_\mathrm{S}) = \left[1 + \frac{1}{2}\alpha_{\mathrm{L}\,pqrs}\left[\hat{k}^p_\mathrm{S}\hat{k}^q_\mathrm{S}\hat{k}^r_\mathrm{S}\hat{k}^s_\mathrm{S}\right]^{\mathrm{TL}_3}\right]\delta(\boldsymbol{k}_\mathrm{S})\,. \tag{D.54}$$

This is an anisotropic (hexadecapole), scale-independent rescaling of the density field. After this transformation, the expectation value of the 4th moment galaxy shape changes to

$$\langle \tilde{g}_{ijkl}\rangle_\alpha = b^{(4)}_{K^2}\left\langle [K_{\mathrm{L},ij}K_{\mathrm{L},kl}]^{\mathrm{TL}_3,\,\mathrm{sym}}\right\rangle_\alpha + c^{(4)}_\mathrm{NG}\left\langle y^{ijkl}_\mathrm{s}\right\rangle_\alpha, \tag{D.55}$$

where

$$\left\langle [K_{\mathrm{L},ij}K_{\mathrm{L},kl}]^{\mathrm{TL}_3,\,\mathrm{sym}}\right\rangle_\alpha = \int \frac{d^3\boldsymbol{k}}{(2\pi)^3}\left[\hat{k}_i\hat{k}_j\hat{k}_k\hat{k}_l\right]^{\mathrm{TL}_3}\left(1 + \alpha_{\mathrm{L}\,pqrs}\left[\hat{k}^p\hat{k}^q\hat{k}^r\hat{k}^s\right]^{\mathrm{TL}_3}\right)\widetilde{W}^2_\mathrm{L}(k)P_\mathrm{m}(k), \tag{D.56}$$

$$\left\langle y^{ijkl}_\mathrm{s}\right\rangle_\alpha = \frac{1}{\sigma^2_y}\int \frac{d^3\boldsymbol{k}}{(2\pi)^3}\left[\hat{k}_i\hat{k}_j\hat{k}_k\hat{k}_l\right]^{\mathrm{TL}_3}\left(1 + \alpha_{\mathrm{L}\,pqrs}\left[\hat{k}^p\hat{k}^q\hat{k}^r\hat{k}^s\right]^{\mathrm{TL}_3}\right)\widetilde{W}_\mathrm{L}(k)\widetilde{W}^2_\mathrm{s}(k)P_\mathrm{m}(k). \tag{D.57}$$

To proceed the computation of Eq. (D.57), we use the following identity:

$$\int \frac{d^2\hat{k}}{4\pi}\hat{k}_{i_1}\cdots\hat{k}_{i_n} = \frac{1}{(n+1)!!}[\delta_{i_1i_2}\cdots\delta_{i_{n-1}i_n}]^{\mathrm{sym}}\,, \tag{D.58}$$

where $[\delta_{i_1i_2}\cdots\delta_{i_{n-1}i_n}]^{\mathrm{sym}}$ means to symmetrize the expression $\delta_{i_1i_2}\cdots\delta_{i_{n-1}i_n}$ in the indices $i_1\cdots i_n$. For instance, the explicit expression for $n=4$ case is given by

$$[\delta_{i_1i_2}\delta_{i_3i_4}]^{\mathrm{sym}} = \delta_{i_1i_2}\delta_{i_3i_4} + \delta_{i_1i_3}\delta_{i_2i_4} + \delta_{i_1i_4}\delta_{i_2i_3}. \tag{D.59}$$

After some algebra, we get

$$\left\langle [K_{\mathrm{L},ij}K_{\mathrm{L},kl}]^{\mathrm{TL}_3,\,\mathrm{sym}}\right\rangle_\alpha \Big/ \left\langle \delta^2_\mathrm{L}\right\rangle = \left\langle y^{ijkl}_\mathrm{s}\right\rangle_\alpha = \frac{4!}{9!!}\alpha_{\mathrm{L}\,ijkl}. \tag{D.60}$$

Then, the expectation of the 4th moment shape function is modified as

$$\langle \tilde{g}_{ijkl}\rangle_\alpha = \left[\frac{8}{315}b^{(4)}_{K^2}\langle\delta^2_\mathrm{L}\rangle + \frac{8}{315}c_\mathrm{NG}\right]\alpha_{\mathrm{L}\,ijkl}. \tag{D.61}$$

This tells us that the linear response of the mean 4th moment of galaxies, through which we define the renormalized bias $b_{\rm NG}^{(4)}$, is given by

$$b_{\rm NG}^{(4)} \equiv \left.\frac{\partial\langle\tilde{g}_{ijkl}\rangle_\alpha}{\alpha_{{\rm L}\,ijkl}}\right|_{\alpha=0} = \frac{8}{315}b_{K^2}^{(4)}\langle\delta_{\rm L}^2\rangle + \frac{8}{315}c_{\rm NG}^{(4)}. \tag{D.62}$$

This means that the counter term should be given by

$$c_{\rm NG}^{(4)} = \frac{315}{8}b_{\rm NG}^{(4)} - b_{K^2}^{(4)}\langle\delta_{\rm L}^2\rangle. \tag{D.63}$$

Plugging this into Eq. (D.47), we obtain

$$\langle\delta(\boldsymbol{x})\tilde{g}_{ijkl}(\boldsymbol{y})\rangle = \frac{35}{4}b_{\rm NG}^{(4)}A_4\mathcal{D}_{ijkl}\xi_{\delta\Psi}(|\boldsymbol{x}-\boldsymbol{y}|). \tag{D.64}$$

Non-Gaussian initial conditions with scaling

In this case, the modulation of the local initial matter power spectrum becomes

$$P_{{\rm m},\alpha}^{\rm ini}(\boldsymbol{k}_{\rm S};\boldsymbol{x}) = \left[1 + h_4\left(\frac{k_{\rm p}}{k_{\rm S}}\right)\alpha_{{\rm L}\,pqrs}(\boldsymbol{x})\left[\hat{k}_{\rm S}^p\hat{k}_{\rm S}^q\hat{k}_{\rm S}^r\hat{k}_{\rm S}^s\right]^{\rm TL_3}\right]P_{\rm m,iso}^{\rm ini}(k_{\rm S}), \tag{D.65}$$

with

$$\alpha_{{\rm L}\,pqrs}(\boldsymbol{x}) \equiv \frac{35}{8}\int\frac{d^3\boldsymbol{k}_{\rm L}}{(2\pi)^3}A_4g_4\left(\frac{k_{\rm L}}{k_{\rm p}}\right)\left[\hat{k}_{{\rm L},p}\hat{k}_{{\rm L},q}\hat{k}_{{\rm L},r}\hat{k}_{{\rm L},s}\right]^{\rm TL_3}\Psi(\boldsymbol{k}_{\rm L})e^{i\boldsymbol{k}_{\rm L}\cdot\boldsymbol{x}}. \tag{D.66}$$

In terms of the density field, the presence of the anisotropic non-Gaussianity alters the local density field such that

$$\delta_\alpha(\boldsymbol{k}_{\rm S}) = \left[1 + \frac{1}{2}h_4\left(\frac{k_{\rm p}}{k_{\rm S}}\right)\alpha_{{\rm L}\,pqrs}\left[\hat{k}_{\rm S}^p\hat{k}_{\rm S}^q\hat{k}_{\rm S}^r\hat{k}_{\rm S}^s\right]^{\rm TL_3}\right]\delta(\boldsymbol{k}_{\rm S}). \tag{D.67}$$

Obviously, in this case the local density field is modulated with the scale-dependence, unlike (D.54) where the local density field is rescaled uniformly. In this case, defining the renormalized bias with respect to the locally uniform modulation leads to the final expression in the Fourier space,

$$\langle\delta(\boldsymbol{k})\tilde{g}_{ijkl}(\boldsymbol{k}')\rangle = \left[\hat{k}_i\hat{k}_j\hat{k}_k\hat{k}_l\right]^{\rm TL_3}\frac{35}{4}b_{\rm NG}^{(4)}A_4g_4\left(\frac{k}{k_{\rm p}}\right)\mathcal{M}^{-1}(k)P_{\rm m}(\boldsymbol{k})(2\pi)^3\delta(\boldsymbol{k}+\boldsymbol{k}'). \tag{D.68}$$

D.5 Contribution of PNG with the global anisotropy

We derive the scale dependent bias for $\tilde{g}_{ij}$ and $\delta_{\rm n}$ in the presence of the PNG with the global anisotropy (B.1). Here, the constant vector $\hat{\boldsymbol{p}}$ is left arbitrary.

D.5.1 Scale dependent bias

Galaxy shape

To compute the scale dependent bias for galaxy shape function, we compute the two point function $\langle \delta(\boldsymbol{x}) \tilde{g}_{ij}(\boldsymbol{y}) \rangle$. Using Eq. (5.61), we find that this two point function includes the three-point functions

$$\langle \delta(\boldsymbol{x}) \delta(\boldsymbol{y}) K_{ij}(\boldsymbol{y}) \rangle \qquad \text{and} \qquad \langle \delta(\boldsymbol{x}) \left[K_{ik} K^{k}{}_{j} - \frac{1}{3} \delta_{ij} (K_{lm})^2 \right] (\boldsymbol{y}) \rangle \,. \tag{D.69}$$

Here, we compute the contribution of the squeezed bispectrum to the first term. The first term can be rewritten as

$$\begin{aligned} \langle \delta(\boldsymbol{x}) \delta(\boldsymbol{y}) K_{ij}(\boldsymbol{y}) \rangle \approx \int \frac{d^3 \boldsymbol{k}_{\mathrm{L}}}{(2\pi)^3} e^{i \boldsymbol{k}_{\mathrm{L}} \cdot \boldsymbol{r}} \mathcal{M}(k_{\mathrm{L}}) \int \frac{d^3 \boldsymbol{k}_1}{(2\pi)^3} \left[\frac{k_{1i} k_{1j}}{k_1^2} - \frac{1}{3} \delta_{ij} \right] \\ \times \mathcal{M}(k_1) \mathcal{M}(|\boldsymbol{k}_1 + \boldsymbol{k}_{\mathrm{L}}|) B_{\Psi}(\boldsymbol{k}_1, -(\boldsymbol{k}_1 + \boldsymbol{k}_{\mathrm{L}}), \boldsymbol{k}_{\mathrm{L}}), \end{aligned} \tag{D.70}$$

where $\boldsymbol{k}_1$ corresponds to the short mode. Since we only take into account the contribution from the squeezed configuration, we used $\approx$ instead of the equality. Expanding this three-point function in terms of $q = k_{\mathrm{L}}/k_{\mathrm{S}} \ll 1$, we obtain

$$\begin{aligned} \langle \delta(\boldsymbol{x}) \delta(\boldsymbol{y}) K_{ij}(\boldsymbol{y}) \rangle \approx \int \frac{d^3 \boldsymbol{k}_{\mathrm{L}}}{(2\pi)^3} e^{i \boldsymbol{k}_{\mathrm{L}} \cdot \boldsymbol{r}} \mathcal{M}(k_{\mathrm{L}}) \int \frac{d^3 \boldsymbol{k}_{\mathrm{S}}}{(2\pi)^3} \left[\frac{k_{\mathrm{S}i} k_{\mathrm{S}j}}{k_{\mathrm{S}}^2} - \frac{1}{3} \delta_{ij} \right] \\ \times \mathcal{M}^2(k_{\mathrm{S}}) P_{\Psi}(k_{\mathrm{L}}) P_{\Psi}(k_{\mathrm{S}}) \sum_{l=0}^{\infty} \left[\bar{A}_l + \bar{B}_l \mu + \mathcal{O}(q) \right] i^{\frac{1-(-1)^l}{2}} \mathcal{P}_l(\hat{\boldsymbol{p}} \cdot \hat{\boldsymbol{k}}_{\mathrm{S}}), \end{aligned} \tag{D.71}$$

with $\mu = \hat{\boldsymbol{k}}_{\mathrm{S}} \cdot \hat{\boldsymbol{k}}_{\mathrm{L}}$. Here, we used $\mathcal{M}(|\boldsymbol{k}_{\mathrm{S}} + \boldsymbol{k}_{\mathrm{L}}|) = \mathcal{M}(k_{\mathrm{S}}) + \mathcal{O}(q)$.

For our computational convenience, we change the coordinate system such that $\boldsymbol{p}$ lies along the z axis as $\tilde{p}^i = \mathcal{R}^i{}_j(\hat{\boldsymbol{p}}) p^j = (0, 0, \tilde{p})$, where $\mathcal{R}^i{}_j(\hat{\boldsymbol{p}})$ is a rotational matrix. Then, $\boldsymbol{k}_{\mathrm{S}}$ and $\boldsymbol{k}_{\mathrm{L}}$ are transformed into

$$\hat{\hat{\boldsymbol{k}}}_a = \left(\sqrt{1 - \mu_a^2} \cos \psi_a, \, \sqrt{1 - \mu_a^2} \sin \psi_a, \, \mu_a \right), \qquad (a = \mathrm{L}, \, \mathrm{S}) \tag{D.72}$$

with

$$\mu = \hat{\boldsymbol{k}}_{\mathrm{S}} \cdot \hat{\boldsymbol{k}}_{\mathrm{L}} = \sqrt{(1 - \mu_{\mathrm{S}}^2)(1 - \mu_{\mathrm{L}}^2)} \cos(\psi_{\mathrm{S}} - \psi_{\mathrm{L}}) + \mu_{\mathrm{S}} \mu_{\mathrm{L}}, \tag{D.73}$$

where we introduced $\mu_X \equiv \hat{\boldsymbol{p}} \cdot \hat{\boldsymbol{k}}_X$. In this coordinate, we obtain

$$\frac{\tilde{k}_{\mathrm{S}i} \tilde{k}_{\mathrm{S}j}}{k_{\mathrm{S}}^2} = \begin{pmatrix} \cos^2 \psi_{\mathrm{S}} (1 - \mu_{\mathrm{S}}^2) & \cos \psi_{\mathrm{S}} \sin \psi_{\mathrm{S}} (1 - \mu_{\mathrm{S}}^2) & \cos \psi_{\mathrm{S}} \mu_{\mathrm{S}} \sqrt{1 - \mu_{\mathrm{S}}^2} \\ \cos \psi_{\mathrm{S}} \sin \psi_{\mathrm{S}} (1 - \mu_{\mathrm{S}}^2) & \sin^2 \psi_{\mathrm{S}} (1 - \mu_{\mathrm{S}}^2) & \sin \psi_{\mathrm{S}} \mu_{\mathrm{S}} \sqrt{1 - \mu_{\mathrm{S}}^2} \\ \cos \psi_{\mathrm{S}} \mu_{\mathrm{S}} \sqrt{1 - \mu_{\mathrm{S}}^2} & \sin \psi_{\mathrm{S}} \mu_{\mathrm{S}} \sqrt{1 - \mu_{\mathrm{S}}^2} & \mu_{\mathrm{S}}^2 \end{pmatrix} . \tag{D.74}$$

Using this expression and integrating with respect to $\psi_{\rm S}$, we obtain

$$\int_0^{2\pi} \frac{d\psi_{\rm S}}{2\pi} \left[\hat{\hat{k}}_{{\rm S}i}\hat{\hat{k}}_{{\rm S}j} - \frac{1}{3}\delta_{ij}\right] = \mathcal{P}_2(\mu_{\rm S}) \left[\hat{\hat{p}}_i\hat{\hat{p}}_j - \frac{1}{3}\delta_{ij}\right] , \tag{D.75}$$

and

$$\begin{aligned}\int_0^{2\pi} \frac{d\psi_{\rm S}}{2\pi}\mu \left[\hat{\hat{k}}_{{\rm S}m}\hat{\hat{k}}_{{\rm S}n} - \frac{1}{3}\delta_{mn}\right] = \frac{1}{5}\left[\mathcal{P}_1(\mu_{\rm S}) - \mathcal{P}_3(\mu_{\rm S})\right] \left[\hat{\hat{p}}_m\hat{\hat{k}}_{{\rm L}n} + \hat{\hat{p}}_n\hat{\hat{k}}_{{\rm L}m} - \frac{2}{3}\mu_{\rm L}\delta_{mn}\right] \\ + \mu_{\rm L}\mathcal{P}_3(\mu_{\rm S}) \left[\hat{\hat{p}}_m\hat{\hat{p}}_n - \frac{1}{3}\delta_{mn}\right] .\end{aligned} \tag{D.76}$$

Notice that as is shown Eq. (D.73), μ depends on $\mu_{\rm S}$, , $\mu_{\rm L}$, $\psi_{\rm S}$, and $\psi_{\rm L}$. Using these formulae, Eq. (D.71) can be recast into

$$\begin{aligned}&\langle\delta(\boldsymbol{x})\delta(\boldsymbol{y})K_{ij}(\boldsymbol{y})\rangle \\ &= \int \frac{d^3\boldsymbol{k}_{\rm L}}{(2\pi)^3} e^{i\boldsymbol{k}_{\rm L}\cdot\boldsymbol{r}}\mathcal{M}(k_{\rm L})P_\Psi(k_{\rm L}) \int \frac{dk_{\rm S}}{(2\pi)^2} k_{\rm S}^2\mathcal{M}^2(k_{\rm S})P_\Psi(k_{\rm S}) \\ &\quad \times \int_{-1}^{1} d\mu_{\rm S} \sum_{l=0}^{\infty} i^{\frac{1-(-1)^l}{2}}\mathcal{P}_l(\mu_{\rm S}) \left\{\left[\hat{p}_i\hat{p}_j - \frac{1}{3}\delta_{ij}\right]\left[\bar{A}_l\mathcal{P}_2(\mu_{\rm S}) + \bar{B}_l\mu_{\rm L}\mathcal{P}_3(\mu_{\rm S})\right]\right. \\ &\qquad \left. + \frac{1}{5}\bar{B}_l\left[\mathcal{P}_1(\mu_{\rm S}) - \mathcal{P}_3(\mu_{\rm S})\right]\left[\hat{p}_i\hat{k}_{{\rm L}j} + \hat{p}_j\hat{k}_{{\rm L}i} - \frac{2}{3}\mu_{\rm L}\delta_{ij}\right] + \mathcal{O}(q)\right\} \\ &= \int \frac{d^3\boldsymbol{k}_{\rm L}}{(2\pi)^3} e^{i\boldsymbol{k}_{\rm L}\cdot\boldsymbol{r}}\mathcal{M}(k_{\rm L})P_\Psi(k_{\rm L}) \int \frac{dk_{\rm S}}{(2\pi)^2} k_{\rm S}^2\mathcal{M}^2(k_{\rm S})P_\Psi(k_{\rm S}) \\ &\quad \times \frac{2}{5}\left\{\frac{1}{3}i\bar{B}_1\left[\hat{p}_i\hat{k}_{{\rm L}j} + \hat{p}_j\hat{k}_{{\rm L}i} - \frac{2}{3}\mu_{\rm L}\delta_{ij}\right] + \bar{A}_2\left[\hat{p}_i\hat{p}_j - \frac{1}{3}\delta_{ij}\right]\right. \\ &\qquad \left. + \frac{5}{7}i\bar{B}_3\left[\mu_{\rm L}\left[\hat{p}_i\hat{p}_j - \frac{1}{3}\delta_{ij}\right] - \frac{1}{5}\left(\hat{p}_i\hat{k}_{{\rm L}j} + \hat{p}_j\hat{k}_{{\rm L}i} - \frac{2}{3}\mu_{\rm L}\delta_{ij}\right)\right] + \mathcal{O}(q)\right\} .\end{aligned} \tag{D.77}$$

Here, we used the orthogonality of the Legendre polynomials. Noticing the fact that the second term in Eq. (D.69) is related to the first term as

$$\langle\delta(\boldsymbol{x})\left[K_{ik}K^k{}_j - \frac{1}{3}\delta_{ij}(K_{lm})^2\right](\boldsymbol{y})\rangle = \frac{1}{3}\langle\delta(\boldsymbol{x})\delta(\boldsymbol{y})K_{ij}(\boldsymbol{y})\rangle + \mathcal{O}(q), \tag{D.78}$$

we can immediately compute the second term.

Using

$$\xi(\boldsymbol{r}) = \int \frac{d^3\boldsymbol{k}_{\rm L}}{(2\pi)^3} e^{i\boldsymbol{k}_{\rm L}\cdot\boldsymbol{r}}\mathcal{M}^2(k_{\rm L})P_\Psi(k_{\rm L}), \tag{D.79}$$

$$\xi_{\delta\Psi}(\boldsymbol{r}) = \int \frac{d^3\boldsymbol{k}_{\rm L}}{(2\pi)^3} e^{i\boldsymbol{k}_{\rm L}\cdot\boldsymbol{r}}\mathcal{M}(k_{\rm L})P_\Psi(k_{\rm L}), \tag{D.80}$$

$$\mathcal{I}(\boldsymbol{r}) = \int \frac{d^3\boldsymbol{k}_{\rm L}}{(2\pi)^3} e^{i\boldsymbol{k}_{\rm L}\cdot\boldsymbol{r}}\frac{\mathcal{M}(k_{\rm L})}{k_{\rm L}}P_\Psi(k_{\rm L}), \tag{D.81}$$

and the variance of the matter density field $\langle\delta^2\rangle$, given by

$$\langle\delta^2\rangle = \int \frac{dk}{2\pi^2} k^2 \mathcal{M}^2(k) P_\Psi(k), \tag{D.82}$$

we finally obtain

$$\begin{aligned}\langle\delta(\boldsymbol{x})\tilde{g}_{ij}(\boldsymbol{y})\rangle = b_K^{(2)}\mathcal{D}_{ij}\xi(\boldsymbol{r}) + \frac{1}{10}\bar{A}_2(b_{\delta K}^{(2)} + \frac{1}{3}b_{K^2}^{(2)}) \left(\hat{p}_i\hat{p}_j - \frac{1}{3}\delta_{ij}\right)\xi_{\delta\Psi}(\boldsymbol{r})\langle\delta^2\rangle \\ + \mathcal{B}_1\left(\hat{p}_i\hat{p}_j - \frac{1}{3}\delta_{ij}\right)\hat{\boldsymbol{p}}\cdot\partial_{\boldsymbol{x}}\,\mathcal{I}(\boldsymbol{r}) + \mathcal{B}_2\left(\hat{p}_i\partial_j + \hat{p}_j\partial_i - \frac{2}{3}\delta_{ij}\hat{p}^k\partial_k\right)\mathcal{I}(\boldsymbol{r}),\end{aligned} \tag{D.83}$$

where $\mathcal{B}_1$, $\mathcal{B}_2$ are

$$\mathcal{B}_1 \equiv \frac{1}{14}(b_{\delta K}^{(2)} + \frac{1}{3}b_{K^2}^{(2)}\bar{B}_3\langle\delta^2\rangle, \tag{D.84}$$

$$\mathcal{B}_2 \equiv \frac{1}{210}(7\bar{B}_1 - 3\bar{B}_3)(b_{\delta K}^{(2)} + \frac{1}{3}b_{K^2}^{(2)})\langle\delta^2\rangle. \tag{D.85}$$

Number density

To compute the scale dependent bias for the galaxy number density, we compute the two-point function $\langle\delta(\boldsymbol{x})\delta_{\rm n}(\boldsymbol{y})\rangle$, which includes the three-point functions

$$\langle\delta(\boldsymbol{x})\delta^2(\boldsymbol{y})\rangle \quad \text{and} \quad \langle\delta(\boldsymbol{x})(K_{ij})^2(\boldsymbol{y})\rangle\,. \tag{D.86}$$

The first term is given by

$$\begin{aligned}\langle\delta(\boldsymbol{x})\delta^2(\boldsymbol{y})\rangle = \int\frac{d^3\boldsymbol{k}_{\rm L}}{(2\pi)^3}e^{i\boldsymbol{k}_{\rm L}\cdot\boldsymbol{r}}\mathcal{M}(k_{\rm L})P_\Psi(k_{\rm L})\int\frac{d^3\boldsymbol{k}_{\rm S}}{(2\pi)^3}\mathcal{M}^2(k_{\rm S})P_\Psi(k_{\rm S}) \\ \times\sum_{\ell=0}^{\infty} i^{\frac{1-(-1)^l}{2}}\left[\bar{A}_l + \bar{B}_l\mu + \mathcal{O}(q)\right]\mathcal{P}_\ell(\mu_{\rm S}),\end{aligned} \tag{D.87}$$

where we used Eq. (B.1) and $\mathcal{M}(|\boldsymbol{k}_{\rm S} + \boldsymbol{k}_{\rm L}|) = \mathcal{M}(k_{\rm S}) + \mathcal{O}(q)$. Since this formula does not depend on the azimuthal direction, μ in the square brackets can be simply replaced with $\mu_{\rm S}\mu_{\rm L}$ after integrating over $\psi_{\rm S}$. Using the orthogonality of Legendre polynomials, we obtain

$$\begin{aligned}\langle\delta(\boldsymbol{x})\delta^2(\boldsymbol{y})\rangle = \int\frac{d^3\boldsymbol{k}_{\rm L}}{(2\pi)^3}e^{i\boldsymbol{k}_{\rm L}\cdot\boldsymbol{r}}\mathcal{M}(k_{\rm L})P_\Psi(k_{\rm L})\int\frac{dk_{\rm S}}{(2\pi)^2}k_{\rm S}^2\mathcal{M}^2(k_{\rm S})P_\Psi(k_{\rm S}) \\ \times\left[2\bar{A}_0 + \frac{2}{3}i\mu_{\rm L}\bar{B}_1\right] + \mathcal{O}(q).\end{aligned} \tag{D.88}$$

Using

$$\left[\hat{k}_{{\rm S}i}\hat{k}_{{\rm S}j} - \frac{1}{3}\delta_{ij}\right]\left[\widehat{(k_{\rm S} + k_{\rm L})}^i\widehat{(k_{\rm S} + k_{\rm L})}^j - \frac{1}{3}\delta^{ij}\right] = \frac{2}{3} + \mathcal{O}(q^2)\,, \tag{D.89}$$

we also can compute $\langle\delta(\boldsymbol{x})(K_{ij})^2(\boldsymbol{y})\rangle$ easily as $\langle\delta(\boldsymbol{x})(K_{ij})^2(\boldsymbol{y})\rangle = \frac{2}{3}\langle\delta(\boldsymbol{x})\delta^2(\boldsymbol{y})\rangle + \mathcal{O}(q^2)$. Using these formulae, we obtain

$$\langle\delta(\boldsymbol{x})\delta_{\rm n}(\boldsymbol{y})\rangle = b_\delta^{(0)}\xi(\boldsymbol{r}) + \frac{1}{2}\bar{A}_0\langle\delta^2\rangle(b_{\delta^2}^{(0)} + \frac{2}{3}b_{K^2}^{(0)})\xi_{\delta\Psi}(\boldsymbol{r}) + \frac{1}{6}\bar{B}_1\langle\delta^2\rangle(b_{\delta^2}^{(0)} + \frac{2}{3}b_{K^2}^{(0)})\hat{\boldsymbol{p}}\cdot\partial_{\boldsymbol{x}}\mathcal{I}(\boldsymbol{r}). \tag{D.90}$$

D.5.2 Derivation and Feature of Angular power spectra

Here, we perform the harmonic expansion of the intrinsic alignment term in the cosmic shear. For our convenience, we decompose the contribution of the intrinsic alignment $a_{lm}^{\rm IA}$ as

$$a_{lm}^{\rm IA} = a_{lm}^{(0)} + a_{lm}^{(p)},$$

where $a_{lm}^{(0)}$ is the contribution from the first term of Eq. (B.3) and $a_{lm}^{(p)}$ is the one from the second term. In the Fourier space, we obtain

$${}_{\pm2}\gamma^{\rm IA}(z,\,\hat{\boldsymbol{n}}) = \int\frac{d^3\boldsymbol{k}}{(2\pi)^3}\,e^{ix\hat{\boldsymbol{k}}\cdot\hat{\boldsymbol{n}}}\,m_\mp^i m_\mp^j\left[b_K^{(2)}\hat{k}_i\hat{k}_j\delta(z,\,\boldsymbol{k}) + 3b_{\rm NG}^p\bar{A}_2\,\hat{p}_i\hat{p}_j\Psi(\boldsymbol{k})\right] \tag{D.91}$$

with $x\equiv k\chi(z)$ and $\hat{\boldsymbol{k}}\equiv\boldsymbol{k}/k$. In performing the expansion in terms of the spherical harmonics, we choose the z axis along the direction of $\hat{\boldsymbol{p}}$, i.e., $\hat{\boldsymbol{p}} = (0,\,0,\,1)$. With this choice, we obtain $m_\pm^i\,\hat{p}_i = -\sin\theta/\sqrt{2}$. For our purpose, we write the basis of the Fourier mode expansion as

$$e^{ix\hat{\boldsymbol{k}}\cdot\hat{\boldsymbol{n}}} = \sum_{l=0}^{\infty}(2l+1)i^l j_l(x)\mathcal{P}_l(\hat{\boldsymbol{k}}\cdot\hat{\boldsymbol{n}}) = 4\pi\sum_{l=0}^{\infty}\sum_{m=-l}^{l}i^l j_l(x)Y_{lm}(\hat{\boldsymbol{n}})Y_{lm}^*(\hat{\boldsymbol{k}})\,. \tag{D.92}$$

Using $\hat{k}_i e^{ix\hat{\boldsymbol{k}}\cdot\hat{\boldsymbol{n}}} = (1/ix)\partial/\partial\hat{n}^i e^{ix\hat{\boldsymbol{k}}\cdot\hat{\boldsymbol{n}}}$ and

$${}_{\pm2}Y_{lm}(\hat{\boldsymbol{n}}) = 2\sqrt{\frac{(l-2)!}{(l+2)!}}m_\mp^i m_\mp^j\frac{\partial^2}{\partial\hat{n}^i\partial\hat{n}^j}Y_{lm}(\hat{\boldsymbol{n}})\,,$$

we obtain the contribution from the first term as

$$a_{lm}^{(0)} = -b_K^{(2)}\sqrt{\frac{(l+2)!}{(l-2)!}}\int\frac{d^3\boldsymbol{k}}{(2\pi)^3}\int dz\frac{dN_{\rm I}}{dz}\frac{1}{x^2}i^l j_l(x)Y_{lm}^*(\hat{\boldsymbol{k}})\delta(z,\,\boldsymbol{k}) \tag{D.93}$$

for $l\geq 2$ and $a_{lm}^{(0)} = 0$ for $l = 0,\,1$. Here, we inserted the redshift distribution of the galaxy sample $dN_{\rm I}/dz$. Using Eq. (D.92), the contribution from the second term can be expressed as

$$\begin{aligned} a_{lm}^{(p)} = (3b_{\rm NG}^p\bar{A}_2)(2\pi)\sqrt{\frac{(l-2)!}{(l+2)!}}\sum_{l'=0}^{\infty}\sum_{m'=-l'}^{l'}i^{l'}\int\frac{d^3\boldsymbol{k}}{(2\pi)^3}\int dz\frac{dN_{\rm I}}{dz}\Psi(\boldsymbol{k})j_{l'}(x)Y_{l'm'}(\hat{\boldsymbol{k}}) \\ \times\int d\Omega_{\boldsymbol{n}}Y_{lm}^*(\hat{\boldsymbol{n}})\bar{\eth}^2\left[Y_{l'm'}(\hat{\boldsymbol{n}})\sin^2\theta\right]\,. \end{aligned} \tag{D.94}$$

Since the constant vector $\hat{\boldsymbol{p}}$ violates the global rotation symmetry, $a_{lm}^{(p)}$ can be contaminated by non-diagonal multipoles with $l' \neq l$ and $m' \neq m$, while $a_{lm}^{(0)}$ does not depend on contributions of other multipoles. Performing the integral over the solid angle of $\hat{\boldsymbol{n}}$, which is lengthy but straightforward, we obtain Eq. (B.4), where coefficients $\alpha_{l,m}^{(s)}$ are given by

$$\alpha_{l,m}^{(0)} = -\frac{2(l-1)(l+2)\{l(l+1)-3m^2\}}{(2l-1)(2l+3)} \qquad (-l \leq m \leq l)\,, \tag{D.95}$$

$$\alpha_{l,m}^{(+1)} = -2m(l-1)\sqrt{\frac{(l-m+1)(l+m+1)}{(2l+1)(2l+3)}} \qquad (l \geq 1,\ -l \leq m \leq l)\,, \tag{D.96}$$

$$\alpha_{l,m}^{(-1)} = 2m(l+2)\sqrt{\frac{(l-m)(l+m)}{(2l-1)(2l+1)}} \qquad (-l+1 \leq m \leq l-1)\,, \tag{D.97}$$

$$\alpha_{l,m}^{(+2)} = \frac{l(l-1)\sqrt{(l-m+2)(l+m+2)(l+m+1)(l-m+1)}}{(2l+3)\sqrt{(2l+1)(2l+5)}} \qquad (l \geq 2,\ -l \leq m \leq l)\,, \tag{D.98}$$

$$\alpha_{l,m}^{(-2)} = \frac{(l+1)(l+2)\sqrt{(l-m)(l+m)(l+m-1)(l-m-1)}}{(2l-1)\sqrt{(2l-3)(2l+1)}} \qquad (-l+2 \leq m \leq l-2)\,, \tag{D.99}$$

and otherwise 0.

Rotation of axis

We calculated the angular power spectrum, choosing the z-axis (with $\theta = 0$) such that being along $\hat{\boldsymbol{p}}$. With this choice, we found that there are no cross-correlations between different ms. Next, we will show that the diagonalization over m is specific for this choice of the axis and in general there exist the cross-correlations.

Rotating the z axis to the direction $(\theta,\, \psi)$ changes the coefficients ${}_s a_{lm}$ of the expansion in terms of the spin weighted spherical harmonics ${}_sY_{lm}$ as

$${}_s\tilde{a}_{lm} = \sqrt{\frac{4\pi}{2l+1}}(-1)^m \sum_{m'} {}_{-m}Y_{l\,m'}(\theta,\, \psi)\, {}_s a_{lm'}\,. \tag{D.100}$$

Using this expression, we find that a_{lm}^{E} and a_{lm}^{B} both transform in the same way as

$$\tilde{a}_{lm}^{X} = \sqrt{\frac{4\pi}{2l+1}}(-1)^m \sum_{m'} {}_{-m}Y_{l\,m'}(\theta,\, \psi)\, a_{lm'}^{X} \tag{D.101}$$

for $X = \mathrm{E},\, \mathrm{B}$ and the angular power spectra in the two frames are related as

$$\begin{aligned}\langle \tilde{a}^{X}_{lm} \tilde{a}^{Y\,*}_{l'm'} \rangle = (-1)^{m+m'} \sqrt{\frac{4\pi}{2l+1}} \sqrt{\frac{4\pi}{2l'+1}} \\ \times \sum_{\bar{m}} {}_{-m}Y_{l\,\bar{m}}(\theta,\, \psi)\, {}_{-m'}Y_{l'\,\bar{m}}{}^{*}(\theta,\, \psi) \langle a^{X}_{l\bar{m}} a^{Y\,*}_{l'\bar{m}} \rangle \end{aligned} \tag{D.102}$$

for $X,\, Y = \mathrm{E},\, \mathrm{B}$. Now, we see that in a general frame, both of l and m are not diagonal.

Bibliography

[1] K. Sato. “First Order Phase Transition of a Vacuum and Expansion of the Universe”. In: *Mon. Not. Roy. Astron. Soc.* 195 (1981), pp. 467–479.

[2] Alan H. Guth. “The Inflationary Universe: A Possible Solution to the Horizon and Flatness Problems”. In: *Phys. Rev.* D23 (1981). [Adv. Ser. Astrophys. Cosmol.3,139(1987)], pp. 347–356. DOI: `10.1103/PhysRevD.23.347`.

[3] Y. Akrami et al. “Planck 2018 results. X. Constraints on inflation”. In: (2018). arXiv: `1807.06211 [astro-ph.CO]`.

[4] T. Matsumura et al. “Mission design of LiteBIRD”. In: *J. Low Temp. Phys.* 176 (2014), p. 733. DOI: `10.1007/s10909-013-0996-1`. arXiv: `1311.2847 [astro-ph.IM]`.

[5] D. Spergel et al. “Wide-Field InfrarRed Survey Telescope-Astrophysics Focused Telescope Assets WFIRST-AFTA 2015 Report”. In: (Mar. 2015). arXiv: `1503.03757 [astro-ph.IM]`.

[6] R. Laureijs et al. “Euclid Definition Study Report”. In: (Oct. 2011). arXiv: `1110.3193 [astro-ph.CO]`.

[7] Olivier Doré et al. “Cosmology with the SPHEREX All-Sky Spectral Survey”. In: (Dec. 2014). arXiv: `1412.4872 [astro-ph.CO]`.

[8] Paul A. Abell et al. “LSST Science Book, Version 2.0”. In: (Dec. 2009). arXiv: `0912.0201 [astro-ph.IM]`.

[9] M. A. Troxel et al. “Dark Energy Survey Year 1 Results: Cosmological Constraints from Cosmic Shear”. In: *ArXiv e-prints* (2017). arXiv: `1708.01538 [astro-ph.CO]`.

[10] Marika Asgari et al. “KiDS-1000 Cosmology: Cosmic shear constraints and comparison between two point statistics”. In: *Astron. Astrophys.* 645 (2021), A104. DOI: `10.1051/0004-6361/202039070`. arXiv: `2007.15633 [astro-ph.CO]`.

[11] Chiaki Hikage et al. “Cosmology from cosmic shear power spectra with Subaru Hyper Suprime-Cam first-year data”. In: *Submitted to: Publ. Astron. Soc. Jap.* (2018). arXiv: `1809.09148 [astro-ph.CO]`.

[12] Andrew Coutts. “The scale and dispersion of galactic alignments”. In: *Monthly Notices of the Royal Astronomical Society* 278.1 (Jan. 1996), pp. 87–94. ISSN: 0035-8711. DOI: `10.1093/mnras/278.1.87`. eprint: `https://academic.oup.com/mnras/article-pdf/278/1/87/3460500/278-1-87.pdf`. URL: `https://doi.org/10.1093/mnras/278.1.87`.

[13] Jounghun Lee and Ue-Li Pen. “Cosmic shear from galaxy spins”. In: *Astrophys. J. Lett.* 532 (2000), p. L5. DOI: 10.1086/312556. arXiv: astro-ph/9911328.

[14] Paolo Catelan, Marc Kamionkowski, and Roger D. Blandford. “Intrinsic and extrinsic galaxy alignment”. In: *Mon. Not. Roy. Astron. Soc.* 320 (2001), pp. L7–L13. DOI: 10.1046/j.1365-8711.2001.04105.x. arXiv: astro-ph/0005470 [astro-ph].

[15] Ue-Li Pen et al. “Cosmic Tides”. In: (Feb. 2012). arXiv: 1202.5804 [astro-ph.CO].

[16] Juan Martin Maldacena. “Non-Gaussian features of primordial fluctuations in single field inflationary models”. In: *JHEP* 05 (2003), p. 013. DOI: 10.1088/1126-6708/2003/05/013. arXiv: astro-ph/0210603.

[17] Clifford Cheung et al. “On the consistency relation of the 3-point function in single field inflation”. In: *JCAP* 02 (2008), p. 021. DOI: 10.1088/1475-7516/2008/02/021. arXiv: 0709.0295 [hep-th].

[18] N. Bartolo, S. Matarrese, and A. Riotto. “Nongaussianity from inflation”. In: *Phys. Rev. D* 65 (2002), p. 103505. DOI: 10.1103/PhysRevD.65.103505. arXiv: hep-ph/0112261.

[19] Christian T. Byrnes, Ki-Young Choi, and Lisa M. H. Hall. “Conditions for large non-Gaussianity in two-field slow-roll inflation”. In: *JCAP* 10 (2008), p. 008. DOI: 10.1088/1475-7516/2008/10/008. arXiv: 0807.1101 [astro-ph].

[20] David H. Lyth, Carlo Ungarelli, and David Wands. “The Primordial density perturbation in the curvaton scenario”. In: *Phys. Rev.* D67 (2003), p. 023503. DOI: 10.1103/PhysRevD.67.023503. arXiv: astro-ph/0208055 [astro-ph].

[21] Nima Arkani-Hamed and Juan Maldacena. “Cosmological Collider Physics”. In: (2015). arXiv: 1503.08043 [hep-th].

[22] Neal Dalal et al. “The imprints of primordial non-gaussianities on large-scale structure: scale dependent bias and abundance of virialized objects”. In: *Phys. Rev.* D77 (2008), p. 123514. DOI: 10.1103/PhysRevD.77.123514. arXiv: 0710.4560 [astro-ph].

[23] Anze Slosar et al. “Constraints on local primordial non-Gaussianity from large scale structure”. In: *JCAP* 0808 (2008), p. 031. DOI: 10.1088/1475-7516/2008/08/031. arXiv: 0805.3580 [astro-ph].

[24] Donghui Jeong, Fabian Schmidt, and Christopher M. Hirata. “Large-scale clustering of galaxies in general relativity”. In: *Phys. Rev. D* 85 (2012), p. 023504. DOI: 10.1103/PhysRevD.85.023504. arXiv: 1107.5427 [astro-ph.CO].

[25] Niayesh Afshordi and Andrew J. Tolley. “Primordial non-gaussianity, statistics of collapsed objects, and the Integrated Sachs-Wolfe effect”. In: *Phys. Rev.* D78 (2008), p. 123507. DOI: 10.1103/PhysRevD.78.123507. arXiv: 0806.1046 [astro-ph].

[26] Tobias Baldauf et al. “Galaxy Bias and non-Linear Structure Formation in General Relativity”. In: *JCAP* 10 (2011), p. 031. DOI: `10.1088/1475-7516/2011/10/031`. arXiv: `1106.5507 [astro-ph.CO]`.

[27] Giovanni Cabass, Enrico Pajer, and Fabian Schmidt. “Imprints of Oscillatory Bispectra on Galaxy Clustering”. In: *JCAP* 09 (2018), p. 003. DOI: `10.1088/1475-7516/2018/09/003`. arXiv: `1804.07295 [astro-ph.CO]`.

[28] Eva-Maria Mueller et al. “The clustering of galaxies in the completed SDSS-IV extended Baryon Oscillation Spectroscopic Survey: Primordial non-Gaussianity in Fourier Space”. In: (June 2021). arXiv: `2106.13725 [astro-ph.CO]`.

[29] Teppei Okumura, Y. P. Jing, and Cheng Li. “Intrinsic Ellipticity Correlation of SDSS Luminous Red Galaxies and Misalignment with their Host Dark Matter Halos”. In: *Astrophys. J.* 694 (2009), pp. 214–221. DOI: `10.1088/0004-637X/694/1/214`. arXiv: `0809.3790 [astro-ph]`.

[30] Sukhdeep Singh and Rachel Mandelbaum. “Intrinsic alignments of BOSS LOWZ galaxies II. Impact of shape measurement methods”. In: *Mon. Not. Roy. Astron. Soc.* 457.3 (2016), pp. 2301–2317. DOI: `10.1093/mnras/stw144`. arXiv: `1510.06752 [astro-ph.CO]`.

[31] Christopher M. Hirata et al. “Intrinsic galaxy alignments from the 2SLAQ and SDSS surveys: Luminosity and redshift scalings and implications for weak lensing surveys”. In: *Mon. Not. Roy. Astron. Soc.* 381 (2007), pp. 1197–1218. DOI: `10.1111/j.1365-2966.2007.12312.x`. arXiv: `astro-ph/0701671 [astro-ph]`.

[32] Nora Elisa Chisari and Cora Dvorkin. “Cosmological Information in the Intrinsic Alignments of Luminous Red Galaxies”. In: *JCAP* 12 (2013), p. 029. DOI: `10.1088/1475-7516/2013/12/029`. arXiv: `1308.5972 [astro-ph.CO]`.

[33] Ji Yao et al. “Unveiling the Intrinsic Alignment of Galaxies with Self-Calibration and DECaLS DR3 data”. In: *Astrophys. J.* 904.2 (2020), p. 135. DOI: `10.3847/1538-4357/abc175`. arXiv: `2002.09826 [astro-ph.CO]`.

[34] Ken Osato et al. “Strong orientation dependence of surface mass density profiles of dark haloes at large scales”. In: *Mon. Not. Roy. Astron. Soc.* 477.2 (2018), pp. 2141–2153. DOI: `10.1093/mnras/sty762`. arXiv: `1712.00094 [astro-ph.CO]`.

[35] Teppei Okumura and Atsushi Taruya. “Anisotropies of galaxy ellipticity correlations in real and redshift space: angular dependence in linear tidal alignment model”. In: *Mon. Not. Roy. Astron. Soc.* 493.1 (2020), pp. L124–L128. DOI: `10.1093/mnrasl/slaa024`. arXiv: `1912.04118 [astro-ph.CO]`.

[36] Teppei Okumura et al. “Intrinsic Alignments and Splashback Radius of Dark Matter Halos from Cosmic Density and Velocity Fields”. In: (June 2017). arXiv: `1706.08860 [astro-ph.CO]`.

[37] Teppei Okumura, Atsushi Taruya, and Takahiro Nishimichi. "Intrinsic alignment statistics of density and velocity fields at large scales: Formulation, modeling and baryon acoustic oscillation features". In: *Phys. Rev. D* 100.10 (2019), p. 103507. DOI: 10.1103/PhysRevD.100.103507. arXiv: 1907.00750 [astro-ph.CO].

[38] Teppei Okumura, Atsushi Taruya, and Takahiro Nishimichi. "Testing tidal alignment models for anisotropic correlations of halo ellipticities with N-body simulations". In: *Mon. Not. Roy. Astron. Soc.* 494.1 (2020), pp. 694–702. DOI: 10.1093/mnras/staa718. arXiv: 2001.05302 [astro-ph.CO].

[39] Toshiki Kurita et al. "Power spectrum of halo intrinsic alignments in simulations". In: *Mon. Not. Roy. Astron. Soc.* 501.1 (2021), pp. 833–852. DOI: 10.1093/mnras/staa3625. arXiv: 2004.12579 [astro-ph.CO].

[40] Christopher M. Hirata and Uros Seljak. "Intrinsic alignment-lensing interference as a contaminant of cosmic shear". In: *Phys. Rev.* D70 (2004). [Erratum: Phys. Rev.D82,049901(2010)], p. 063526. DOI: 10.1103/PhysRevD.82.049901, 10.1103/PhysRevD.70.063526. arXiv: astro-ph/0406275 [astro-ph].

[41] Fabian Schmidt, Nora Elisa Chisari, and Cora Dvorkin. "Imprint of inflation on galaxy shape correlations". In: *JCAP* 1510.10 (2015), p. 032. DOI: 10.1088/1475-7516/2015/10/032. arXiv: 1506.02671 [astro-ph.CO].

[42] Kazuyuki Akitsu et al. "Imprint of anisotropic primordial non-Gaussianity on halo intrinsic alignments in simulations". In: *Phys. Rev. D* 103.8 (2021), p. 083508. DOI: 10.1103/PhysRevD.103.083508. arXiv: 2007.03670 [astro-ph.CO].

[43] Kazuhiro Kogai et al. "Intrinsic galaxy alignment from angular dependent primordial non-Gaussianity". In: *JCAP* 1808.08 (2018), p. 014. DOI: 10.1088/1475-7516/2018/08/014. arXiv: 1804.06284 [astro-ph.CO].

[44] Kazuhiro Kogai et al. "Galaxy imaging surveys as spin-sensitive detector for cosmological colliders". In: *JCAP* 03 (2021), p. 060. DOI: 10.1088/1475-7516/2021/03/060. arXiv: 2009.05517 [astro-ph.CO].

[45] Planck Collaboration VI. "Planck 2018 results. VI. Cosmological parameters". In: (2018). arXiv: 1807.06209 [astro-ph.CO].

[46] Yi Wang. "Inflation, Cosmic Perturbations and Non-Gaussianities". In: *Commun. Theor. Phys.* 62 (2014), pp. 109–166. DOI: 10.1088/0253-6102/62/1/19. arXiv: 1303.1523 [hep-th].

[47] David H. Lyth and Andrew R. Liddle. *The primordial density perturbation: Cosmology, inflation and the origin of structure*. 2009.

[48] N. Bartolo et al. "Non-Gaussianity from inflation: Theory and observations". In: *Phys. Rept.* 402 (2004), pp. 103–266. DOI: 10.1016/j.physrep.2004.08.022. arXiv: astro-ph/0406398.

[49] Xingang Chen. “Primordial Non-Gaussianities from Inflation Models”. In: *Adv. Astron.* 2010 (2010), p. 638979. DOI: `10.1155/2010/638979`. arXiv: `1002.1416 [astro-ph.CO]`.

[50] Tomo Takahashi. “Primordial non-Gaussianity and the inflationary Universe”. In: *PTEP* 2014.6 (2014), 06B105. DOI: `10.1093/ptep/ptu060`.

[51] David H. Lyth and David Wands. “Generating the curvature perturbation without an inflaton”. In: *Phys. Lett. B* 524 (2002), pp. 5–14. DOI: `10.1016/S0370-2693(01)01366-1`. arXiv: `hep-ph/0110002`.

[52] Takeo Moroi and Tomo Takahashi. “Effects of cosmological moduli fields on cosmic microwave background”. In: *Phys. Lett. B* 522 (2001). [Erratum: Phys.Lett.B 539, 303–303 (2002)], pp. 215–221. DOI: `10.1016/S0370-2693(01)01295-3`. arXiv: `hep-ph/0110096`.

[53] Francis Bernardeau and Jean-Philippe Uzan. “NonGaussianity in multifield inflation”. In: *Phys. Rev. D* 66 (2002), p. 103506. DOI: `10.1103/PhysRevD.66.103506`. arXiv: `hep-ph/0207295`.

[54] Christian T. Byrnes and David Wands. “Curvature and isocurvature perturbations from two-field inflation in a slow-roll expansion”. In: *Phys. Rev. D* 74 (2006), p. 043529. DOI: `10.1103/PhysRevD.74.043529`. arXiv: `astro-ph/0605679`.

[55] Paolo Creminelli and Matias Zaldarriaga. “Single field consistency relation for the 3-point function”. In: *JCAP* 10 (2004), p. 006. DOI: `10.1088/1475-7516/2004/10/006`. arXiv: `astro-ph/0407059`.

[56] Eva Silverstein and David Tong. “Scalar speed limits and cosmology: Acceleration from D-cceleration”. In: *Phys. Rev. D* 70 (2004), p. 103505. DOI: `10.1103/PhysRevD.70.103505`. arXiv: `hep-th/0310221`.

[57] Pieter Daniel Meerburg, Jan Pieter van der Schaar, and Pier Stefano Corasaniti. “Signatures of Initial State Modifications on Bispectrum Statistics”. In: *JCAP* 0905 (2009), p. 018. DOI: `10.1088/1475-7516/2009/05/018`. arXiv: `0901.4044 [hep-th]`.

[58] Y. Akrami et al. “Planck 2018 results. IX. Constraints on primordial non-Gaussianity”. In: (May 2019). arXiv: `1905.05697 [astro-ph.CO]`.

[59] Ashley J. Ross et al. “The Clustering of Galaxies in SDSS-III DR9 Baryon Oscillation Spectroscopic Survey: Constraints on Primordial Non-Gaussianity”. In: *Mon. Not. Roy. Astron. Soc.* 428 (2013), pp. 1116–1127. DOI: `10.1093/mnras/sts094`. arXiv: `1208.1491 [astro-ph.CO]`.

[60] Xingang Chen and Yi Wang. “Quasi-Single Field Inflation and Non-Gaussianities”. In: *JCAP* 1004 (2010), p. 027. DOI: `10.1088/1475-7516/2010/04/027`. arXiv: `0911.3380 [hep-th]`.

[61] Hayden Lee, Daniel Baumann, and Guilherme L. Pimentel. “Non-Gaussianity as a Particle Detector”. In: *JHEP* 12 (2016), p. 040. DOI: `10.1007/JHEP12(2016)040`. arXiv: `1607.03735 [hep-th]`.

[62] Archisman Ghosh et al. “Conformal Invariance and the Four Point Scalar Correlator in Slow-Roll Inflation”. In: *JHEP* 07 (2014), p. 011. DOI: `10.1007/JHEP07(2014)011`. arXiv: `1401.1426 [hep-th]`.

[63] Nima Arkani-Hamed et al. “The Cosmological Bootstrap: Inflationary Correlators from Symmetries and Singularities”. In: (2018). arXiv: `1811.00024 [hep-th]`.

[64] Rakibur Rahman and Massimo Taronna. “From Higher Spins to Strings: A Primer”. In: (Dec. 2015). arXiv: `1512.07932 [hep-th]`.

[65] Xian O. Camanho et al. “Causality Constraints on Corrections to the Graviton Three-Point Coupling”. In: *JHEP* 02 (2016), p. 020. DOI: `10.1007/JHEP02(2016)020`. arXiv: `1407.5597 [hep-th]`.

[66] Clifford Cheung et al. “The Effective Field Theory of Inflation”. In: *JHEP* 03 (2008), p. 014. DOI: `10.1088/1126-6708/2008/03/014`. arXiv: `0709.0293 [hep-th]`.

[67] Valentin Assassi et al. “Effective theory of large-scale structure with primordial non-Gaussianity”. In: *JCAP* 1511 (2015), p. 024. DOI: `10.1088/1475-7516/2015/11/024`. arXiv: `1505.06668 [astro-ph.CO]`.

[68] Valentin Assassi, Daniel Baumann, and Fabian Schmidt. “Galaxy Bias and Primordial Non-Gaussianity”. In: *JCAP* 1512.12 (2015), p. 043. DOI: `10.1088/1475-7516/2015/12/043`. arXiv: `1510.03723 [astro-ph.CO]`.

[69] Soubhik Kumar and Raman Sundrum. “Heavy-Lifting of Gauge Theories By Cosmic Inflation”. In: *JHEP* 05 (2018), p. 011. DOI: `10.1007/JHEP05(2018)011`. arXiv: `1711.03988 [hep-ph]`.

[70] Daniel Baumann and Daniel Green. “Signatures of Supersymmetry from the Early Universe”. In: *Phys. Rev. D* 85 (2012), p. 103520. DOI: `10.1103/PhysRevD.85.103520`. arXiv: `1109.0292 [hep-th]`.

[71] Soubhik Kumar and Raman Sundrum. “Cosmological Collider Physics and the Curvaton”. In: *JHEP* 04 (2020), p. 077. DOI: `10.1007/JHEP04(2020)077`. arXiv: `1908.11378 [hep-ph]`.

[72] Soubhik Kumar and Raman Sundrum. “Seeing Higher-Dimensional Grand Unification In Primordial Non-Gaussianities”. In: *JHEP* 04 (2019), p. 120. DOI: `10.1007/JHEP04(2019)120`. arXiv: `1811.11200 [hep-ph]`.

[73] Lian-Tao Wang and Zhong-Zhi Xianyu. “In Search of Large Signals at the Cosmological Collider”. In: *JHEP* 02 (2020), p. 044. DOI: `10.1007/JHEP02(2020)044`. arXiv: `1910.12876 [hep-ph]`.

[74] Lian-Tao Wang and Zhong-Zhi Xianyu. "Gauge Boson Signals at the Cosmological Collider". In: (Apr. 2020). arXiv: `2004.02887 [hep-ph]`.

[75] Xingang Chen, Yi Wang, and Zhong-Zhi Xianyu. "Neutrino Signatures in Primordial Non-Gaussianities". In: *JHEP* 09 (2018), p. 022. DOI: `10.1007/JHEP09(2018)022`. arXiv: `1805.02656 [hep-ph]`.

[76] Anson Hook, Junwu Huang, and Davide Racco. "Searches for other vacua. Part II. A new Higgstory at the cosmological collider". In: *JHEP* 01 (2020), p. 105. DOI: `10.1007/JHEP01(2020)105`. arXiv: `1907.10624 [hep-ph]`.

[77] Atsushi Higuchi. "Forbidden Mass Range for Spin-2 Field Theory in De Sitter Space-time". In: *Nucl. Phys.* B282 (1987), pp. 397–436. DOI: `10.1016/0550-3213(87)90691-2`.

[78] Alex Kehagias and Antonio Riotto. "On the Inflationary Perturbations of Massive Higher-Spin Fields". In: *JCAP* 1707.07 (2017), p. 046. DOI: `10.1088/1475-7516/2017/07/046`. arXiv: `1705.05834 [hep-th]`.

[79] Lorenzo Bordin et al. "Light Particles with Spin in Inflation". In: *JCAP* 1810.10 (2018), p. 013. DOI: `10.1088/1475-7516/2018/10/013`. arXiv: `1806.10587 [hep-th]`.

[80] Gabriele Franciolini et al. "Detecting higher spin fields through statistical anisotropy in the CMB bispectrum". In: *Phys. Rev.* D98.4 (2018), p. 043533. DOI: `10.1103/PhysRevD.98.043533`. arXiv: `1803.03814 [astro-ph.CO]`.

[81] Maresuke Shiraishi et al. "Signatures of anisotropic sources in the squeezed-limit bispectrum of the cosmic microwave background". In: *JCAP* 1305 (2013), p. 002. DOI: `10.1088/1475-7516/2013/05/002`. arXiv: `1302.3056 [astro-ph.CO]`.

[82] Azadeh Moradinezhad Dizgah et al. "Constraints on long-lived, higher-spin particles from galaxy bispectrum". In: *Phys. Rev.* D98.6 (2018), p. 063520. DOI: `10.1103/PhysRevD.98.063520`. arXiv: `1805.10247 [astro-ph.CO]`.

[83] Azadeh Moradinezhad Dizgah and Cora Dvorkin. "Scale-Dependent Galaxy Bias from Massive Particles with Spin during Inflation". In: *JCAP* 1801.01 (2018), p. 010. DOI: `10.1088/1475-7516/2018/01/010`. arXiv: `1708.06473 [astro-ph.CO]`.

[84] Zachary Slepian and Daniel J. Eisenstein. "A practical computational method for the anisotropic redshift-space three-point correlation function". In: *Mon. Not. Roy. Astron. Soc.* 478.2 (2018), pp. 1468–1483. DOI: `10.1093/mnras/sty1063`. arXiv: `1709.10150 [astro-ph.CO]`.

[85] Naonori S. Sugiyama et al. "A complete FFT-based decomposition formalism for the redshift-space bispectrum". In: *Mon. Not. Roy. Astron. Soc.* 484.1 (2019), pp. 364–384. DOI: `10.1093/mnras/sty3249`. arXiv: `1803.02132 [astro-ph.CO]`.

[86] Yasushi Suto and Misao Sasaki. “Quasinonlinear theory of cosmological self-gravitating systems”. In: *Phys. Rev. Lett.* 66 (3 1991), pp. 264–267. DOI: `10.1103/PhysRevLett.66.264`. URL: `https://link.aps.org/doi/10.1103/PhysRevLett.66.264`.

[87] Nobuyoshi Makino, Misao Sasaki, and Yasushi Suto. “Analytic approach to the perturbative expansion of nonlinear gravitational fluctuations in cosmological density and velocity fields”. In: *Phys. Rev. D* 46 (2 1992), pp. 585–602. DOI: `10.1103/PhysRevD.46.585`. URL: `https://link.aps.org/doi/10.1103/PhysRevD.46.585`.

[88] Enrico Pajer and Matias Zaldarriaga. “On the Renormalization of the Effective Field Theory of Large Scale Structures”. In: *JCAP* 1308 (2013), p. 037. DOI: `10.1088/1475-7516/2013/08/037`. arXiv: `1301.7182 [astro-ph.CO]`.

[89] Scott Dodelson and Fabian Schmidt. *Modern Cosmology Second Edition*. Amsterdam: Academic Press, 2021. ISBN: 978-0-12-815948-4.

[90] Pablo Fosalba and Enrique Gaztanaga. “Cosmological perturbation theory and the spherical collapse model: Part 1. Gaussian initial conditions”. In: *Mon. Not. Roy. Astron. Soc.* 301 (1998), pp. 503–523. DOI: `10.1046/j.1365-8711.1998.02033.x`. arXiv: `astro-ph/9712095`.

[91] F. Bernardeau et al. “Large scale structure of the universe and cosmological perturbation theory”. In: *Phys. Rept.* 367 (2002), pp. 1–248. DOI: `10.1016/S0370-1573(02)00135-7`. arXiv: `astro-ph/0112551 [astro-ph]`.

[92] Bhuvnesh Jain and Edmund Bertschinger. “Second order power spectrum and nonlinear evolution at high redshift”. In: *Astrophys. J.* 431 (1994), p. 495. DOI: `10.1086/174502`. arXiv: `astro-ph/9311070`.

[93] Ryuichi Takahashi. “Third Order Density Perturbation and One-loop Power Spectrum in a Dark Energy Dominated Universe”. In: *Prog. Theor. Phys.* 120 (2008), pp. 549–559. DOI: `10.1143/PTP.120.549`. arXiv: `0806.1437 [astro-ph]`.

[94] Diego Blas, Mathias Garny, and Thomas Konstandin. “Cosmological perturbation theory at three-loop order”. In: *JCAP* 01 (2014), p. 010. DOI: `10.1088/1475-7516/2014/01/010`. arXiv: `1309.3308 [astro-ph.CO]`.

[95] Asantha Cooray and Ravi K. Sheth. “Halo Models of Large Scale Structure”. In: *Phys. Rept.* 372 (2002), pp. 1–129. DOI: `10.1016/S0370-1573(02)00276-4`. arXiv: `astro-ph/0206508`.

[96] Zvonimir Vlah, Nora Elisa Chisari, and Fabian Schmidt. “An EFT description of galaxy intrinsic alignments”. In: *JCAP* 2001.01 (2020), p. 025. DOI: `10.1088/1475-7516/2020/01/025`. arXiv: `1910.08085 [astro-ph.CO]`.

[97] Patrick McDonald. "Clustering of dark matter tracers: Renormalizing the bias parameters". In: *Phys. Rev. D* 74 (2006). [Erratum: Phys.Rev.D 74, 129901 (2006)], p. 103512. DOI: `10.1103/PhysRevD.74.129901`. arXiv: `astro-ph/0609413`.

[98] Fabian Schmidt, Donghui Jeong, and Vincent Desjacques. "Peak-Background Split, Renormalization, and Galaxy Clustering". In: *Phys. Rev.* D88.2 (2013), p. 023515. DOI: `10.1103/PhysRevD.88.023515`. arXiv: `1212.0868 [astro-ph.CO]`.

[99] Shuichiro Yokoyama and Jiro Soda. "Primordial statistical anisotropy generated at the end of inflation". In: *JCAP* 0808 (2008), p. 005. DOI: `10.1088/1475-7516/2008/08/005`. arXiv: `0805.4265 [astro-ph]`.

[100] Fabian Schmidt and Donghui Jeong. "Cosmic Rulers". In: *Phys. Rev.* D86 (2012), p. 083527. DOI: `10.1103/PhysRevD.86.083527`. arXiv: `1204.3625 [astro-ph.CO]`.

[101] Pierre Fleury, Julien Larena, and Jean-Philippe Uzan. "Weak lensing distortions beyond shear". In: *Phys. Rev. D* 99.2 (2019), p. 023526. DOI: `10.1103/PhysRevD.99.023526`. arXiv: `1809.03924 [astro-ph.CO]`.

[102] Slava G. Turyshev and Viktor T. Toth. "Multipole decomposition of gravitational lensing". In: (July 2021). arXiv: `2107.13126 [gr-qc]`.

[103] Marc Kamionkowski et al. "Theory and statistics of weak lensing from large scale mass inhomogeneities". In: *Mon. Not. Roy. Astron. Soc.* 301 (1998), p. 1064. DOI: `10.1046/j.1365-8711.1998.02054.x`. arXiv: `astro-ph/9712030`.

[104] Marc Kamionkowski and Ely D. Kovetz. "The Quest for B Modes from Inflationary Gravitational Waves". In: *Ann. Rev. Astron. Astrophys.* 54 (2016), pp. 227–269. DOI: `10.1146/annurev-astro-081915-023433`. arXiv: `1510.06042 [astro-ph.CO]`.

[105] David M. Goldberg and David J. Bacon. "Galaxy-galaxy flexion: Weak lensing to second order". In: *Astrophys. J.* 619 (2005), pp. 741–748. DOI: `10.1086/426782`. arXiv: `astro-ph/0406376 [astro-ph]`.

[106] Yuki Okura, Keiichi Umetsu, and Toshifumi Futamase. "A New Measure for Weak Lensing Flexion". In: *Astrophys. J.* 660 (2007), pp. 995–1002. DOI: `10.1086/513135`. arXiv: `astro-ph/0607288 [astro-ph]`.

[107] J. N. Goldberg et al. "Spin-s Spherical Harmonics and ð". In: *Journal of Mathematical Physics* 8.11 (1967), pp. 2155–2161. DOI: `10.1063/1.1705135`. URL: `https://doi.org/10.1063/1.1705135`.

[108] Steven Weinberg. *Cosmology.* 2008. ISBN: 978-0-19-852682-7.

[109] Matias Zaldarriaga. "Nature of the E B decomposition of CMB polarization". In: *Phys. Rev. D* 64 (2001), p. 103001. DOI: `10.1103/PhysRevD.64.103001`. arXiv: `astro-ph/0106174`.

[110] Fabian Schmidt, Enrico Pajer, and Matias Zaldarriaga. "Large-Scale Structure and Gravitational Waves III: Tidal Effects". In: *Phys. Rev. D* 89.8 (2014), p. 083507. DOI: `10.1103/PhysRevD.89.083507`. arXiv: `1312.5616 [astro-ph.CO]`.

[111] Matteo Biagetti and Giorgio Orlando. "Primordial Gravitational Waves from Galaxy Intrinsic Alignments". In: *JCAP* 07 (2020), p. 005. DOI: `10.1088/1475-7516/2020/07/005`. arXiv: `2001.05930 [astro-ph.CO]`.

[112] J. J. Dalcanton, D. N. Spergel, and F J Summers. "The formation of disk galaxies". In: *Astrophys. J.* 482 (1997), pp. 659–676. DOI: `10.1086/304182`. arXiv: `astro-ph/9611226`.

[113] Vincent Desjacques, Donghui Jeong, and Fabian Schmidt. "Large-Scale Galaxy Bias". In: *Phys. Rept.* 733 (2018), pp. 1–193. DOI: `10.1016/j.physrep.2017.12.002`. arXiv: `1611.09787 [astro-ph.CO]`.

[114] Mehrdad Mirbabayi, Fabian Schmidt, and Matias Zaldarriaga. "Biased Tracers and Time Evolution". In: *JCAP* 1507.07 (2015), p. 030. DOI: `10.1088/1475-7516/2015/07/030`. arXiv: `1412.5169 [astro-ph.CO]`.

[115] Ananth Tenneti et al. "Intrinsic alignments of galaxies in the MassiveBlack-II simulation: analysis of two-point statistics". In: *Mon. Not. Roy. Astron. Soc.* 448.4 (2015), pp. 3522–3544. DOI: `10.1093/mnras/stv272`. arXiv: `1409.7297 [astro-ph.CO]`.

[116] Ananth Tenneti et al. "Galaxy shapes and alignments in the MassiveBlack-II hydrodynamic and dark matter-only simulations". In: *Mon. Not. Roy. Astron. Soc.* 453.1 (2015), pp. 469–482. DOI: `10.1093/mnras/stv1625`. arXiv: `1505.03124 [astro-ph.CO]`.

[117] Nora Elisa Chisari et al. "Redshift and luminosity evolution of the intrinsic alignments of galaxies in Horizon-AGN". In: *Mon. Not. Roy. Astron. Soc.* 461.3 (2016), pp. 2702–2721. DOI: `10.1093/mnras/stw1409`. arXiv: `1602.08373 [astro-ph.CO]`.

[118] Jonathan Blazek et al. "Beyond linear galaxy alignments". In: *Phys. Rev. D* 100.10 (2019), p. 103506. DOI: `10.1103/PhysRevD.100.103506`. arXiv: `1708.09247 [astro-ph.CO]`.

[119] Sukhdeep Singh, Rachel Mandelbaum, and Surhud More. "Intrinsic alignments of SDSS-III BOSS LOWZ sample galaxies". In: *Mon. Not. Roy. Astron. Soc.* 450.2 (2015), pp. 2195–2216. DOI: `10.1093/mnras/stv778`. arXiv: `1411.1755 [astro-ph.CO]`.

[120] Raul Angulo et al. "On the Statistics of Biased Tracers in the Effective Field Theory of Large Scale Structures". In: *JCAP* 09 (2015), p. 029. DOI: `10.1088/1475-7516/2015/9/029`. arXiv: `1503.08826 [astro-ph.CO]`.

[121] Phillip James Edwin Peebles. *The Large-Scale Structure of the Universe*. Princeton University Press, 1980.

[122] Ali Akbar Abolhasani, Mehrdad Mirbabayi, and Enrico Pajer. “Systematic Renormalization of the Effective Theory of Large Scale Structure”. In: *JCAP* 05 (2016), p. 063. DOI: `10.1088/1475-7516/2016/05/063`. arXiv: `1509.07886 [hep-th]`.

[123] Simon Foreman, Hideki Perrier, and Leonardo Senatore. “Precision Comparison of the Power Spectrum in the EFTofLSS with Simulations”. In: *JCAP* 1605.05 (2016), p. 027. DOI: `10.1088/1475-7516/2016/05/027`. arXiv: `1507.05326 [astro-ph.CO]`.

[124] Simon Foreman and Leonardo Senatore. “The EFT of Large Scale Structures at All Redshifts: Analytical Predictions for Lensing”. In: *JCAP* 04 (2016), p. 033. DOI: `10.1088/1475-7516/2016/04/033`. arXiv: `1503.01775 [astro-ph.CO]`.

[125] Yannick Mellier. “Probing the universe with weak lensing”. In: *Ann. Rev. Astron. Astrophys.* 37 (1999), pp. 127–189. DOI: `10.1146/annurev.astro.37.1.127`. arXiv: `astro-ph/9812172 [astro-ph]`.

[126] Elisabeth Krause and Christopher M. Hirata. “Weak lensing power spectra for precision cosmology: Multiple-deflection, reduced shear and lensing bias corrections”. In: *Astron. Astrophys.* 523 (2010), A28. DOI: `10.1051/0004-6361/200913524`. arXiv: `0910.3786 [astro-ph.CO]`.

[127] Massimo Viola, Peter Melchior, and Matthias Bartelmann. “Shear-flexion crosstalk in weak-lensing measurements”. In: *Mon. Not. Roy. Astron. Soc.* 419 (2012), p. 2215. DOI: `10.1111/j.1365-2966.2011.19872.x`. arXiv: `1107.3920 [astro-ph.CO]`.

[128] C. Chang et al. “The Effective Number Density of Galaxies for Weak Lensing Measurements in the LSST Project”. In: *Mon. Not. Roy. Astron. Soc.* 434 (2013), p. 2121. DOI: `10.1093/mnras/stt1156`. arXiv: `1305.0793 [astro-ph.CO]`.

[129] Nora Elisa Chisari et al. “Multitracing Anisotropic Non-Gaussianity with Galaxy Shapes”. In: *Phys. Rev.* D94.12 (2016), p. 123507. DOI: `10.1103/PhysRevD.94.123507`. arXiv: `1607.05232 [astro-ph.CO]`.

[130] Max Tegmark, Andy Taylor, and Alan Heavens. “Karhunen-Loeve eigenvalue problems in cosmology: How should we tackle large data sets?” In: *Astrophys. J.* 480 (1997), p. 22. DOI: `10.1086/303939`. arXiv: `astro-ph/9603021`.

[131] Douglas Scott et al. “The information content of cosmic microwave background anisotropies”. In: *JCAP* 1606.06 (2016), p. 046. DOI: `10.1088/1475-7516/2016/06/046`. arXiv: `1603.03550 [astro-ph.CO]`.

[132] Licia Verde. “Statistical methods in cosmology”. In: *Lect. Notes Phys.* 800 (2010), pp. 147–177. DOI: `10.1007/978-3-642-10598-2_4`. arXiv: `0911.3105 [astro-ph.CO]`.

[133] Sabino Matarrese and Licia Verde. “The effect of primordial non-Gaussianity on halo bias”. In: *Astrophys. J.* 677 (2008), pp. L77–L80. DOI: `10.1086/587840`. arXiv: `0801.4826 [astro-ph]`.

[134] Fabian Schmidt and Marc Kamionkowski. “Halo Clustering with Non-Local Non-Gaussianity”. In: *Phys. Rev.* D82 (2010), p. 103002. DOI: `10.1103/PhysRevD.82.103002`. arXiv: `1008.0638 [astro-ph.CO]`.

[135] Takahiko Matsubara. “Deriving an Accurate Formula of Scale-dependent Bias with Primordial Non-Gaussianity: An Application of the Integrated Perturbation Theory”. In: *Phys. Rev.* D86 (2012), p. 063518. DOI: `10.1103/PhysRevD.86.063518`. arXiv: `1206.0562 [astro-ph.CO]`.

[136] Jonathan Blazek, Zvonimir Vlah, and Uroš Seljak. “Tidal alignment of galaxies”. In: *JCAP* 1508.08 (2015), p. 015. DOI: `10.1088/1475-7516/2015/08/015`. arXiv: `1504.02510 [astro-ph.CO]`.

[137] Planck Collaboration XIII. “Planck 2015 results. XIII. Cosmological parameters”. In: *A&A* 594 (2016), A13. DOI: `10.1051/0004-6361/201525830`. arXiv: `1502.01589 [astro-ph.CO]`.

[138] David Alonso et al. “Ultra large-scale cosmology in next-generation experiments with single tracers”. In: *Astrophys. J.* 814.2 (2015), p. 145. DOI: `10.1088/0004-637X/814/2/145`. arXiv: `1505.07596 [astro-ph.CO]`.

[139] Azadeh Moradinezhad Dizgah et al. “Galaxy Bispectrum from Massive Spinning Particles”. In: *JCAP* 1805.05 (2018), p. 013. DOI: `10.1088/1475-7516/2018/05/013`. arXiv: `1801.07265 [astro-ph.CO]`.

[140] Jérôme Gleyzes et al. “Biasing and the search for primordial non-Gaussianity beyond the local type”. In: *JCAP* 1704.04 (2017), p. 002. DOI: `10.1088/1475-7516/2017/04/002`. arXiv: `1612.06366 [astro-ph.CO]`.

[141] D. Nelson Limber. “The Analysis of Counts of the Extragalactic Nebulae in Terms of a Fluctuating Density Field. II”. In: *Astrophys. J.* 119 (1954), p. 655. DOI: `10.1086/145870`.

[142] Marilena LoVerde and Niayesh Afshordi. “Extended Limber Approximation”. In: *Phys. Rev.* D78 (2008), p. 123506. DOI: `10.1103/PhysRevD.78.123506`. arXiv: `0809.5112 [astro-ph]`.

[143] Emiliano Sefusatti et al. “Effects and Detectability of Quasi-Single Field Inflation in the Large-Scale Structure and Cosmic Microwave Background”. In: *JCAP* 1208 (2012), p. 033. DOI: `10.1088/1475-7516/2012/08/033`. arXiv: `1204.6318 [astro-ph.CO]`.

[144] N. Bartolo et al. “An Estimator for statistical anisotropy from the CMB bispectrum”. In: *JCAP* 1201 (2012), p. 029. DOI: `10.1088/1475-7516/2012/01/029`. arXiv: `1107.4304 [astro-ph.CO]`.

[145] Jaiseung Kim and Eiichiro Komatsu. “Limits on anisotropic inflation from the Planck data”. In: *Phys. Rev.* D88 (2013), p. 101301. DOI: `10.1103/PhysRevD.88.101301`. arXiv: `1310.1605 [astro-ph.CO]`.

[146] Maresuke Shiraishi, Naonori S. Sugiyama, and Teppei Okumura. "Polypolar spherical harmonic decomposition of galaxy correlators in redshift space: Toward testing cosmic rotational symmetry". In: *Phys. Rev.* D95.6 (2017), p. 063508. DOI: `10.1103/PhysRevD.95.063508`. arXiv: `1612.02645 [astro-ph.CO]`.

[147] Naonori S. Sugiyama, Maresuke Shiraishi, and Teppei Okumura. "Limits on statistical anisotropy from BOSS DR12 galaxies using bipolar spherical harmonics". In: *Mon. Not. Roy. Astron. Soc.* 473.2 (2018), pp. 2737–2752. DOI: `10.1093/mnras/stx2333`. arXiv: `1704.02868 [astro-ph.CO]`.

[148] Nicola Bartolo et al. "Detecting higher spin fields through statistical anisotropy in the CMB and galaxy power spectra". In: *Phys. Rev.* D97.2 (2018), p. 023503. DOI: `10.1103/PhysRevD.97.023503`. arXiv: `1709.05695 [astro-ph.CO]`.

[149] Gabriele Franciolini, Alex Kehagias, and Antonio Riotto. "Imprints of Spinning Particles on Primordial Cosmological Perturbations". In: *JCAP* 1802.02 (2018), p. 023. DOI: `10.1088/1475-7516/2018/02/023`. arXiv: `1712.06626 [hep-th]`.

[150] Kazuyuki Akitsu, Masahiro Takada, and Yin Li. "Large-scale tidal effect on redshift-space power spectrum in a finite-volume survey". In: *Phys. Rev.* D95.8 (2017), p. 083522. DOI: `10.1103/PhysRevD.95.083522`. arXiv: `1611.04723 [astro-ph.CO]`.

[151] Masahiro Takada and Wayne Hu. "Power Spectrum Super-Sample Covariance". In: *Phys. Rev.* D87.12 (2013), p. 123504. DOI: `10.1103/PhysRevD.87.123504`. arXiv: `1302.6994 [astro-ph.CO]`.

[152] Asantha Cooray and Wayne Hu. "Second order corrections to weak lensing by large scale structure". In: *Astrophys. J.* 574 (2002), p. 19. DOI: `10.1086/340892`. arXiv: `astro-ph/0202411`.

[153] H. Ehrentraut and W. Muschik. "On Symmetric irreducible tensors in d-dimensions". In: *ARI - An International Journal for Physical and Engineering Sciences* 51.2 (1998), pp. 149–159. ISSN: 1434-565X. DOI: `10.1007/s007770050048`. URL: `https://doi.org/10.1007/s007770050048`.

[154] Andreas S. Schmidt et al. "Cosmological N-Body Simulations with a Large-Scale Tidal Field". In: *Mon. Not. Roy. Astron. Soc.* 479.1 (2018), pp. 162–170. DOI: `10.1093/mnras/sty1430`. arXiv: `1803.03274 [astro-ph.CO]`.

[155] Shogo Masaki, Takahiro Nishimichi, and Masahiro Takada. "Anisotropic separate universe simulations". In: *Mon. Not. Roy. Astron. Soc.* 496.1 (2020), pp. 483–496. DOI: `10.1093/mnras/staa1579`. arXiv: `2003.10052 [astro-ph.CO]`.

[156] Kazuyuki Akitsu, Yin Li, and Teppei Okumura. "Cosmological simulation in tides: power spectrum and halo shape responses, and shape assembly bias". In: (Nov. 2020). arXiv: `2011.06584 [astro-ph.CO]`.